

The  $Q_{Weak}^p$  Experiment:  
“A Search for New Physics at the TeV Scale  
via a Measurement of the Proton’s Weak Charge”

Jlab E02-020

December 6, 2004

**The Collaboration**

D.S. Armstrong<sup>1</sup>, T. Averett<sup>1</sup>, J. Birchall<sup>7</sup>, T. Botto<sup>8</sup>, P. Bosted<sup>9</sup>, J.D. Bowman<sup>5</sup>, A. Bruell<sup>9</sup>, R. Carlini<sup>9</sup> (Principal Investigator), S. Chattopadhyay<sup>9</sup>, S. Covrig<sup>1,2</sup>, C.A. Davis<sup>11</sup>, J. Doornbos<sup>11</sup>, K. Dow<sup>8</sup>, J. Dunne<sup>14</sup>, J. Erler<sup>3</sup>, R. Ent<sup>9</sup>, W. Falk<sup>7</sup>, M. Farkhondeh<sup>8</sup>, J.M. Finn<sup>1</sup>, T.A. Forest<sup>6</sup>, W. Franklin<sup>8</sup>, D. Gaskell<sup>9</sup>, M. Gericke<sup>7</sup>, K. Grimm<sup>8</sup>, F.W. Hersman<sup>12</sup>, M. Holtrop<sup>12</sup>, K. Johnston<sup>6</sup>, R. Jones<sup>2</sup>, K. Joo<sup>2</sup>, C. Keppel<sup>18</sup>, E. Korkmaz<sup>15</sup>, S. Kowalski<sup>8</sup>, L. Lee<sup>7</sup>, Y. Liang<sup>17</sup>, A. Lung<sup>9</sup>, D. Mack<sup>9</sup>, S. Majewski<sup>9</sup>, J. Mammei<sup>10</sup>, R. Mammei<sup>10</sup>, J. Martin<sup>20</sup>, D. Meekins<sup>9</sup>, H. Mkrtchyan<sup>13</sup>, G.S. Mitchell<sup>5</sup>, N. Morgan<sup>10</sup>, A. K. Opper<sup>17</sup>, S.A. Page<sup>7</sup>, S. Penttila<sup>5</sup>, M. Pitt<sup>10</sup>, M. Poelker<sup>9</sup>, T. Porcelli<sup>15</sup>, Y. Prok<sup>8</sup>, W. D. Ramsay<sup>7</sup>, M. Ramsey-Musolf<sup>4</sup>, J. Roche<sup>1,9</sup>, N. Simicevic<sup>6</sup>, G. Smith<sup>9</sup> (Project Manager), T. Smith<sup>19</sup>, R. Suleiman<sup>10</sup>, E. Tsentalovich<sup>8</sup>, W.T.H. van Oers<sup>7</sup>, S. Wells<sup>6</sup>, W.S. Wilburn<sup>5</sup>, S.A. Wood<sup>9</sup>, C. Zorn<sup>9</sup>

**The Institutions**

<sup>1</sup>College of William and Mary, Williamsburg, VA, <sup>2</sup>University of Connecticut, Storrs, Connecticut, <sup>3</sup>Instituto de Fisica, Universidad Nacional Autonoma de Mexico, Mexico, <sup>4</sup>Kellogg Radiation Laboratory, California Institute of Technology, Pasadena, California, <sup>5</sup>Los Alamos National Laboratory, Los Alamos, New Mexico, <sup>6</sup>Louisiana Tech University, Ruston, Louisiana, <sup>7</sup>University of Manitoba, Winnipeg, Manitoba, Canada, <sup>8</sup>Massachusetts Institute of Technology, Cambridge, Massachusetts, <sup>9</sup>TJNAF, Newport News, VA, <sup>10</sup>Virginia Polytechnic Institute, Blacksburg, Virginia, <sup>11</sup>TRIUMF, Vancouver, Canada, <sup>12</sup>University of New Hampshire, <sup>13</sup>Yerevan Physics Institute, <sup>14</sup>Mississippi State University, <sup>15</sup>University of Northern British Columbia, <sup>17</sup>Ohio University, <sup>18</sup>Hampton University, <sup>19</sup>Dartmouth College, <sup>20</sup>University of Winnipeg, Manitoba, Canada

# Contents

<b>1</b>	<b>Introduction</b>	<b>7</b>
<b>2</b>	<b>Physics Motivation</b>	<b>9</b>
2.1	Running of $\sin^2 \theta_W$ . . . . .	10
2.2	Theoretical Interpretability . . . . .	13
2.3	Beyond the Standard Model . . . . .	16
2.4	Model Independent Constraints . . . . .	17
2.4.1	Experimental Constraints on the Vector Weak Charges of u-, d-quarks . . . . .	18
2.4.2	Constraints on Couplings and Charges Associated with Possible New Physics . . . . .	18
2.4.3	Relation to Other Measurements . . . . .	19
2.5	Model Dependent Constraints . . . . .	22
2.5.1	Extra Neutral Gauge Interactions . . . . .	22
2.5.2	Supersymmetry . . . . .	23
2.5.3	Leptoquarks . . . . .	25
2.6	Summary . . . . .	28
<b>3</b>	<b>Overview of the Experiment</b>	<b>29</b>
<b>4</b>	<b>Magnetic Spectrometer and Collimation System</b>	<b>34</b>
4.1	Basic Design Criteria . . . . .	34
4.2	Geometry and Magnetic Properties . . . . .	34
4.3	Field Calculations and Magnet Optics . . . . .	34
4.4	Detailed Coil Design . . . . .	40
4.5	Fabrication and Alignment Tolerances . . . . .	40
4.6	Magnetic Field Verification . . . . .	43
4.7	QTOR Support Structure . . . . .	44
4.8	Electrical Specification of Magnet and Power Supply . . . . .	46
4.9	QTOR Fabrication and Assembly . . . . .	47
4.10	Collimator Design . . . . .	48

<b>5</b>	<b>Detector System</b>	<b>54</b>
5.1	Design criteria . . . . .	54
5.2	Technical solutions . . . . .	55
5.2.1	Radiator . . . . .	55
5.2.2	Photomultipliers . . . . .	57
5.2.3	Front-end electronics and ADC's . . . . .	59
5.3	Expected detector system performance . . . . .	61
5.3.1	Photoelectron yield and position dependence . . . . .	61
5.3.2	System linearity . . . . .	62
5.3.3	Excess noise . . . . .	63
5.4	Validation of detector performance . . . . .	65
5.4.1	Excess noise . . . . .	65
5.4.2	Ground loops . . . . .	66
<b>6</b>	<b>Tracking System</b>	<b>68</b>
6.1	$Q^2$ Determination Requirements . . . . .	69
6.2	Tracking System Overview . . . . .	71
6.3	Rate Considerations for Tracking Chambers . . . . .	73
6.4	Mini-Torus Møller Electron Sweeping Magnet . . . . .	73
6.5	Region 1: Vertex Detectors (GEM) . . . . .	74
6.6	Region 2: Magnet Entrance Chambers (HDC) . . . . .	77
6.7	Region 3: Focal Plane Chambers (VDC) . . . . .	79
6.8	Scintillation Detectors . . . . .	83
<b>7</b>	<b>Liquid Hydrogen Target System</b>	<b>86</b>
7.1	Refrigeration . . . . .	87
7.2	Boiling and Density Fluctuations . . . . .	89
7.3	Basic Conceptual Target Design . . . . .	92
7.3.1	Heat Exchanger . . . . .	94
7.3.2	Cryogenic Pump . . . . .	94

7.3.3	Target Heater . . . . .	94
7.3.4	Target Cell . . . . .	95
<b>8</b>	<b>Backgrounds</b>	<b>96</b>
8.1	Prompt backgrounds . . . . .	96
8.1.1	Target window backgrounds . . . . .	97
8.1.2	Pion electroproduction . . . . .	98
8.2	Soft backgrounds . . . . .	99
8.2.1	GEANT simulations . . . . .	100
8.2.2	Measurement of soft backgrounds . . . . .	102
<b>9</b>	<b>Systematic Errors</b>	<b>106</b>
9.1	Overview . . . . .	106
9.2	Sensitivity to Helicity-Correlated Beam Motion . . . . .	106
9.3	Sensitivity to Beam Size Modulation . . . . .	108
9.4	Sensitivity to Angle of Beam on Target . . . . .	109
9.5	Summary of Beam Requirements . . . . .	109
9.6	Feedback for Control of Helicity-Correlated Beam Parameters . . . . .	110
9.7	Luminosity monitor . . . . .	111
9.8	Effects due to transverse polarization . . . . .	115
9.9	Hadronic Structure Contributions . . . . .	116
<b>10</b>	<b>Beam Diagnostics</b>	<b>119</b>
10.1	Current mode . . . . .	119
10.1.1	Cavity-Style Beam Charge Monitors . . . . .	120
10.1.2	Beam Position Monitors . . . . .	122
10.2	Low Current Diagnostics . . . . .	126
<b>11</b>	<b>Polarized Source Issues for the <math>Q_{Weak}^p</math> Experiment</b>	<b>128</b>
<b>12</b>	<b>Precision Beam Polarimetry</b>	<b>132</b>

12.1	Basel Møller Polarimeter in Hall C . . . . .	132
12.2	Hall C Compton Polarimeter . . . . .	135
<b>13</b>	<b>Data Acquisition</b>	<b>139</b>
13.1	Current mode DAQ . . . . .	139
13.2	Low current tracking DAQ . . . . .	139
13.3	Beam Feedback . . . . .	140
<b>14</b>	<b>Beam Request</b>	<b>141</b>
<b>15</b>	<b>Collaboration and Management Issues</b>	<b>144</b>
<b>A</b>	<b>Miscellaneous Administrative Limits</b>	<b>151</b>
A.1	Beam Dump Current Density Limit . . . . .	151
A.2	Site Boundary Dose . . . . .	151
A.3	Beam Containment Policy Current Limit . . . . .	153
A.4	Physics Division Administrative Limit . . . . .	153

## Abstract

We propose<sup>1</sup> a precision measurement of parity violating electron scattering on the proton at very low  $Q^2$  and forward angles to challenge predictions of the Standard Model and search for new physics. A unique opportunity exists to carry out the first precision measurement of the proton's weak charge,  $Q_{Weak}^p = 1 - 4\sin^2\theta_W$ , at JLab, building on technical advances that have been made in the laboratory's world-leading parity violation program and using the results of earlier experiments to constrain hadronic corrections. A 2200 hour (production running) measurement of the parity violating asymmetry in elastic  $ep$  scattering at  $Q^2 = 0.03 \text{ (GeV/c)}^2$  employing 180  $\mu A$  of 85% polarized beam on a 35 cm liquid hydrogen target will determine the proton's weak charge with  $\simeq 4\%$  combined statistical and systematic errors. The Standard Model makes a firm prediction of  $Q_{Weak}^p$ , based on the running of the weak mixing angle,  $\sin^2\theta_W$ , from the  $Z^0$  pole down to low energies, corresponding to a  $10\sigma$  effect in our experiment. Any significant deviation of  $\sin^2\theta_W$  from the Standard Model prediction at low  $Q^2$  would be a signal of new physics, whereas agreement would place new and significant constraints on possible Standard Model extensions. In the absence of physics beyond the Standard Model, our experiment will provide a  $\simeq 0.3\%$  measurement of  $\sin^2\theta_W$ , making this the most precise standalone measurement of the weak mixing angle at low  $Q^2$ .

---

<sup>1</sup>This proposal and other documents are available at the home page of the  $Q_{Weak}^p$  Collaboration: <http://www.jlab.org/Qweak/>.

# 1 Introduction

The  $Q_{Weak}^p$  experiment (E02-020) was initially approved at the 21st meeting of the Jefferson Laboratory Program Advisory Committee in January, 2002, and was awarded an “A” scientific rating. Since that time, our collaboration has grown significantly<sup>2</sup>, formal DOE project approval has been obtained, and full funding has been approved through NSERC, NSF, DOE and University matching contributions. The project underwent a successful technical review in 2003 chaired by David Cassel of Cornell University, and a DOE approved Project Management Plan is in place<sup>3</sup>. Major equipment construction activities are underway at collaborating institutions and commercial vendors. A schedule has been adopted for the experiment, with the aim of initial installation in JLab’s Hall C in late 2007 or early 2008. This document is an updated version of the 2002  $Q_{Weak}^p$  proposal, in which we review the scientific justification for the experiment, we describe in detail the proposed experimental technique, and we include new results from extensive Monte Carlo simulations which help to validate our technical and scientific approach.

The  $Q_{Weak}^p$  experiment will provide the first precision measurement of the proton’s weak charge,  $Q_{Weak}^p = 1 - 4\sin^2\theta_W$  by measuring the parity-violating asymmetry in electron-proton elastic scattering at very small momentum transfer:  $Q^2 = 0.03 (GeV/c)^2$ . This in turn will constitute a precision measurement of the weak mixing angle  $\sin^2\theta_W$  (to  $\pm 0.3\%$ ), at low energy, which is uniquely sensitive to new physics beyond the Standard Model.

The present suite of completed weak charge measurements at low  $Q^2$  consists of:

- the atomic cesium measurement[1] of  $Q_{Weak}(N, Z)$ , whose interpretation is limited by many-body theoretical uncertainties;
- the high energy neutrino-nucleus scattering NuTeV measurement[2], which observes a  $2.5\sigma$  deviation from the SM prediction that (although not proven) is suspected of being due to hadronic structure associated with the use of an Iron target; and
- the electron weak charge measurement carried out via parity violating Møller scattering in SLAC E158[3], which although eminently interpretable is no more precise than the NuTeV measurement and there are no plans to conduct additional running to further reduce uncertainties.

These three measurements each achieved roughly the same uncertainty on the extracted value of  $\sin^2\theta_W$ . The  $Q_{Weak}^p$  experiment should produce a final error bar that is a factor of two more precise than any of the previous measurements. Further, we believe that the  $Q_{Weak}^p$  measurement will be very clean with respect to theoretical interpretability, as we rely primarily upon experimental data, not theoretical calculations, to remove the dominant hadronic background.

---

<sup>2</sup>The original proposal cited 30 collaborators from 11 institutions;  $Q_{Weak}^p$  now has 63 collaborators from 20 scientific institutions.

<sup>3</sup>The Project Management Plan (PMP), Technical Design Report (TDR) with Cassel Committee review findings, and this proposal are available at the home page of the  $Q_{Weak}^p$  Collaboration: <http://www.jlab.org/Qweak/>.

The experiment proposed here builds upon the successful parity violation program at Jefferson Lab. The current parity-violation experiments (HAPPEX, HAPPEX II, HAPPEX  $^4\text{He}$ , and  $G^0$ ) will provide high quality data on form factors that will be used to determine the contributions of hadronic structure to the proposed measurement. Unlike the other elements of this program, the  $Q_{Weak}^p$  experiment will constitute the first precision Standard Model test to be carried out at Jefferson Lab. The technical developments that are required for this experiment to proceed are relatively straightforward extensions of what has already been achieved with Jefferson Lab’s world-leading polarized electron source or planned for future elements of the laboratory’s parity program. The technical concept of the experiment is very straightforward, and we are confident that the experiment can be carried out to the stated precision goals. It is worth noting that the majority of critical “parity quality” beam requirements necessary for the success of  $Q_{Weak}^p$  have in fact already been achieved during the running of previous parity experiments at JLab. These requirements will be discussed in detail later in the proposal.

The  $Q_{Weak}^p$  program of measurements is most logically conducted in two steps, with potentially a third step to further decrease the error bar, depending on the outcome of what is proposed here, as follows:

- In step 1, we will perform an 8% measurement of  $Q_{Weak}^p$ , which will match the precision of the cesium atomic parity violation, SLAC E-158, and NuTeV measurements. This can be achieved in about 14 days of production running. An 8% measurement of  $Q_{Weak}^p$  will produce a  $5\sigma$  measurement of the running of  $\sin^2\theta_W$  from the  $Z^\circ$  pole, and will be sensitive enough to eliminate any coupling constant “conspiracy” that might be masking the possible appearance of new physics in the cesium  $Q_{Weak}(N, Z)$  measurement.
- In step 2, we will perform a 4% precision measurement of  $Q_{Weak}^p$  which can be achieved in about 92 days of production running. This will provide a  $10\sigma$  measurement of the running of  $\sin^2\theta_W$  with respect to the  $Z^\circ$  pole, which will provide a significant stand alone constraint on (or possibly evidence for) classes of Leptoquark extensions to the Standard Model which are not visible in  $Q_{Weak}^e$  measurements. Additionally, if a  $Z'$  is discovered at the LHC and our experiment finds a significant discrepancy with the Standard Model prediction, the  $Q_{Weak}^p$  result could be used to determine the sign of the coupling constant associated with this new physics.
- Building on the above effort, a possible third generation 2.5% precision measurement of  $Q_{Weak}^p$  would offer significantly increased sensitivity to new physics at the TeV scale.

The  $Q_{Weak}^p$  experiment has significant discovery potential and has become a major new thrust of the scientific program at Jefferson Lab. The collaboration is actively investigating the limits of our experimental technique to determine if additional runs possibly with higher beam currents and of longer duration would allow a measurement of  $Q_{Weak}^p$  approaching the  $\simeq 2.5\%$  level. Experience and technology developed for the  $Q_{Weak}^p$  experiment will be essential if the parity program at JLab is to continue into a 12 GeV phase with a possible precision measurement of the electron’s weak charge via parity violating Møller scattering. It should be noted that the

NSAC Long Range Plan has identified the search for physics beyond the Standard Model as one of the five primary scientific goals for nuclear science during the coming decade. Like the parity violating deep inelastic scattering experiment performed at SLAC in the 1970's which had such a major impact on the fields of nuclear and particle physics [4,5], the  $Q_{Weak}^p$  measurement proposed here could become Jefferson Laboratory's signature contribution to the quest for physics beyond the Standard Model.

It should also be noted that key theorists continue to play a very active role in the collaboration, contributing to a sharpened physics case for the proposed measurement in the context of plausible competing theories for Standard Model extensions. The theory section of this proposal contains predictions of alternate theories and their implications for  $Q_{Weak}^p$ .

## 2 Physics Motivation

Precision tests have traditionally played a crucial role in elucidating the structure of the electroweak interaction. Measurements to date have provided an impressive array of constraints both on the Standard Model as well as on proposed scenarios for extending it. Measurements at the  $Z^0$  pole have constrained the weak mixing angle  $\sin^2 \theta_W$  to impressive precision at that energy scale. However, an experimental study of the evolution of the weak mixing angle to lower energies with a comparable precision has not yet been carried out.

We will determine  $Q_{Weak}^p$  by measuring the parity violating asymmetry in elastic  $ep$  scattering at  $Q^2 = 0.03 (GeV/c)^2$ . A toroidal magnetic field will focus elastically scattered electrons onto a set of 8 rectangular quartz Cerenkov detectors coupled to photomultiplier tubes which will be read out in current mode. The acceptance averaged asymmetry in our design is -0.28 ppm; we will measure this asymmetry to about  $\pm 2.2\%$  combined statistical and systematic errors in a 2200 hour (production running) measurement with 180  $\mu A$  of 85% polarized beam on a 35 cm liquid Hydrogen target. This measurement will determine the proton's weak charge with  $\simeq 4\%$  combined statistical and systematic errors, leading to a determination of  $\sin^2 \theta_W$  at the  $\pm 0.3\%$  level at low energy.

The Standard Model evolution predicts a shift of  $\Delta \sin^2 \theta_W = +0.007$  at low  $Q^2$  with respect to the  $Z^0$  pole best fit value of  $0.23113 \pm 0.00015$ . Figure 1 shows a calculation by Erler and Ramsey-Musolf for  $\sin^2 \theta_W$  together with existing and proposed world data[6][7]. The very precise measurements near the  $Z^0$  pole set the overall magnitude of the curve. Testing this prediction requires a set of precision measurements at a variety of energy scales with sufficiently small and well understood experimental and theoretical uncertainties that the results can be interpreted with confidence. The expected evolution of  $\sin^2 \theta_W$  corresponds to a 10 standard deviation effect in our proposed measurement, including both experimental and theoretical systematic errors[6]. Any significant deviation of  $\sin^2 \theta_W$  from the Standard Model prediction at low  $Q^2$  would be a signal of new physics, whereas agreement would place new and significant constraints on possible Standard Model extensions.

It must be stressed that there is an essential complementarity between high energy studies at

the  $Z^0$  pole in  $e^+e^-$  collisions and precision low energy tests, of which the  $Q_{Weak}^p$  experiment is one. Small but perceptible deviations of a handful of low energy observables from their Standard Model predicted values are already beginning to provide new clues about the nature of physics that lies beyond. Measurements have been done to look for deviations from the Standard Model evolution of  $\sin^2\theta_W$  extracted from atomic parity violation and neutrino deep inelastic scattering experiments, but significant uncertainties in the theoretical interpretation of these measurements limit the impact of their results. In contrast, a precision measurement of the weak charge of the proton,  $Q_{Weak}^p = 1 - 4\sin^2\theta_W$ , proposed here at Jefferson Laboratory, addresses similar physics issues but is free of many-body theoretical uncertainties and will have a factor of two better precision. The dominant hadronic effects that must be accounted for in extracting  $Q_{Weak}^p$  from the data are contained in form factor contributions which can be sufficiently constrained by the current program of parity violating electron scattering measurements without heavy reliance on theoretical nucleon structure calculations.

This new experiment will be a crucial element of a program of very sensitive low energy tests of the Standard Model as it will be both precise and complementary to previous efforts such as the recently completed SLAC E158[3] which carried out parity violating asymmetry measurements at a similar  $Q^2$  in the purely leptonic sector.

## 2.1 Running of $\sin^2\theta_W$

An essential, but not yet well-tested, prediction of the Standard Model is the variation of  $\sin^2\theta_W$  with momentum transfer  $Q^2$ , referred to as the “running of  $\sin^2\theta_W$ ”. As with the QED and QCD couplings,  $\alpha(\mu^2)$  and  $\alpha_s(\mu^2)$ , the running of  $\sin^2\theta_W(\mu^2)$  is an effective parameter defined at a scale  $\mu^2 \sim Q^2$  at which a given experiment is performed. The  $\mu$ -dependence arises from loop corrections to the electroweak gauge couplings and, thus, reflects the content of the Standard Model beyond tree-level.

Testing the Standard Model prediction for the running of  $\sin^2\theta_W$  requires input from both experiment and theory. Experimentally, one requires a set of precision measurements at a variety of  $Q^2$  points, with sufficiently small and well understood theoretical uncertainties associated with the extraction of  $\sin^2\theta_W$ , that one can interpret the results with confidence. It clearly also requires a careful evaluation of the Standard Model loop effects that enter  $\sin^2\theta_W$ . At one-loop order, these effects contain large logarithms that are properly resummed using the renormalization group (RG). An analogous situation occurs for both  $\alpha(\mu^2)$  and  $\alpha_s(\mu^2)$ . In the latter case, experimental tests have been crucial in establishing QCD as the correct theory of the strong interaction [8], while the RG evolution of the QED coupling has also been demonstrated experimentally [9]. However, a definitive, analogous test for the electroweak gauge sector of the Standard Model has yet to be realized.

As with  $\alpha(\mu^2)$  and  $\alpha_s(\mu^2)$ , the evolution of  $\sin^2\theta_W(\mu^2)$  depends on choice of renormalization scheme. Here, we follow Ref. [7] and use the  $\overline{\text{MS}}$  scheme, wherein the loop effects that determine the low-energy weak mixing angle are common to all low-energy neutral current experiments, including both E158 and  $Q_{Weak}^p$ . We note that the  $\overline{\text{MS}}$  quantity  $\sin^2\hat{\theta}_W(\mu^2)$  is gauge invariant.

# Weak Mixing Angle

Scale dependence in  $\overline{\text{MS}}$  scheme including higher orders

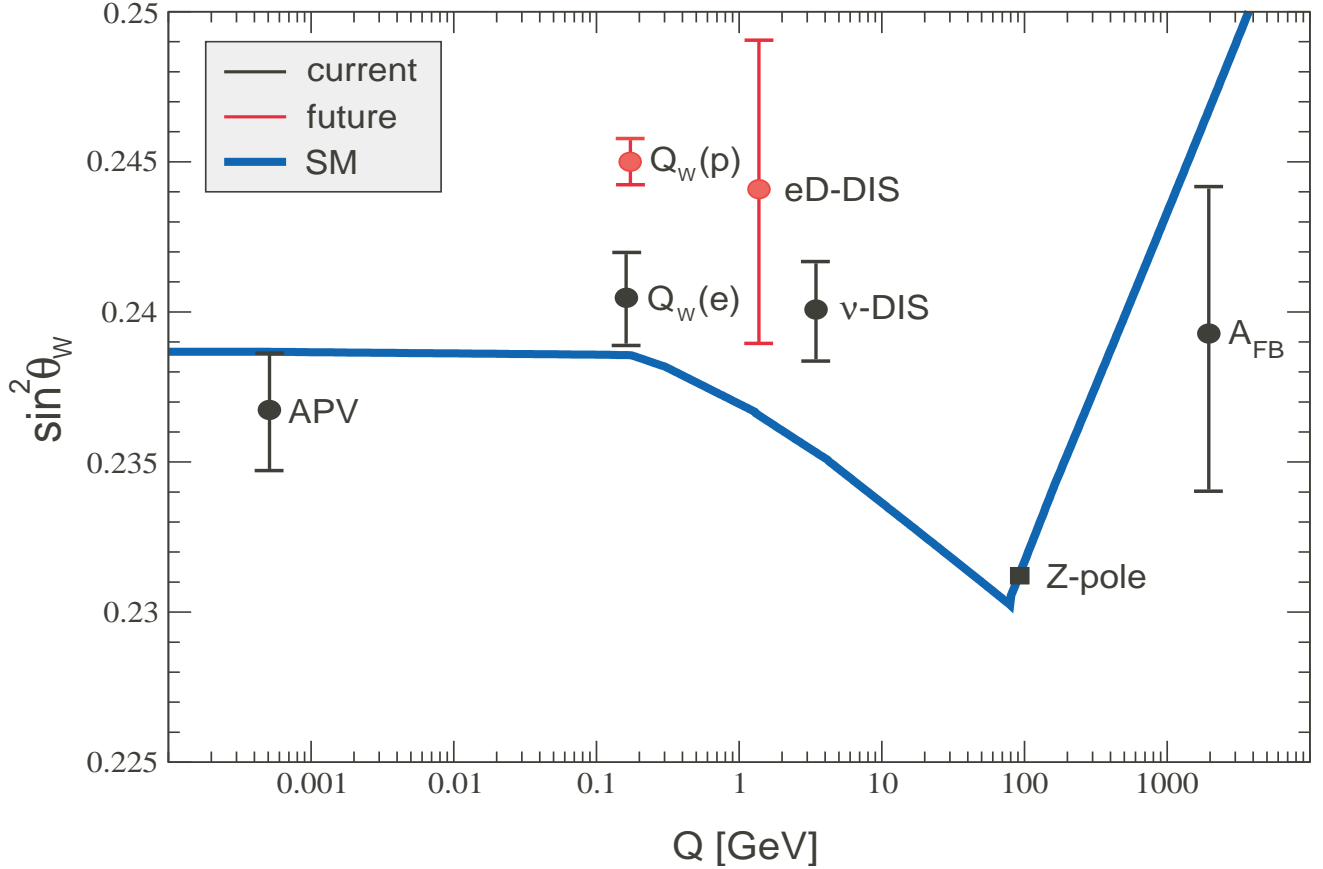


Figure 1: Calculated running of the weak mixing angle in the Standard Model, as defined in the modified minimal subtraction scheme. The black error bars show the current situation, while the red error bars (with arbitrarily chosen vertical location) refer to the proposed 4%  $Q_{W_{eak}}^p$  measurement and other possible future measurements. The "current" measurements are determinations from atomic parity violation (APV), SLAC E-158, deep inelastic neutrino-nucleus scattering (NuTeV), and from  $Z^0$  pole asymmetries (LEP+SLC).

The RG resummation of the leading, large logarithmic contributions to  $\sin^2 \hat{\theta}_W(\mu^2)$  as well as a variety of sub-leading effects has recently been carried out by Erler and Ramsey-Musolf in Ref. [7]. For both E158 and  $Q_{W_{eak}}^p$ , the result is a rather substantial change in the weak charge from its tree-level value.

In addition to the effect from the running of  $\sin^2 \hat{\theta}_W(\mu^2)$ , there is a WW box graph contribution to the proton weak charge that does not appear in the Møller case. This box graph compensates numerically for nearly all of the effect of the running of the weak mixing angle, so that the final Standard Model result for the proton weak charge is close to what it would be at tree-level. However, this WW-box contribution is qualitatively distinct from the running of  $\sin^2 \theta_W$

and should, therefore, be discussed as a separate effect. Consequently, an appropriate way to compare the different experiments is to subtract this contribution (along with other process-dependent radiative corrections) from  $Q_{Weak}^p$ , then to extract the running weak mixing angle from the result and compare with the analogous extracted quantity for the Møller experiment. Any mismatch between the two extracted values could then signal the presence of new physics that is important at low-energy but not at the  $Z$ -pole.

As is shown previously in Figure 1, the very precise measurements near the  $Z^0$  pole merely set the overall magnitude of the curve; to test its shape one needs precise off-peak measurements. Currently there are three off-peak measurements of  $\sin^2 \theta_W$  which test the running at a significant level: one from atomic parity violation (APV), one from high energy neutrino-nucleus scattering (NuTeV), and one from E-158 at SLAC which measured  $\sin^2 \theta_W$  from parity violating  $\vec{e}e$  (Møller) scattering at low  $Q^2$  [3]. Our proposed measurement of  $Q_{Weak}^p$  will be performed with significantly smaller statistical and systematic errors than existing low  $Q^2$  data.

The importance of a precision  $Q_{Weak}^p$  measurement is underlined by the recent history surrounding the interpretation of both the cesium atomic parity violation measurements and the NuTeV result. To date, the most precise measurement of extremely low-energy neutral current interactions has been carried out by exploiting parity-violating effects in Cesium, which allow a determination of the weak charge of the Cesium nucleus. The reliability of this determination has been subject to considerable theoretical atomic structure uncertainties. In the course of a few years, the value of the Cesium weak charge has changed as the associated many body corrections have been refined. This time evolution is shown in Figure 2. The present consensus from the atomic theory community is that all of the important corrections have now been incorporated.

The NuTeV Collaboration [2] determined  $\sin^2 \theta_W$  at  $Q^2 \sim 10 (GeV/c)^2$  in deep inelastic scattering of neutrinos from an approximately isoscalar target. The result is about  $2.5\sigma$  above the Standard Model expectation, and has a slightly greater precision than the one from atomic parity violation. The uncertainty is claimed to be dominated by statistics. It is conceivable that isospin symmetry violating parton distribution functions are responsible for part of the effect, but it seems difficult to account for the entire deviation in this way. The deviation seen by NuTeV may well be due to unknown systematic or theoretical effects; on the other hand, they may also be a hint at new physics in a sector which has never been tested precisely. Again referring back to Figure 1, it is clear that the Jefferson Lab  $Q_{Weak}^p$  experiment should be able to measure the weak mixing angle at low energies to unprecedented precision.

The recently completed SLAC E158 measurement has obtained a measurement for the weak charge of the electron,  $Q_W^e$ , which within its statistical and systematic accuracy is consistent with the SM. Although, the interpretation of this purely leptonic measurement is very clean, the experimental uncertainty is still large enough that a plausible magnitude "pull" on the resulting numerical value due to many classes of possible new physics might not be observable. Indeed, as will be discussed later scalar leptoquarks extension models for example cannot manifest themselves in a purely leptonic measurement such as the SLAC E158.

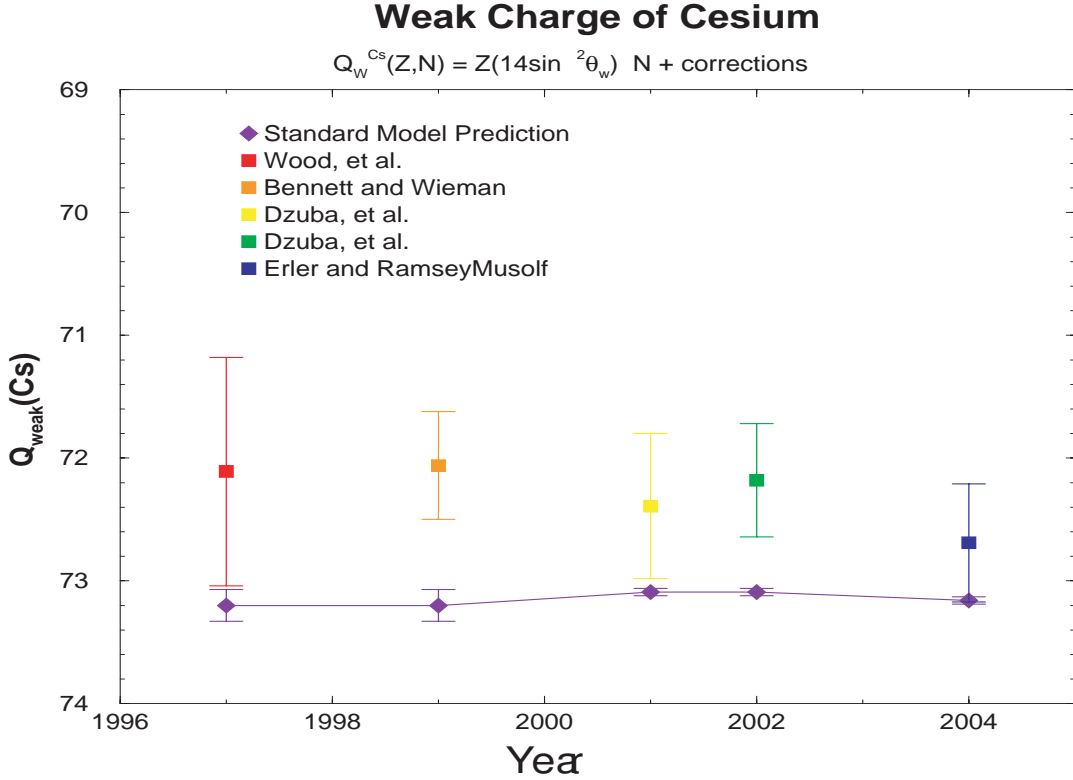


Figure 2: *Time evolution of the value and uncertainty of the Cesium weak charge due to refinements in the many body corrections. Also shown is the history of the corresponding SM prediction as extracted from high energy measurements.*

## 2.2 Theoretical Interpretability

An important consideration for the interpretability of the  $Q_{Weak}^p$  measurement is the degree to which hadronic contributions are under sufficient theoretical control. While in general one might worry about incalculable, non-perturbative QCD effects for a hadronic target – especially in the case of an ultra-precise measurement - several factors conspire to minimize the hadronic uncertainties for  $Q_{Weak}^p$ . In order to understand these factors, it is useful to delineate two types of hadronic effects: those which depend on  $Q^2$ , and those which are  $Q^2$  independent.

The  $Q^2$ -dependent effects include contributions from the  $Q^2$  dependence of various nucleon electroweak form factors, including the strange-quark form factors, as well as the 2  $\gamma$ -exchange box graphs entering the QED radiative corrections. After dividing out the leading  $Q^2$ -dependence of the PV asymmetry, these residual  $Q^2$ -dependent effects vanish at  $Q^2 = 0$ . The recent and future program of PV measurements at Jefferson Lab, MIT-Bates, and Mainz are designed to measure these contributions at somewhat larger values of  $Q^2$  than will be employed for  $Q_{Weak}^p$  ( $Q^2 = 0.03 \text{ GeV}^2$ ). The extrapolation from these higher values of  $Q^2$  to  $0.03 \text{ GeV}^2$  will introduce some uncertainty into the extraction of  $Q_{Weak}^p$  from the measured asymmetry. This extrapolation can be

carried out using curve fitting functions consistent with chiral perturbation theory. The existing and future PV measurements, as well as the world data set for electromagnetic form factors, should constrain all of the relevant low-energy constants. As will be shown later in the proposal we anticipate further refinement of this uncertainty estimate such as using the recent calculation of  $\mu_s$  by Leinweber, Thomas et al. [10]. However, no theoretical nucleon structure computations are absolutely required. Once the existing program of PV measurements (SAMPLE, HAPPEX I, HAPPEX II, G0, PVA4) are fully completed, we estimate that the uncertainty in  $Q_{Weak}^p$  due to these  $Q^2$ -dependent effects will be about 1.9%.

The second source of hadronic effects enter  $Q_{Weak}^p$  directly and do not vanish at  $Q^2 = 0$ . These include hadronic loops in the running of  $\sin^2 \theta_W$  and strong interaction corrections to the  $WW$ ,  $ZZ$ , and  $Z\gamma$  box graphs. Current conservation suppresses all other potential sources of hadronic effects, including isospin mixing in the proton wavefunction. A detailed analysis of these  $Q^2$ -independent effects are given in Ref. [6]. The QCD corrections to the  $WW$  and  $ZZ$  box graphs are perturbative and have been computed in that work through  $\mathcal{O}(\alpha_s)$ . Higher order corrections [of order  $(\alpha_s^2)$ ] contribute well below the one percent level. The leading, non-perturbative effects in the  $Z\gamma$  box diagrams are suppressed by a  $1 - 4\sin^2 \theta_W$  prefactor. The associated uncertainty has also been estimated in Ref. [6] to be on the order of 0.7% , though this estimate could conservatively be inflated by a factor of five and still fall below the anticipated experimental error in  $Q_W^p$ . Finally, the hadronic loop contributions to the running of  $\sin^2 \theta_W$  are constrained by  $e^+e^-$  data and the running of  $\alpha$ . The uncertainty associated with this effect is below one percent. In short, for the level of precision anticipated in the  $Q_{Weak}^p$  measurement, theoretical strong interaction uncertainties do not pose a barrier to interpretability.

Use of a proton target offers the simplest possible system on which to perform a low-energy search for new neutral current physics in the semileptonic sector. As in the case of neutron  $\beta$ -decay, where a combination of measurements (lifetime and asymmetry parameter) allow one to perform an extraction of the charged current vector coupling constant with minimal hadronic complications, the proposed measurement of  $Q_{Weak}^p$  - in conjunction with the anticipated results of the G0, HAPPEX, SAMPLE, and Mainz parity-violation experiments - will allow for a clean determination of the weak neutral current vector coupling constant (*i.e.*,  $Q_{Weak}^p$ ). Once  $Q_{Weak}^p$  is determined, the extraction of information on various new physics scenarios is similarly free from theoretically uncertain corrections, as alluded to above.

The quantity  $A_{LR}(^1H)$  (henceforth simply  $A$ ) is the asymmetry in the cross section for elastic scattering of longitudinally polarized electrons (normalized to  $P = 1$ ) with positive and negative helicities from unpolarized protons:

$$A = \frac{\sigma_+ - \sigma_-}{\sigma_+ + \sigma_-}, \quad (1)$$

which, expressed in terms of Sachs electromagnetic form factors  $G_E^\gamma, G_M^\gamma$ , weak neutral form factors  $G_E^Z, G_M^Z$  and the neutral weak axial form factor  $G_A$ , has the form [11]:

$$A = \left[ \frac{-G_F Q^2}{4\pi\alpha\sqrt{2}} \right] \left[ \frac{\varepsilon G_E^\gamma G_E^Z + \tau G_M^\gamma G_M^Z - (1 - 4\sin^2\theta_W)\varepsilon' G_M^\gamma G_A^Z}{\varepsilon(G_E^\gamma)^2 + \tau(G_M^\gamma)^2} \right] \quad (2)$$

where

$$\varepsilon = \frac{1}{1 + 2(1 + \tau) \tan^2 \frac{\theta}{2}}, \quad \varepsilon' = \sqrt{\tau(1 + \tau)(1 - \varepsilon^2)} \quad (3)$$

are kinematical quantities,  $Q^2$  is the four-momentum transfer,  $\tau = Q^2/4M^2$  where  $M$  is the proton mass, and  $\theta$  is the laboratory electron scattering angle. It was shown in [35] that for forward-angle scattering where  $\theta \rightarrow 0$ ,  $\varepsilon \rightarrow 1$ , and  $\tau \ll 1$ , the asymmetry can be written as:

$$A = \left[ \frac{-G_F}{4\pi\alpha\sqrt{2}} \right] [Q^2 Q_w^p + F^p(Q^2, \theta)] \rightarrow \left[ \frac{-G_F}{4\pi\alpha\sqrt{2}} \right] [Q^2 Q_w^p + Q^4 B(Q^2)] \quad (4)$$

where  $F^p$  is a form factor. Neglecting radiative corrections, the leading term in the equation is simply  $Q_{Weak}^p = 1 - 4\sin^2\theta_W$ . The  $B(Q^2)$  is the leading term in the nucleon structure defined in terms of neutron and proton electromagnetic and weak form factors. An accurate measurement of  $\sin^2\theta_W$  thus requires higher order, yet significant, corrections for nucleon structure. Nucleon structure contributions in  $B(Q^2)$  (which enter to order  $Q^4$ ) can be reduced by going to lower momentum transfer. However, this also reduces the sensitivity to  $Q_{Weak}^p$  (which enters to leading order in  $Q^2$ ) making it statistically more difficult to measure. The value of  $B(Q^2)$  can be determined experimentally by extrapolation from the ongoing program of forward angle parity-violating experiments at higher  $Q^2$ . We have estimated the optimum value of  $Q^2$  to be near  $0.03 (GeV/c)^2$  based on our estimate of the anticipated final precision of the various HAPPEX, HAPPEX II,  $G^0$ , and Mainz A4 measurements.

The remaining theoretical uncertainties are those which enter  $Q_{Weak}^p$  itself. Strong interaction uncertainties entering the Standard Model prediction for  $Q_{Weak}^p$  lie below the proposed experimental error. The sources of these uncertainties include the following:

- (i) Hadronic contributions to the running of  $\sin^2\theta_W$ :  $\Delta Q_W^p \sim \pm 0.4\%$
- (ii) Strong corrections to  $\gamma Z$ -box graphs:  $\Delta Q_W^p \sim \pm 0.7\%$
- (iii) Strong corrections to  $WW$ -box graphs:  $\Delta Q_W^p \sim \pm 0.1\%$
- (iv) Strong corrections to  $ZZ$ -box graphs:  $\Delta Q_W^p \sim \pm 0.01\%$
- (v) Isospin-breaking effects in nucleon current matrix elements is zero to all orders.

Finally, there is the uncertainty in  $\sin^2\theta_W$  determined from experiments at the  $Z$ -pole. This contributes an uncertainty of  $\Delta Q_W^p \sim \pm 0.8\%$ . The theoretical errors in  $Q_{Weak}^p$  are small compared to our anticipated total uncertainty of  $\pm 4\%$ .

Table 1 contains a brief summary of the key uncertainties and error budgets for this experiment. These have been refined through extensive simulations and updated calculations performed over the past three years. The experiment model now fully accounts for the effects of all bremsstrahlung losses, including those inside the target flask. In addition, the simulation contains a far more realistic collimator/detector system. Each of the contributions to the error budget is discussed in detail later in the proposal. The bottom line is that after extensive thought and simulation there does not appear to be any fundamental issue that should prevent us from achieving our goal of a  $\pm 4\%$  measurement of the proton’s weak charge. Indeed, with some additional refinement, it appears that the basic experimental technique may have the potential to achieve even a higher precision measurement if motivated by initial results that disagree with the Standard Model prediction.

Table 1: *Total error estimate for the  $Q_{Weak}^p$  experiment. The contributions to both the physics asymmetry and the extracted  $Q_{Weak}^p$  are given. In most cases, the error magnification due to the 39% hadronic dilution is a factor of 1.64. The enhancement for the  $Q^2$  term is somewhat larger.*

Source of error	Contribution to $\Delta A_{phys}/A_{phys}$	Contribution to $\Delta Q_{Weak}^p/Q_{Weak}^p$
Counting Statistics	1.8%	2.9%
Hadronic structure	—	1.9 %
Beam polarimetry	1.0 %	1.6%
Absolute $Q^2$	0.5%	1.1%
Backgrounds	0.5%	0.8%
Helicity-correlated beam properties	0.5%	0.8%
TOTAL:	2.2%	4.1%

## 2.3 Beyond the Standard Model

From a theoretical standpoint, there exist strong reasons to believe that the Standard Model is only a low energy effective theory within some larger framework. These reasons include the large number of parameters (masses, mixing angles, couplings) which must be put in by hand rather than following as natural consequences of the theory, the mass hierarchy problem, and the apparent lack of coupling unification when the couplings are run perturbatively up to the expected grand unification scale. In addition, the Standard Model does not explain the observed gauge symmetries and fermion representations or why discrete symmetries such as parity are violated; it simply incorporates these phenomenological observations in the structure of the model. One expects that a more complete theory will provide deeper explanations for these features of the Standard Model and address these conceptual open questions.

Looking beyond the Standard Model, precision measurements are beginning to sketch the outlines of a more complete theory. For example, the azimuthal dependence of the atmospheric  $\nu_\mu$  deficit

observed by the Super Kamiokande collaboration implies nearly maximal mixing between the  $\nu_\mu$  and  $\nu_\tau$ . Furthermore, the recent reanalysis of the results for the anomalous magnetic moment of the muon,  $(g-2)_\mu$ , shows a  $2.4\sigma$  deviation from the Standard Model, providing tantalizing hints of supersymmetry if questions regarding hadronic loop effects can be settled. Confirmation of the  $(g-2)_\mu$  result in other regimes is essential to determining which extensions of the Standard Model should be pursued, and therefore low energy experiments will continue to play an important role in the search for this more complete theory. Indeed, the BNL  $(g-2)_\mu$  collaboration is currently seeking funding for a renewed program to reduce their error further to see if the effect holds up. Experiments at the  $Z^0$  pole are sensitive to new physics (such as modifications of the Standard Model vector boson propagators) which affect physics at  $s \simeq M_Z^2$ . Low energy electroweak observables, on the other hand, are sensitive to new physics which does not resonate with the  $Z^0$  boson such as a  $Z'$  boson with  $M_{Z'} \neq M_{Z^0}$ .

In the present experiment, we propose to measure the weak charge of the proton,  $Q_{Weak}^p$ . The proton's weak charge is a fundamental property of the proton which has never been measured. It is the neutral current analog of the vector coupling  $G_V$  which enters in neutron and nuclear  $\beta$ -decay. In contrast to  $Q_W(Z, N)$  for a heavy atom, which is a large number of order  $N$ , the observable  $Q_{Weak}^p$  is fortuitously suppressed in the Standard Model. This is because  $Q_{Weak}^p = 1 - 4 \sin^2 \theta_W$  and the value of the weak mixing angle,  $\sin^2 \theta_W$ , is numerically close to  $1/4$ . This is characteristic for protons and electrons but *not* neutrons, making a weak charge measurement on the proton particularly sensitive to deviations arising from new physics. Consequently, the required experimental precision is about an order of magnitude less stringent than what is needed for atomic parity violation new physics searches. Roughly speaking, a 13% measurement of  $Q_{Weak}^p$  is equivalent in new physics sensitivity to a 1% measurement of  $Q_{Weak}(N, Z)$ . Moreover, the parity violating  $ep$  asymmetry,  $A_{LR}(^1H)$ , is sufficiently free from theoretical uncertainties at low  $Q^2$  to make it interpretable as a new physics probe.

## 2.4 Model Independent Constraints

We first consider the model independent implications of our proposed 4%  $Q_{Weak}^p$  measurement. The low-energy effective *electron – quark* Lagrangian of the form  $A(e) \times V(q)$  is given by,

$$\mathcal{L} = \mathcal{L}_{SM}^{PV} + \mathcal{L}_{NEW}^{PV}, \quad (5)$$

where

$$\mathcal{L}_{SM}^{PV} = -\frac{G_F}{\sqrt{2}} \bar{e} \gamma_\mu \gamma_5 e \sum_q C_{1q} \bar{q} \gamma^\mu q, \quad (6)$$

$$\mathcal{L}_{NEW}^{PV} = \frac{g^2}{4\Lambda^2} \bar{e} \gamma_\mu \gamma_5 e \sum_f h_V^q \bar{q} \gamma^\mu q, \quad (7)$$

and  $g$ ,  $\Lambda$ , and the  $h_V^q$  are, respectively, the coupling constant, the mass scale, and one-half the weak charges associated with the new physics.

The Standard Model coefficients take the values  $C_{1u}/2 = -0.09425 \pm 0.00010$  and  $C_{1d}/2 = +0.17070 \pm 0.00008$  [13], for up and down quarks, respectively, and

$$Q_W^p(\text{SM}) = -2(2C_{1u} + C_{1d}) \approx 0.0712. \quad (8)$$

With the above formalism in hand, the new physics reach of our experiment will now be presented several different ways.

### 2.4.1 Experimental Constraints on the Vector Weak Charges of u-, d-quarks

In Figure 3, we plot the present constraints on  $\Delta C_{1u}$  and  $\Delta C_{1d}$ , the shifts in the  $C_{1q}$  caused by new physics. The present constraints are derived from the Cesium weak charge results [1] and MIT-Bates  $^{12}\text{C}$  [14] and SLAC Deuterium [5] parity violation measurements. As long as  $h_V^u$  and  $h_V^d$  are almost perfectly correlated, only an extremely weak limit on the mass-to-coupling ratio  $\Lambda/g$  can be derived from the data. The impact of the proposed  $Q_{Weak}^p$  measurement is indicated by the ellipse, assuming the experimental central value equals the Standard Model prediction. The dramatic reduction in the allowed phase space for new physics in this model-independent parametrization arises from the high precision of the  $Q_{Weak}^p$  measurement and its complementarity to existing data.

### 2.4.2 Constraints on Couplings and Charges Associated with Possible New Physics

The observable sensitive to new physics is

$$Q_W^{New} \equiv Q_W^{Exp} - Q_W^{SM}$$

where

$$\Delta Q_W^{New} \simeq \Delta Q_W^{Exp}$$

since the SM errors are relatively small. Using the above Lagrangians, the significance  $S$  of the observation of an amplitude associated with new physics is

$$S = \left( \frac{g^2}{4\Lambda^2} Q_{SW}^p \right) / \left( \frac{G_F}{\sqrt{2}} \Delta Q_W^{Exp} \right)$$

where  $Q_{SW}^p = 2(2h_1^u + h_1^d)$ . On rearranging terms this yields

$$\Lambda^2 \cdot \frac{1}{g^2 Q_{SW}^p} = - \frac{1}{2\sqrt{2}G_F} \frac{1}{S \Delta Q_W^{Exp}} \quad (9)$$

This equation can be used to show the constraints our 4% measurement will place on the square of the mass parameter,  $\Lambda^2$ , and the sign and absolute value of new physics couplings  $g^2 Q_{SW}^p$ , as shown in Figure 4. In the next section, we emphasize the sensitivity of  $Q_{Weak}^p$  to  $Z'$  bosons with TeV-scale masses.

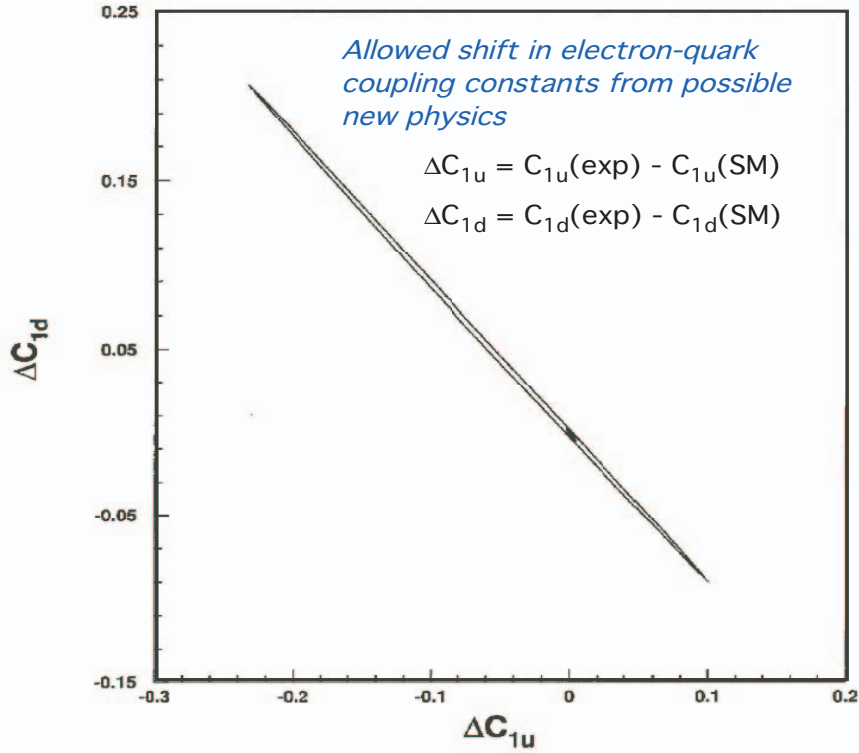


Figure 3: Present and prospective 90% C.L. constraints on new physics contributions to electron–quark couplings [6],  $\Delta C_{1q}$ . The larger ellipse denotes the present limits. The smaller ellipse indicates the constraints after the inclusion of the  $Q_{Weak}^p$  measurement, assuming the central experimental value coincides with the Standard Model prediction. The reduction in allowed phase space is dramatic.

### 2.4.3 Relation to Other Measurements

We would like to make a comparison between the mass scale sensitivity of the  $Q_{Weak}^p$  measurement, other precision measurements of the weak charge, and measurements at the energy frontier. Such a comparison cannot rigorously be made since the various precision weak charge measurements probe different forms of matter (*e.g.*, electrons or various isospin combinations of quarks), and only measurements at the energy frontier can actually materialize new particles and directly measure their masses. However, this comparison is important in order to illustrate that Jefferson Laboratory has the unique potential to either discover TeV-scale physics or tightly constrain its couplings to light quarks.

To make an order of magnitude estimate of the mass scale sensitivity of a precision  $Q_W^p$  measurement, we assume that the strength of the force is largely determined by  $\Lambda$  and that the couplings are  $O(1)$ . Taking equation 9 and setting  $g^2 Q_{SW}^p \rightarrow 1$ , and interpreting the result at

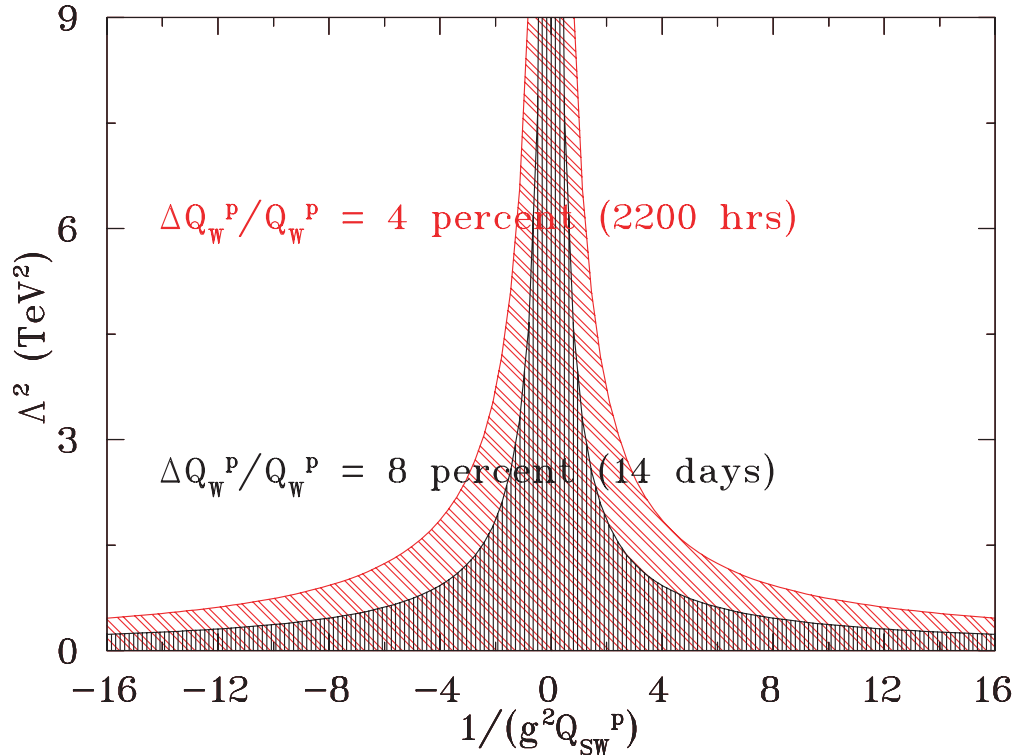


Figure 4: *Prospective constraints on the mass/coupling ratio and charges attributable to new physics, with  $Q_{SW} \equiv -2(2h_1^u + h_1^d)$ . If our  $Q_W^p$  experiment is found to agree perfectly with the Standard Model, the denoted phase space would be excluded at  $\geq 95\%$  confidence level.*

95% confidence level ( $S \simeq 2 \sigma$ ), we find

$$\Lambda = \frac{1}{\sqrt{2}\sqrt{2}G_F} \frac{1}{\sqrt{2\Delta Q_W^{Exp}}} = 2.3 \text{ TeV} \quad (10)$$

for a 4% measurement of  $Q_W^p$ . This result should be interpreted as  $O(2.3)$  TeV. The sensitivity of the experiment to higher mass scales varies as  $1/\sqrt{\Delta Q_W}$  or, for a statistics dominated measurement such as ours, as the inverse fourth root of the figure of merit. The explanation for our sensitivity to large mass scales is firstly that we are making a measurement on the weak scale,  $G_F$ , secondly that we are measuring a suppressed weak scale quantity,  $1 - 4\sin^2\theta_W$ , and finally that our measurement has relatively high precision.

Figure 5 suggests that our 4%  $Q_{Weak}^p$  experiment could, given “reasonable” coupling constants, see the effects of new physics at  $< 2.3$  TeV with high confidence, and be pulled significantly away from the Standard Model value by physics at mass scales of 2.3-3.3 TeV. The latter observation would tightly constrain the *sign* of the new couplings of any new particles discovered at LHC, which might be sufficient information to choose between possible models.

While limits within particular models may vary from this value (for a recent review, see Ref.

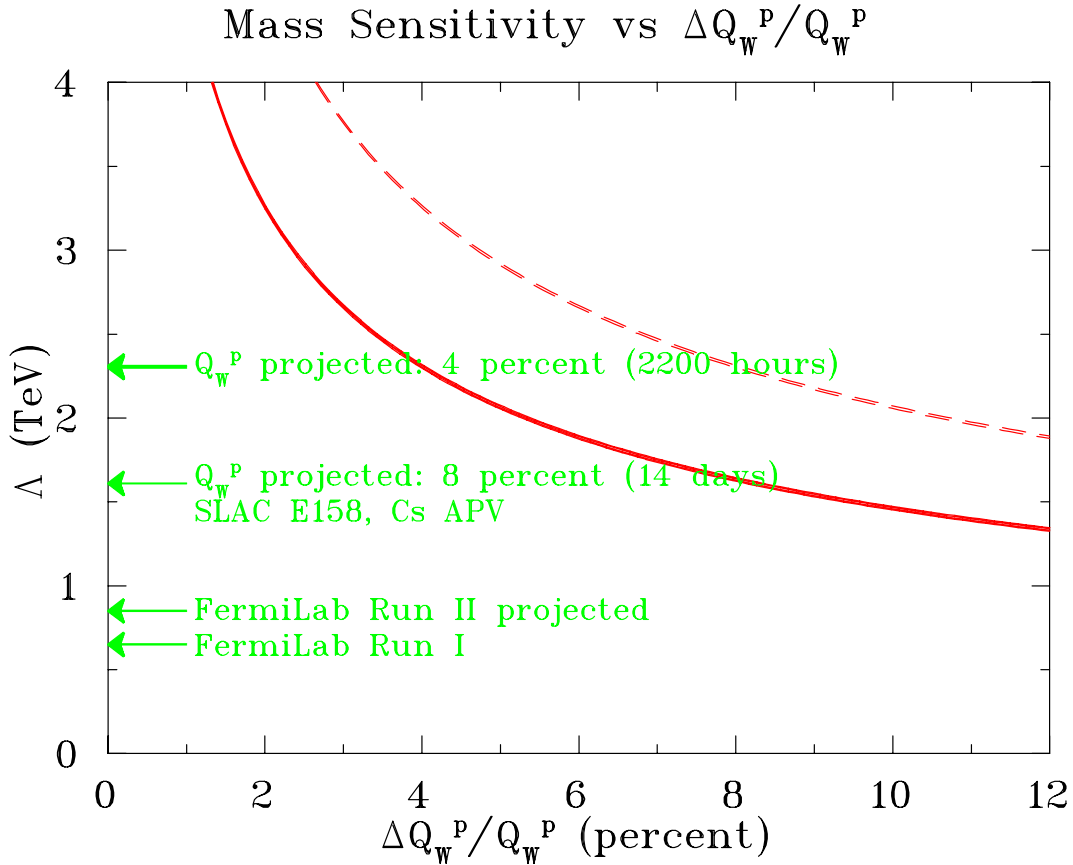


Figure 5: The sensitivity to TeV-scale masses is shown versus the relative error in  $Q_{Weak}^P$  in the solid (dashed) curve corresponding to 95% (68%) confidence level. The weak charge measurements are somewhat more restrictive than the collider measurements in that they are only sensitive to new neutral-current physics which is parity violating. The various weak charge experiments actually probe different combinations of new electron, up quark, and down quark couplings.

[15]), this model independent analysis illustrates the decisive role a  $Q_{Weak}^P$  measurement could play. For example, a particularly well-motivated class of new physics models predict the existence of extra TeV scale  $Z'$  bosons. In the simplest models based on Grand Unified Theories (GUT), one expects  $g \sim 0.45$ , so that one can study  $Z'$  bosons (with unit charges) up to  $M_{Z'} \approx 2.1$  TeV.  $Z'$  bosons are predicted in very many extensions of the SM ranging from the more classical GUT and technicolor models to supersymmetry and string theories. The sensitivity to non-perturbative theories (such as technicolor and other strong coupling dynamics) with  $g \sim 2\pi$  could even reach  $\Lambda \approx 14.5$  TeV.

## 2.5 Model Dependent Constraints

### 2.5.1 Extra Neutral Gauge Interactions

The introduction of neutral gauge symmetries beyond those associated with the photon and the  $Z^0$  boson have long been considered as one of the best motivated extensions of the SM. In the context of supersymmetry, they do not spoil the approximate gauge coupling unification predicted by the simplest and most economic SUSY scenarios. Moreover, in many SUSY models (though not the simplest  $SO(10)$  ones), the additional  $U(1)'$  gauge symmetry forbids an elementary bilinear Higgs  $\mu$ -term, while allowing an effective  $\mu$  to be generated at the scale of  $U(1)'$  breaking without introducing cosmological problems [16]. In various string-motivated models of radiative breaking, this scale is comparable to the electroweak scale (*i.e.*, less than a TeV) [16], thereby providing a solution to the  $\mu$ -problem [17] and enhancing the prospects that a  $Z'$  could be detected in collider experiments or seen indirectly via precision electroweak data. An extra  $U(1)'$  symmetry could also explain proton stability, which is not automatic in supersymmetric models, or it could solve both, the  $\mu$  and proton lifetime problems, *simultaneously* [18].

From a phenomenological standpoint, direct searches at the Tevatron [19] have as yet yielded no evidence<sup>4</sup> for the existence of the extra neutral  $Z'$  boson associated with the  $U(1)'$ , providing instead only lower bounds of about 600 GeV (depending on the precise nature of the  $Z'$ ).

On the other hand, several indirect effects could be attributed to a  $Z'$ . The  $Z^0$  lineshape fit at LEP [21] yields a significantly larger value for the hadronic peak cross section,  $\sigma_{\text{had}}$ , than is predicted in the SM. This implies, *e.g.*, that the effective number of massless neutrinos  $N_\nu$  is  $2.986 \pm 0.008$ , which is roughly  $2\sigma$  lower than the SM prediction,  $N_\nu = 3$ . As a consequence, the  $Z^0$ -pole data currently favors  $Z'$  scenarios with a small amount of  $Z^0$ - $Z'$ -mixing which mimics a negative contribution to the invisible  $Z^0$  decay width. Finally, the result by the NuTeV Collaboration [2] can be brought into better agreement when one allows a  $Z'$  if assumed not to be just some missing correction due to the use of an iron target. Although the improvement is modest, it is non-trivial, since the deviations in the weak mixing angles derived from NuTeV and APV show opposite signs, but can nevertheless both be improved by assuming  $Z'$  effects.

In analyzing the impact of a  $Z'$  on  $Q_{Weak}^p$ , we employ Eq. (7) with  $\Lambda = M_{Z'}$  and  $g = g_{Z'} = \sqrt{5/3} \sin \theta_W \sqrt{\lambda} g_Z$  [22], with  $\lambda = 1$  in the simplest models.  $g_Z^2 = 8G_F M_Z^2 / \sqrt{2}$  is the SM coupling constant for the ordinary  $Z^0$ . Consider the Abelian subgroups of  $E_6$ ,

$$E_6 \rightarrow SO(10) \times U(1)_\psi \rightarrow SU(5) \times U(1)_\chi \times U(1)_\psi \rightarrow SU(3)_C \times SU(2)_L \times U(1)_Y \times U(1)_\chi \times U(1)_\psi.$$

Then, the  $Z'$  can be written as the linear combination,

$$Z' \sim -\cos \alpha \cos \beta Z_\chi + \sin \alpha \cos \beta Z_Y - \sin \beta Z_\psi. \quad (11)$$

Considerations of gauge anomaly cancellation and the  $\mu$  and proton lifetime problems in SUSY models mentioned earlier, also favor a  $Z'$  of that type [18]. The assignment of SM fermions to

---

<sup>4</sup>See, however, Ref. [20] which reports a  $2\sigma$  deficit in the highest mass bin of the leptonic forward-backward b quark asymmetry seen by the CDF Collaboration.

representations of  $SO(10)$  implies that the  $Z_\psi$  has only axial-vector couplings and can generate no PV  $e-f$  interactions of the type in Eq. (7), whereas the  $Z_\chi$  generates only PV  $e-d$  and  $e-e$  interactions of this type. In fact, in this class of models the weak charges of the proton and the electron have equal magnitude. Although, strictly speaking the SLAC E158 result (Runs I, II and II combined) is in agreement with the SM its final uncertainty ended up being similar to that of APV and NuTeV. So being “in agreement” with the SM in the cases of SLAC E158 and APV does not imply that there is not a shift due to new physics, just that the accuracy of these measurements were perhaps insufficient to detect a signature. What is required are weak charge measurements with higher accuracy. However, should the measurement proposed here (or one of its potential follow on measurements) show a significant deviation from the SM prediction, a comparison with the SLAC-E-158, APV, NuTeV and other SM tests should still be a very useful way to get some discrimination between classes of models and other SM extensions.

To study the impact of a  $Z'$  on  $Q_{Weak}^p$  we consider the current best fit values[6],  $\alpha = -0.8_{-1.2}^{+1.4}$ ,  $\beta = 1.0_{-0.8}^{+0.4}$ , and  $\sin\theta = 0.0010_{-0.0006}^{+0.0012}$ , obtained for  $\lambda = 1$ . In this case,  $Q_{Weak}^p = 0.0747$  is predicted, that is a  $1.1\sigma$  effect. The impact of the measurement would be to reduce the allowed region of the parameters  $\alpha$  and  $\beta$  by approximately 30%. In view of the very high precision and very high energy measurements at the  $Z^0$  factories LEP and SLC, it is remarkable that a 4% measurement at very low  $Q^2$  and operating with a several orders of magnitude lower budget offers a more sensitive probe of TeV scale physics.

Even if a  $Z'$  is detected at the LHC first, it will be important to constrain its properties. Its mass will be measured in the course of the discovery, and  $\sin\theta$  is mainly constrained by LEP 2. The  $U(1)'$  charges and the couplings to quarks and leptons, however, are best determined by low-energy precision measurements.

## 2.5.2 Supersymmetry

Supersymmetry (SUSY) has long been considered a likely ingredient of an “extended” Standard Model. The theoretical motivation includes superstring theories, for which the existence of low-energy SUSY is a prediction; resolution of the “hierarchy problem” associated with Higgs mass renormalization and stability of the weak scale without resorting to fine tuning of parameters; and gauge coupling unification at the GUT scale. From a phenomenological standpoint, the recently reported deviation of the muon anomaly from the Standard Model prediction provides a tantalizing hint of SUSY, since contributions from “superpartner” loops provide a natural explanation for the effect.

The detailed way in which low-energy SUSY becomes manifest remains an open question. Since no superpartners have yet been seen in direct search measurements, their masses must be split from those of the Standard Model particles, thus implying some break down of exact SUSY. There exists a theoretical bias that SUSY breaking occurs at some high scale in a “hidden” sector and that its effects are transferred to low-energy phenomena via new gravitational or gauge interactions. These models of gravity or gauge mediated SUSY breaking make strong predictions for superpartner mass hierarchies. Low-energy charged current data, on the other hand, are not

consistent with these predictions unless a symmetry known as “R parity” is violated[23,24]. This symmetry is equivalent to conservation of baryon minus lepton number, and its violation implies the nonconservation of either B and/or L.

In order to evade present limits on proton decay, one typically sets  $\Delta B \neq 0$  R parity violating (RPV) interactions to zero, leaving only  $\Delta L \neq 0$  effects. Two types of L-violating RPV interactions occur: those which are purely leptonic, involving the exchange of “sleptons” (Figure 6a), and semileptonic interactions arising from “squark” exchange (Figure 6b). We denote corrections induced by purely leptonic interactions as  $\Delta_{ijk}$  and those arising from the semileptonic effects as  $\Delta'_{ijk}$ , where the indices refer to different generations. Low-energy observables are sensitive to both types of corrections. The dependence of semileptonic observables on  $\Delta_{ijk}$  arises from the normalization of amplitudes in terms of the muon decay Fermi constant and from the definition of the weak mixing angle.

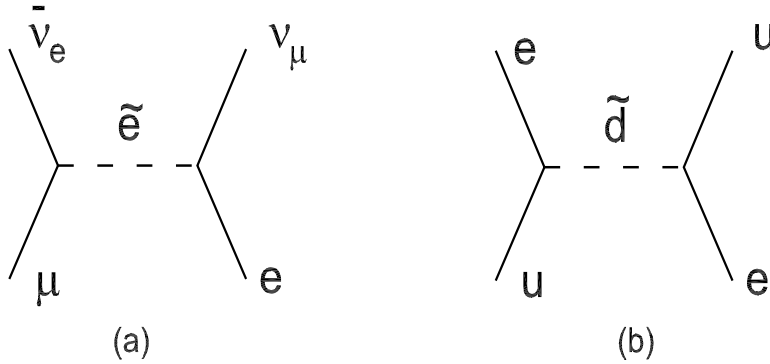


Figure 6: *Slepton and squark exchange contributions to muon decay (a) and eq interactions (b) arising in R parity violating SUSY models.*

If R Parity is conserved, then the lightest SUSY particle is stable and presumably contributes to dark matter. However, under the condition of R Parity violation, then the lightest SUSY particles long ago decayed to photons, etc, and don’t contribute to dark matter. Figure 7, is a plot the relative shifts in electron and proton weak charges due to SUSY effects. Dots indicate MSSM loop corrections for approximately 3000 randomly-generated SUSY-breaking parameters. Depending on the outcome of the proposed  $Q_{Weak}^p$  measurement, the impact on this new physics could be significant. At present SUSY provides one of the only simultaneous explanations of both the charged current and neutral current low-energy deviations from the SM (superallowed  $\beta$ -decay and Cesium atomic PV, respectively). The  $Q_{Weak}^p$  measurement would provide an important diagnostic as to whether this solution remains a viable one. In contrast, the prospective impact of the PV Møller asymmetry measurement on the plots in Figure 7 is less pronounced, since it competes directly with  $W$ -mass measurements, whose effects are already included in the fit.

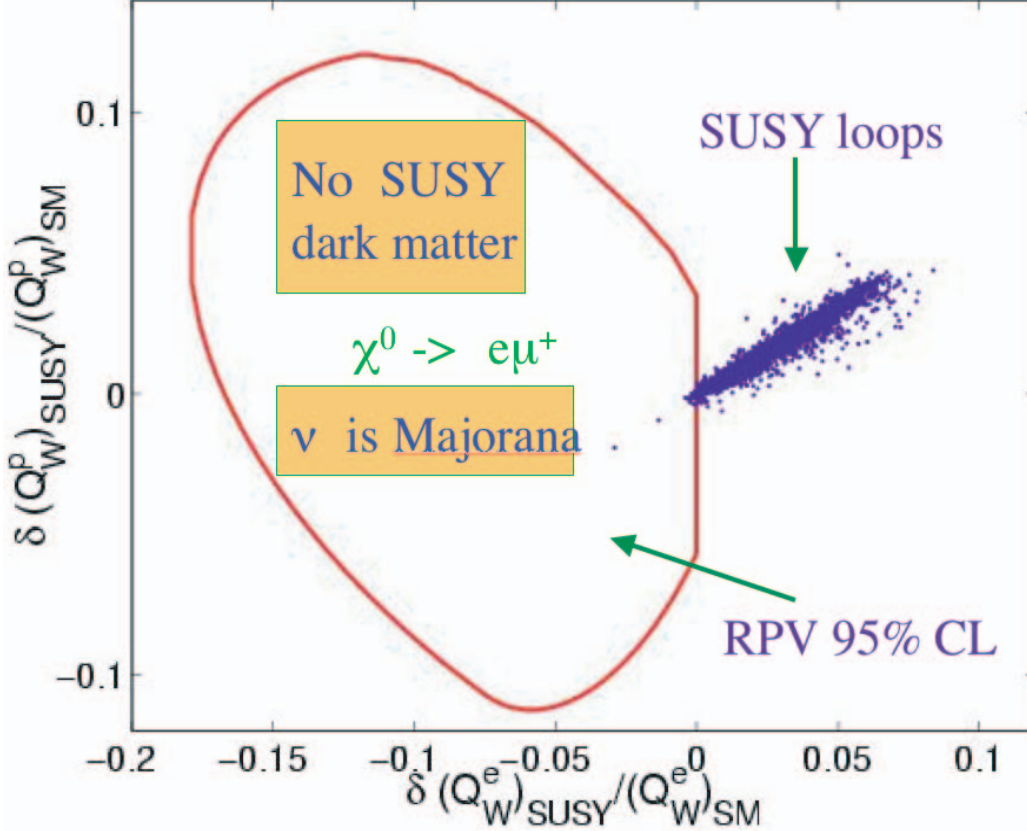


Figure 7: Relative shifts in electron and proton weak charges due to SUSY effects. Dots indicate MSSM loop corrections for approximately 3000 randomly-generated SUSY-breaking parameters. Interior of truncated elliptical region gives possible shifts due to R-parity non-conserving SUSY interactions (95% confidence).

### 2.5.3 Leptoquarks

Leptoquarks – bosons which have both nonzero baryon number  $B$  and lepton number  $L$  – have long been a popular, though somewhat exotic, candidate for new physics. In leptoquark models consistent with the  $SU(3)_c \times S(2)_L \times U(1)_Y$  symmetry of the SM [25,26], they can give rise to new tree-level, parity violating  $e - q$  interactions, as illustrated in Figure 8. Theoretically, spin-1 (vector) leptoquarks arise naturally in models of extended gauge symmetry, where they correspond to additional gauge bosons required by gauge invariance. Scalar leptoquarks occur naturally in RPV SUSY models, where they coincide with the exchanged squarks of Figure 8<sup>5</sup>. Thus, it is useful to consider the prospective impact of the  $Q_{Weak}^p$  on leptoquark models.

The implications of electroweak data for scalar leptoquark models have been analyzed recently in

<sup>5</sup>Technically speaking, the squarks in Figure 8 are not leptoquarks, since they do not carry lepton number. However, their effects are indistinguishable from scalar leptoquark exchange.

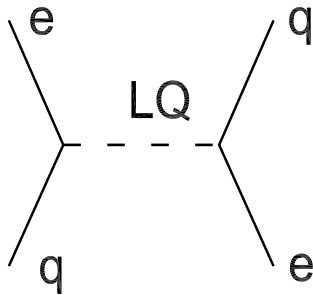


Figure 8: *Leptoquark (LQ) exchange contributions to parity violating eq interaction.*

Refs. [27,28]. Included in those analyses are data from deep inelastic neutral current scattering at HERA, Drell-Yan dilepton production at the Tevatron, hadronic cross sections at LEP 2, neutrino-nucleus deep inelastic scattering, light quark  $\beta$ -decay, atomic parity violation, and the SLAC, Mainz, and MIT-Bates parity violating electron scattering experiments. At the time of Ref. [27], the Cesium weak charge was believed to deviate from the SM by  $2.3\sigma$ . The analysis of Ref. [28], in contrast, was performed after inclusion of Breit corrections moved the Cesium result into agreement with the SM.

Although, the Cesium atomic PV measurement is now technically in agreement with the SM it is important to ask how well its accuracy and interpretability can rule out classes of leptoquark extensions to the SM. For example, in the analysis of Ref. [27] in which a  $2.3\sigma$  deviation for Cesium was assumed, two species of leptoquarks were found to provide an explanation for the effect while maintaining consistency with all other electroweak data:  $R_2^R$  and  $\vec{S}_3$  (in the notation of Ref. [26]). While the effects of the Cesium result were not included in a global fit, one can estimate the prospective impact of  $R_2^R$  and  $\vec{S}_3$  on  $Q_{Weak}^p$ . Were either of these leptoquarks to account for the assumed  $2.3\sigma$  deviation of Cesium from the SM value, they would each have produced a 10% shift in  $Q_{Weak}^p$ , respectively. However, in a subsequent calculation the same leptoquarks could also produce significant deviations of  $Q_{Weak}^p$  from the SM prediction even if the Cesium weak charge is taken to agree with the SM as assumed in Ref. [28]. The current Cesium measurement at its level of experimental and theoretical uncertainty cannot exclude all leptoquark based SM extensions. Therefore, one could anticipate sizeable effects in  $Q_{Weak}^p$  if low-energy leptoquarks constitute part of an extended Standard Model.

We note that, as in the case of other scenarios discussed above, the comparison of a  $Q_{Weak}^p$  measurement with results from the Møller parity violation experiment can provide a useful diagnostic. Specifically, leptoquark effects enter parity violating Møller scattering only at loop level, and their effects are considerably smaller than the anticipated final precision of the recently completed E-158 measurement [15]. Both experiments would have to deviate from the SM prediction by two or more standard deviations, to conclude the effect was not generated by leptoquarks. This scenario is presently excluded if SLAC E158 runs I, II and III are averaged together. On the other hand, a significant deviation of  $Q_{Weak}^p$  of the scale indicated by the allowed “pulls” shown in Figure 9[6], coupled with the absence of any significant deviation in the Møller results,

could point toward leptoquark interactions.

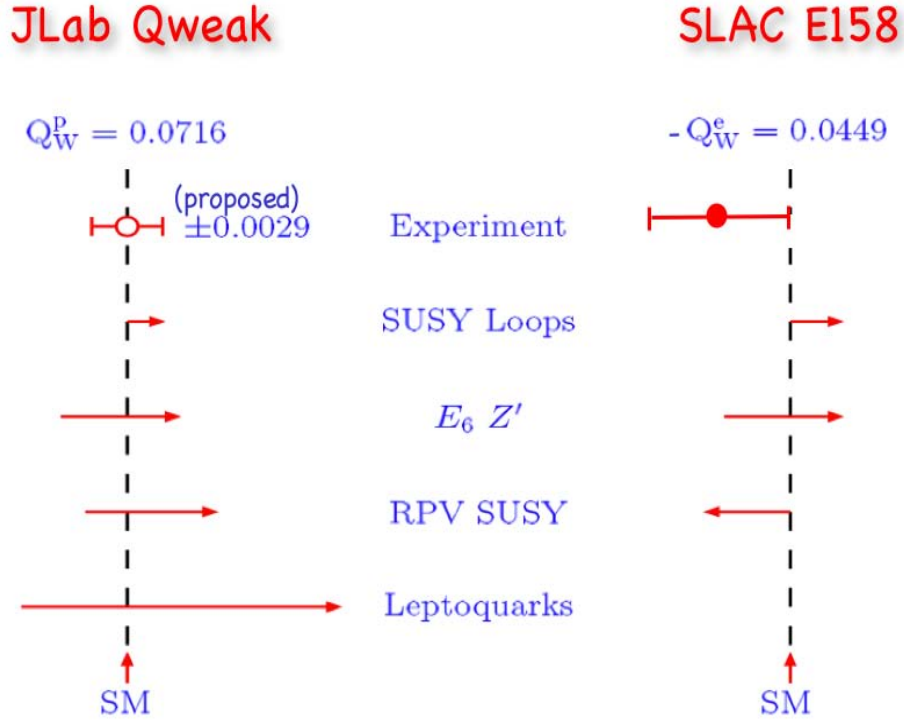


Figure 9: Comparison of anticipated errors for a 4%  $Q_{Weak}^p$  measurement and preliminary results from the SLAC E158  $Q_W^e$  measurement with possible deviations from the Standard Model allowed by fits to existing world data in the context of several plausible extension theories. Numerical values shown for both weak charges correspond to SM prediction. In the case of scalar leptoquarks, only the  $Q_{Weak}^p$  measurement will be sensitive while the  $Q_W^e$  measurement serves as a control. Together with other measurements, these two highly complementary experiments have the potential to put constraints on and possibly provide evidence for physics beyond the Standard Model.

Additional information is available in APPENDIX B, which is a reproduction of the paper [6], by: J. Erler, A. Kurylov, and M.J. Ramsey-Musolf, “Weak Charge of the Proton and New Physics”, Phys. Rev. D **68**, 016006 (2003) from which much of the theory section was derived.

## 2.6 Summary

We have demonstrated that the proposed measurement of  $Q_{Weak}^p$  at Jefferson Laboratory will provide a stringent test of the Standard Model prediction for the running of  $\sin^2 \theta_W$ . In the case of agreement with the Standard Model, our measurement will provide the single most significant confirmation of this essential prediction of the running coupling constant away from the  $Z^0$  pole, and the result will dramatically reduce the model-independent phase space for possible new parity violating electron-quark couplings. In *any* case, our experiment will provide important new constraints on new physics. We have explored the implications of existing world data for possible deviations that might be seen in our  $Q_{Weak}^p$  experiment in the context of several strong candidate extension theories, and we conclude that the proposed measurement can have a significant impact.

### 3 Overview of the Experiment

The  $Q_{Weak}^p$  collaboration will carry out the first precision measurement of the proton's weak charge,  $Q_{wp} = 1 - 4 \sin^2(\theta_W)$ . We will do this by measuring the parity violating asymmetry in elastic electron-proton scattering at very low momentum transfer, given by:

$$A = \left[ \frac{-G_F}{4\pi\alpha\sqrt{2}} \right] [Q^2 Q_w^p + Q^4 B(Q^2)]$$

where  $\sigma_+$  and  $\sigma_-$  are cross sections for positive and negative helicity incident electrons, and  $B(Q^2)$  is a hadronic form factor contribution, as discussed in section 1. The results of earlier experiments in parity violating electron-proton scattering will be used to constrain hadronic corrections to the data. A 2200 hour measurement of the parity violating asymmetry in elastic electron-proton scattering at a momentum transfer of  $Q^2 = 0.03 \text{ (GeV/c)}^2$  employing 180  $\mu\text{A}$  of 85% polarized beam on a 35 cm liquid hydrogen target will determine the proton's weak charge with 4% combined statistical and systematic errors; this in turn implies a determination of  $\sin^2(\theta_W)$  at the  $\pm 0.3\%$  level at low energy. As a standalone measurement of  $\sin^2(\theta_W)$ , the  $Q_{weak}$  experiment is competitive with any channel measured in the recently completed SLD and LEP programs at the Z resonance.

A sketch showing the layout of the experiment is given in Figure 10. A longitudinally polarized electron beam, a liquid hydrogen target, a room temperature toroidal magnetic spectrometer, and a set of Čerenkov detectors for the scattered electrons at forward angles are the key elements of the experimental apparatus. The toroidal magnetic field will focus elastically scattered electrons onto a set of 8, rectangular fused silica (synthetic quartz) Čerenkov detectors coupled to photomultiplier tubes, which will be read out in current mode to achieve the high statistical precision required for the measurements. Inelastically scattered electrons are bent out of the detector acceptance by the spectrometer and make only a minimal contribution to the Čerenkov signal. A new high power cryotarget is being developed and built at Jefferson lab for the experiment.

Basic parameters of the experiment are summarized in Table 2. The main technical challenges result from the small expected asymmetry of approximately -0.3 ppm; we will measure this asymmetry to  $\pm 1.8\%$  statistical and  $\pm 1.3\%$  systematic errors. The optimum kinematics corresponds to an incident beam energy of  $E_0 = 1.165 \text{ GeV}$ , scattered electron polar angles  $\theta_e = 8.4 \pm 3$  degrees, and azimuthal detector acceptance as large as possible (8 electron detectors with acceptance  $\Delta\phi_e = 24$  degrees each, totalling 53% of  $2\pi$ ). Fixing  $Q^2 = 0.03 \text{ (GeV/c)}^2$  limits nucleon structure contributions which increase with  $Q^2$  and avoids very small asymmetries where corrections from helicity correlated beam parameters begin to dominate the measurement uncertainty. With these constraints applied the figure-of-merit becomes relatively insensitive to the primary beam energy; using a higher beam energy will result in a physically longer experiment with stronger magnetic field requirements, smaller scattering angles, and the possibility of opening new secondary production channels that might contribute to backgrounds.

The high statistical precision required implies high beam current (180  $\mu\text{A}$ ), a long liquid hydrogen target (35 cm) and a large-acceptance detector operated in current mode. We assume that the

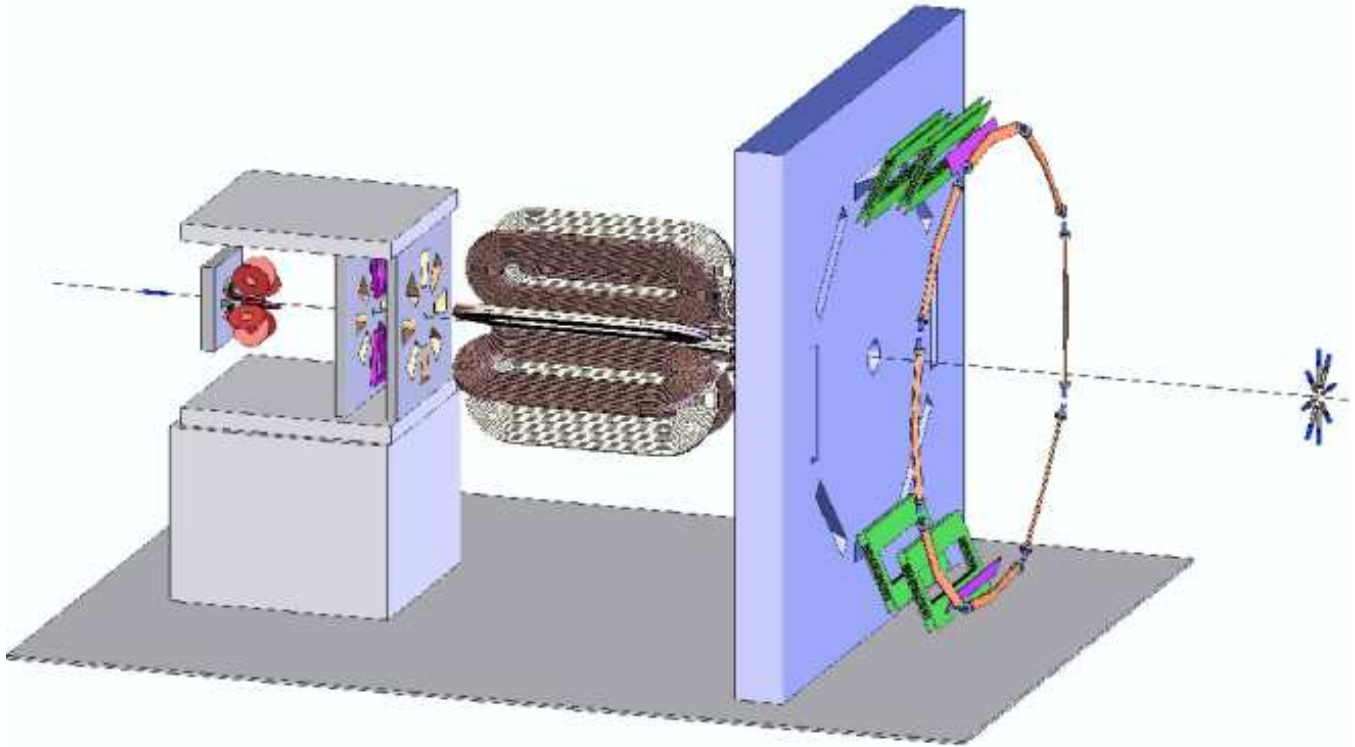


Figure 10: CAD layout of the  $Q_{Weak}^p$  apparatus. The beam and scattered electrons travel from left to right, through the target, the first collimator, the Region 1 GEM detectors, the mini-torus, the two-stage second precision collimator which surrounds the region 2 drift chambers, the toroidal magnet, the shielding wall, the region 3 drift chambers, the trigger scintillators and finally through the quartz Čerenkov detectors. The tracking system chambers and trigger scintillators, which instrument two opposing octants of the apparatus to map the  $Q^2$  response and study backgrounds, will be retracted during high current running when  $Q_{Weak}^p$  asymmetry data are acquired. The  $Q_{Weak}^p$  luminosity monitor, which will be used to monitor target fluctuations and to provide a sensitive null asymmetry test, is located downstream of the apparatus very close to the beam pipe as shown.

Table 2: *Basic parameters of the  $Q_{weak}^p$  experiment.*

Parameter	Value
Incident Beam Energy	1.165 GeV
Beam Polarization	85%
Beam Current	180 $\mu$ A
Target Thickness	35 cm (0.04 $X_0$ )
Running Time	2200 hours
Nominal Scattering Angle	8.4°
Scattering Angle Acceptance	$\pm 3^\circ$
$\phi$ Acceptance	53% of $2\pi$
Solid Angle	$\Delta\Omega = 45$ msr
Acceptance Averaged $Q^2$	$\langle Q^2 \rangle = 0.030$ (GeV/c) <sup>2</sup>
Acceptance Averaged Physics Asymmetry	$\langle A \rangle = -0.288$ ppm
Acceptance Averaged Expt'l Asymmetry	$\langle A \rangle = -0.24$ ppm
Integrated Cross Section	3.9 $\mu$ b
Integrated Rate (all sectors)	6.4 GHz (or .80 GHz per sector)
Statistical Error on the Asymmetry	1.8%
Statistical Error on $Q_W^p$	2.9%

source group will meet their stated goal of routine high current beam delivery at 85% polarization by the time  $Q_{Weak}^p$  is ready to take data; developments for  $Q_{Weak}^p$  will focus on more reliable operation at higher current of the new Superlattice GaAs photocathode materials which have already demonstrated over 85% polarization for the HAPPEX-II helium experiment.

Radiation hardness, insensitivity to backgrounds, uniformity of response, and low intrinsic noise are criteria that are optimized by the choice of quartz Čerenkov bars for the main detectors. The combined beam current and target length requirements lead to a cooling requirement of approximately 2.5 kW, considerably over the present capacity of the JLab End Station Refrigerator (ESR). This will require us to draw additional refrigeration capacity from the central helium liquefier (CHL), providing a cost effective solution for the required target cooling power. We note that the combination of high beam current and a long target flask will make the  $Q_{Weak}^p$  target the highest power cryotarget in the world by a factor of several; although the experiment could be run with a lower power cryotarget, the length of the run would have to be increased correspondingly.

It is essential to maximize the fraction of the detector signal (total Čerenkov light output in current mode) arising from the electrons of interest, and to measure this fraction experimentally. In addition, the asymmetry due to background must be corrected for, and we must measure both the detector-signal-weighted  $\langle Q^2 \rangle$  and  $\langle Q^4 \rangle$  – the latter in order to subtract the appropriate hadronic form factor contribution – in order to be able to extract a precise value for  $Q_{Weak}^p$  from the measured asymmetry. The  $Q^2$  definition will be optimized by ensuring that the entrance aperture of the main collimator will define the acceptance for elastically scattered

events. Careful construction and precise surveying of the collimator geometry together with optics and GEANT Monte Carlo studies are essential to understand the  $Q^2$  acceptance of the system.

This information will be extracted from ancillary measurements at low beam current, in which the quartz Čerenkov detectors are read out in pulse mode and individual particles are tracked through the spectrometer system. The Čerenkov detector front end electronics are designed to operate in both current mode and pulse mode for compatibility with both the parity measurements and the ancillary  $\langle Q^2 \rangle$  calibration runs. The tracking system will be capable of mapping the  $\langle Q^2 \rangle$  acceptance to  $\pm 1\%$  in two opposing octants simultaneously; the tracking chambers will be mounted on a rotating wheel assembly as shown in figure 10 so that the entire system can be mapped in 4 sequential measurements. A small “mini-toroid” magnet will be installed downstream of the first collimator to sweep low energy Møller electrons out of the acceptance of the middle tracking chambers; this will not significantly affect the optics for the elastic electrons of interest in the  $Q_{Weak}^p$  measurements. The front chambers are based on the CERN ‘GEM’ design, chosen for their fast time response and good position resolution. The chambers plus trigger scintillator system will be retracted during normal  $Q_{Weak}^p$  data taking at high current.

The experimental asymmetry must be corrected for inelastic and room background contributions as well as hadronic form factor effects. Initial simulations indicate that the former will be small, the main contribution coming from target walls, which can be measured and subtracted. The quadrature sum of the hadronic form factor error contribution to  $Q_{Weak}^p$  is expected to be 1.9%, as noted earlier. Experimental systematic errors are minimized by construction of a symmetric apparatus, optimization of the target design and shielding, utilization of feedback loops in the electron source to null out helicity correlated beam excursions and careful attention to beam polarimetry. We will carry out a program of ancillary measurements to determine the system response to helicity correlated beam properties and background terms.

The electron beam polarization must be measured with an absolute uncertainty at the 1% level. At present, this can be achieved in Hall C using an existing Møller polarimeter, which can only be operated at currents below 8  $\mu\text{A}$ . A program to upgrade the Møller for high beam current operation is currently underway, as discussed later in this proposal. A major effort to design and build a Compton polarimeter in Hall C at Jefferson Lab is also underway as part of the laboratory’s support of this and other experiments where precise beam polarimetry is an issue; the Compton polarimeter will provide a continuous on-line measurement of the beam polarization at full current (180  $\mu\text{A}$ ) which would otherwise not be achievable. Table 3 summarizes the statistical and systematic error contributions to the proton weak charge measurement that are anticipated for the experiment; the details of our beam request are given in section 14.

The  $Q_{Weak}^p$  apparatus also includes a luminosity monitor consisting of an array of Čerenkov detectors located downstream of the  $Q_{Weak}^p$  experiment at a very small scattering angle. The detectors will be instrumented with radiation-hardened vacuum photodiodes with external current-to-voltage converters. The high rate (29 GHz/octant integrating mode) and the resulting small statistical error in the luminosity monitor signals will enable us to use this device for removing our sensitivity to target density fluctuations. In addition, the luminosity monitor will provide a

Table 3: *Total error estimate for the  $Q_{Weak}^p$  experiment. The contributions to both the physics asymmetry and the extracted  $Q_{Weak}^p$  are given. In most cases, the error magnification due to the 39% hadronic dilution is a factor of 1.64. The enhancement for the  $Q^2$  term is somewhat larger.*

<b>Source of error</b>	<b>Contribution to <math>\Delta A_{phys}/A_{phys}</math></b>	<b>Contribution to <math>\Delta Q_{Weak}^p/Q_{Weak}^p</math></b>
Counting Statistics	1.8%	2.9%
Hadronic structure	—	1.9 %
Beam polarimetry	1.0 %	1.6%
Absolute $Q^2$	0.5%	1.1%
Backgrounds	0.5%	0.8%
Helicity-correlated beam properties	0.5%	0.8%
<b>TOTAL:</b>	<b>2.2%</b>	<b>4.1%</b>

valuable null asymmetry test, since it is expected to have a negligible physics asymmetry as compared to the main detector. We will apply the same corrections procedure for helicity correlated beam properties to both the main detectors and to the luminosity monitor - if the systematic error sensitivities are well understood, we should be able to correct the luminosity monitor to zero asymmetry within errors, which gives an independent validation of the corrections procedure used to analyze the main detector data.

In the remainder of this document, the individual elements of the apparatus, the measurement procedures, backgrounds and systematic error analyses are discussed in detail. We conclude the proposal with an updated beam request and information about the collaboration and institutional responsibilities in the project.

## 4 Magnetic Spectrometer and Collimation System

A key component of the  $Q_{Weak}^p$  apparatus is a magnetic spectrometer ‘QTOR’, whose toroidal field will focus elastically scattered electrons onto a set of eight V-shaped, rectangular in cross section synthetic quartz Čerenkov detectors. The main requirement for the spectrometer is to provide a clean separation between elastic and inelastic electrons so that a detector system of reasonable size can be mounted at the focal plane to measure the elastic asymmetry with negligible contamination from inelastic scattering and other background processes. The axially symmetric acceptance in this geometry is very important because it reduces the sensitivity to a number of systematic error contributions. A resistive toroidal spectrometer magnet with water-cooled coils has been chosen for  $Q_{Weak}^p$  because of the low cost and inherent reliability relative to a superconducting solution.

### 4.1 Basic Design Criteria

The QTOR magnet is required to bend the elastically scattered electrons at  $\theta_e = 8.0^\circ$  with momentum  $p' \simeq 1.165$  GeV/c by approximately  $13^\circ$ . This implies a magnetic field integral  $\int \vec{B} \cdot d\vec{\ell}$  of approximately 0.89 T·m. The focussing properties must provide clean separation of the elastic and inelastic channels, corresponding to a momentum resolution of about 10%. The magnetic field also provides background reduction. The QTOR magnet design provides a field free region along the beam axis. It has an open geometry to allow for maximum detector solid angle and the magnet must be symmetric for systematic error reduction.

### 4.2 Geometry and Magnetic Properties

The coil geometry has been optimized in a series of simulation studies using GEANT plus numerical integration over the conductor’s current distributions to determine the magnetic field. Several geometries were explored, including the use of circular coils, simple racetrack coils, tilted racetrack coils, and the BLAST modified racetrack coil shape. The simplest and least expensive QTOR coil design that has been adopted and that meets the needs of the  $Q_{Weak}^p$  experiment is a simple racetrack structure with a layout shown in Figure 11. Each coil package consists of a double pancake structure, with each layer consisting of two, 2.20 m long straight sections, and two semicircular curved sections with inner radius 0.235 m and outer radius 0.75 m. The copper conductor has a cross section of 2.3 in by 1.5 in with a center hole of 0.8 in in diameter. The total DC current under operating conditions will be 8650 A at 146 V.

### 4.3 Field Calculations and Magnet Optics

The magnetic field was calculated using the Biot-Savart Law and performing numerical integration over the distribution of conductor current density. Each field coil was represented by a



Figure 11: *Layout of the 8 magnetic field coils of the QTOR spectrometer.*

set of arcs and straight conductor segments. The field calculations were carried out assuming a nominal current density of  $454 \text{ A/cm}^2$ . Since the magnetic field scales in proportion to the current density, the calculated field map can be rescaled to any desired value.

A plot of the azimuthal magnetic field component  $B_\phi$  is shown in Figure 12 as a 3d function of position along the beam axis ( $Z$ ) and the radial distance ( $R$ ) from the beam axis. The magnetic field on the beam axis is zero, and increases rapidly with distance from the beam axis, reaching a maximum at  $R=0.56 \text{ m}$ . From that point, the field falls off as  $1/R$ . For a target located upstream of the magnet, the field integral experienced by the scattered electrons depends on the scattering angle. Electrons with smaller polar angles  $\theta_e$  will experience larger field integrals and will be deflected more strongly than electrons scattered at larger polar angles, which results in a focussing effect for the scattered electrons. Figure 12 also gives  $B_\phi$  as a function of  $R$  and  $\phi$  at the center of the magnet, which is defined as  $Z = 0.0 \text{ m}$ . The field profile in this plane indicates that there is an acceptably small variation in the toroidal field strength as a function of the azimuthal angle of the scattered electrons.

For an ideal toroid, the  $z$  component of the field is zero, while for a real toroidal magnet this component should be negligibly small compared to the  $B_\phi$  component. The calculated  $B_z$  component for the QTOR design is shown in Figure 13 in the median plane between a pair of coils. As seen from this figure, the maximum strength of  $B_z$  is 1.5% of that of the main toroidal field  $B_\phi$ ; again, the small field imperfections are acceptably small for the  $Q_{Weak}^p$  measurements.

The kinematics of the  $Q_{Weak}^p$  experiment have been chosen to optimize the figure of merit for the extraction of  $Q_{wp}$  from the elastic asymmetry. This being done, the focussing properties of the magnet for the electrons of interest depend on the choice of target length and position. The target length has been fixed at  $0.35 \text{ m}$  to achieve the highest practical luminosity, and the

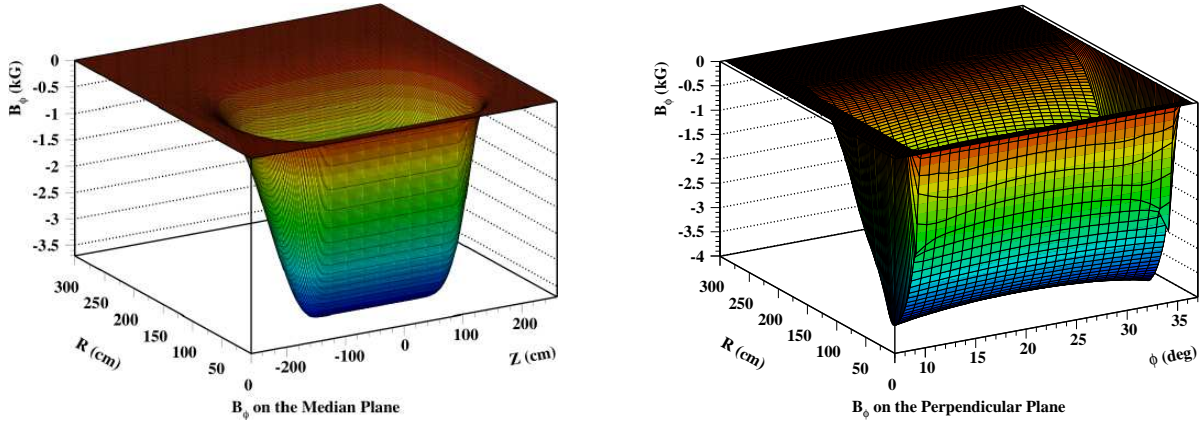


Figure 12: *Left: Three dimensional plot of the toroidal magnetic field component  $B_\phi$  in the median plane between a pair of coils, as a function of position along the beam axis ( $Z$ ) and the radial distance from the beam axis ( $R$ ) . Right: A similar plot of  $B_\phi$  as a function of  $\phi$  and  $R$  in the midplane of the magnet, perpendicular to the beam axis at  $Z = 0$  (magnet center).*

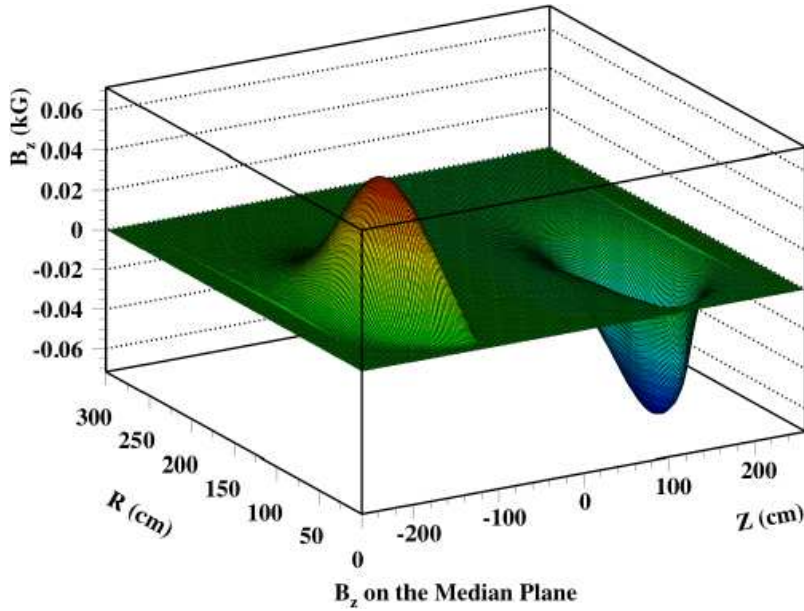


Figure 13: *Three dimensional plot of the  $z$  component of  $B$  on the median plane between two coils as a function of position along the beam axis  $Z$  and radial distance from the beam axis  $R$ . The maximum strength of this minor field component is about 1.5% of the main toroidal field  $B_\phi$ .*

target assembly will be located outside and upstream of the magnet to allow for the detection of scattered electrons at angles from approximately 6 to 10 degrees. By examining the scattered electron trajectories for various target locations, the optimum position of the target was found to be 0.650 m upstream of the midpoint of the QTOR magnet.

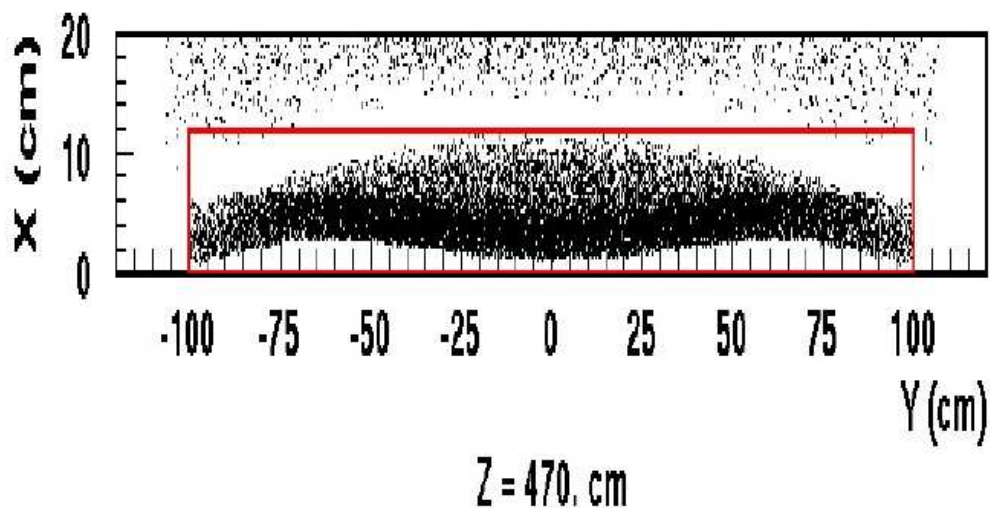


Figure 14: *Initial simulation showing separation of elastically (lower distribution) and inelastically (upper distribution) scattered electrons at a plane 4.70 m downstream from the center of the QTOR magnet. The kinematics are restricted to  $\theta_e = 9.0 \pm 2.0$  deg, and  $\phi_e = 0.0 \pm 15.0$  deg; on the scale, ‘x’ indicates the direction of increasing  $\theta$ , while ‘y’ covers the acceptance in  $\phi$ . A preliminary quartz detector shape has been outlined on the figure. No energy loss, multiple scattering or radiative effects were included in this simulation.*

During the initial stages of the QTOR spectrometer design, the optical properties of the magnetic field were explored by simulating the electron trajectories using GEANT, with initial scattering angles restricted to  $\theta_e = 9.0 \pm 2.0$  degrees and azimuthal angles in the range  $\Delta\phi_e = \pm 15.0$  degrees for both elastic scattering and pion production reactions ( $ep \rightarrow en\pi^+$  and  $ep \rightarrow ep\pi^0$ )<sup>6</sup>. In these early simulations, there were no energy loss or radiative effects included in the Monte Carlo, and simple cuts were placed on the electron scattering angles without reference to a realistic collimator design. This approach allowed us to study the effect of the magnet’s optical resolution on the trajectories of the charged particles, independent of ‘smearing’ effects caused by physical interactions of the electrons in the target and along the path to the detectors. Figure 14 shows the distribution of elastic and inelastic electrons 4.70 m downstream from the center of the magnet, where a  $2.00 \times 0.12 \times 0.025$  m<sup>3</sup> quartz Čerenkov bar cleanly intercepts the elastic scattering distribution with no contamination of inelastics. These simulations show that the QTOR magnet has the required focussing property, which is essential for performing the  $Q_{Weak}^p$  measurements, as it results in a clean separation between elastic and inelastic scattered particles.

A more realistic simulation requires the kinematics of the experiment as defined by the collimators, as well as accounting for multiple scattering and all secondary reactions. Figure 15 shows the results of a full GEANT simulation for elastically scattered electrons whose kinematics are

<sup>6</sup>This was the reference design used in the 2001 PAC proposal.

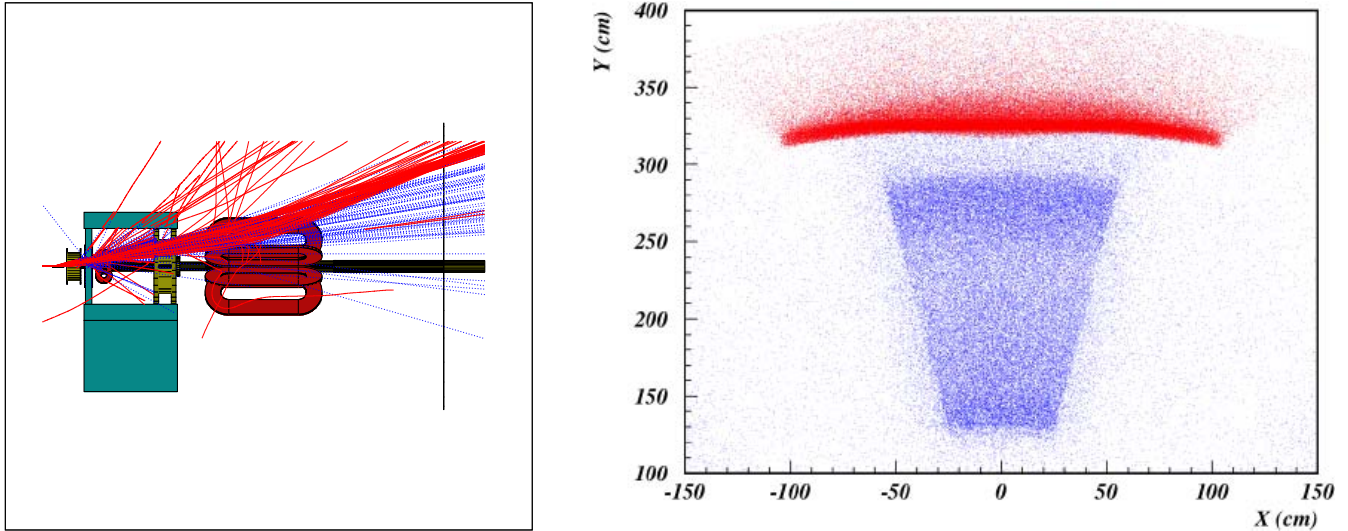


Figure 15: *Left panel: Side view of the experimental setup, consisting of a 0.35 m liquid hydrogen target, conical collimator, QTOR spectrometer, and a focal plane detector. Electron kinematics are defined by the collimator, and all secondary reactions are included. The electron trajectories (red) are distinguished from photon trajectories (blue). Right panel: Separation of elastically scattered electrons (narrow dark band near  $y=3.00$  m) and electromagnetic shower events shadowing the collimator walls, projected onto the focal plane at 5.70 m downstream of the QTOR magnet center. The 2.10 m long quartz Čerenkov bars will be placed to intercept the elastically scattered electrons shown in the figure.*

selected by a tapered input collimator. The secondary reactions consist mostly of bremsstrahlung radiation produced by electrons which strike the collimator walls. These events are well separated from the elastic electrons at the position of the focal plane, since the photons are not deflected in the magnetic field. The figure also shows a narrow band of elastic electrons sitting above the broad electromagnetic shower distribution. The projection of the collimator shape, which is clearly visible in the lower part of the figure, results from most of the showering occurring on the collimator walls. While the detailed collimator design has not yet fully been optimized, this simple initial choice is sufficient to demonstrate the general features of collimator showering effects; the contamination of the Čerenkov signal is already in this case acceptably small. The minimum design distance of 0.15 m between the beam pipe and the inner coil windings is sufficient to accommodate the necessary beam pipe shielding taking into consideration the beam broadening that occurs in the 0.35 m liquid hydrogen target.

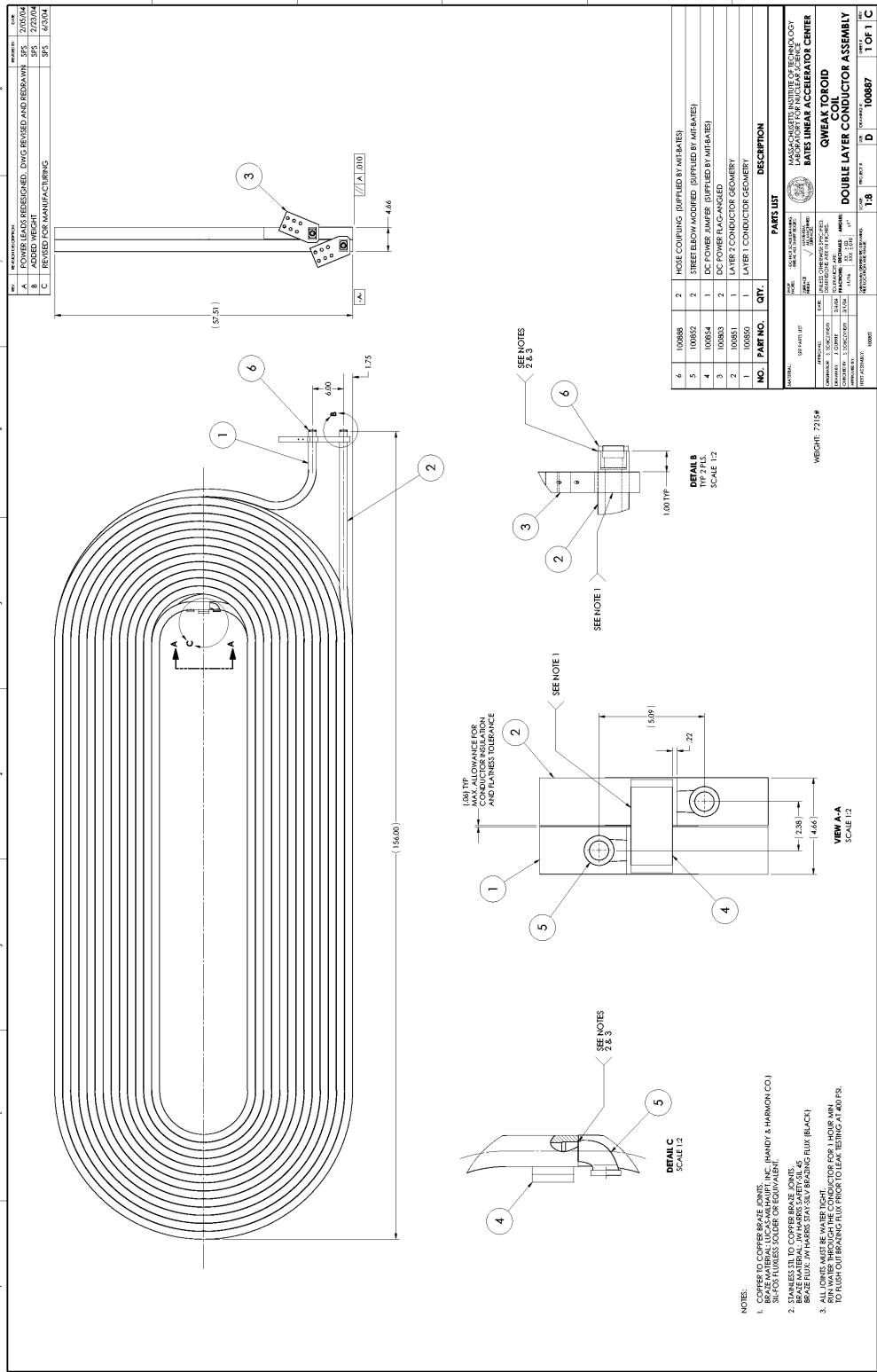


Figure 16:  $Q_{weak}$  toroidal spectrometer coil specifications.

## 4.4 Detailed Coil Design

The  $Q_{Weak}^p$  collaboration has benefited greatly from experience acquired in design and construction of the BLAST toroidal spectrometer at MIT-Bates. The field integral requirements and basic geometry for QTOR are comparable, but fabrication and alignment tolerances are less stringent than for the BLAST design, which involved a modified racetrack coil shape to accommodate polarized internal targets in the Bates South Hall Ring. A simpler coil shape has been adopted for QTOR, but the methods of design, fabrication, water cooling and controls for the BLAST magnet, as well as the support structure and power supply requirements, have been adapted to meet the needs of the  $Q_{Weak}^p$  experiment.

The shape adopted for the QTOR coil design is shown in Figure 16. This is the simplest and least expensive coil design, and is being built with a relatively simple winding fixture. The coil consists of two, 2.20 m long straight sections, and two semicircular curved sections with inner radius 0.235 m and outer radius 0.75 m. The total length of the coil is 3.96 m. The coils will be built using a similar procedure as the BLAST magnet coils, consisting of a two-layer pancake structure, each having 13 turns of OFHC copper (CDA 102) conductor material with square outer dimensions of  $2.3 \times 1.5$  in<sup>2</sup> ( $3.81 \times 5.84$  cm<sup>2</sup>) and an inner water cooling pipe diameter of 0.8 in (2.03 cm). Coil sections will be epoxy vacuum cast in a permanent mold. Reference points to locate the individual coils within the epoxy casing have been incorporated and will be used in surveying and alignment of the coils when they are mounted on the frame, discussed further below. A total of nine coils are being fabricated in order to have one spare available in case of failure. Taking into account the required groundwrap and epoxy insulating layers, the final cross-sectional dimension of the coil will be  $0.125 \times 0.525$  m<sup>2</sup>. Eight such coils will be assembled into a toroidal magnet configuration, which will be radially aligned and spaced at angles of  $\pm 22.5^\circ$  around the beam axis. The shortest distance between a coil and the beamline will be 0.15 m.

## 4.5 Fabrication and Alignment Tolerances

A GEANT Monte Carlo simulation has been used to study the effects of coil misalignments on the  $\langle Q^2 \rangle$  distribution at the focal plane as well as on the asymmetry of the 8-octant system as required for systematic error reduction. The most stringent requirement is for symmetry of the eight octants to minimize sensitivity to helicity-correlated beam motion: imperfections that affect all eight coils in the same manner are much less of a concern for  $Q_{Weak}^p$ .

The sensitivity to an overall position offset of the magnet with respect to the symmetry axis of the collimator and beamline has been explored using GEANT. The effect of this type of misalignment is to shift the image of the elastically scattered events across the width of a Čerenkov bar. Moving the whole magnet sideways changes the magnetic field through which the electrons pass, increasing it on one side, decreasing it on the other. For example, if the magnet is moved 0.01 m to the left, then electrons that are scattered to the left pass through an increased field and are deflected about 0.02 m more than the nominal value at the Čerenkov bar. The opposite effect

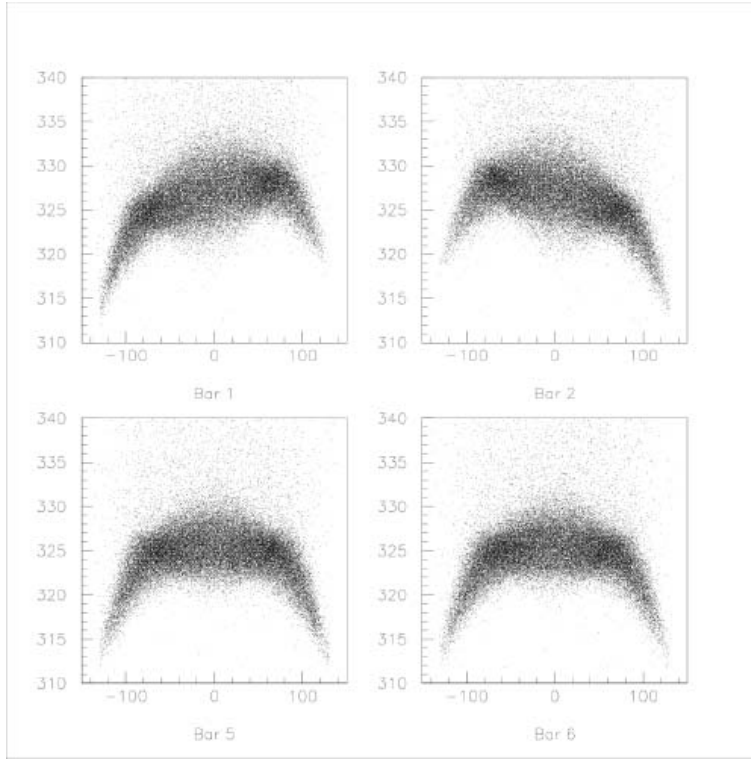


Figure 17: *Plots of the image formed by electrons on the Čerenkov bars. Coil 1, which lies between sectors 1 and 2 of the QTOR magnet, has been pulled out radially by 4 cm. The top two plots show the image formed by electrons striking bars 1 and 2. There is marked skewness caused by increased deflection of electrons on the sides close to the coil that has been moved. The two lower plots for the diametrically opposite bars exhibit no skewness.*

is seen in electrons that are scattered to the right. The effect of displacing the magnet is that electron distributions are shifted across the width of the Čerenkov bars, so that clipping of the tails of the distributions is possible. If also the beam position changes on helicity flip, then there is a false asymmetry. A 0.01 m displacement of the magnet as a whole shifts the neutral axis by about 0.4 mm. To limit the false asymmetry to  $\pm 6 \times 10^{-9}$  without trimming the currents in individual coils of the QTOR magnet, the magnet should be positioned to no worse than 0.003 m.

The effects of misaligning individual coils of the magnet have also been investigated. Pulling a coil out radially has the effect of increasing the magnetic field in the sectors of the magnet neighbouring that coil, but has little effect elsewhere. Figure 17 shows the effect of moving the coil at azimuthal angle  $22.5^\circ$  outward by 0.04 m. The upper two plots show the “moustache” (image of electrons on the Čerenkov bars, expanded greatly in the vertical direction in the plots) for the two neighboring bars centered at azimuthal angles of  $0^\circ$  and  $45^\circ$ . The moustaches are clearly pulled up toward the coil that has been moved and have become asymmetric. The two lower plots show the images on the diametrically opposite bars; they appear to be symmetric.

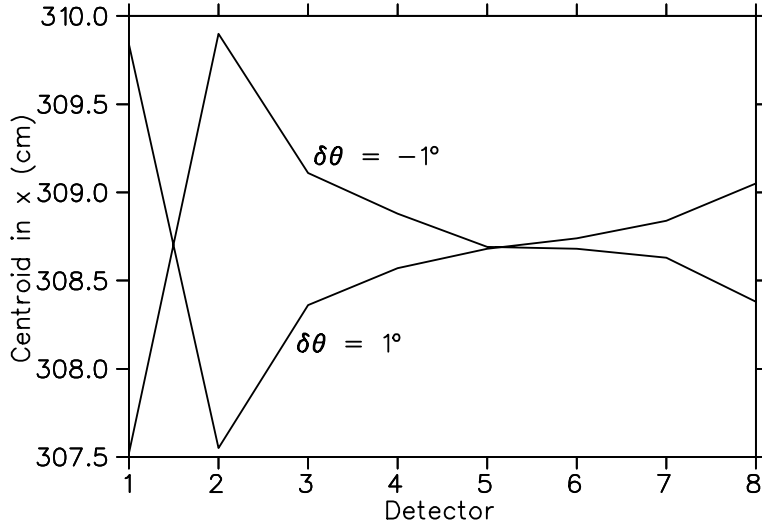


Figure 18: Centroids of images on the Čerenkov bars in the deflection direction when coil 1 of the QTOR magnet is rotated azimuthally by  $\pm 1^\circ$  about the beam axis.

The false asymmetry that results sets a limit of about 3 mm in the required radial positioning of individual coils.

In addition, the effects of rotating a coil azimuthally about the beam axis have been studied. Rotating one coil at azimuthal angle  $\phi = 22.5^\circ$  by  $1^\circ$ , for example, reduces the magnetic field for electrons travelling toward the Čerenkov bar at  $\phi = 0^\circ$  and increases the field for electrons travelling to the next bar at  $\phi = 45^\circ$ . There are lesser changes for the other bars. Figure 18 shows the centroids of the images on the Čerenkov bars in the deflection direction for rotations of the coil by  $\pm 1^\circ$ . The false asymmetry is negligible (the neutral axis is moved by no more than  $50 \mu\text{m}$  and the sensitivity to position modulation is increased by only 5% for a  $1^\circ$  rotation). A more practical concern is that the images no longer line up on the Čerenkov bars. To line them up to 1 mm without resorting to trim coils or adjusting the currents in individual coils, the coils should be aligned to  $0.08^\circ$  in the azimuthal direction, that is to 1.3 mm azimuthally at a radius of 0.93 m at the centre of a coil.

Simulations have shown that by instrumenting each coil with an adjustable ‘trim’ power supply with up to  $\pm 1\%$  of the main magnet current, we should be able to compensate for coil misalignments up to a few mm. The criterion to be used for adjusting the trim coil supplies is the matching of elastic event distributions across the quartz Čerenkov bars, which will be verified with the auxiliary tracking system at low beam current. Perfectly matched detector event distributions will result in the minimum combined sensitivity to beam position modulation, which will be checked independently in calibration experiments with artificially induced helicity correlated position modulations, as is currently done for the G0 experiment.

## 4.6 Magnetic Field Verification

It is essential that the QTOR spectrometer coils be fabricated and assembled to the required tolerances in order to ensure that the desired  $Q^2$  distribution of elastically scattered electrons is focused on the quartz Cerenkov detector for each of the 8 sectors of the device. Sector to sector uniformity is crucial in order to minimize the sensitivity to helicity correlated systematic errors. When the apparatus is fully assembled in Hall C, the  $Q_{Weak}^p$  tracking system will be used in calibration runs at low beam current to map the distribution of elastic electrons striking each detector. Ultimately, these measurements will be able to confirm that the desired sector-to-sector uniformity has been achieved in the magnet construction, but we must first verify the magnetic field and its symmetry independently before beginning the experimental program.

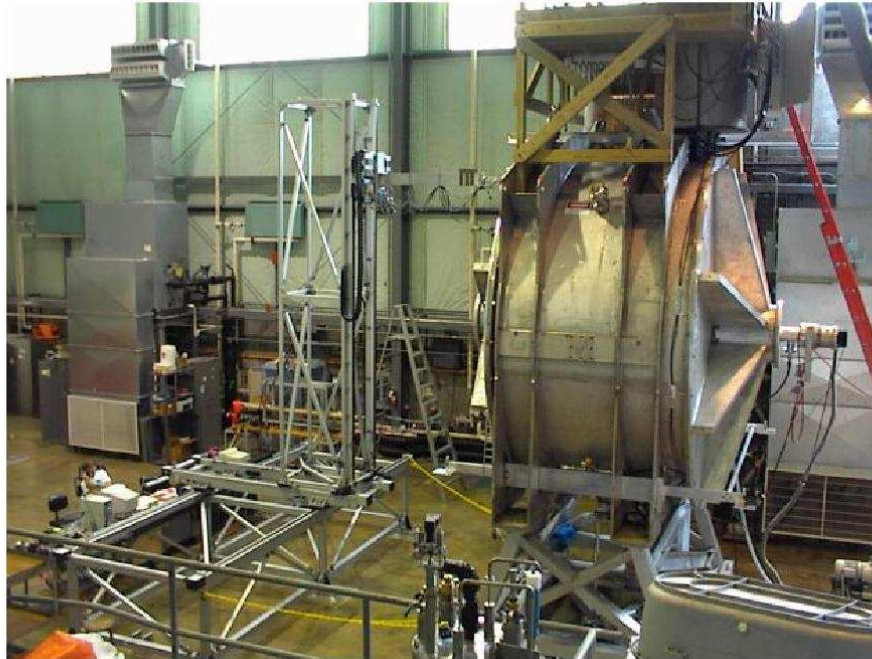


Figure 19: *Photograph of the magnetic verification device, on location at UIUC for mapping the G0 magnet.*

The open structure of the  $Q_{Weak}^p$  magnet provides for easy access not only to the end regions but also to the strong field regions between the coils. Optical alignment will locate the coils geometrically, in the first instance, to the required tolerances. A magnetic field mapping apparatus, built by the Canadian Group for the G0 experiment, will then be used to map the QTOR magnetic spectrometer field. The field mapping system consists of a programmable gantry with full 3D motion within a  $(4 \times 4 \times 2) m^2$  volume, and a set of high precision Hall probes, thermocouples, and clinometers (which measure tilt angle) mounted on the end of a probe boom on the gantry. The field mapping device on location at the Nuclear Physics Laboratory of the University of

Illinois for mapping of the G0 magnet, is shown in Figure 19. The system is capable of providing an absolute position determination of  $\pm 0.2$  mm and a field determination of  $\pm 0.2$  Gauss.

For the G0 experiment, the automated field measuring apparatus was used to determine the locations of a set of zero-crossing points of specific magnetic field components at selected points of symmetry of the magnet. Determination of these zero-crossing points then allowed the determination of actual coil locations and hence in principle the complete specification of the magnetic field. The sensitivity of these measurements to the individual coil misalignments is determined by the gradients of the field components at their zero crossing points, which in general are larger for QTOR than for the G0 spectrometer. The excellent performance of the magnetic verification device and the analysis procedure in extracting the coil positions for the G0 superconducting magnet provides confidence that the QTOR magnet coil positions can similarly be located to the required accuracy.

For the  $Q_{Weak}^p$  experiment, detailed calculations of the magnetic field have been made based on the technical drawings sent to the coil manufacturer, accounting for the exact coil geometry. This has been done for coils in both their nominal positions and in displaced positions according to a random distribution with a standard deviation of 3.5 mm in  $x, y$  and  $z$  directions and with a standard deviation of  $0.25^\circ$  in angle about these coordinate directions. Measurements of the zero-crossing points of selected field components in the planes at either end of the magnet ( $z = \pm 1.85m$ ) should permit determination of the coil positions to  $\pm 1.5$  mm and rotations to  $\pm 0.1$  degree, with the G0 field mapping apparatus<sup>7</sup>, which meets the specifications outlined in the previous section. Alignment corrections to the coil positions could then be made as required, reducing to an acceptable level the sensitivities to beam motion that would be measured for the detector bars in ancillary calibration experiments.

## 4.7 QTOR Support Structure

Like the QTOR coils themselves, the QTOR support structure design has been carried out by MIT-Bates engineers, and benefits directly from their design, fabrication and commissioning experience with the similar BLAST magnet at MIT-Bates.

The QTOR support system consists of two parts plus the individual coil holders or carriers. One part concerns the Toroidal Magnet Assembly including the alignment and support of the eight racetrack coils in their coil holders. The other lower part or Base Support consists of the necessary elements to allow support, alignment, and safe-tracked rail motion to and from the beam line. The array of racetrack coils have an axis which is horizontal and a radius of about 1.65 m ( $D = 3.30$  m) with an axial length of just over 3.65 m. The two part frame and support scheme allows assembly and testing of the Toroidal Magnet System first at MIT-Bates and then in Hall C before being moved to the beamline in Hall C at JLab.

---

<sup>7</sup>with Hall probes suitably modified for the scale of the QTOR field



Figure 20: *Aluminum Support Structure Assembly.*

The QTOR support structure design represents the evolution of the MIT BLAST Frame to meet the specific requirements of the  $Q_{Weak}^p$  experiment. It retains many aspects of the BLAST Frame design that has proven to work well, and at the same time incorporates important, yet subtle improvements to specific design deficiencies which surfaced during the early stages of BLAST's assembly and commissioning. The support structure has to be non-magnetic. Aluminum was chosen as a construction material for three reasons: ease of manufacturing, lower cost, and much greater availability of various standard structural shapes as compared to stainless steel. Figure 20 shows a CAD drawing of the QTOR support structure as designed.

The QTOR support structure is modular by design. It consists of two main weldments, an upstream support frame and downstream support frame, and longitudinal braces which join the two support frames together. The design is based on readily available 6061-T6 aluminum I-beams, C-channels and flat plates. Individual weldments can be fabricated by any number of pre-qualified fabricators, and shipped to MIT-Bates for assembly and testing and then to JLab for final testing and installation on the beamline. At the time of assembly, no welding will be required – all the individual modules will simply be bolted together using brass bolts throughout. Stress and deflection calculations have shown that the proposed design is sound, and that the required coil position stability and repeatability can be achieved. Additional detailed finite element stress and deflection analysis have verified the proper behavior of the support structure as designed.



Figure 21: *QTOR coils and bracing fixtures.*

Each of the eight coils, spaced evenly every 45 degrees around the longitudinal axis of the toroid, is supported by a coil fixture (or coil holder) as shown in Figure 21. The coil fixture is fabricated from individual pieces of 5 in and 1.25 in thick aluminum plate, in order to achieve the necessary rigidity and positional stability of each coil. The connection between the coil and the coil fixture guarantees  $\pm 1$  mm positional reproducibility of each coil, while allowing unrestricted coil length expansion and contraction due to temperature changes.

Coil fixtures are bolted to the support structure in such a way that the position of each coil can be independently adjusted to  $\pm 0.0025$  m in any direction. The fully assembled QTOR is 5.23 m wide, 6.45 m tall, and 5.08 m long. Its aperture centerline is 3.66 m above the floor, which corresponds to the beam height in Hall C, at JLab. The fully assembled and loaded structure is illustrated in Figure 22.

#### 4.8 Electrical Specification of Magnet and Power Supply

QTOR requires over 1700 kVA of power to run the DC power supply which converts the AC to the required DC current and voltage; JLab has scheduled an upgrade to the AC power for Hall-C, which will be more than adequate to the needs of the  $Q_{Weak}^p$  project. The DC power supply required for QTOR is rated at 160 V and 9500 A for a maximum power of 1.52 MW. The supply current should be regulated to better than 1 part in  $10^5$  with a ripple of less than  $\pm 5$

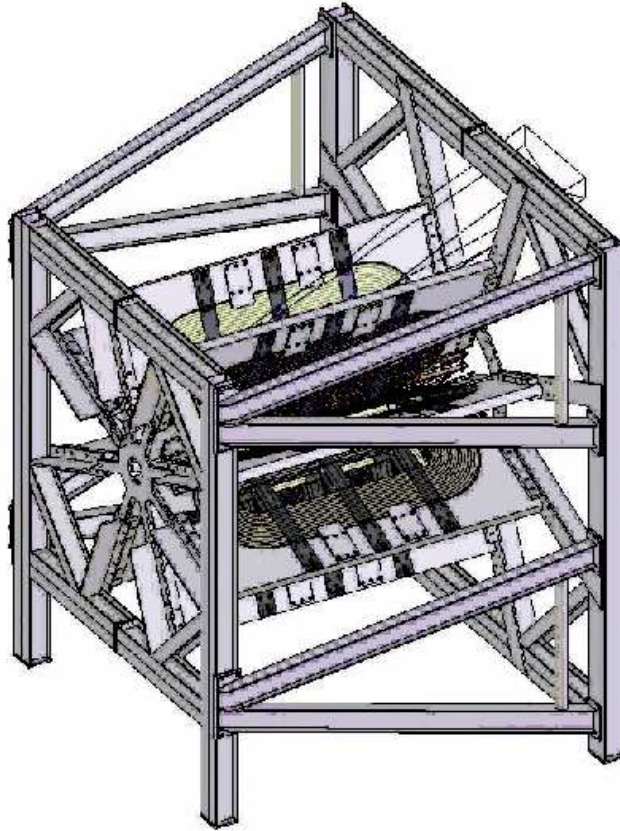


Figure 22: *Isometric view of the final QTOR Toroid Assembly.*

parts in  $10^4$ . The power supply unit will include: a local control panel, AC input monitoring panel, TJNAF interlock module, RS232/RS422 interface; 16 bit current readback; AC input line filter (EMC), water flow and over temperature switches. Negotiations are underway to secure the power supply with a 12 months delivery schedule.

Hall C has enough water to easily meet the cooling needs of QTOR and its power supply with the necessary inlet temperature of about  $30^\circ\text{C}$  and an inlet pressure of 200 psig with a back pressure of 60-80 psig. The cooling water requirements of  $Q_{Weak}^p$  are 265 GPM for QTOR, 40 GPM for the DC power supply, and perhaps another 25 GPM for the DC feeds of QTOR, for a total of 330 GPM. A compilation of data regarding the DC power supply is given in Table 4.

## 4.9 QTOR Fabrication and Assembly

The contract for fabrication of the nine QTOR spectrometer coils was awarded to SigmaPhi in June, 2004, with TRIUMF providing the contract management, and construction is currently underway. The magnet and support structure will first be assembled and tested at MIT-Bates

Table 4: *High current magnet power supply for the  $Q_{Weak}^p$  experiment.*

Parameter	Requirements
Rectifier Filter	12 pulse SCR bridge with passive LCR
Output Current	0-9500 Amps
Output Ripple	less than 0.5% OF $V_{out}$ @ 720 Hz
Current Setting	18 bit DAC
Current Readback	16 bit ADC by DCCT supplied
Stability Required	10 ppm (8 hours standard)
AC input mains	480, 3 Phase, 60 Hz
AC input maximum	1500 kVA (soft start circuit required)
Cooling water	less than 40 GPM @ 80 psid

and then delivered to JLab. Delivery of the nine coils to MIT-Bates is expected to take place at the end of February 2005 after final inspection at the manufacturer's plant in Vannes, France. The construction schedule calls for fabrication of the coil holders between April 1 and June 30, 2005; this part of the QTOR fabrication will also be managed by TRIUMF. A final review of the QTOR support structure was held at JLab in December, 2004. Fabrication of the support structure at MIT-Bates is scheduled for the first half of 2005.

By July 1, 2005, all parts of QTOR should have been delivered to MIT-Bates and assembly of the coils in their holders, and these in turn in the support structure, will be initiated. The assembly will be surveyed and mechanically aligned to the required tolerances. Initially use will be made of the BLAST power supply to power the QTOR magnet up to 7000 A, corresponding to about 80% of the required operating current. Under these conditions, the magnetic field will be mapped and effective coil locations verified according to the zero-crossing procedure described earlier. This field mapping and verification will need to be repeated once QTOR has been installed in Hall C at JLab and can be powered up to full current with a dedicated power supply; the latter may occur as early as mid-2006.

## 4.10 Collimator Design

Since the original proposal, a great deal of effort has gone into realistic GEANT simulations of the experiment with the aim of maximizing the figure-of-merit  $fom = A^2 \times R$  where  $R$  is the detected elastic event rate and  $A$  is the physics asymmetry, while keeping the systematic error sensitivities acceptably small. Refinements to the GEANT simulation code include incorporation of radiative effects - both internal and external Bremsstrahlung contributions - as well as more realistic modelling of various collimation schemes, and inclusion of a small 'mini-Torus' to deflect low energy Møller electrons out of the intermediate region chambers of the  $Q_{Weak}^p$  tracking system. Studies have been performed of the sensitivity of the apparatus to helicity-correlated position and

size modulation, which is exacerbated by the ‘moustache’ shape of the elastic electron distribution at the focal plane of the magnet that arises due to the nonideal nature of the 8-coil toroidal field. Realistic simulations have enabled us to arrive at a nearly optimal collimator reference design.

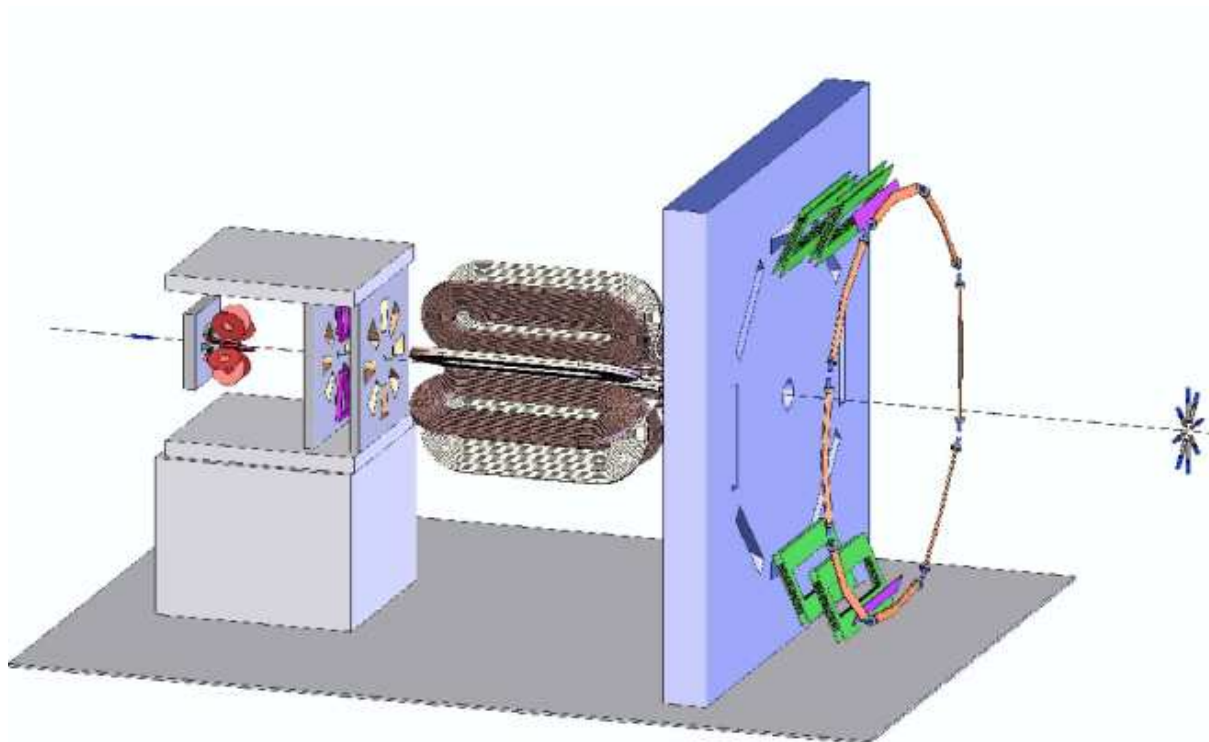


Figure 23: *Layout of the apparatus showing the locations of collimators.*

The collimator reference design maximizes the figure of merit, while keeping the inelastic contribution to the detector rate acceptably small. The layout of the  $Q_{Weak}^p$  apparatus showing the locations of the collimators in the reference design is shown in figure 23. The system consists of a forward collimator to shield the forward GEM detectors of the  $Q_{Weak}^p$  tracking system, followed by a two-stage collimator at the entrance of the QTOR magnet. A cutaway view of the collimation system is shown in figure 24. The first stage of the magnet entrance collimator defines the angular acceptance of the experiment, while the second stage performs a ‘cleanup’ function. To maximize the counting rate, the collimation system has the widest acceptance that is practical, while to reduce the inelastic contribution to acceptable levels, the quartz detectors are formed into a ‘V’ shape in order to better match the elastic electron distribution. The reference design assumes that the scattered electrons propagate through helium downstream of the target through to the quartz detector assembly.

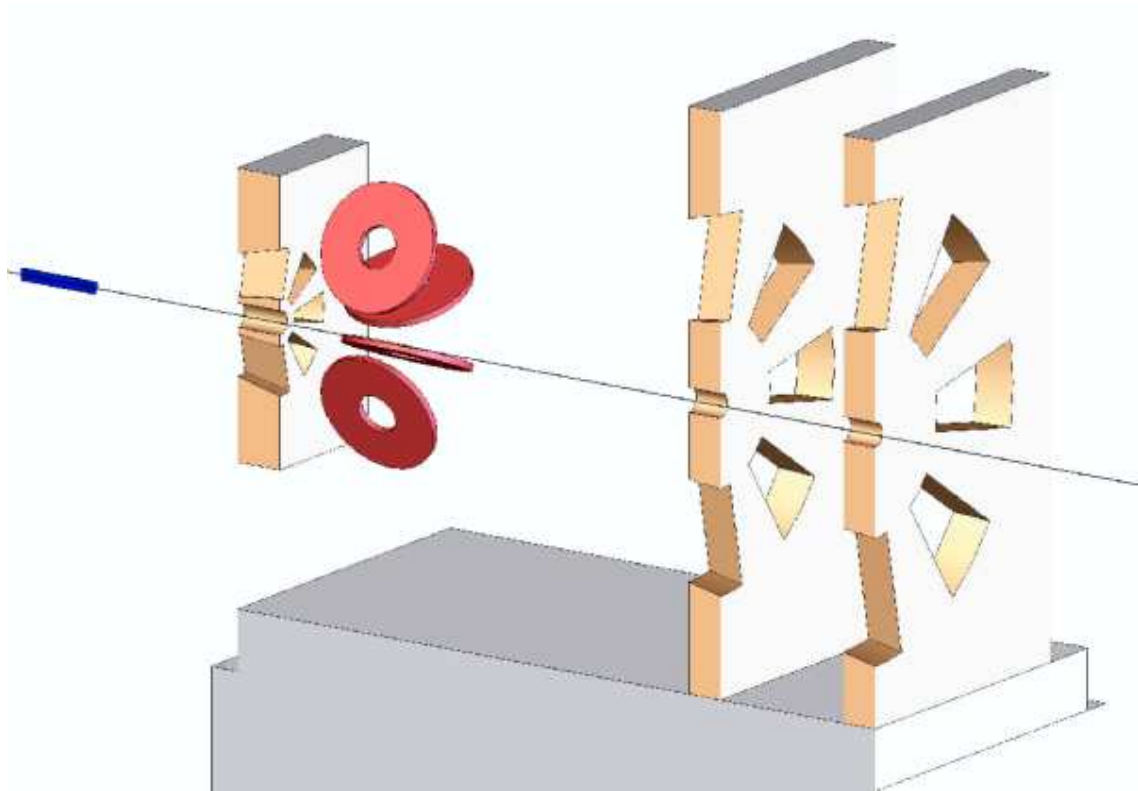


Figure 24: *Close up view of the reference design collimation system. The beam enters from the left. The first collimator is followed by the ‘mini-torus’ to sweep Møller electrons out of the acceptance of the region 2 tracking chambers for calibration measurements (tracking chambers not shown). The first stage of the second collimator at the entrance to the QTOR magnet defines the angular acceptance of the experiment, while the second stage performs a ‘cleanup’ function. To maximize the counting rate, the collimation system has the widest acceptance that is practical.*

The distribution of elastic and inelastic electrons in the reference design, on which the outline of a quartz detector element is superposed, is shown in figure 25. The elastic event rate per octant is 801 MHz; the inelastic rate is 0.21 kHz or 0.026% of the elastic rate, and the average  $Q^2$  is  $0.030 \text{ (GeV/c)}^2$ . The distributions of  $Q^2$ , and event rates along the length and width of the detectors for elastic events in the reference design are shown in figure 27; figure 26 shows the distributions of  $Q^2$  and electron energies incident on a quartz detector in the reference design. The detailed detector shape and simulations of the detector response are discussed in section 5.

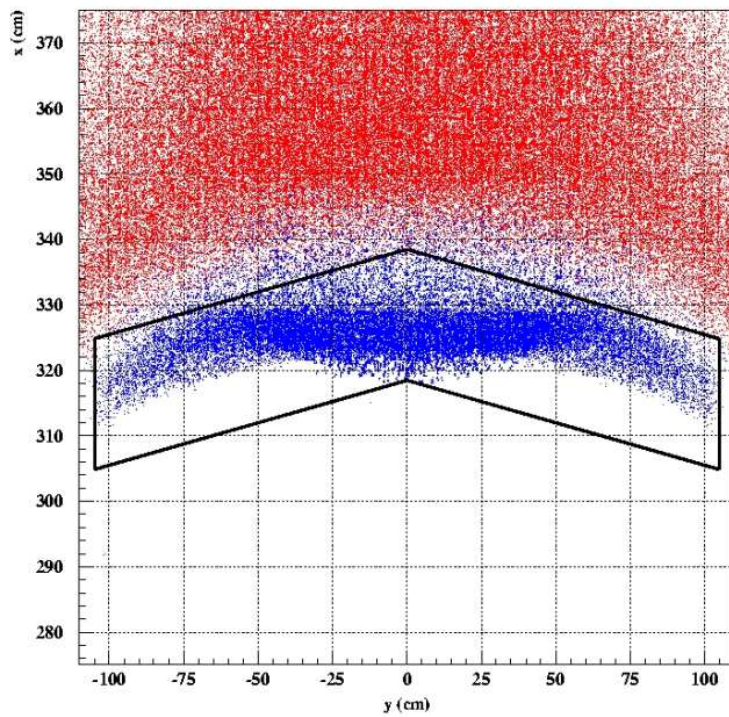


Figure 25: *Distribution of elastic and inelastic electrons at the detector plane with the reference collimator design. The V-shaped quartz detector bar outline is shown.*

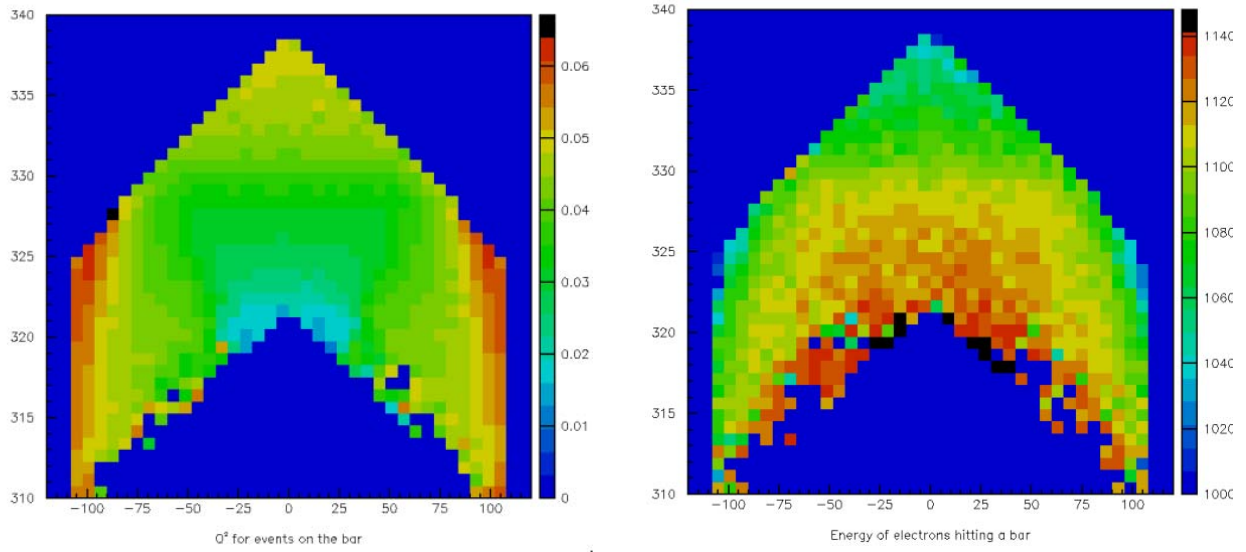


Figure 26: Left: The distribution of  $Q^2$  for elastic events falling on a V-shaped detector bar. The scale at the right shows  $Q^2$  in  $(\text{GeV}/c)^2$ . Right: The distribution of electron energies for elastic events falling on a V-shaped detector bar. The scale at the right shows  $E$  in MeV.

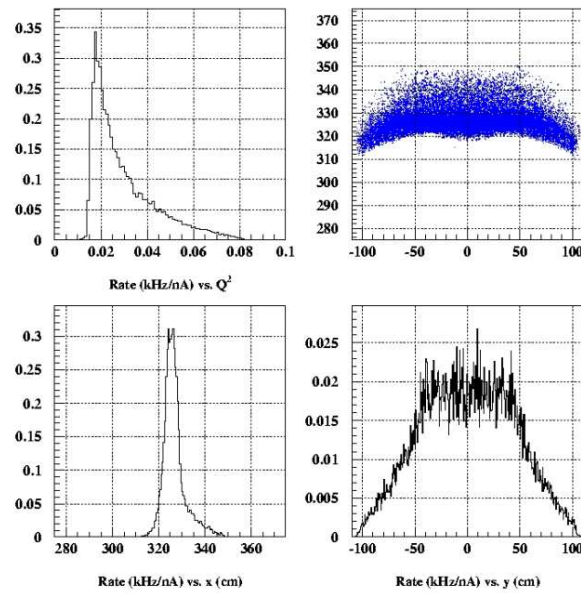


Figure 27: Distributions of  $Q^2$  and event rate along the detector bars for elastic events with the reference collimator design.

Systematic error simulations as described in section 9 have been used to set geometrical tolerances on fabrication and alignment of the collimation system. The crucial element is the upstream section of the second collimator, since it defines the  $Q^2$  acceptance. Symmetry of the 8 collimator sections is required in order that the images of the elastic event distributions on the 8 quartz Čerenkov bars be sufficiently similar for systematic error cancellation (sensitivity to helicity correlated beam motion and size). Overall, alignment and construction tolerances at the  $\simeq 0.3$  mm level are required for this collimator. Some prototyping has been done to explore the precision that can be achieved with water jet cutting of lead samples, as illustrated in figure 28. This technique will not be precise enough for machining of the  $Q^2$  defining apertures, as the tolerances achieved were approximately  $\pm 0.5$  mm. However, the downstream ‘cleanup’ collimator is an excellent candidate for this technology, as its tolerances are more relaxed. The final  $Q^2$  defining collimator material will likely be either Pb-loaded brass or Tungsten, depending on the outcome of further development work.

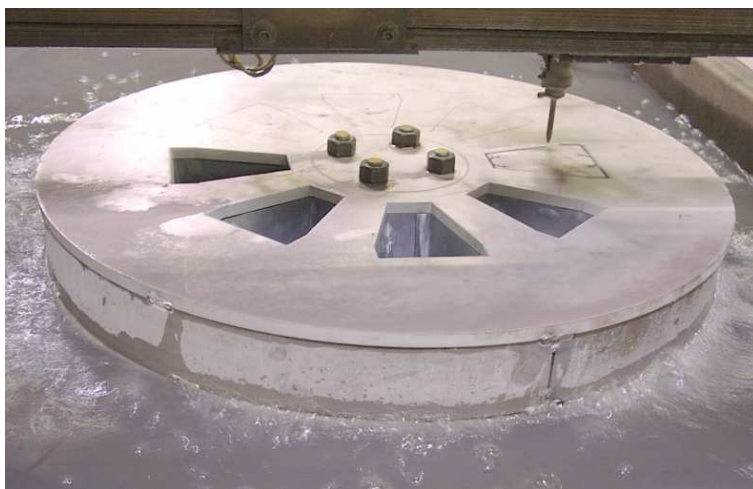


Figure 28: *Photograph of prototype precision collimator for the Qweak experiment*

## 5 Detector System

The  $Q_{Weak}^p$  experiment will detect Čerenkov light from scattered electrons in eight large, fused silica (synthetic glassy quartz) bars. The high rate of approximately 800 MHz per octant requires us to integrate the signal. Although integration frees us from the deadtime of a counting experiment, we still have to meet modest requirements on the linearity and rather stringent requirements on excess noise and backgrounds (without the ability to make event-by-event cuts). The Čerenkov light is converted to current by 5" photomultiplier tubes (PMT's) which are located on each end of a bar. Summing the signals in software from the two ends of a bar yields, after gain-matching, a response which is independent of position to within a few percent. Because we are detecting elastically scattered electrons at forward angles and low  $Q^2$ , most backgrounds are expected to be small. Occasionally, the beam current will be greatly reduced so the detectors can be used in pulse counting mode to study the average  $Q^2$  acceptance and potential backgrounds.

In this section on the "detector system" we will describe the main detector for PV measurements, its local analog electronics, the remote digitizing electronics, diagnostics which permit us to observe the beam envelope at the detector plane during current mode operations, and our plans for validating the expected detector performance. Other apparatus for estimating the magnitude of soft backgrounds during current mode operations is discussed in section 8. The Region I, II, and III tracking detectors, which are only used in pulsed-mode at low beam currents, are discussed in the Section 6.

### 5.1 Design criteria

For current-mode operations, our detector system must meet the following specifications:

- It must isolate the electrons of the  $e+p$  elastic channel from electrons from  $e+p \rightarrow e+N+\pi$ , limiting contamination to a few times 0.01% in yield.
- It must achieve a noise level which allows the experimental statistical error to be dominated by the rate of elastic electrons through the detector (*e.g.*,  $\sim 50$  ppm per pair at 30 Hz).
- It must be insensitive to soft backgrounds.
- It must possess an integral nonlinearity less than 1%.
- It must have mechanical and optical properties which are stable with time.
- It must incorporate engineered solutions to minimize or monitor cross-talk between the apparatus and the reversal signal, rather than simply relying on delayed reporting and half-wave plate reversal.

In pulsed mode operations:

- Changes in the background and acceptance of the quartz bars must be negligible.
- It must be possible to increase the gain of the signals to the  $10^7$  level for single photoelectron sensitivity.
- The bandwidth in pulsed mode should be at least 100 MHz so that signal and background pulses can be better resolved.

## 5.2 Technical solutions

The spectrometer optics focuses most of the collimated elastic electrons into an envelope which is roughly 10 cm tall in the dispersive direction, but over 2 meters wide in the non-dispersive direction. Due to large  $\phi$ -dependent aberrations, some curvature of the elastic event envelope results in a moustache-like droop near the ends. The QTOR is hard-wired to focus  $e + p$  elastics for a particular beam energy and angle, and is therefore not a momentum focusing spectrometer. Nevertheless, there is a strong correlation between the radial coordinate and momentum, so elastic scattering from the target windows<sup>8</sup> appears (poorly focused) at slightly smaller radius, while threshold pion production intercepts the focal plane at slightly larger radius. *Positive* particles of low momentum are bent inward and prevented from striking the opposite octant by thick shielding around the beamline.

In order to maximize the experimental figure of merit while minimizing backgrounds, we require the detector active area to be somewhat V-shaped as shown in Figure 29. A width of roughly 16 cm and a length of 210 cm, incorporating a  $7.5^\circ$  slant, will cover the entire elastic envelope.

### 5.2.1 Radiator

For electron detection, Čerenkov light production has the advantage that nonrelativistic charged particles and low energy photons produce little or no signal in the detector. The use of a thin (in terms of radiation length) solid radiator with good UV transmission can yield plenty of photoelectrons while minimizing cost, excess noise, and radiation dose to the material. We therefore chose to build Čerenkov detectors with 2.5 cm thick quartz radiators. There will be one quartz bar per octant, roughly perpendicular to the electron tracks, which will integrate the elastic electron beam envelope and an acceptably small fraction of the radiative tail.

The bars will acquire a radiation dose of approximately 100 kRad by the end of the experiment. The optical transmission of natural quartz would deteriorate rapidly under such conditions[59], diminishing the number of photoelectrons and causing unacceptable time-dependent changes in the sensitivities and  $Q^2$  and  $Q^4$  biases. We selected the Spectrosil 2000 material because it is sufficiently radiation-hard for our application and produces negligible light via scintillation and luminescence.

---

<sup>8</sup>For initial measurements, the target cell will be made from aluminum, but the possibility of using beryllium entrance and exit windows is being investigated in the longer term, as described in section 7.

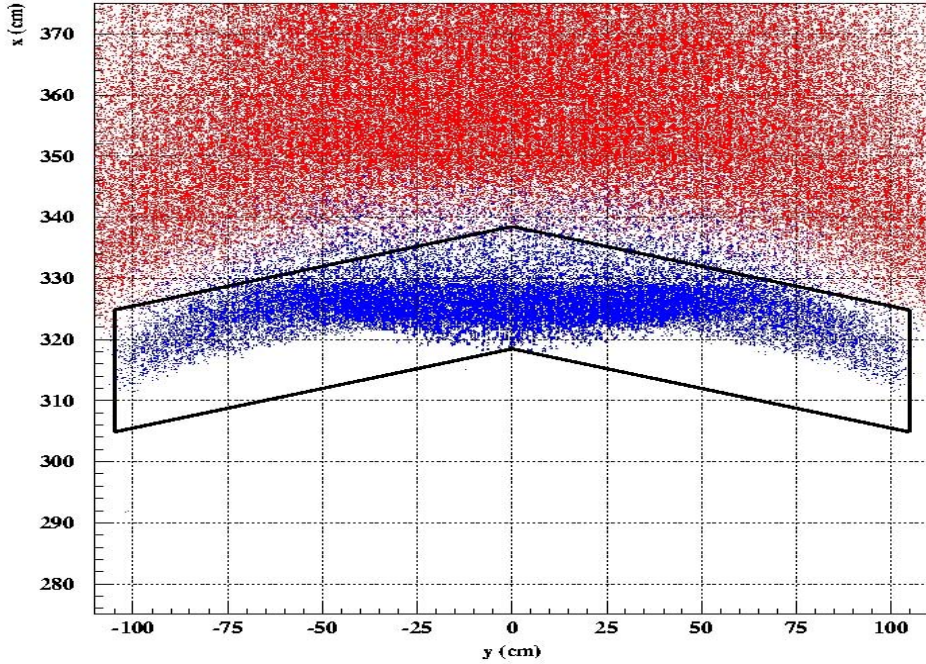


Figure 29: *Separation of elastic electrons (lower blue distribution) and inelastic electrons from pion production (upper red distribution) at the detector plane. The required active area of the detector is outlined in black. Multiple scattering in all materials as well as radiative effects are included.*

The quartz bars will be located 570 cm downstream of the center of the magnet, and approximately 325 cm from the beam axis. A schematic of the detector arrangement is shown in Fig. 29. Each bar will be 210 cm long, 16 cm high, and 2.5 cm thick. A thickness of 2.5 cm was selected for our prototype to conservatively provide enough photoelectrons while keeping the excess noise from shower generation (about 1%/cm) under control. The optimum thickness appears to be 2-2.5 cm, with a shallow minimum which depends on the surface reflectivity assumptions. However, the net excess noise using this technology is a nearly model-independent  $\sim 3\%$ .

The position dependence of the light output is highly linear (Figure 30), so when the two PMT's are summed the result is roughly constant. Adding lightguides to the simulation will improve the uniformity further. Realistic systematic variations in bar thickness are  $\pm 250 \mu\text{m}$  (or 1%), with point-to-point variations in thickness due to polishing quality of  $25 \text{ \AA}$  rms. These tolerances, combined with the fact that our optics produce only a weak correlation between position and  $Q^2$ , will produce negligible excess noise and a very small correction for  $Q^2$  bias.

During production running conditions, we must employ current-mode diagnostics if we are to check that the beam envelope has the correct shape and position at the detector plane. The simplest solution appears to be to insert specially prepared thin sheets of scintillator just after the detectors and image the result with CCD cameras. A scintillator with short attenuation length will be used, and all surfaces will be glass bead-blasted to suppress total internal reflection. This

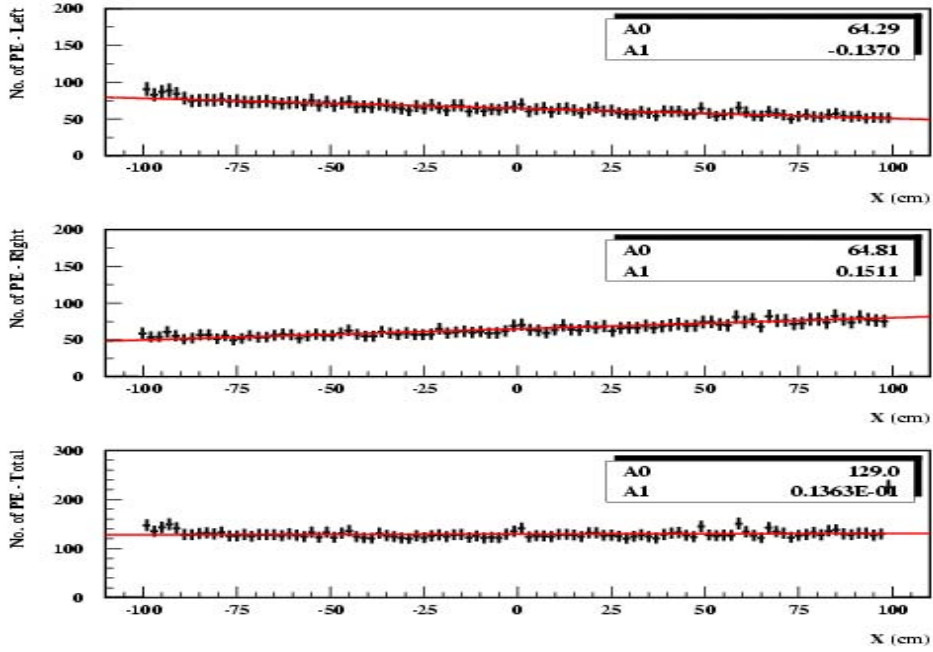


Figure 30: *The simulated position dependence of light collection in the V-shaped bars for PMT at the negative end, positive end, and the sum of the two ends. UV-glass windows, bi-alkali photocathodes, and no bevels were assumed. The final configuration will employ S20 photocathodes yielding a total of 80 photoelectrons per electron track.*

should provide a linear display of the beam envelope with good position resolution. A reticle drawn on the scintillator, previously aligned with respect to the quartz, will allow us to check the alignment between the beam envelope and the quartz bar at the mm level. The scintillator sheets will be withdrawn when not in use to prevent burning an after-image into the plastic.

Relevant parameters for the radiators are summarized in Table 5.

### 5.2.2 Photomultipliers

For our PMT we have selected the Electron Tubes D753WKB which is a UV glass, S20 photocathode variant of the Electron Tubes 9390KB. UV glass windows will produce a short wavelength cutoff at about 250 nm, which is a reasonable compromise between maximizing the number of photoelectrons and desensitizing the detectors to radiation damage. The combination of high rates and high photoelectron numbers produces an aggressive, continuous photocathode current of 6 nA. Use of standard bi-alkali photocathodes would lead to  $IR$  drops across the photocathode of many 10's of volts, contributing to nonlinearities and multiplication noise. We will therefore use S20 (multi-alkali) photocathodes which have 3 orders of magnitude smaller resistivity. A disadvantage of the S20 photocathode is its 200 times higher thermionic emission rate, but the

Table 5: Čerenkov radiator parameters.

Parameter	Value
Detector Position	z: 570 cm from magnet center r: 322.5 cm from beam axis
Bar Length	210 cm
Bar Width	16 cm
Bar Thickness	2.5 cm
Polishing Quality	Optical Polish (25 Angstrom rms)
Material	Spectrosil 2000 (Vitreous Silica)

resulting dilution will be less than 0.01% during our current mode operations.

Considerations of PMT lifetime limit us to a maximum anode current of about 6  $\mu\text{A}$ , and thus (for a fixed photocathode current of 6 nA) a maximum gain of 1000. To achieve this low gain, while maintaining the high interstage voltages required for linear operation, we will only use the first  $\sim 5$  stages of the PMT. The remaining stages will be tied together electrically as a single anode. For pulsed mode operation, the base will be switched from low gain mode to a much higher gain mode by enabling all the dynodes. To lessen the risk of damage to the PMT's from repeatedly swapping bases, we will incorporate both divider chains inside the same base (switch selectable).

The PMT gain is expected to drop less than a factor of 2 over the entire experiment due to ageing effects[61]. This will be verified with two samples of our custom PMT's in bench tests. To keep the signal into the ADC roughly constant during the experiment, we will increase the PMT high voltage or amplifier gain. No significant radiation damage to the PMT is expected. UV glass windows have been shown to retain 90% of their transmittance for light of  $\lambda > 300$  nm for gamma radiation dose of up to 140 kRad [62]. This is several orders of magnitude higher than the anticipated dose to the PMT window. Several LEDs, spanning the range from red to near-UV, will be coupled to the quartz bars. These will be occasionally pulsed during the experiment to check the stability of the optical transmission and gain. Other LED's will serve as a low-noise detector bias for noise and isolation tests as discussed in section 5.4.2.

The change from current to pulsed mode operation, which may occur several times during the experiment, will require a hall entry. The signal cables will be changed to an alternate anode output which has 50  $\Omega$  input termination to dampen reflections which would otherwise complicate our pulsed mode background studies. The other end of the signal cables must be connected to a patch panel which routes the signals to an event-mode data acquisition system. A switch on the PMT bases must also be toggled and larger high voltages downloaded. A combination of administrative procedures, power supply current limits, and gas-filled surge-suppressors will protect the PMT and base in the event that the higher voltages of the pulsed mode are accidentally applied to the few stages of the current mode divider.

Relevant parameters for the PMT's and bases are summarized in Table 6.

Table 6: Čerenkov PMT and base parameters. Nominal values for the signal in current-mode and pulsed-mode are included. Pulse heights are averaged over 10 nsec assuming a 50Ω load.

Parameter	Value
PMT:	
type	Electron Tubes D753WKB (variant of 9390KB)
photocathode	S20 (multi-alkali)
window	UV glass
coupling	DC (electrostatic shield at cathode potential)
Current mode divider:	
$I_{cathode}$	6 nA
gain	x1000 ( $I_{anode} = 6 \mu\text{A}$ )
Pulsed mode divider:	
$I_{cathode}$	< 10 pA at < 1 MHz
gain	x10 <sup>7</sup> ( $I_{anode} = 64 \mu\text{A}$ )
$V_{signal}$	8 mV for 1 pe; 320 mV for 40 pe

### 5.2.3 Front-end electronics and ADC's

In the front-end electronics, which will be custom built at TRIUMF for the  $Q_{Weak}^p$  experiment, the PMT anode signal is sent to a nearby, high gain, ultralinear current to voltage (I-to-V) operational amplifier. With a PMT anode current of 6  $\mu\text{A}$  and a transimpedance gain of 1  $M\Omega$ , the I-to-V amplifier output is 6 Volts.<sup>9</sup> A schematic of the amplifier is shown at the top of Figure 31. The I-to-V amplifier is connected to the PMT by up to 5 m of low-capacitance coaxial cable. The noise voltage output is dominated by the combination of input cable capacitance and the value of the input protection resistor. A bandwidth of 30 kHz will follow a spin flip settling time of 50  $\mu\text{sec}$ .

Because of concerns about single-event upsets and long term damage due to radiation, we have decided to do the digitization outside the experimental area. The I-to-V amplifier is followed by a cable-driving stage with an optional diagnostic offset voltage. Both front-end amplifiers are powered by isolated DC-DC converters. The two stages can be configured for a gain of 1  $M\Omega$  or 10  $M\Omega$ . This stage must drive the large capacitive load presented by the 130 m of RG213 cable to the electronics in the counting house.

Our custom VME digital integrator (shown at the bottom of Figure 31) is located in the electronics cage on the second floor of the counting house. An instrumentation amplifier at the input

<sup>9</sup>The signals from either end of a bar will be summed in software rather than hardware, so that the relative gains can be adjusted offline to optimize the uniformity of response.

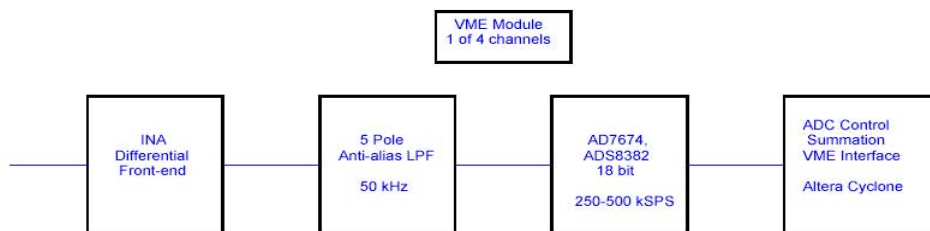
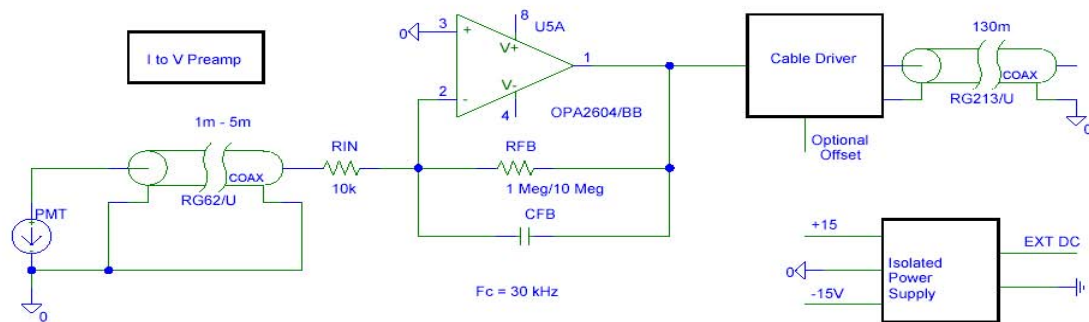


Figure 31: The top figure is a schematic showing how a current signal at the PMT anode (left) becomes a voltage signal at the ADC inputs in the counting house (right). The bottom figure is a block diagram of one of the VME sampling ADC modules.

provides common mode noise rejection and is followed by a 50 kHz anti-alias filter. The combination of front-end transimpedance amplifier and anti-alias filter allows the system settling time and noise bandwidth to be controlled separately. An 18-bit ADC operates at a fixed sampling rate up to 500K samples per second, sampling being controlled by signals derived from external clock and gate signals. The combination of 18-bit precision and fast sampling allows us to spread even our lowest noise signal over 9 channels (FWHM), so dithering the signal before the input to the ADC will probably not be required. The output of each ADC in the module is summed for a selectable number of samples and made available to the DAQ system through the VME interface. All control, summation and VME logic resides in a Field Programmable Gate array (FPGA).

Relevant parameters for the TRIUMF front end- and digitizing electronics are summarized in Table 7.

Table 7: *Parameters of the TRIUMF front end- and digitizing electronics.*

Parameter	Value
Amplifier:	
type	OPA2604/BB
transimpedance	1 M $\Omega$
$I_{in}, V_{out}$	6 $\mu$ A $\rightarrow$ 6 V
nonlinearity	$< 10^{-4}$
ADC:	
type	AD7674 or ADS8382
precision	18 bits
sampling frequency	250-500 kSPS
nonlinearity	$< 10^{-4}$

## 5.3 Expected detector system performance

### 5.3.1 Photoelectron yield and position dependence

Prototype quartz bar Čerenkov detectors were built at LANL and JLab. The rectangular bars were made of Spectrosil 2000 and had dimensions 100 cm by 12.5 cm by 2.5 cm (roughly 1/2 the final length). All surfaces were polished with a standard optical-grade finish except for  $\sim$ 1.5 mm beveled edges which the polishing subcontractor missed. The detectors were instrumented with 5" PMT's and bases that happened to be on hand. PMT's were glued directly to the ends of the bars. The LANL module was tested with cosmic ray muons, while the JLab module was tested in the SOS detector hut using a mixed beam of 1 GeV/c pions and electrons. The slightly greater response to electrons relative to pions (due to showering of the electrons) can be clearly

seen in Figure 32. A correction for the bar vs photocathode matching (the bar was wider than the active diameter of the PMT) leads to the experimental value of 38 pe's in Table 8.

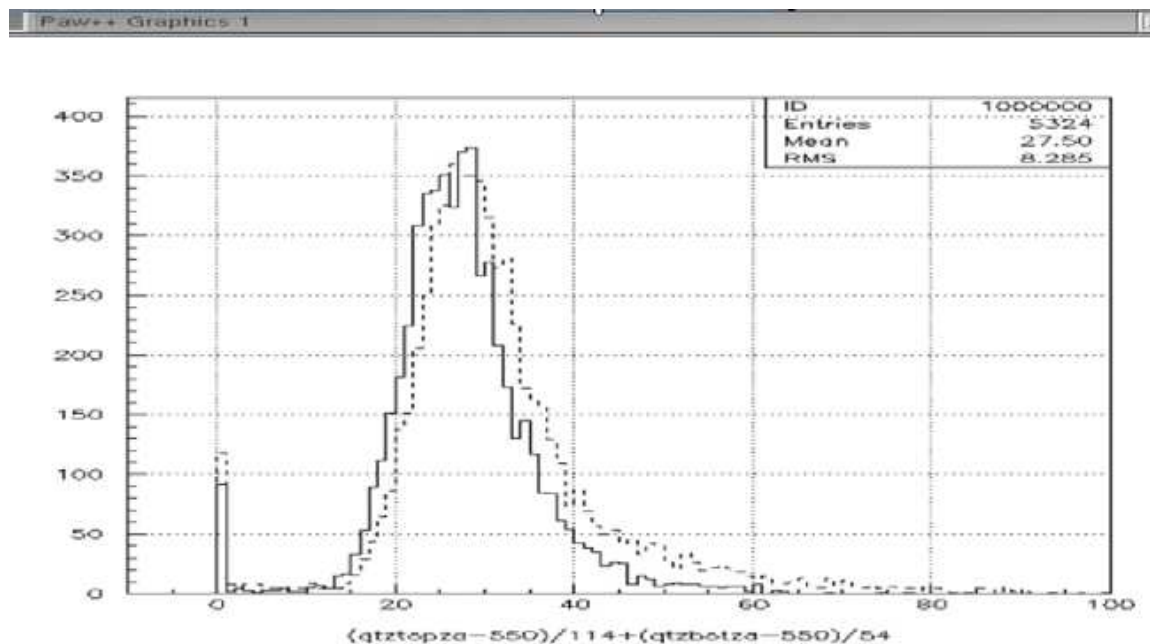


Figure 32: Yield versus photoelectrons per track for pions (solid) and electrons (dashed) in the 2.5" thick quartz JLab prototype bar. The electrons produce slightly more light due to showering. A correction for the bar vs photocathode matching leads to the experimental value of 38 pe's in Table 8.

LaTech has developed sophisticated simulations of light transport in the bars based on GEANT. Software extensions have been written to incorporate the wavelength dependence of the index of refraction, imperfect total internal reflection, quantum efficiency of the photocathodes, etc. This was our first opportunity to benchmark the simulations, and we immediately discovered that the size and polish quality of the bevels was not negligible. The simulations indicated that the existing unpolished bevels reduced the number of photoelectrons by about 40%. Once unpolished bevels were included in the simulations, the agreement with measurements was good. (Table 8, bottom row) This agreement gives us confidence that the LaTech simulations will give accurate results for evolutionary modifications such as the new V-shape of our updated reference design. By specifying polished bevels of <0.5 mm for the final detectors, we expect an S20 photocathode to yield about 80 pe's (Table 8, last column). Despite the lower quantum efficiency of the S20 photocathode, we should have 4 times more photoelectrons than needed.

### 5.3.2 System linearity

In reference [63], it was found that a detector system (integral) nonlinearity of < 1% would be adequate provided that reasonable constraints are met for the charge asymmetry and the beam

Table 8: *Simulated photoelectron yields for different window, photocathode, bevel size, and bevel polishing configurations. Prototype results (with about 15% errors) are compared to the corresponding simulations in the bottom row. We expect about 80 pe's for the final  $Q_{Weak}^p$  configuration, which will have polished bevels of  $<0.5$  mm, and S20 photocathodes.*

Bevel Configuration	JLab Test Lime Glass bi-alkali	LANL Test UV Glass bi-alkali	$Q_{Weak}^p$ UV Glass S20
no bevel	70	133	89
polished 1 mm	57	108	72
unpolished 1.5 mm	40 ( <b>38 expt.</b> )	76 ( <b>87 expt.</b> )	51

intensity variance asymmetry. We expect to have a system with nonlinearity that is 1-2 orders of magnitude smaller than this criterion, so corrections for nonlinearities in the detector system should be negligible. The amplifier and ADC are linear to within 1 part in  $10^4$ . Considerations of track occupancy in small regions of the quartz bar suggest that light production from the Čerenkov process will be at least this linear. The weakest link is the PMT where  $IR$  drops on the photocathode, and space charge effects near the anode, are both potential sources of significant nonlinearity. However, our use of S20 photocathodes and low gain ( $\times 1000$ ) operation as discussed above should allow the PMT to operate with a nonlinearity of  $10^{-3} - 10^{-4}$ .

Our custom PMT's have been ordered, and the voltage dividers are under design. Once both are available, their linearity will be tested with an extremely sensitive two-LED technique. One LED will operated in DC mode to provide a relatively large, adjustable load, while the other LED will be operated in AC mode as a small, fixed-magnitude signal. The AC component will be detected by lock-in amplifier, and its sensitivity to changes in the DC load will be used to measure the linearity.

### 5.3.3 Excess noise

It is critical in a statistics-limited experiment like ours that excess noise sources be small. Only then can the experiment converge to its error goal at the optimal rate dictated by electron counting statistics. It is also valuable for the electronics chain to have a noise level which is many orders of magnitude below counting statistics, so that we can quickly measure isolation of the experiment from the reversal signal in the injector.

The experimental asymmetry is given as:

$$A = \frac{Y_+ - Y_-}{Y_+ + Y_-} \simeq -0.26 \text{ ppm}$$

where  $Y$  is the total integrated detector signal normalized to the incident beam charge. The

statistical error in the measurement of  $A$  for perfect detectors is given by counting statistics:

$$\Delta A_{count} = \frac{1}{\sqrt{N}}$$

for a given total number of detected electrons  $N$ . In reality, there will be additional random errors due to noise sources in the detector itself, e.g. fluctuations in the number of photoelectrons per incident scattered electron, and in the electronics. We define the quadrature sum of these additional random errors as a noise factor  $\alpha$ , such that:

$$\Delta A = \Delta A_{count} \times \sqrt{1 + \alpha^2}$$

where

$$\alpha^2 = \left(\frac{\sigma_{N_{pe}}}{N_{pe}}\right)^2 + \dots$$

The ‘excess noise’ in the measurement of  $A$  is then defined as the fractional amount by which the statistical error in  $A$  exceeds the counting statistics value, i.e.

$$excess\ noise = \sqrt{1 + \alpha^2} - 1$$

The electronic noise is dominated by the current noise of the preamplifier and the ADC to 0.2 ppm/ $\sqrt{Hz}$  (Table 9). Although an individual read of our 18 bit ADC has a least bit error of 7.6 ppm at 1/2 full scale, this is reduced to a negligible level by rapid sampling. Noise sources in the radiator and PMT’s are of equal or greater importance to the electronic noise. First of all, shower fluctuations in the 2.5 cm thick quartz bars contribute about 2.5% excess noise. The finite number of photoelectrons (80) also contributes a small amount of excess noise (0.6%) since the electron tracks are randomly given slightly different weights. Multiplication noise in the dynodes increases the latter to about 0.8%.

Other potential sources of excess noise have been considered, but those which are luminosity-*independent* (such as cosmic rays striking the PMT glass envelope) can largely be ignored. Individual PMT’s could show excess noise from luminosity-*dependent* multiplication noise, sparking, or after-pulsing. Multiplication noise can be thought of as the single photoelectron resolution and is a relatively small effect for large photoelectron numbers like ours. Sparking can result from the charging up of insulated structures or (in a current-mode application like ours) failure to hold the electrostatic shield at cathode potential. After-pulsing is due to the ionization of residual gas (or Helium contamination), yielding large, late “echos” of the original signal. Since sparking and after-pulsing are both largely proportional to anode current, it will be a simple matter to qualify all our PMT’s before the experiment by measuring noise levels with an LED light source. Subsequent measurements made during the run would quickly indicate whether a given PMT needed to be replaced due to Helium poisoning, for example.

Methods for verifying the predicted excess noise levels and measurement of the isolation from the reversal signal are discussed in Section 5.4.

Table 9: *Noise contributions for a single detector octant for a time interval of 1 second. The total excess noise of about 3.4% is dominated by shower fluctuations in the quartz. The excess noise due to finite photoelectron number (80) includes a factor of 1.15 for multiplication noise. (The noise values for the interval of 1 second can conveniently be interpreted in units of ppm/ $\sqrt{\text{Hz}}$  and scaled to other time intervals and number of octants by  $1/\sqrt{N_{\text{octants}}t(\text{sec})}$ .)*

Noise Source	ppm for 1 second
Electron track	
counting statistics	35.4 ppm
I-to-V current noise	0.16 ppm
I-to-V voltage noise	0.00 ppm
I-to-V Johnson noise	0.02 ppm
ADC	0.12 ppm
shower fluctuations (2.5 cm)	8 ppm
finite pe's	4.5 ppm
5% nonuniformity	1.6 ppm
Total:	36.6 ppm (3.4% excess noise)

## 5.4 Validation of detector performance

### 5.4.1 Excess noise

The detector system noise performance discussed can be largely validated by introducing low noise inputs during occasional beam-off periods. These signals will have the approximate magnitude of real signals. By replacing elastic electrons with an equivalent amount of light into the PMT, the statistical noise can be reduced by the factor  $1/\sqrt{N_{pe}} = 0.11$  assuming 80 pe's per track.<sup>10</sup> (Figure 33) Since the LED test uses the PMT, it is a sensitive test for such excess noise sources as after-pulsing or sparking. An even more sensitive test (approaching the shot noise limit of the 6  $\mu\text{A}$  input) is to replace the light sources altogether with a current source at the input to the I-to-V amplifier. The shot noise limit is more than 2 orders of magnitude *smaller* than the electron track statistical error, so a current source could allow a sensitive test of amplifier and ADC noise.

Because the LED- and current source-biased runs have so little noise compared to the counting statistics of electron tracks, the time needed to identify excess noise at a significant level is very short. If we take 10% excess noise as our threshold for concern (which would increase the statistical by only 0.5% over counting statistics), this would yield a 100% change in the predicted noise level of an LED run or a 1000% change in the expected level using a current source. Thus, even one second would be plenty of time to make a determination of whether the apparatus itself

<sup>10</sup>A more careful analysis is required which takes the single photoelectron resolution into account, but the simple scaling argument above is only optimistic by perhaps  $\sqrt{2}$ .

(in the absence of beam) was a significant source of excess noise. By monitoring these noise levels intermittently throughout the experiment, we will be able to track potentially increasing noise levels from radiation damage to the amplifier, Helium poisoning to the PMT's, etc.

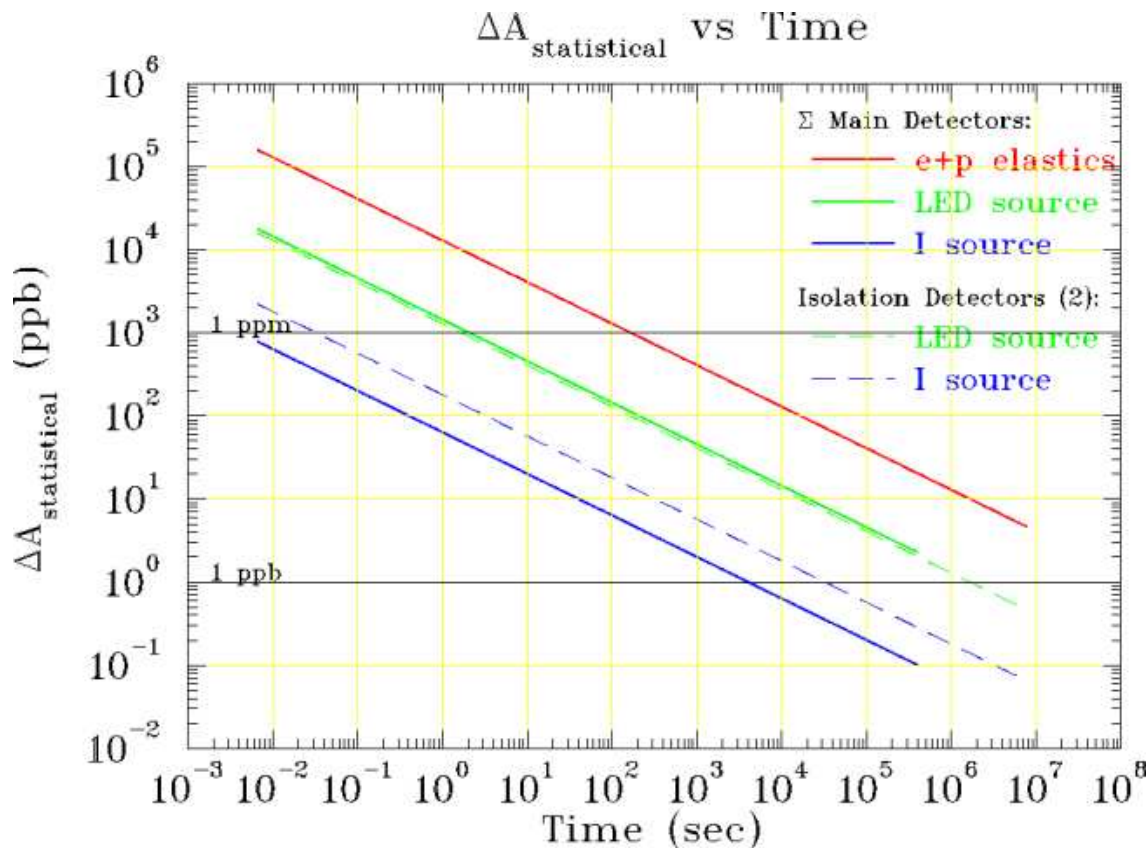


Figure 33: *Statistical error versus time for the main detectors with  $e+p$  elastic counting statistics (top red solid line), main detectors biased with low noise sources for up to 5% of the experiment (green and blue solid lines), and dedicated isolation detectors biased with low noise sources for 100% of the experiment (green and blue dashed lines).*

#### 5.4.2 Ground loops

Another important validation of the detector system involves the isolation of the detector signals from the helicity reversal signal. Here the concern is a false asymmetry, rather than excess noise. Although delayed reporting will in principle protect the detector system from egregious cross-talk between the reversal and detector signals within the counting house, the helicity reversal in the injector can still be communicated directly to the detector system via the accelerator ground. Occasional reversal of the half-wave plate throughout the experiment has the potential to cancel the majority of such effects, since it reverses the sign of the physics asymmetry without changes

to the electrical state of the system. However, this technique alone is unsatisfactory since the magnitude of the cross talk is never actually measured. For example, if the cross talk changes in magnitude over time, the cancellation achieved by blindly reversing the half-wave plate could still lead to unacceptably large errors. We plan to directly measure (or tightly bound) the isolation of the detector system from the reversal signal.

Figure 33 shows that, while low noise current source measurements can be made using the main detectors at the ppb level in a few hours, an LED run using the main detectors at the ppb level would barely be possible during an extended maintenance period. Unfortunately, measurements made during long maintenance periods may be rendered uninterpretable due to work in the injector (regrounding, switching off the Pockels cell, etc.) To get around this problem, and provide continuous coverage with current sources, we will incorporate two well-shielded “isolation detectors” inside the detector hut which will operate at 100% duty factor. (dashed lines in Figure 33) These two isolation detectors will be electrically similar to the main detectors; one will be biased with an LED and the other with a current source. The current source will reach ppb-level sensitivity to ground-loops in approximately one eight hour shift. The LED source will take much longer to reach ppb-level sensitivity, approximately 23 days, but it will provide several measurements of this precision during the experiment. The LED data are valuable because they include the effect of the PMT and its HV supply.

The isolation detectors described here will not be sensitive to coupling of the reversal signal to the beamline current and position monitors. These critical measurements require different techniques and are discussed in section 9.

## 6 Tracking System

Excellent  $Q^2$  determination is critical to the  $Q_{Weak}^p$  experiment, since the asymmetry at low  $Q^2$  is directly proportional to  $Q^2$ . Thus, an error in  $Q^2$  directly translates to an error in the extraction of  $Q_{Weak}^p$ . We need to determine the acceptance-weighted distribution of  $Q^2$ , averaged over the acceptance and weighted by the analog response of the Čerenkov detectors with  $\approx 1\%$  accuracy. The primary purpose of the tracking system is this  $Q^2$  measurement; an additional motivation is the measurement of any backgrounds contributing to the asymmetry measurement.

For elastic scattering,

$$Q^2 = \frac{4E^2 \sin^2 \theta/2}{1 + 2\frac{E}{M} \sin^2 \theta/2}$$

where  $E$  is the incident electron energy,  $\theta$  the scattering angle and  $M$  the proton mass. In principle, a measurement of any two of  $E$ ,  $\theta$ , or  $E'$  (the scattered energy) yields  $Q^2$ . The absolute beam energy will be known to  $\leq 0.1\%$  accuracy using the Hall C energy measurement system, corresponding to a  $0.2\%$  error in  $Q^2$ . As the entrance collimator is designed to be the sole limiting aperture for elastically scattered events, good knowledge of the collimator geometry and location with respect to the target and the beam axis might seem to suffice for determining  $Q^2$ . The central scattering angle for each collimator will be determined by redundant survey techniques to  $\leq 1$  mrad, corresponding to  $1.2\%$  in  $Q^2$ .

However, this is overly simplistic. One needs to a) account for beam energy loss and radiation in the target (affecting  $E$ ), b) ensure that only elastic events contribute to the  $Q^2$  measurement, and c) weight the result with the analog response of the Čerenkov detector. Rather than rely solely on a simulation to account for these effects, we choose to *measure* them with a dedicated tracking system. These measurements will be made in dedicated calibration runs in which the beam current is reduced to less than 100 nA, allowing the use of the tracking system. In this  $Q^2$  measurement mode, the Čerenkov detectors will be read out in pulse mode and individual particles tracked through the spectrometer system using a set of chambers (Region 1, Region 2, and Region 3, described below). This information will allow us to determine, on an event-by-event basis, the scattering angle, interaction vertex (to correct  $E$  for dE/dx and radiation in the target),  $E'$  (to confirm elastic scattering) and location and entrance angle of the electron on the Čerenkov detector.

As we will sum the signals from the two ends of the Čerenkov detector (as described in section 5), the net analog response will be as independent of  $Q^2$  as possible. The long axis of the detector is along the azimuthal coordinate  $\phi$  and, although the rate will necessarily change over the two meter length of the detector, there should be little physics dependence along this axis. To first order, ignoring finite target length, the optics focuses the elastic peak to a point along the short axis and thereby maps all  $Q^2$  to the similar detector regions, although with differing angles of incidence. Thus the variation of the amplitude of the Čerenkov signal with incident angle and

location along the detector should have only a small effect of the acceptance-averaged kinematics ( $Q^2$ ).

As we will be sampling the  $Q^2$  distribution at low beam currents, we will have to model (or otherwise determine) any changes in the target density profile due to target heating at higher currents.

A conceptually similar  $Q^2$  measurement was made for the Hall A Proton Parity Experiment (HAPPEX) [34]; indeed, in the first HAPPEX experiment, extracting the proper acceptance-averaged value of  $Q^2$  was the most difficult part of the data analysis. Unlike the HAPPEX case, which used the Hall A High Resolution Spectrometers, the intrinsic resolution and focusing properties of the  $Q_{Weak}^p$  spectrometer will not be sufficient to adequately determine the acceptance-weighted  $Q^2$  solely by the use of rear tracking chambers; hence, the need for a three-region tracking system as described here.

In addition to the precise determination of  $Q^2$ , the tracking system will enable us to determine the ‘dilution factor’: the contribution of non-elastic scattering events to the Čerenkov detector signal, such as inelastic events from the target, events arising from the detector walls, and any general background in the experimental hall.

## 6.1 $Q^2$ Determination Requirements

The parity-violating asymmetry can be separated into a term linear in  $Q^2$  involving  $Q_{weak}$ , and additional terms (due to hadronic structure) entering at higher powers of  $Q^2$ , called the QCD correction [35] :

$$A = -a_0\tau Q_{weak} + A_{QCD},$$

with

$$A_{QCD} = a_0\tau^2 \left\{ \frac{\varepsilon G_E^\gamma (G_E^n + G_E^s) + \tau G_M^\gamma (G_M^n + G_M^s) - \varepsilon' [1 - \sin^2 \theta_W] G_M^p G_A^Z}{\varepsilon (G_E^\gamma)^2 + \tau (G_M^\gamma)^2} \right\},$$

where  $\tau = Q^2/4M^2$ ,  $\varepsilon$  and  $\varepsilon'$  are kinematic factors which are functions of  $\tau$  and  $M/E$ ,  $a_0 = G_F M^2 / \sqrt{2} \pi \alpha \approx 316.7$  ppm, and the  $G$ 's are nucleon form factors which depend only on  $\tau$ .

At low energies and very forward angles, as  $\tau \rightarrow 0$ , we have  $\varepsilon \rightarrow 1$  and  $\varepsilon' \rightarrow 2\tau \frac{M}{E}$ , therefore the QCD correction can be expanded in a power series in  $\tau$  [35]:

$$A_{QCD} = a_0\tau^2 \left( \sum_{n=0} B_{V,n} \left(\frac{M}{E}\right) \tau^n + 2\frac{M}{E} B_{A,n} \left(\frac{M}{E}\right) \tau^n \right).$$

The moments  $B_{V,n}$  and  $B_{A,n}$  will be extracted from a combined analysis of the SAMPLE, HAPPEX, HAPPEX-II, HAPPEX-He, G0, and PVA4 data.

The leading contributions have been calculated by Ramsey-Musolf[35] using the  $\overline{\text{MS}}$  coupling scheme:

$$Q_{weak} = (1 + R_V^p) [1 - 4 \sin^2 \theta_W],$$

$$B_{V,0} = (1 + R_V^n) [\mu_p \mu_n + \rho_n] + (1 + R_V^s) [\mu_p \mu_s + \rho_s],$$

$$B_{A,0} = [1 - 4 \sin^2 \theta_W] \{-2[1 + R_A^3]G_A^3(0) + \sqrt{3}R_A^3 G_A^8(0) + [1 + R_A^s]G_A^s(0)\},$$

$$G_A^3(0) = \frac{g_A}{2}, \quad G_A^8(0) = \frac{g_A}{2\sqrt{3}} \left( \frac{3f - 1}{f + 1} \right),$$

$$\rho_{n,s} = \left. \frac{dG_E^{n,s}}{d\tau} \right|_{\tau=0}, \quad g_A = 1.261, \quad f = F/D \approx 0.64.$$

Here,  $R_{V,A}$  denote weak vector and axial-vector radiative corrections, respectively. If we define the acceptance averaged measurement of the asymmetry as the average over the extended target and spectrometer acceptance and weighted by the analog response of the detector, *i.e.*,  $\langle A_{\text{exp}} \rangle$ , then,  $Q_{Weak}^p$  can be extracted from the data using

$$Q_{weak} = \frac{1}{a_0} \frac{\langle A_{\text{exp}} \rangle - \langle A_{QCD} \rangle}{\langle \tau \rangle} \approx \frac{\langle A_{\text{exp}} \rangle - B_V(0)a_0 \langle \tau^2 \rangle - 2B_A(0)a_0 \langle \tau^2 M/E \rangle}{a_0 \langle \tau \rangle}.$$

Of course, in a full Monte Carlo analysis, all significant moments are included, but since  $\tau \approx 0.01$ , the higher moments are hardly significant for  $Q_{Weak}^p$  kinematics. The incident energy  $E$  is a constant in the absence of straggling and Bremsstrahlung in the target.

Reconstruction of the  $Q^2$  calibration data will give the important moments,  $\langle \tau \rangle$ ,  $\langle \tau^2 \rangle$ , and  $\langle \tau^2 M/E \rangle$  with high accuracy. However, in comparing theory to measurement, there are two completing definitions of  $Q^2$  that are in play, the experimentally measured  $Q^2$  and the true  $Q^2$  of the scattering vertex, corrected for radiative and straggling effects. Moreover, both can be well defined only in the peaking or "effective radiator" approximation, since we have no direct knowledge of nucleon form factors far off the mass shell.

1) The  $Q^2$  of the scattering vertex is the  $Q^2$  of interest, since it relates directly to the scattering asymmetry, but is not directly measurable. It needs to be corrected for all energy losses (virtual and real Bremsstrahlung, as well as ionization energy losses) occurring before the scattering, *i.e.*, along the incoming electron direction. The definition of the initial electron energy at the scattering vertex ( $x$ ) is given by

$$E_{\text{vertex}} = E_0 - dE_{\text{before}}(x) - d\omega_{\text{before}}$$

Here,  $E_0$  is the beam energy,  $dE_{\text{before}}(x)$  is the mean ionization energy loss up to the scattering vertex, and  $d\omega_{\text{before}}$  is the radiative energy loss along the incident electron direction.

2) The measured  $Q^2$  is generated by using beam position monitors along with trace-back from the front Region I and II chambers. A coincidence with the Region III chambers is used to select only elastic scattering events and to allow for analog-weighting of the Čerenkov detector response. This defines  $Q^2$  in terms of a direction and a point in the target. The final electron energy is ignored. Using this definition, one can correct the  $Q^2$  for the most probable energy loss up to the scattering vertex, but there is no way to account for real and virtual radiative losses. Therefore the calculations assume the most probable value for this, i.e., zero radiation before the vertex. The definition of the electron energy at the vertex is given by

$$E_{\text{vertex}}(0) = E_0 - dE_{\text{before}}(x)$$

With either of these definitions of the vertex energy, and knowledge of the scattering angle,  $Q^2$  can be calculated for elastic scattering at the vertex. Monte Carlo estimates of difference between the two definitions is small  $\leq 1\%$ , and the Monte Carlo routines can reliably be used to reduce the residual error due to the correction to negligible proportions. Note that both definitions are defective in that they ignore the possibility of large angle Bremsstrahlung. Fortunately, this is an extremely small effect (except possibly for very large radiative losses that won't appear in our cuts). Multiple scattering can be treated as a resolution effect in the simulations.

The estimated total kinematic correction for radiative effects leads to a reduction in  $Q^2$  of less than 1% for the  $Q_{\text{Weak}}^p$  kinematics, similar to the HAPPEX experience [36].

## 6.2 Tracking System Overview

The  $Q_{\text{Weak}}^p$  toroidal spectrometer, QTOR, views most of the  $2\pi$  azimuthal acceptance at small forward scattering angles and is segmented into 8 octants. Figure 29 shows the expected distribution of events in the focal plane. In the absence of radiative processes, the elastic peak is entirely contained within the detector volume, minimizing edge effects. The inelastic response begins at pion threshold and is largely outside of the volume of acceptance. The focal plane of each octant is large, with a perpendicular cross-sectional area just before the 'V'-shaped quartz Čerenkov detectors of  $\sim 16 \times 210 \text{ cm}^2$ . To cover this area, wire chambers would have to be somewhat wider: about 50 cm wide, by 2 m long.

Three regions of tracking chambers are being constructed: The Region 1 vertex chamber, based on GEM (Gas Electron Multiplier) technology, will have excellent position resolution and will be registered directly to the rear face of the primary collimator. Downstream from that, at the entrance of the spectrometer, will be the Region 2 magnet entrance chambers, based on a horizontal drift chamber (HDC) architecture. The spatial separation between the Region 1 and

Region 2 chambers will define the scattering angle of elastically scattered events to high accuracy. The Region 3 chambers, which will be a pair of vertical drift chambers (VDCs), will be located just upstream of the focal surface. Their use is to momentum-analyze the events (to ensure that the detected events are true elastic electrons), as well as to provide a complete characterization of the particle trajectories entering the Čerenkov detector and of its response. Finally, trigger scintillators will be positioned between the Region 3 VDCs and the Čerenkov bars in order to provide a trigger to the electronics and a timing reference.

Figure 34 shows a cross section of the spectrometers indicating the positions of the three chamber packages. To contain costs, we are constructing only two complete sets of chambers on opposite sides of the beam line. We will rotate them to sample all other sectors sequentially as shown in Figure 34. The calibration runs will not be time intensive nor will it need to be repeated frequently, therefore the beam time overhead involved with this approach is acceptable.

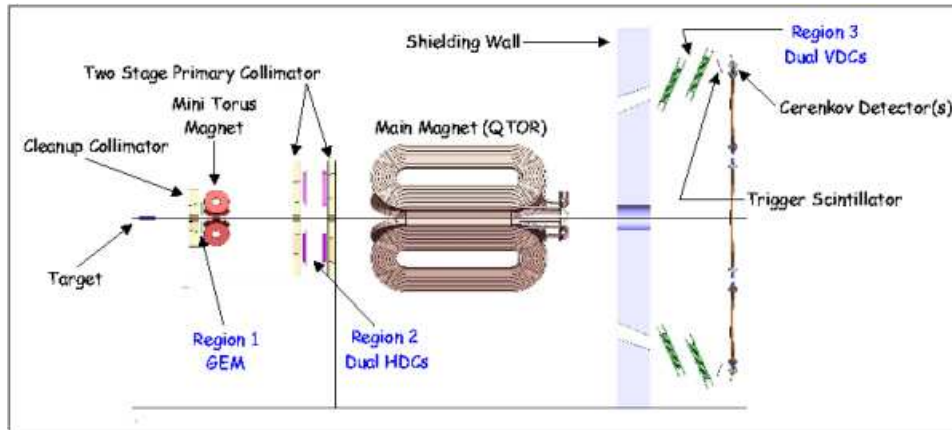


Figure 34:  $Q_{Weak}^p$  spectrometer schematic showing the locations of the Regions 1, 2 and 3 tracking chambers in relation to the overall apparatus.

A shielding hut will protect the Čerenkov detectors from room backgrounds which are expected to be significant during the asymmetry measurement and to scale down during the calibration measurements. There is no need to expose the Region 3 drift chambers and trigger scintillators to the unshielded room background, so the shielding hut will be large enough to accommodate them and the Ferris wheel that supports them, the Čerenkov bars and their support frame, and any electronics that need to be in the Hall.

The front wall of the shielding hut will have an aperture for each octant and the apertures will be sufficiently large so as to not define the acceptance of the detectors. Detailed GEANT simulation of the shielding and the apertures is underway. A wall thickness of 1 meter of concrete appears adequate. During the asymmetry measurement, the rate of elastically scattered electrons will be  $\sim 800$  MHz on each octant; incident photon rates due to Bremsstrahlung processes will be  $\sim 200$  MHz in air or 100 MHz if the electron path between the target and the detector hut is filled

with helium; the latter is assumed in the  $Q_{Weak}^p$  reference design.

### 6.3 Rate Considerations for Tracking Chambers

The instantaneous counting rate per octant at the focal plane in the asymmetry measurement is high, about 800 MHz. Fortunately, the beam current can be reduced from 180  $\mu\text{A}$  to 10 nA for the  $Q^2$  calibration and background and dilution factor measurements. This results in instantaneous counting mode rate of about 45 kHz/octant at the focal plane. These rates correspond to rates per mm of wire per second that are orders of smaller magnitude than rates at which similar chambers routinely operate, so the Region 3 drift chambers should have no difficulties. The trigger rate will be pre-scaled down to provide a manageable data acquisition rate. At the entrance to the spectrometer, however, rates will be three orders of magnitude higher, dominated by low-energy Møller electrons that fall within the collimator acceptance. To compensate, the Region 1 chambers will be GEM detectors, which are radiation hard and can work at the anticipated rates (see below), and a Mini-Toroid sweeping magnet will be installed to reduce the rate for the Region 2 chambers, as described below.

### 6.4 Mini-Torus Møller Electron Sweeping Magnet

A low-field mini-torus sweeping magnet will be installed between the locations of the Region 1 GEMs and the Region 2 drift chambers to prevent Møller electrons from reaching the Region 2 chambers during the low-current calibration studies. The Region 2 drift chambers are conventional horizontal drift chambers, so they need to operate at a total rate of  $< 1$  MHz for high tracking and reconstruction efficiency. With no sweeping magnet, the region 2 drift chambers would be exposed to a total Møller electron rate of  $\sim 2600$  kHz/nA of beam current, with the Møller energies ranging from 20 - 80 MeV. This would correspond to an unacceptable rate of 26 MHz at our desired calibration run beam current of 10 nA. The mini-torus magnet will sweep the low energy Møller electrons into the inner radius of the primary collimator (see Fig. 35), limiting the incident rate of Møller electrons on the region 2 chambers to  $\sim 73$  kHz/nA, which leads to an acceptable chamber rate of about 730 kHz at the 10 nA beam current. This rate was determined from GEANT simulations using a field map for the mini-torus structure described below, assuming the mini-torus magnet operates at its maximum allowed current density.

The mini-torus magnet consists of eight circular coils arranged symmetrically around the beam pipe in the same manner as the main QTOR magnet. The device has a total field integral of about 0.020 T-m (about 3% of the main QTOR magnet field integral). It bends the Møller electrons in the direction of the beam pipe by about 6 - 10°, causing them to be incident on the inner part of the primary collimator where they are absorbed. Since we will perform the  $Q^2$  calibration studies with the mini-torus on, we will leave it on during the production running as well. The mini-torus only bends the primary e-p elastic electrons by about 0.30°, which is only

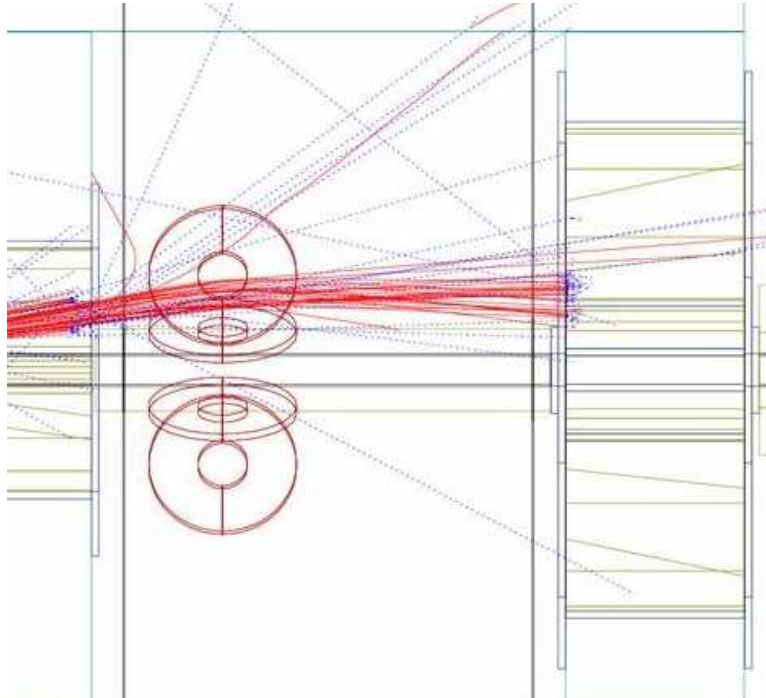


Figure 35: A *GEANT* schematic of the mini-torus coils sweeping Møller electrons into the inner radius of the upstream face of the primary collimator.

3% of the  $10^\circ$  bend they experience in the main QTOR magnet<sup>11</sup>.

The mini-torus magnet will be made from copper conductor of square cross section (7 mm x 7 mm) with a 3.9 mm diameter hole in the middle to allow for the circulation of cooling water. Each coil will consist of two “double-pancake” structures. Each double-pancake has a coil built of 2 x 25 turns; thus, the total conductor cross section of a given coil will be 2.8 cm x 17.5 cm. The coils will be 2.8 cm thick. The inner radius of the coils will be 8.75 cm and the outer radius 26.25 cm. At the maximum recommended current density for water-cooled copper coils (560 A/cm<sup>2</sup>), the current will be 208 amps at 94 volts, assuming that the coils are run in series. This leads to the requirement for a 19.5 kW power supply. Assuming 16 parallel water lines, the cooling water needs of the device are modest - 2.4 gallons per minute for a 30°C temperature rise. The weight of each coil will be about 106 pounds.

## 6.5 Region 1: Vertex Detectors (GEM)

A front tracking system for  $Q_{Weak}^p$  needs to be more resistive to radiation than the remaining downstream elements because of its close proximity to the target. Even though the elastic rates

<sup>11</sup>It should be noted that all rate calculations and acceptance studies reported in this proposal have been performed with the mini-torus ‘on’ and operating at its nominal current setting.

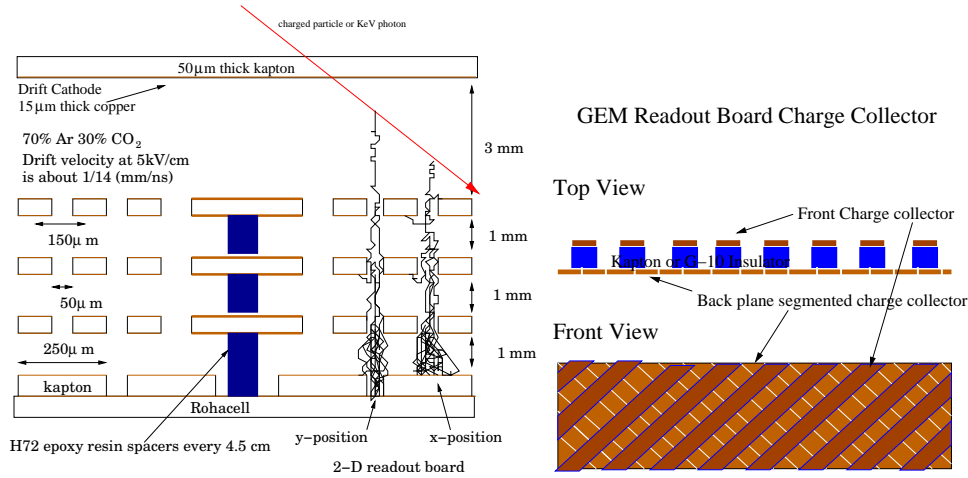


Figure 36: *The left image is the side view of an ionization based tracking chamber with three GEM preamps and a 2-D readout board. The right image is a schematic of the GEM readout board.*

at a beam current of 10 nA would approach 45 kHz, a large, low electron momentum (50 MeV) background due to Møller scattering will be present which is at least a factor of 100 larger than the elastic rate. This large signal from Møller scattering will prevent the use of traditional drift chambers in the forward region. A tracking system in the forward region would need to survive for an extended period of time in a high radiation environment with doses of 1 Mrad/year and sustain a particle flux on the order of 1,000 particles per square millimeter of detector area every second.

The Gas Electron Multiplier (GEM) is a high flux structure used to amplify the ionized charge within a gas chamber and thereby facilitate charged particle detection. Micropattern gaseous detectors have matured substantially since the first introduction [39]. Expensive and fragile microstrip gas chambers have been replaced by robust and inexpensive structures. A GEM is a thin polymer foil, metal-clad on both sides and perforated by holes having a radius on the order of  $50 \mu\text{m}$  in a staggered grid pattern in which the distance between adjacent holes is on the order of  $100 \mu\text{m}$ . The foil acts as a pre-amplifier when immersed in the gas volume of an ionization chamber. Charge multiplication occurs when the electrons pass through the foil holes whose sides have had a electric potential difference applied to produce electric fields on the order of 40 kV/cm. The large amplification, beyond  $10^4$  for a multi-stage device, facilitates single particle detection by charge collectors which may be as simple as a printed circuit board.

The design of the Region 1 system is based on that used by COMPASS [37] and has a well established performance record. In addition to adopting the triple GEM pre-amplification method employed by COMPASS, a similar multiplexing system will be used to reduce the amount of readout electronics, taking advantage of the small electron angle variation normal to the detector which limits the trajectory to a transverse distance of  $\approx 5 \text{ mm}$  across the face of the detector.

The detector will have an area of  $(10 \text{ cm})^2$ , a thickness of  $\sim 6 \text{ mm}$  and will be located just behind the first collimator. The detector will be mounted on a rail system to move out of the acceptance for the high current physics measurement. A rotation system will be used to move the detector between 4 octants. An identical detector mounted on the opposite side of the beam will be used for the remaining octants.

The ionization chamber is a lightweight structure built from Rohacell and copper clad kapton foils with a fiberglass support structure. The front entrance window to the detector is a sheet of 1mm thick Rohacell which supports a copper-clad kapton sheet  $50 \mu\text{m}$  thick. The walls of the ionization region are created using a 8mm thick fiberglass frames. The charge collector is mounted on the bottom of the ionization chamber and then three GEM foils are stacked on top as shown in Figure 36. The ionization chamber will be built using the students, faculty and staff at Louisiana Tech. The GEM foils and charge collector will be purchased from CERN. The charge collector will have a pitch of  $400 \mu\text{m}$  and will provide sufficient resolution to facilitate a measurement of  $Q^2$  with the desired relative error.

Once charge is accumulated at the collector, pulse shaping and amplification electronics are needed which will convert a charge equivalent to 500 electrons to a mV signal. A multiplexing circuit [42] was developed by ASIC laboratories and used by COMPASS to reduce the number of modules used to read out the charge collector signals. The pulse shaping and amplification electronics are incorporated into the multiplexing chip and wire-bonded to kapton leads that are connected to individual charge collector output channels. Four readout boards containing the Helix chip [42] have been acquired which have sufficient channels to read out two detectors.

Much of the performance information for the proposed GEM-based ionization chamber is available from the studies done for COMPASS [38]. An average tracking efficiency of  $(99.0 \pm 0.1)\%$  was achieved with a total rate of 60 MHz and a peak flux of  $10^4 \text{ Hz/mm}^2$ . For  $Q_{weak}$  the design goal will be a substantially lower operating point of 12 MHz with particle fluxes of  $< 500 \text{ Hz/mm}^2$ .

The Region 1 GEM detector will have an active area  $10 \text{ cm} \times 10 \text{ cm}$ , a thickness of about 6 mm, and be located just behind the first collimator. The entire detector will be mounted on a rail system to move radially so it may be used during low (nA) current measurements of  $Q^2$  and then move out of the acceptance for the physics measurement at high currents of  $180 \mu\text{A}$ . A rotation system will be used to move the detector between octants. To date, two prototype detectors have been built and readout electronics are being installed. Gain and quantum efficiency tests have been completed using an Iron source and a pulsed X-ray system is being installed for timing studies. The final GEM design has been completed, and detailed CAD drawings made.

## 6.6 Region 2: Magnet Entrance Chambers (HDC)

This second set of chambers will be located just upstream of the QTOR magnet. Their purpose is to determine the position and direction cosines of the scattered electrons as they enter the magnet. The combination of these detectors and the Region 1 vertex detectors will provide an accurate measurement of the target vertex and scattering angle. They can also be used to reject events where the scattered particle originates from secondary scattering at the collimator between the Region 1 and 2 chambers. Finally, the region 2 chambers provide an accurate measurement of the entrance angle into the QTOR magnet. When combined with the exit angle determination from the Region 3 detectors and a QTOR field map, the scattered particle's momentum can be determined. With measurements of the scattered particle's momentum and scattering angle, we can properly tag elastically scattered electrons in the  $\langle Q^2 \rangle$  calibration process.

We would like to be able to determine the angle through these chambers with a precision of about 0.6 mrad. In the space we have we can make a self-contained unit with two chambers separated by 0.4 m. This implies that a 170  $\mu\text{m}$  spatial resolution is necessary. We also desire a small amount of material to reduce multiple scattering. The rough area needed for these chambers is about 50 cm x 70 cm. These requirements and dimensions are very similar to those of horizontal drift chambers from other experiments that have operated reliably for years of running. In particular, the HERMES front chambers [43] and the Hall C SOS drift chambers are examples that we pattern our design after. Both of these sets of chambers have been operating for several years with typical resolutions of  $\sim 170 - 200 \mu\text{m}$ .

For the Region 2 chambers, we propose to build two sets of 2 chambers each separated by 0.4 meters. The chambers will be located about 3.8 meters downstream of the  $Q_{Weak}^p$  target at a radial distance of about 70 cm from the beam centerline in a region where the residual field from the QTOR magnet is small ( $< 3$  G). Due to the need to keep the chambers out of the flux of scattered particles from neighboring octants, the chamber frames will have a trapezoidal shape, being larger at the top.

A summary of the details of the chamber properties is shown in Table 10. The drift cell size will be 0.72 cm. Each chamber will have  $x, x', u, u', v, v'$  planes. The second plane of cells in each case will be offset by 1/2 cell to help resolve left-right ambiguities. The stereo  $u$  and  $v$  planes will be at an angle of  $\pm 45^\circ$ . Each chamber will have an active area of approximately 50 cm x 70 cm. There will be 2x48  $x$  wires, 2x80  $u$  wires, and 2x80  $v$  wires. Thus, we will need 416 electronic channels/chamber for a total of 1664 electronic channels for the four chambers. The cathode foils and anode and field shaping wires will be supported by frames made of ertalyte or G10. The anode wires will be attached to amplifier and discriminator cards mounted on the chamber frames. The frontend electronics cards will be the Nanometrics Systems N-277, which have been used reliably in many drift chambers in the past. The signals will be digitized with JLAB F1 TDCs.

Table 10: *Properties of the Region 2 drift chambers.*

Distance from target	3.6, 4.0 m
Active area: horizontal	50 cm
Active area: vertical	70 cm
Cell design	horizontal drift
Cell size	0.72 cm
Anode wire material	Gold-plated tungsten
Anode wire diameter	20 $\mu\text{m}$
Field shaping wires	Gold-plated copper/beryllium
Field shaping wire diameter	75 $\mu\text{m}$
Cathode material	Aluminized mylar
Cathode material thickness	6.4 $\mu\text{m}$
$u, v$ stereo angle	$\pm 45.0^\circ$
Wires in each $x$ plane	48
Wires in each $u, v$ plane	80
configuration	$x, x', u, u', v, v'$
Radiation length per chamber	0.075 %
Total electronic channels	1664

These chambers will be mounted in a similar (but appropriately scaled down) ferris wheel rotating hub structure like that used to mount the region 3 drift chambers. The chambers will have two pinned positions - “in beam” for the calibration runs and “parked” where they will sit with the protection of the shielding during the production running. This simple pinned scheme will make alignment more reliable and reproducible.

To date, a prototype chamber with a single plane of wires using ertalyte frames has been constructed. Testing with cosmic rays is in progress.

## 6.7 Region 3: Focal Plane Chambers (VDC)

The Region 3 focal plane chambers will be vertical drift chambers (VDCs). Two sets of UV chambers will be used to provide excellent position and angle reconstruction. The chambers will be similar in design and geometry to VDCs used in the Hall A HRS; a detailed report on those chambers can be found elsewhere [44]. Figure 37 shows a schematic of the Jlab Hall A VDCs. The particle trajectory is defined by a set of 4 zero-crossing points, one per plane, for a two chamber system separated by 30 cm. The chambers will be oriented at  $45^\circ$  with respect to the nominal elastic scattering trajectory. We plan to have similar cell dimensions to the Hall A VDCs, so that we can assume similar drift times and resolution properties, but we will reduce the electronics cost substantially by multiplexing the readout using delay lines. In contrast with an HDC design, where redundancy and thereby high efficiency is obtained by having multiple wire planes, the high number of wires hit per plane gives the same result in the VDC design. This further reduces the cost and complexity of the chambers.

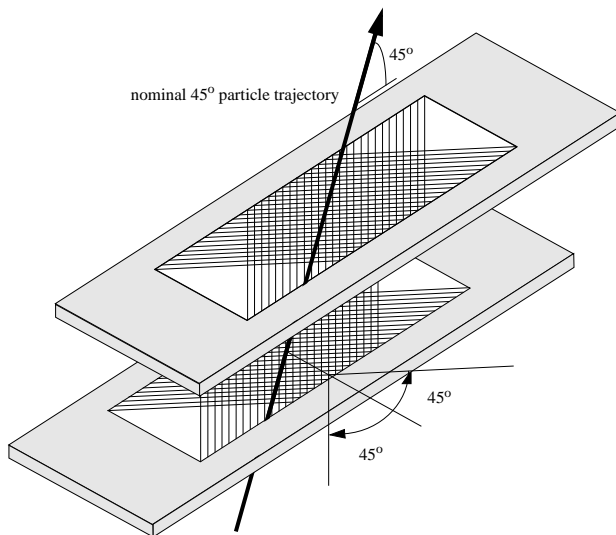


Figure 37: *Schematic of the Hall A VDC layout. The orthogonal wire directions ( $UV$ ) are rotated by  $45^\circ$  relative to the ( $XY$ ) coordinates of the chamber frame.*

The VDC detector length is almost identical to that of the Hall A chambers, although our chambers will be significantly wider (50 cm vs. 25 cm). The chambers will be mounted on a Ferris Wheel, of 3 meters radius, which can be rotated about the beam line axis to provide coverage for all octants. Two sets of counter-balancing chambers will be attached to the Wheel. As noted previously, sequential sampling of opposing pairs of octants is planned. The entire assembly would be placed immediately before the  $Q_{Weak}^p$  Čerenkov detectors, inside the shielding hut, along with the scintillator trigger counters. The angular resolution of a set of two UV chambers would be about 1-2 mrad, sufficient to map out the analog response of the Čerenkov detectors. The chambers can be moved to avoid direct view of the beam by sliding radially them along a Ferris wheel spoke to avoid damage in the high-luminosity production mode. Like the Region 2 design, there would be two positions “in” and “out” of direct view of the elastically scattered electrons.

A full GEANT 4 simulation of the experiment is being developed, and is being used to finalize the Region 3 design. Figure 38 shows the results of simulation of the number of wires hit per plane, using a full GEANT simulation of the accepted elastic scattering events. Our design criterion is that the number of wire cells hit per plane should be between 4 and 8 to ensure efficient track reconstruction. The present design has a cell spacing of  $\sim 5.5$  mm which should yield an intrinsic position resolution of about  $100 \mu\text{m}$ . The pitch angle of the wires is still being optimized; at present a value of  $30^\circ$  (vs.  $45^\circ$  of the Hall A design) appears optimal. Figure 39 shows GEANT 4 simulated events as detected by the VDCs and the Čerenkov bars.

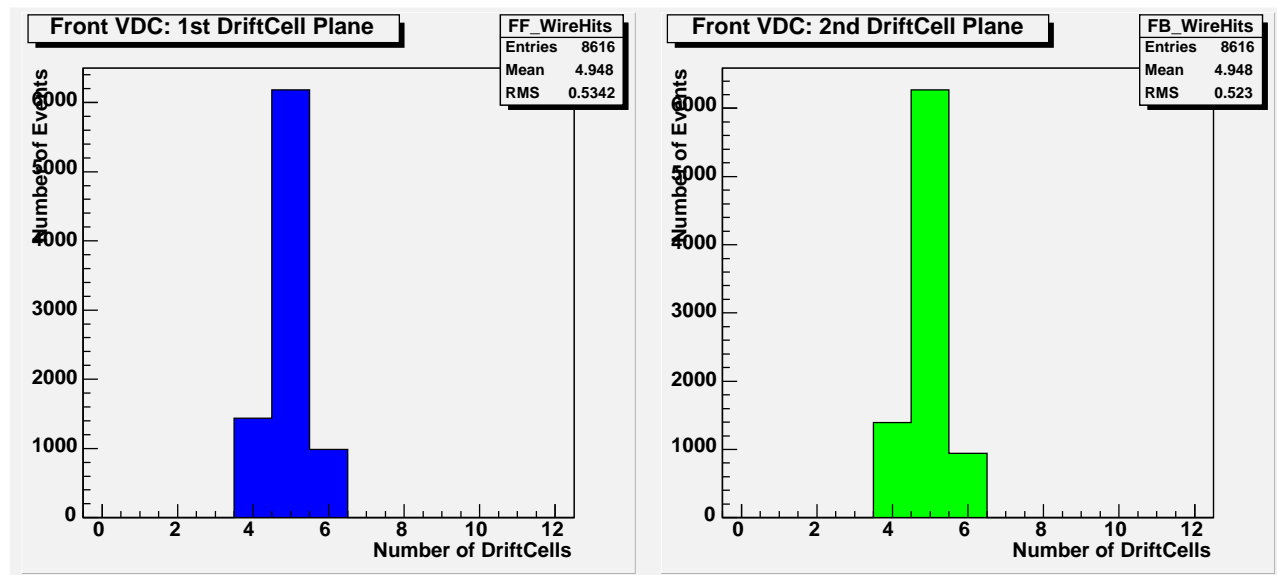


Figure 38: *Simulated number of DC cells hit for the front (upstream) Region 3 VDC, for elastically scattered electrons. The left and right halves of this figure represent the U and V planes of this VDC. Results are similar for the back VDC. These results are for a  $30^\circ$  wire pitch angle.*

The chambers are 10 cm deep and have 3 high voltage planes and two wire planes. The sense wires are  $25 \mu\text{m}$  diameter gold-plated tungsten. In the Hall A design, the wires pass through

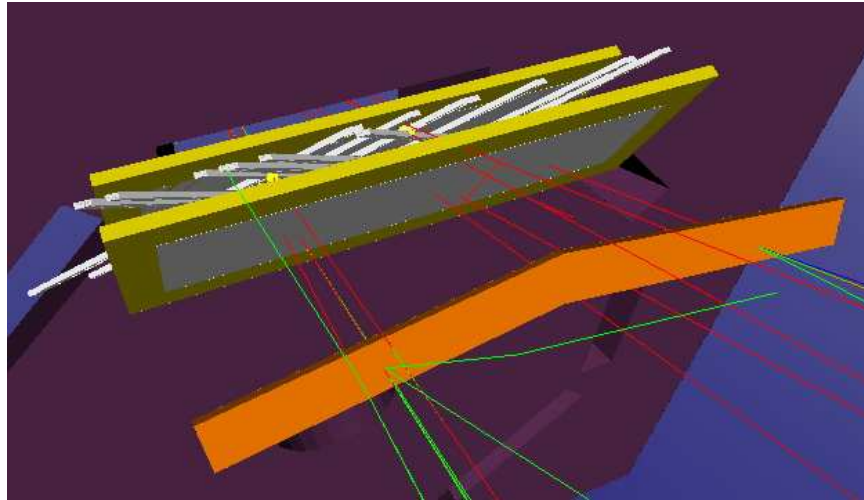


Figure 39: *GEANT 4 simulation of several elastic scattering events as detected by the two VDC chambers (yellow frames); the struck wire cells are visible in light gray; the Čerenkov bars are in orange. The apertures for the shielding hut are seen behind the VDCs.)*

precision-drilled holes and are spring mounted. We plan to modify the design, using the simpler, and more traditional, method of soldering wires onto photo-etched kapton foils. This is a trade-off in expensive machinist time for student labor. As in the Hall A design, there will be no guard wires. This requires a more sophisticated read out algorithm, but eliminates dead zones. The chamber efficiency should be high; the Hall A VDCs have run for years with a hit efficiency of nearly 100%. Dead time will be nearly independent of position for these chambers, and should be small in any event.

Figure 40 shows a Garfield [45] simulation of the electric field lines and isochrones for the VDC design. The measurement of drift times is used to determine the zero-crossing point of the geodesics. A simulated first electron arrival-time distribution for one particular gas mixture is shown in Fig. 41. The correlation between the arrival time and the perpendicular distance from the wire to the track is a function of the track inclination, as depicted in Fig. 42, and algorithms for extracting the position from the drift time accurately and efficiently are under development. The exact cell geometry (and thus the wire spacing and the total number of wires per plane) are still being optimized using the Garfield GEANT 4 simulations. Assuming a 5.5 mm wire spacing and a 30° pitch angle, there will be 190 wires per plane, or 380 wires per chamber.

The front-end electronics for the Region 3 VDCs will be based on a fast preamp/discriminator chip, the MAD chip [46], which was developed at CERN specifically for wire chamber readout. There will be a preamp and discriminator for each sense wire, mounted directly to the chambers on PC Boards. Every 8th wire will be multiplexed, with 40 wires per delay line, 2 ns delay per wire, adding 80 ns to the readout time. Both ends of the delay line will be read out, requiring 19 channels of TDC per chamber. The time difference between the two ends will yield the wire

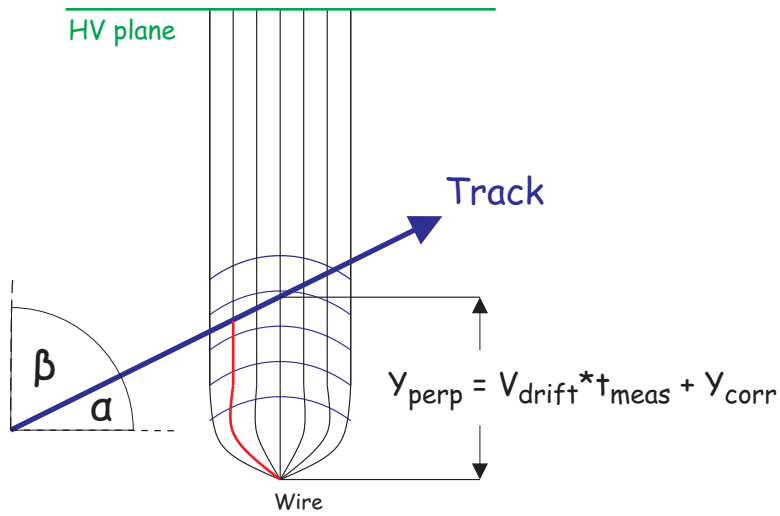


Figure 40: *The electric field lines and drift isochrones for a single cell of the VDC.*

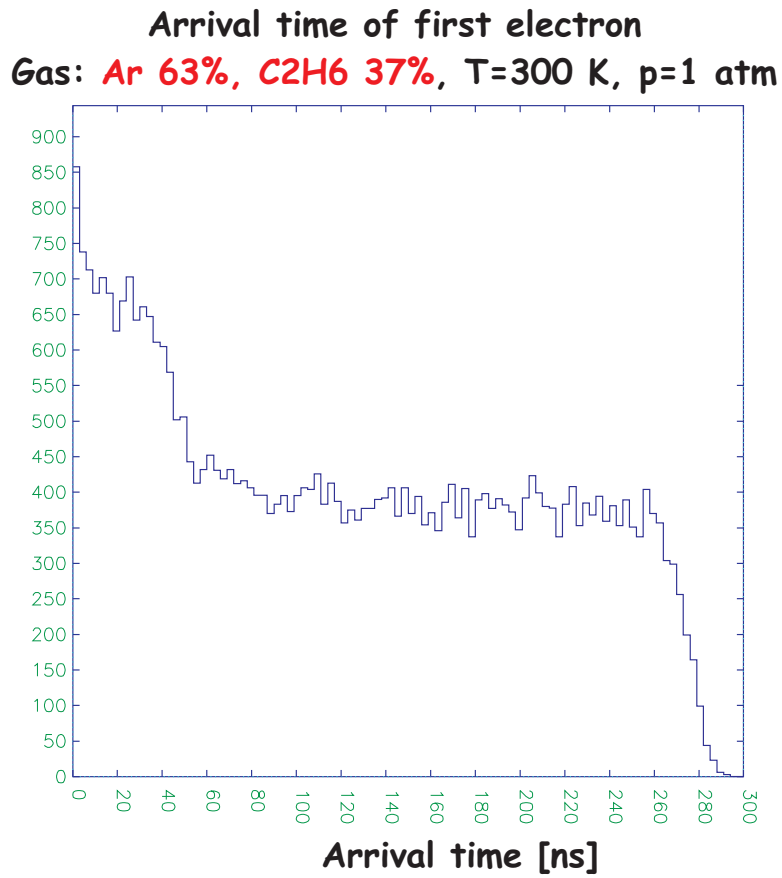


Figure 41: *Garfield-simulated arrival time distribution.*

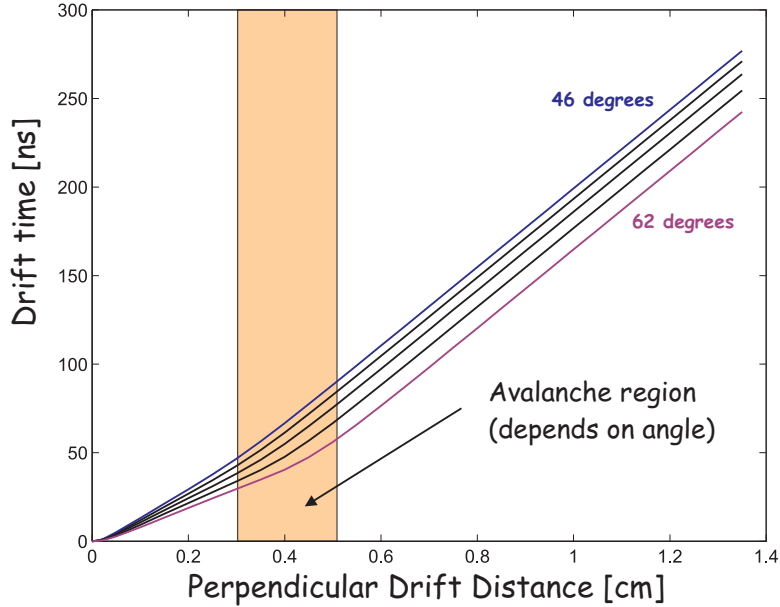


Figure 42: *Garfield-simulated relationship between perpendicular drift distance and arrival time for tracks crossing the chamber at various angles.*

number, and the time sum provides the drift time spectra. The increased dead time due to delay line readout is not an issue at these rates. The new JLAB F1 multihit VME TDC will be used for the digitization; with 64 channels per module, we would require only two such modules.

The conceptual design for the Region 3 Ferris wheel is an Aluminum wheel-like structure that rotates around a pair of 12" brass Garlock bushings. The axle is a 12 inch OD tube that is 3 ft long with an inverted Vee stand 13 ft high. The wheel is made from 4 x 4" Al square tube. The wire chamber pair is mounted to the face of the wheel. An indexing collar is used to position the chambers in any of eight positions so each chamber may be indexed to each octant of the QTOR magnet. The wheel would be moved by a circular worm gear.

## 6.8 Scintillation Detectors

Scintillation counters will provide the trigger and time reference for the calibration system. These detectors must shadow the quartz Čerenkov bars and have sufficient energy resolution and timing capabilities so as to identify multiparticle events and veto neutrals. The scintillators will be long bars, each with an area just slightly larger than the Čerenkov bars and mounted immediately downstream of the Region 3 chambers. Each scintillator will have a photomultiplier tube at each end and have a mean time resolution of 250 ps or better.

Because neutron detection efficiencies are  $\sim 1\%$ /cm of plastic and we need to minimize false trig-

gers from neutrals, the thickness of the trigger scintillators must be minimized without loss of the signal from the elastically scattered electrons. The scintillators will be made from Eljen-200, which is equivalent to BC408, and is a fast ( $\sim 3$  ns) scintillator yielding 10 photons for every keV of energy deposited in it. The elastically scattered electrons will deposit about 2 MeV of energy in a 1 cm thick scintillator, which will then produce about 20,000 photons. Simulations with GUIDIT indicate that 1.8% (5.3%) of the photons generated at the far (near) end of the PMT will make it through the 2 m long scintillator, through a rectangular lightguide, and to the photocathode of the PMT. Photocathode efficiencies are typically 20% so we can expect 70 to 210 electrons to be produced by the photocathode for every electron going through the scintillator. Combining this with a high gain PMT ( $\sim 10^7$ ) yields 100 to 300 pC of charge in the 3 ns of the signal. When this is coupled to  $50 \Omega$  electronics we expect a signal between 1 and 3 V for each elastically scattered electron that passes through the 1 cm thick plastic trigger scintillator.

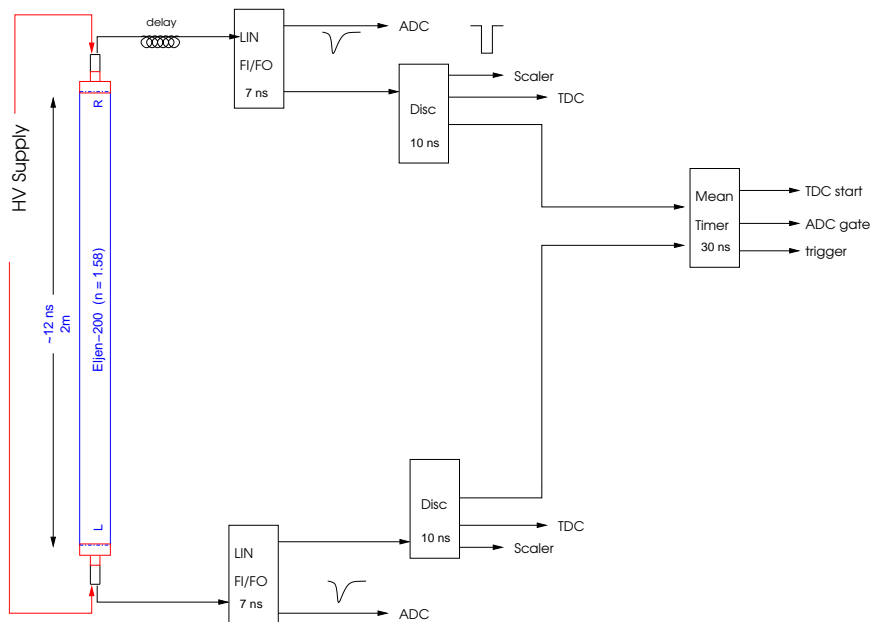


Figure 43: Schematic of trigger electronics using a meantimer.

Each scintillator will be 214 cm long and 30 cm high, to shadow the Čerenkov bars, and 1 cm thick. Light guides coupling the scintillator to the PMTs need not be transparent to UV light as those wavelengths will have been attenuated away as the light passes through up to 2 m of scintillator. To minimize loss of light from the scintillator corners, each light guide will be made of a row of “fingers” that couple to the  $30 \text{ cm} \times 1 \text{ cm}$  ends of the scintillator and overlap each other to form a square that is circumscribed within the PMT. Three inch PMTs have photocathodes that are 6.8 cm in diameter; this corresponds to a photocathode area of  $36.3 \text{ cm}^2$ , which will couple nicely to the  $30 \text{ cm}^2$  scintillator ends. We will use Photonis XP4312B 3 inch PMTs which have a high gain ( $\sim 3 \times 10^7$ ) and a uniform response over their photocathode areas [47].

The long edges of the scintillators will be diamond milled and the ends finished to a 600 grit sanded finish. Given the extreme ratio of thickness to length, the scintillator counters must be supported by a frame which is then mountable to the rear chamber package. To reduce radiation damage, this package will be removed from direct view of the beam for the high current running mode.

The trigger electronics must be fast, so that the GEMs are triggered as quickly as possible, and the trigger timing must be independent of the where the electron passes through the trigger scintillator. We will use a meantimer and the simple circuit shown in Fig. 43 to trigger the electronics.

## 7 Liquid Hydrogen Target System

The  $Q_{Weak}^p$  liquid hydrogen target must operate safely and reliably for sustained periods of time at the design current of  $180 \mu\text{A}$ . The current mode operation of the main Čerenkov detectors makes the experiment particularly sensitive to target density fluctuations, which must be minimized by careful target design. The target must be azimuthally symmetric in order to minimize the sensitivity to helicity correlated beam motion. It is also important to minimize the target window and wall thicknesses to minimize background contributions to the detector signal, and to minimize multiple scattering of the scattered electrons of interest, which are selected in the range  $\theta \simeq 8^\circ \pm 2^\circ$  by the  $Q_{Weak}^p$  collimation system. The operating requirements for the  $Q_{Weak}^p$  liquid hydrogen target are summarized in table 11.

Table 11: *Operating Requirements for the  $Q_{Weak}^p$  Liquid Hydrogen Target.*

Parameter	Requirements
Beam Energy	1.165 GeV
Target Length	35 cm (3.9% $X_0$ )
Beam Current	180 $\mu\text{A}$
Beam Power	2120 W
Raster size	$4 \times 4 \text{ mm}^2$
Total cooling power	2500 W
30 Hz density fluctuations	$< 10 \text{ ppm}$

The power deposited by the  $180 \mu\text{A}$ , 1.165 GeV electron beam in the 35 cm long  $Q_{Weak}^p$  LH<sub>2</sub> target (3.9%  $X_0$ ) is that associated with ionization energy loss; at 4.65 MeV/g/cm<sup>2</sup>, this corresponds to 2120 W of beam power (neglecting energy loss in the target windows). In addition to the beam power requirement, the  $Q_{Weak}^p$  target needs several hundred Watts of cooling power to account for conductive heat losses, circulation fan heat load, reserve heat load for feedback control, etc. As a result, the cooling power goal for  $Q_{Weak}^p$  is 2500 W. To put our target coolant requirements in perspective, we show in Figure 44 a plot of beam current vs beam power for several relevant targets. We note that the beam current required for  $Q_{Weak}^p$  is only 30% higher than has already been employed in Hall A for physics production, and that the SAMPLE target at MIT Bates is 5 cm longer than the  $Q_{Weak}^p$  target. However, the combination of high beam current and a long target flask will make the  $Q_{Weak}^p$  target the highest power cryotarget in the world by a factor of several. Clearly, the first question to be addressed for the  $Q_{Weak}^p$  target is how to supply the required cooling power. We demonstrate in the next section that several viable options exist, and we report recent progress at obtaining a solution that has been endorsed by the JLab Cryogenics group, the Target group and the  $Q_{Weak}^p$  collaboration.

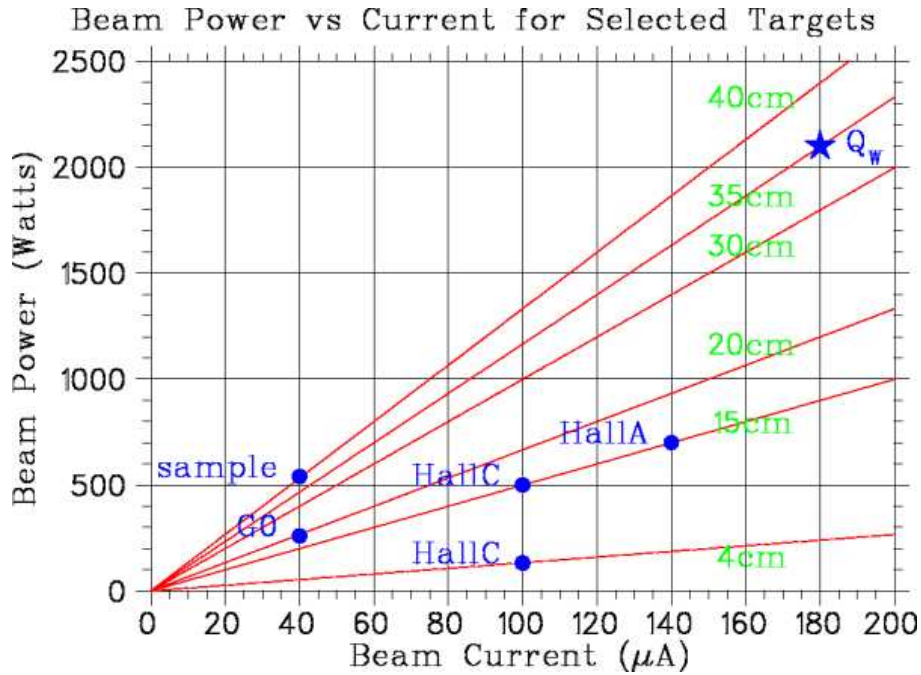


Figure 44: Values of the beam power deposited in LH<sub>2</sub> targets as a function of beam current, for target cells varying between 4 cm and 40 cm in length. The solid point indicates the expected  $Q_{Weak}^p$  configuration (35 cm target, 180 μA, 2.1 kW).

## 7.1 Refrigeration

The cooling power available to the target is given by the change in enthalpy  $\Delta H$  of the coolant. For LH<sub>2</sub> targets, nominally 15 atm 15 K coolant is supplied by the JLab End Station Refrigerator (ESR), and is returned at 19 K and 3 atm with an enthalpy change  $\Delta H = 31$  J/g. At maximum capacity, the ESR can supply about 25 g/s of this 15 K coolant, corresponding to a maximum cooling power of 775 W, which is only about 30% of what is required for  $Q_{Weak}^p$ .

Alternatively, the 3 atm 4 K supply ( $H=9.5$  J/g) from the ESR can be used. For sustained operation, the coolant must be returned cold at 1.2 atm and 5 K ( $H=35$  J/g). A flow of 25 g/s would only result in 625 W of cooling power in this case, which corresponds to 25% of what is required for  $Q_{Weak}^p$ .

However, there is a third possibility which has been employed as recently as summer 2004 for the HAPPEX experiment. The Central Helium Liquefier (CHL) has some excess 4 K liquefaction capacity. This source of coolant has the advantage that the 4 K 3atm supply can be returned warm. The enthalpy change corresponding to a 19 K LH<sub>2</sub> target is about 103 J/g; thus, 25 g/s of 4 K 3 atm supply returned warm to the CHL at 19 K and 1.2 atm would provide 2575 W of cooling, meeting the requirements of the  $Q_{Weak}^p$  target. Although a sustained flow capacity of 25 g/s is barely available on a typical day at present, the Cryogenics group is willing to guarantee that 24 g/s will be available for  $Q_{Weak}^p$  in the future, assuming the present system loads do not

change appreciably. This means that 24 g/s of 4 K coolant would be available for the  $Q_{Weak}^p$  target in parallel with the Hall C Møller polarimeter and a program in Hall A (and B) that does not also require a high power target.

The CHL solution described above is just shy of what we require for  $Q_{Weak}^p$ . Furthermore, we do not wish to run so close to the maximum cooling capacity, even though the above 24 g/s figure includes a 5 g/s reserve for the CHL. Therefore, we have worked out a solution which has been accepted by the JLab Cryogenics group, the JLab Target group, and  $Q_{Weak}^p$  experimenters, which shares the cooling load between the CHL and the ESR. This agreement, which has been signed by all relevant parties in November, 2004, specifies the cooling requirements of the  $Q_{Weak}^p$  experiment, and the cooling capacity that is available from JLab under various scenarios.

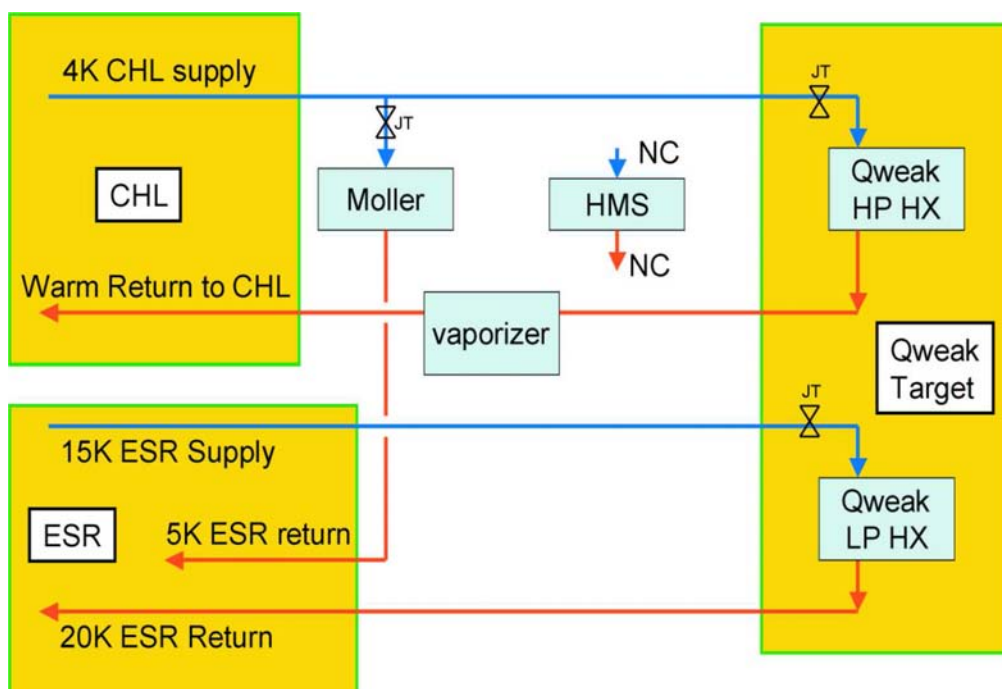


Figure 45: A schematic of the cooling scheme that will be employed for the  $Q_{Weak}^p$  target. Two independent heat exchangers will be used in order to make use of the cooling power of the ESR and the CHL at JLab.

The  $Q_{Weak}^p$  target is being designed to run with two independent heat exchangers, as shown schematically in Fig. 45. One will be fed from the standard ESR 15 K supply and returned to the ESR at 19 or 20K. Up to 800 W of cooling power can be supplied in this manner. The remainder of the cooling power required will be obtained with a separate, independent 4 K heat exchanger fed with the CHL excess 4 K capacity and returned warm to the CHL. This combination of resources will provide the greatest possible cooling power and provides the flexibility to dynamically balance the relative loads on the two refrigerators. With this approach, the  $Q_{Weak}^p$  target cooling requirements can be met in parallel with Hall A programs and with the

cooling requirements of the Hall C Møller polarimeter. We wish to emphasize that this solution has been endorsed by the JLab cryogenics group and can be met with existing resources. An inexpensive vaporizer will be added to the Hall C warm return line to prevent ice buildup on that line, exactly as was done for HAPPEX last summer in Hall A.

The above solution will work assuming no additional loads are placed on the CHL or the ESR above beyond what currently exists. However, new loads can appear anytime, which is a potential source of concern. We are pleased to note that Swapan Chattopadhyay (Associate Director of the JLab Accelerator Division) made the clear and unequivocal statement at the November 18, 2004 JROC meeting that the laboratory will provide the cooling needs of the  $Q_{Weak}^p$  experiment in any scenario, via the most appropriate of several options that were presented to the committee. The approach chosen for the target design, namely use of both 4K and 15K heat exchangers, gives laboratory management the greatest flexibility in choosing a solution when the experiment is on the floor.

It should be noted that a small shortfall in cooling power can be compensated, if necessary, by running the target at a slightly higher temperature, since the cooling power available to the target is proportional to  $\Delta T$ , the difference between the coolant supply and return temperatures. The only drawback to running at a higher temperature is that ideally the target should be operated at least three degrees below the boiling point to minimize the probability of boiling. This drawback can be compensated for by running the target at a slightly higher pressure as well, since the boiling temperature is higher at higher pressures, as illustrated in Fig. 46. Since the mechanical strength (window thickness) is driven by the boil-off pressure and not the operating pressure, there are no negative consequences to running at a slightly elevated operating pressure. The boil-off pressure will be kept low by increasing the size of the ballast volume and using appropriately sized relief lines.

## 7.2 Boiling and Density Fluctuations

In previous parity violation experiments, two different approaches have been taken to the problem of target boiling and density fluctuations near the standard 30 Hz helicity reversal frequency. One approach is to pay careful attention to minimizing these effects in the target design, to normalize the main detectors to an upstream beam current monitor, and to use luminosity monitors<sup>12</sup> to measure and if necessary, correct for effects of target density changes. This was the approach taken by the SAMPLE experiment at MIT/Bates. The other approach is to use luminosity monitors, rather than incident beam current monitors, as the primary normalization in the experiment. The latter approach has been taken in the Mainz A4 experiment. For  $Q_{Weak}^p$ , we plan to follow the SAMPLE approach with a target that is carefully designed to minimize boiling and density fluctuations, and use our luminosity monitors as a check that this is indeed the case.

---

<sup>12</sup>A luminosity monitor is typically an auxiliary current mode detector placed at very forward angle where the scattered electron rate is much higher and the parity violating asymmetry is much smaller than in the main detector; such a device is primarily sensitive to target density fluctuations and may be used to correct for such effects in the main detector data. The  $Q_{Weak}^p$  luminosity monitor is described in section 9.7.

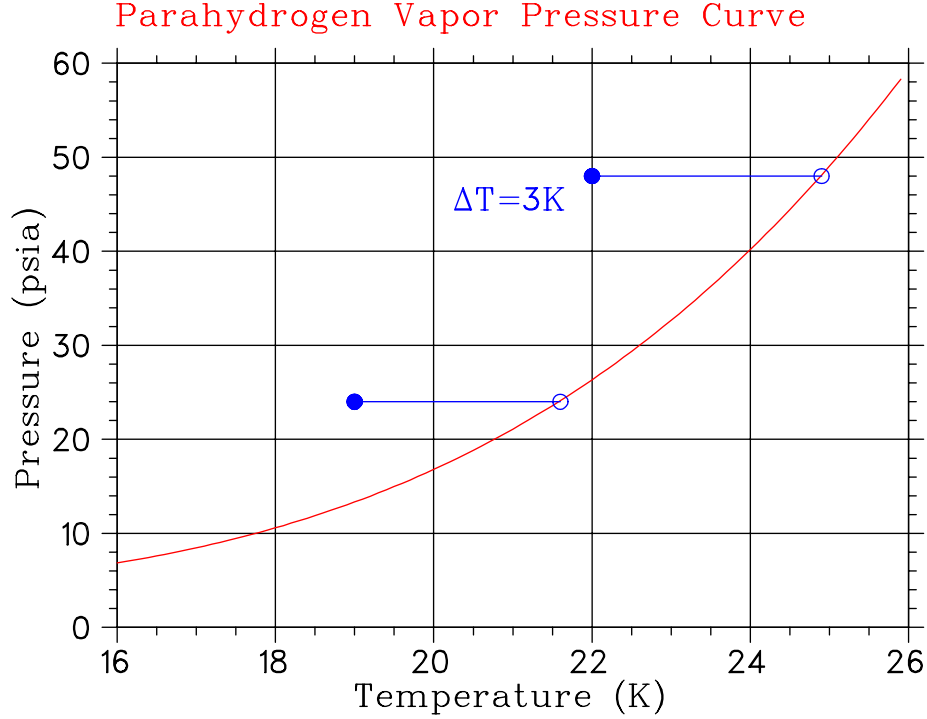


Figure 46: The vapor pressure curve for parahydrogen. The usual operating condition at 19K and 24 psia is compared to the proposed one at 22K and 48 psia. Both are three degrees below the boiling point.

To understand the requirements that target boiling and 30 Hz density fluctuations place on the  $Q_{Weak}^p$  target, we consider each effect in turn. Boiling is a bulk effect, and may be estimated by recasting the basic definition of specific heat ( $c_p = \frac{\Delta Q}{m\Delta T}$ ) as

$$\Delta T = \frac{\Delta E / \Delta x I_b}{c_p d_r v_s},$$

where  $\Delta T$  is the temperature rise of the LH<sub>2</sub> in K,  $\Delta E / \Delta x$  is the energy loss in MeV/g/cm<sup>2</sup>,  $I_b$  the beam current in  $\mu$ A,  $c_p$  the specific heat of H<sub>2</sub> in J/gK,  $d_r$  the raster size in cm, and  $v_s$  the stream velocity of the LH<sub>2</sub> in the target cell in cm/s. With  $\Delta E / \Delta x = 4.7$  MeV/g/cm<sup>2</sup>,  $I_b = 180$   $\mu$ A,  $c_p = 10$  J/gK,  $d_r = 0.4$  cm, and  $v_s = 700$  cm/s, then  $\Delta T = 0.3$  K. Since the target operating temperature is (at least) 3 K below the boiling point, there is no bulk boiling. We point out that the 700 cm/s stream velocity is that appropriate for the G0 target at 30 Hz, and is a much slower stream velocity than what we expect to employ for the  $Q_{Weak}^p$  target.

The counting rate expected in the  $Q_{Weak}^p$  detectors is about 800 MHz per octant, which translates to a statistical error of  $\sim 50$  ppm per pulse pair. If target density fluctuations on the time scale of the helicity reversal frequency contribute significantly to this width, then the experiment must run longer to achieve the same goals. To limit the extra running time to 10% of the original goal, then the target would have to contribute less than about 15 ppm to the asymmetry width.

For comparison, the G0 target contributed about 150 ppm to the measured asymmetry width for pulse pairs at 30 Hz. We expect the target fluctuations to scale inversely with the raster area and beam power, and as the third power of the pump speed. Thus, we can predict the asymmetry width for  $Q_{Weak}^p$  based on experience with the G0 target to be:

$$\Delta A_{tgt} \sim 150 \text{ ppm} \left( \frac{2 \times 2 \text{ mm}^2}{4 \times 4 \text{ mm}^2} \right) \left( \frac{35 \text{ cm}}{20 \text{ cm}} \right) \left( \frac{180 \mu\text{A}}{40 \mu\text{A}} \right) \left( \frac{30 \text{ Hz}}{120 \text{ Hz}} \right)^3 \sim 5 \text{ ppm}$$

However, it must be admitted that the dependence on pump speed is somewhat uncertain. When this dependence was studied in Hall A for a target of a very different design, the dependence was faster than linear but slower than quadratic. If we assume a quadratic dependence instead of a cubic dependence and rescale the G0 asymmetry width as indicated above, we find that the expected  $Q_{Weak}^p \Delta A_{tgt} \sim 18 \text{ ppm}$ , which is uncomfortably large.

There are several possibilities that can be explored which could further reduce  $\Delta A_{tgt}$ . There is anecdotal evidence that a larger intrinsic beam diameter improves the situation. Since there is no vertex reconstruction in the  $Q_{Weak}^p$  experiment, there is no penalty to increasing the intrinsic beam size beyond the canonical  $100 \mu\text{m}$ . Another potential area for improvement is the raster frequency, which is currently around 25 kHz. The raster frequency could be doubled without too much effort, although higher frequencies than that would require a major development effort. Depending on the physical mechanism responsible for the 30 Hz density fluctuations, a doubled raster frequency could reduce  $\Delta A_{tgt}$  by a factor of 2. Another possibility is to sub-cool the target even further; tests performed with the G0 target indicate that small improvements in  $\Delta A_{tgt}$  can be achieved by sub-cooling by more than the usual 3 K.

By far the most promising method to mitigate the effects of target density fluctuations is to increase the helicity reversal frequency, since the target noise requirement becomes less severe for shorter sampling times as the counting statistics error increases. For example, if the helicity reversal rate is increased by a factor of 10 to 300 Hz, then  $\Delta A_{stat} \sim 150 \text{ ppm}$ , and the requirement on  $\Delta A_{tgt}$  becomes three times less severe. In addition, the target noise spectrum is expected to be significantly quieter at higher frequencies. Figure 47 shows the frequency dependence of the asymmetry width measured with solid and liquid targets in Hall A [48]. The data were taken with a UVT lucite Čerenkov detector that was normalized to a beam current monitor, sampled every 2.5 ms. The solid target was carbon, and the liquid target was 15 cm LD<sub>2</sub> with a 60 cm/s stream velocity. The beam current was 100  $\mu\text{A}$  and the raster size was  $2 \times 2 \text{ mm}^2$ . The noise in the liquid target measurements clearly falls off at higher frequencies and approaches the noise floor corresponding to a solid target. Given that these test measurements were bandwidth limited, with errors in excess of electron counting statistics even for the solid target, these data indicate that there is *at least* a factor of 10 in target noise reduction alone to be gained to be gained in running  $Q_{Weak}^p$  at a higher helicity reversal frequency.

Since  $Q_{Weak}^p$  is an integrating experiment with relatively few words per event to read out, there is no difficulty reading data at event rates up to a few kHz. The JLab source group has indicated there is no fundamental obstacle to running at higher helicity reversal frequencies, although it would be essential to significantly reduce the current 500  $\mu\text{s}$  switching/settling time of the Pockels cell, as discussed in section 11. In order to take advantage of the dramatic reduction

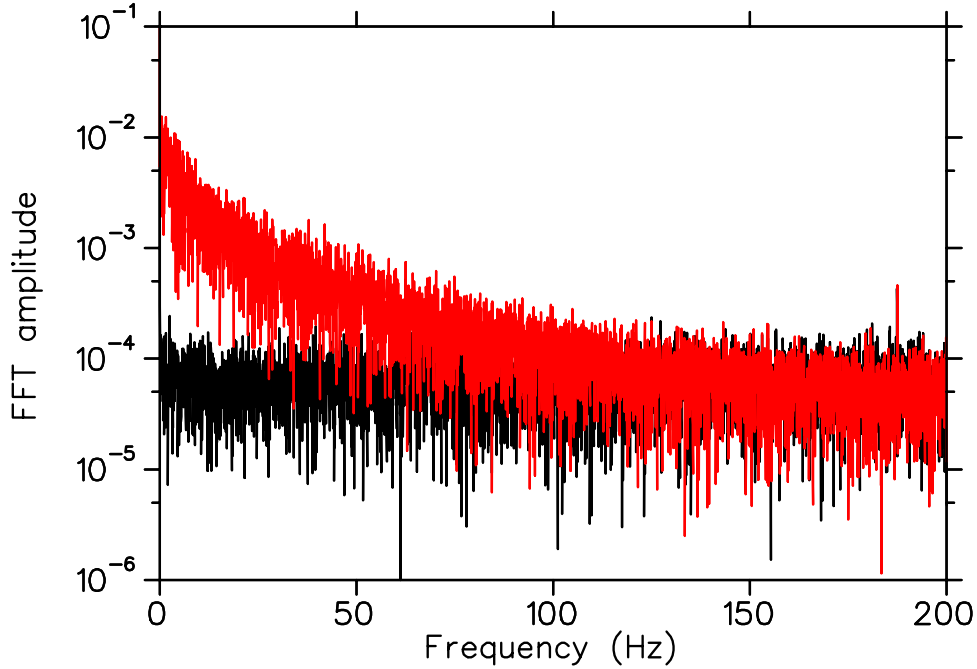
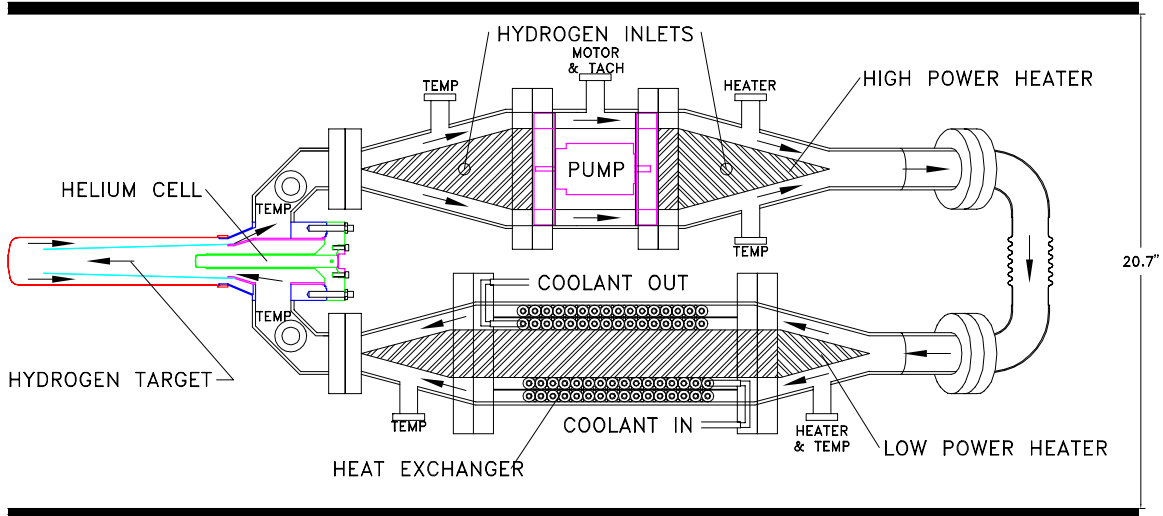


Figure 47: *Noise frequency spectrum measured for solid (C, black) and cryogenic liquid (LD<sub>2</sub>, red) targets in Hall A. The additional noise due to random target fluctuations decreases dramatically as the measurement frequency increases.*

in target density fluctuations at higher frequency, the  $Q_{Weak}^p$  collaboration has adopted 250 Hz as the nominal helicity reversal frequency for the experiment. Source developments required to implement this strategy are described in section 11.

### 7.3 Basic Conceptual Target Design

The target concept of choice for the  $Q_{Weak}^p$  experiment is the SAMPLE/G0 design. The density fluctuations experienced with these targets were studied extensively, and the results were extraordinarily good. A sketch of the G0 target loop is shown in Figure 48. A high flow velocity is achieved in both of these targets by means of a perforated tapered cylindrical windsock concentric to an outer cylindrical cell. The flow area depends on the gap between the windsock and the target cell, as well as their respective radii, and the perforations. As a result, the flow area can be made arbitrarily small and is almost independent of the length of the target cell. The small flow area inherent in this design contributes to the high flow velocity required by  $Q_{Weak}^p$ . A flow velocity of 500 cm/s (at 30 Hz) was achieved by the SAMPLE target, and as noted previously the G0 target flow velocity is designed to be 700 cm/s (also at 30 Hz). Although it would seem that these large flow velocities are moot since most of the flow appears to be longitudinal to the beam axis, in fact the high degree of turbulence (Reynold's number  $\sim 10^7$ ) in these systems results in a significant transverse flow component.



NOTE: The port positions for electrical and transducer feedthroughs may be rotated into other planes.

Figure 48: A sketch of the G0 target configuration, which we are using as a model for the  $Q_{Weak}^p$  target design.

Much of the experience gained with the G0 target will carry over to  $Q_{Weak}^p$ . However, important changes need to be made for  $Q_{Weak}^p$ . The target length will need to be increased from 20 to 35 cm<sup>13</sup>. In addition, the heat exchanger and high power heater capacity will need to be increased by a factor of 3 to 4. Whereas the SAMPLE and G0 targets share many common characteristics, they do have important differences. The SAMPLE impellers are powered by an external motor, whereas the G0 impellers are powered by a submersible pump. The SAMPLE heat exchanger is an open design, in which the cryogen flows unobstructed through a large pipe. The helium refrigerant flows through copper piping wound around the outside of this large pipe. The G0 heat exchanger is modelled more closely on standard practice at JLab, with the cryogen flowing in direct contact with finned copper tubing that carries the refrigerant. The 25 liter SAMPLE cryogenic loop is vertical, whereas the 6 liter G0 loop is horizontal. Finally, the diameters of the SAMPLE cell and associated windows are about twice as large as the corresponding diameters in the G0 target, which helps mitigate beam halo issues. From preliminary discussions with the JLab Target group leader (M. Seely), we think that the  $Q_{Weak}^p$  target should be based more upon the SAMPLE design choices, with the exception of the heat exchanger. In addition, we are currently studying the possibility of fabricating the target cell or at least the windows from beryllium in order to reduce background in the  $Q_{Weak}^p$  measurements.

In the following sections, we provide some brief remarks about each of the  $Q_{Weak}^p$  target components.

<sup>13</sup>By comparison, the SAMPLE target cell is 40 cm long.

### 7.3.1 Heat Exchanger

The proposed design for the 15 K  $Q_{Weak}^p$  heat exchanger is basically a copy of the existing  $\sim 1000$  W design for G0. The 30 cm long G0 heat exchanger has been tested to 550 W. It consists of a tube with a plug (flow diverter) along the central axis. Finned copper tubing is wound in 2 helical layers between the plug and the tube. The copper tubing is 1/4" diameter, with 1/8" long fins (14 fins/inch). The liquid hydrogen is forced to flow past the finned tubing by the plug, where heat is exchanged with the refrigerant counter-flowing through the finned tubing.

The 4 K  $Q_{Weak}^p$  heat exchanger will be of similar design, except that the finned copper tubing will be larger in diameter and will consist of at least three layers plumbed in parallel. These changes are necessary because of the lower pressure drop that can be tolerated with the 4 K coolant, which is supplied at 3 atm and returned at 1.2 atm.

### 7.3.2 Cryogenic Pump

The  $Q_{Weak}^p$  pump must be able to provide a volume flow rate of at least 25 l/s and about 5 psi of head. This represents about a factor of 5 improvement over G0. The motor must have enough torque to push liquid neon through the loop (at 10 Hz) during commissioning. The motor should be capable of running 30–120 Hz with LH2 in the loop, without depositing more than 50 W into the system. Materials prone to radiation damage, like Teflon, must be avoided.

Two solutions are being studied for the re-circulation pump. The first would follow the same general design as the G0 pump, i.e. a submersible pump fabricated commercially. The G0 pump is powered by a 50 oz-in brushless DC motor, and performed very well for the G0 forward angle measurements. A similar design could be engineered for  $Q_{Weak}^p$ . However, the company (Barber-Nichols) which was contracted for the G0 pump recommended that a radial pump would be better suited for our application. Such a pump could provide superior head and volume flow relative to the vane-axial design. This solution would be configured such that the pump motor would be exterior to the loop. One advantage to this design is that the heat dissipated by the motor would not contribute to the heat load of the target. However, the cost associated with a commercial solution, coupled with budget restrictions has led us to consider building a pump in-house, and R&D for the pump is currently underway.

### 7.3.3 Target Heater

The heater is of standard design. Its function is to replace the power deposited in the target by the beam when the beam current drops, in order to maintain a stable temperature in the loop independent of beam current. It must be capable of providing at least 2500 W. Typically, resistive nichrome wire (0.19  $\Omega$ /ft) is wound around a conical G10 standoff which is situated directly in the flow path. For  $Q_{Weak}^p$ , we envision using several independent  $\sim 1$  kW heaters in the loop. The power supplied to the heater will be controlled in a feedback loop in a manner similar to that

being used by G0. For G0, the heater power is adjusted automatically to keep the temperature in the loop constant with reference to a thermometer just upstream of the target cell. However, a signal from a beam current monitor is also used in the feedback logic to provide large and sudden changes in the heater power in response to sudden and dramatic changes in the beam current. This dual input PID (Proportional Integral Differential) logic keeps the temperature well within 100 mK of the goal temperature even during repeated beam on and off cycles.

### 7.3.4 Target Cell

The target cell will be modelled after the SAMPLE and G0 designs. In the SAMPLE target, illustrated in figure 49, LH<sub>2</sub> flowed along the axis of a 0.13 mm thick (5 mil) perforated windsock. The windsock was tapered to a diameter of 3 cm at its narrow end. The windsock was surrounded by a 7 cm diameter cylindrical tube 0.38 mm (15 mils) thick, and 40 cm long. The LH<sub>2</sub> was returned in the space between the windsock and the outer cylinder. The windsock was perforated to promote flow transverse to the (central) beam axis, and to counteract the Bernoulli effect which would otherwise crush the windsock. Both the windsock and the outer cell were fabricated of 6061-T6 aluminum. They were connected to a baffled manifold which directed the flow of hydrogen through the inside of the windsock and back along the outside of the windsock.

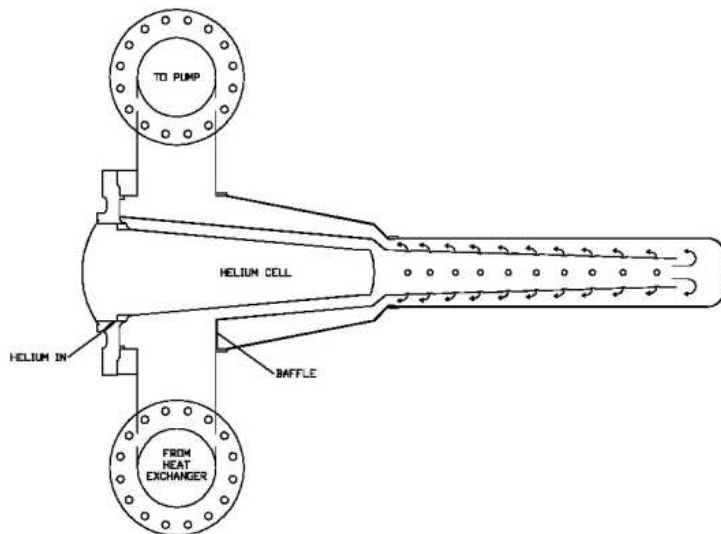


Figure 49: *Schematic of the SAMPLE target cell [49]*

For  $Q_{Weak}^p$ , the target liquid and the windsock will be enclosed in a cylindrical cell. Initially this cell will be aluminum, 7 mils thick as we currently use, except for thinner nipples where the cell is intercepted by the beam. We are investigating the possibility of an alternate design based on beryllium to reduce background in the  $Q_{Weak}^p$  measurements, at least at the entrance and exit of the cell, but perhaps for the entire cell. Initial running of  $Q_{Weak}^p$  will likely be done with an aluminum cell but we aim to produce a cell with at least Be end windows for Run II.

## 8 Backgrounds

Detailed background simulations are critical for the success of new experiments, since it is not always possible to solve problems uncovered during commissioning by shifting around piles of lead bricks! The basic layout of the experiment must be largely optimized before commissioning even begins. However, while signal rates are easy to calculate, proper background estimates are notoriously difficult. Our collaboration benefits from having a strong multi-institutional background simulation effort, founded on LaTech GEANT models. As the detector and collimator designs evolve in attempt to improve the  $Q_{Weak}^p$  figure of merit, the background simulations must evolve in parallel. In this section, we report on the present status of background simulations using the latest collimator design (Oct., 2004) as described in section 4.10. Re-optimization of the beamline shielding for this configuration has not yet been completed.

Neglecting radiative corrections, the raw experimental asymmetry is given by:

$$A_{exp}^{raw} = P \frac{A_{ep \rightarrow ep} Y_{ep \rightarrow ep} + A_{bkg} Y_{bkg}}{Y_{ep \rightarrow ep} + Y_{bkg}}$$

where  $P$  is the beam polarization during production running, the  $Y$ 's are the *detector current-weighted yields*, and any  $A$  without the subscript “*exp*” is a physics asymmetry. Reorganizing this expression, and generalizing to an arbitrary number of background reactions, one finds

$$A_{ep \rightarrow ep} = \frac{A_{exp}^{raw}}{P} + \sum_{i=1}^n \left( \frac{A_{exp}^{raw}}{P} - A_{bkg,i} \right) \frac{Y_{bkg,i}}{Y_{ep \rightarrow ep}}$$

Hence, to determine the physics asymmetry  $A_{ep \rightarrow ep}$  we must measure the raw experimental asymmetry at a known beam polarization, then make small corrections for each background channel,  $i$ . Both the current-weighted fractional yield,  $Y_{bkg,i}/Y_{ep \rightarrow ep}$ , and the difference of the asymmetries  $A_{exp}/P - A_{bkg,i}$ , must be measured or well bounded.

In the sections below we will distinguish between prompt and non-prompt or, equivalently, hard and soft backgrounds since the techniques for estimation and measurement are very different.<sup>14</sup> Background estimates are summarized in Table 12.

### 8.1 Prompt backgrounds

*Prompt* backgrounds such as elastic scattering from the aluminum target windows, or inelastic electrons from pion production near threshold, can be directly measured using standard techniques while operating in current mode. Our tracking detectors will provide valuable supplementary information about hard backgrounds (in pulsed mode only), such as the fraction of events from the collimator edges, and the relative yields of the elastic peak and pion threshold regions.

---

<sup>14</sup>We do not address potential backgrounds from magnetic impurities (*e.g.* in the collimators), although material specifications are being developed.

Table 12: *Summary of background estimates for the  $Q_{Weak}^p$  experiment.*

Source	Asymmetry-Weighted Fractional Yield	How to measure
Hard:		
Al windows: elastic + QE	+11.1% -3.3%	Al dummy target, vary QTOR field
pion electroproduction	-0.5%	lower QTOR field
Soft:		
photons from beamline	0.4%	plug the collimator holes
$e^+e^-$ from beamline	0.1%	plug the collimator holes
neutrons	$\simeq 0\%$	background detectors in hut
quartz luminescence	$\simeq 0\%$	beam off intervals

### 8.1.1 Target window backgrounds

Our largest single background will be elastic scattering from the 3.5 mil thick aluminum target windows<sup>15</sup>. Despite the fact that the contribution of elastic scattering on aluminum to the overall rate is small (1.1%), the effective contribution is significant because  $A_{Al} \simeq 10A_{ep \rightarrow ep}$ . This is primarily due to the difference in the weak couplings:  $(1 - 4\sin^2\theta_W)$  for elastic scattering on the proton versus  $4\sin^2\theta_W$  for elastic scattering on the aluminum nucleus. Thus, we expect a *positive* elastic aluminum background of about 11% of the free  $e + p$  elastic asymmetry, which must be measured and corrected for. This conservative estimate, which may be high by as much as a factor of 2, assumes all the elastic electrons strike the quartz detector bars. An aluminum elastic event generator for GEANT is being written to better quantify the acceptance for elastic scattered events from aluminum.

Quasi-free backgrounds from aluminum have also been estimated. Although the neutron asymmetry is very large, the dominant quasi-free background is from bound protons, since  $\sigma_{ep}$  is much larger than  $\sigma_{en}$  in our kinematics. In the plane wave impulse approximation, quasi-free proton backgrounds would look much like our  $e + p$  elastic signal. However, at the low momentum transfer of the  $Q_{Weak}^p$  experiment, it has been shown that nuclear final state interaction corrections to the free proton and neutron asymmetries can be relatively large. From the work of Hadjimichael *et al.* [57], these effects are estimated to increase the quasi-free background from 1.1% to 3.3% of the free  $e + p$  elastic asymmetry; the quasi-free asymmetry is *negative*, i.e., it has the same sign as the free  $e + p$  elastic asymmetry.

The window background will be directly measured using special empty target cells with windows about 10 and 20 times thicker than the full target cell windows (*i.e.*, 50% and 100% of the normal radiation length of the full target). In addition to the nominal QTOR setting, the field will be set to slightly higher and lower values to check the momentum dependence. While it

<sup>15</sup>This section is based on calculations from the  $Q_{Weak}^p$  technical note by Mark Pitt [56].

may only be possible to operate the aluminum targets at 40-60  $\mu\text{A}$  without danger of melting, the relatively large aluminum asymmetry (and therefore figure of merit) means this program of window background measurements can be completed in 2 days.

### 8.1.2 Pion electroproduction

Figure 50 shows the distribution of the elastic and inelastic electrons directly hitting the Čerenkov detector. (The contribution of pions and protons is negligible.) Just as for the elastics, the inelastic electrons droop toward smaller radii near the coils due to the strong  $\phi$ -dependent field aberrations. Any attempt to increase the figure of merit by increasing the  $\phi$  acceptance, while retaining a simple rectangular quartz radiator, therefore runs into increasing inelastic contamination. To control this inelastic background, the radiator sensitive area must be better matched to the elastic locus. With the present V-shaped design, GEANT simulations show the inelastic fraction by yield is only 0.026%.

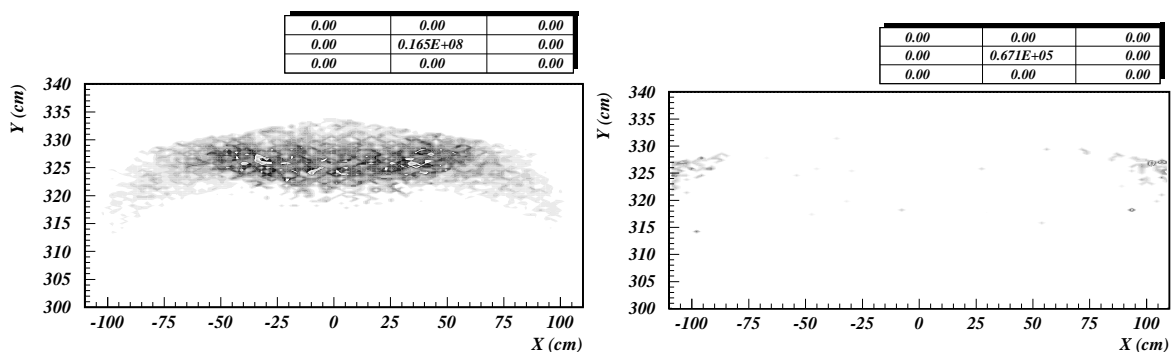


Figure 50: *Left: the distribution of elastic electrons over the Čerenkov detector. Right: the distribution of inelastic electrons over the Čerenkov detector. The distributions are weighted by appropriate cross sections.*

Reference [58] estimates the asymmetry in the pion threshold and  $\Delta$  resonance regions to be surprisingly constant,  $\sim -10^{-4}Q^2$ . Even allowing for the 10 times larger PV asymmetry of these electrons, the asymmetry-weighted contribution to the experimental asymmetry in  $Q_{Weak}^p$  is still a nearly negligible  $\sim 0.26\%$  of the elastic  $e + p$  asymmetry. The inclusion of quartz light guides which can intercept more of the inelastic electrons has the potential to roughly double this background fraction (to 0.5%), but on the other hand, the addition of thick, acceptance-defining tungsten masks might succeed in suppressing the inelastics altogether. The final optimization cannot be done until the collimator design is frozen, but it is clear that in any case, the net effect of the inelastic background will be small.

To measure the asymmetry from pion electroproduction it will only be necessary to reduce the QTOR field by about 10%. In principle, the time needed to measure such a small background (with a relatively large figure of merit) is extremely short. However, a full day will be allocated

to taking data with multiple field settings to verify that both our large- $\phi$  optics and our physics models are well understood.

## 8.2 Soft backgrounds

The integrating nature of our experiment, and the continuous beam also makes us potentially sensitive to non-prompt backgrounds. Because of extensive shielding (both material and magnetic), the soft backgrounds in our experiment are dominated by neutral radiation. Measuring such soft backgrounds requires special techniques since any attempt to change the experimental configuration (for example, removing the target) may alter an important source term and invalidate the measurement. Thus, non-prompt backgrounds must be measured with as little modification to the production configuration as feasible.

Soft backgrounds fall into two broad categories: those that are independent of luminosity, and those that are dependent on luminosity. An example of a luminosity-independent source is thermionic emission from the PMT photocathodes which is only non-negligible during our pulsed-mode measurements. An example of a luminosity-dependent, non-prompt background is the GEANT-estimated 0.4% contribution to the PMT anode current resulting from gamma rays. These simulations lack thermal neutron transport and capture, so it is important to confirm them with measurements.

Since the original proposal, there has been a great improvement in the understanding of the Čerenkov detector properties [52,53,54,55]. Our background simulations include not only the number of particles which traverse the sensitive area of the detector, but the probability of interaction and the resulting light output. Figure 51 shows the number of photoelectrons as a function of energy for possible detected particle types.

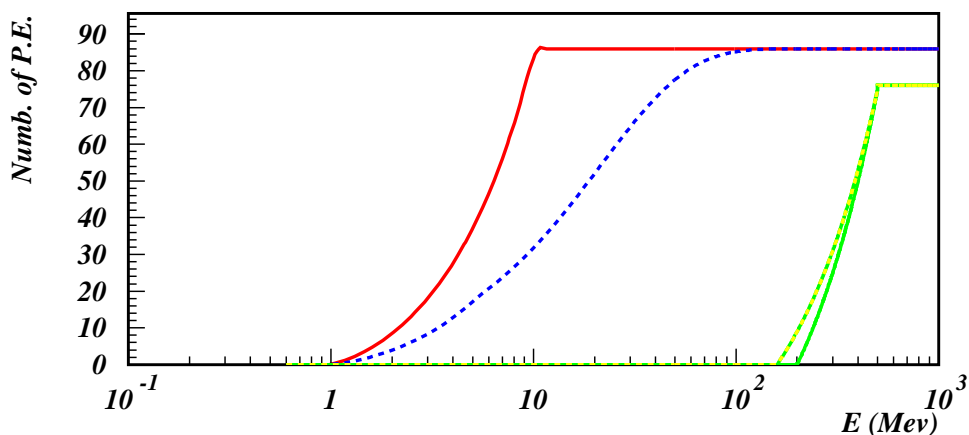


Figure 51: Number of photoelectrons as a function of particle energy for interacting particles. Red curve is  $e$ 's, dashed blue is  $\gamma$ 's, yellow-green is  $\mu$ 's, and green is  $\pi$ 's.

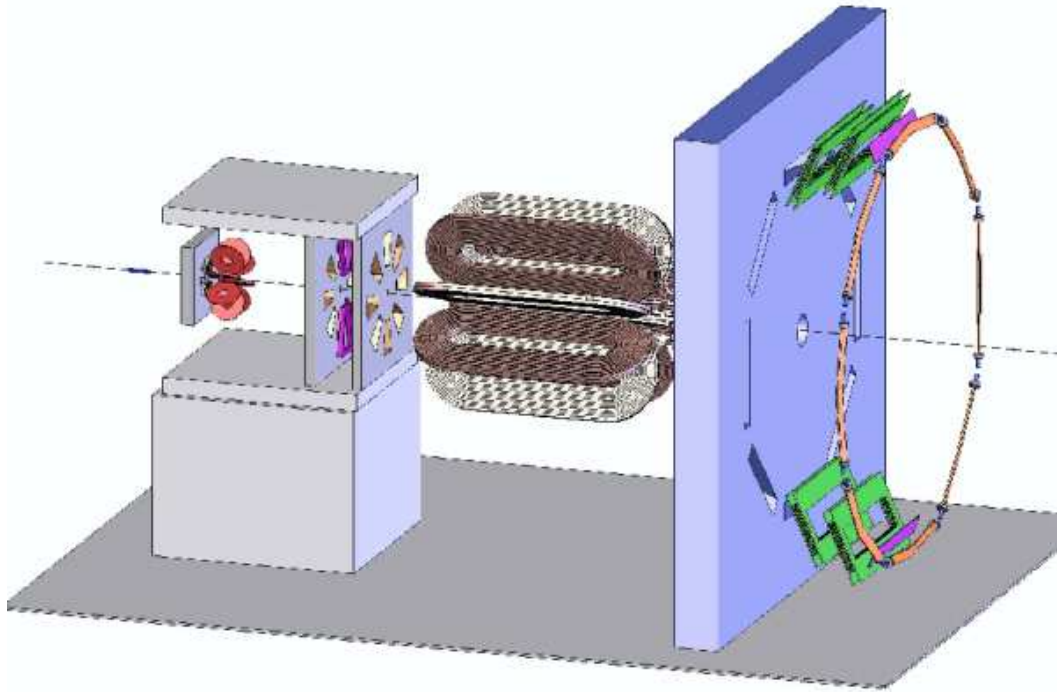


Figure 52: A 3-D perspective of the collimating system in relation to the QTOR coils.

### 8.2.1 GEANT simulations

The experiment is designed such that, in principle, only elastically scattered electrons can make it through the collimation system and be detected in the Čerenkov counters. However, multiple scattering provides a mechanism for circumventing this condition at some level, which must be studied in the GEANT simulations.

As described in section 4.10, the collimator reference design consists of a forward collimator to shield the forward GEM detectors of the  $Q_{Weak}^p$  tracking system, followed by a two-stage collimator at the entrance of the QTOR magnet. The first stage of the magnet entrance collimator defines the angular acceptance of the experiment, while the second stage performs a ‘cleanup’ function. To maximize the counting rate, the collimation system has the widest acceptance that is practical, while to reduce the inelastic contribution to acceptable levels, the quartz detectors are formed into a ‘V’ shape in order to better match the elastic electron distribution. Figure 52 shows the two-stage collimation system in relation to the QTOR. Although the detector will be located inside a shield house, the shallow bend angle of QTOR means the detector can directly view the beamline which passes through the magnet. Therefore, this region of beamline must be surrounded by lead. In the simulations presented here, the lead thickness was only 2.5 inches.

Figure 53 shows how low energy charged particles generated in the target or collimation are swept away by the magnetic field. Neutral particles which survive the collimation stages pass straight through the magnetic field and impact the detector shield house wall below the detector window (*i.e.*, at smaller radius).

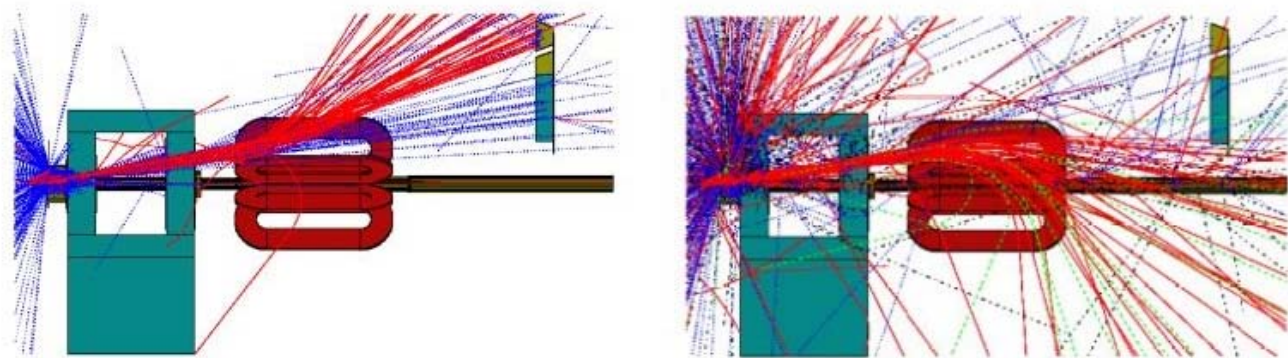


Figure 53: *Shielding from the inelastic channels by the QTOR magnetic field. The magnetic field bends inelastic electrons upward (left drawing) and positive pions inward (right drawing), away from the detector acceptance. The collimator was designed such that neutral particles generated in the target or at the collimator walls, unaffected by the field, impact the shield house below the detector window.*

The Čerenkov detector acceptance for secondary particles is very low, so it was necessary to simulate a large number of scattering events ( $\simeq 10^8$ ) to yield even marginal statistics on the background. In the present beamline design, soft backgrounds are dominated by photons of 1-10 MeV from the section of beamline passing through QTOR which is directly viewed by the Čerenkov detectors (Figures 54 and 55). Although the soft photon flux through the bars is comparable to the elastic electron rate, the low interaction probability and the low Čerenkov response for low energy charged particles yields a detector current-weighted background of only 0.5%. Most of this background (80%) is due to photons, while only 20% of it is due to secondary electrons and positrons. The contribution of other particle types is negligible. For the time being we assume that these events have negligible PV asymmetry. We will either directly measure this asymmetry, or add more shielding to lower the background another order of magnitude.

The contribution from re-scattering is a special case. Elastic electrons which rescatter in the air and emit photons which contribute to the Čerenkov signal are not strictly a background, but rather a source of excess noise in the detector system. Similarly, the contribution from cross talk, *i.e.* the background in one detector produced mostly by elastic electrons that rescatter from other (usually adjacent) octants, is estimated to be only 10% of the other backgrounds. Since this background carries the  $e - p$  elastic asymmetry that we are aiming to measure, it is best treated as a small source of excess noise.

While the backgrounds were estimated using the latest collimator design, the shielding surrounding the downstream beam pipe is not yet optimized. Because this section of beamline is illuminated by scattering from upstream collimators, it is not practical to finalize the beamline shielding until we freeze the collimator design. However, obvious improvements can be made. One is to modify the geometry so the detector cannot directly view the cleanup collimator. This will also reduce the number of meters of visible beamline. Secondly, additional lead shielding can be placed around the beamline. Although photons of 1-10 MeV have fairly long attenuation length (10-20  $g/cm^2$  in lead), another 1.5" of lead would provide more than two additional attenuation lengths. There is plenty of room for this amount of lead to be added.

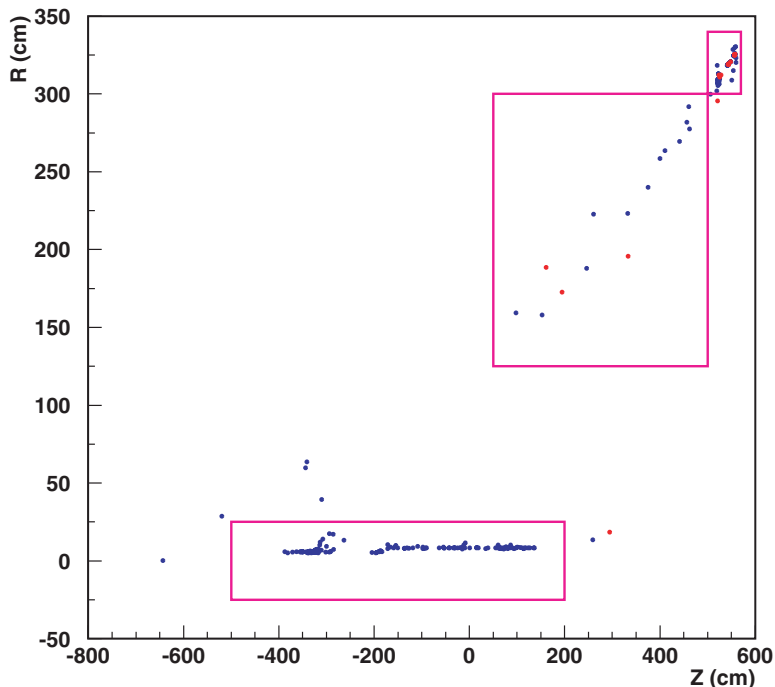


Figure 54: *Source vertices of detector backgrounds. The center of QTOR is at  $z = 0$ . The region at the lower left is dominated by photons from the beamline. The regions at upper right represent vertices produced in air and the shield house window. Most of the latter secondaries constitute excess noise rather than a true background because they carry the elastic  $e + p$  parity signal.*

### 8.2.2 Measurement of soft backgrounds

We have plans for measuring non-prompt backgrounds in both pulsed and current mode. Each has its advantages and disadvantages, and one will provide a valuable cross-check on the other. The combination of pulsed-mode and current-mode measurements outlined below will allow us to measure soft backgrounds at the 0.1% level in terms of light-weighted yield and, furthermore, measure any significant PV asymmetries of the background.

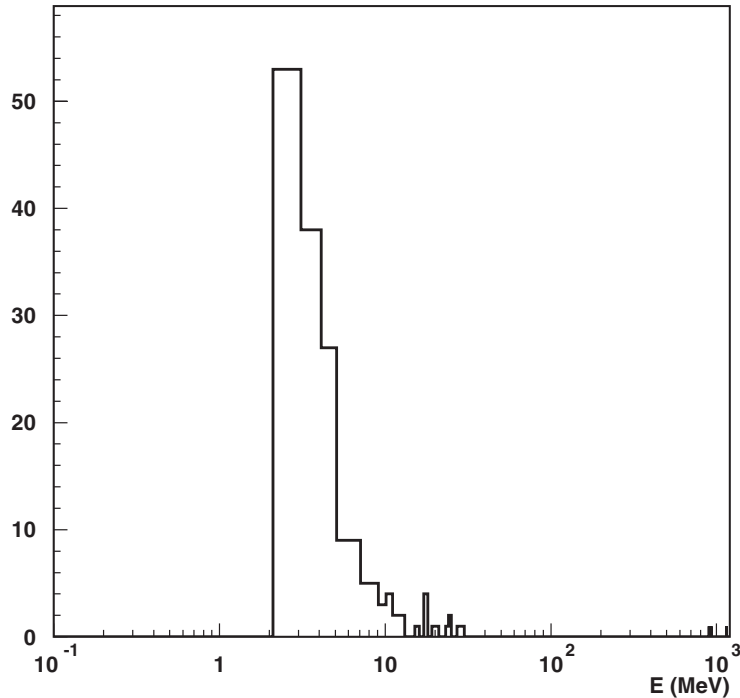


Figure 55: *Energy distribution of background sources. Low energy photons from 1-10 MeV which leak out of the beamline are the dominant source of background in the Čerenkov detectors.*

### Pulsed mode measurements

Pulsed mode running will only occur at dramatically reduced beam current so that the tracking detectors can operate efficiently. These detectors will allow us to correlate each normal, signal-size pulse in the quartz PMT's with a good track in the Region III chambers, a clean signal in an adjacent trigger scintillator, and an essentially straight track back to the target in the Region I and II trackers. To account for *all* the signal current, we have to make unbiased measurements which constrain the energy spectrum at (and even below) the single photoelectron level. This will require a likelihood analysis since, for example, there is no way to attribute a particular single photoelectron to thermionic emission in the PMT, a background gamma ray, or the low energy tail of the signal pulses with an inefficient Region III chamber. Similarly, large pulses could be due to the high energy tail of the signal pulses, or to showering in the Helium-filled channel. Our approach will be to use both our tracking detectors and the rich time-domain information afforded by Flash ADC's to study these effects.

First, beam-off data will determine the rate and pulse height distributions for cosmic rays and PMT dark current. Then, data will be taken at several beam currents which are as high as possible consistent with high tracking efficiencies. A random trigger would cause the Flash ADC to sample the quartz and scintillator signals until at least 10,000 good elastic electrons are accumulated per run. (The drift chambers will simultaneously be read out with pipeline TDC's.) Data would also be taken during intervening beam off intervals to constrain long lived lumines-

cence.<sup>16</sup> Offline, the complete dataset will be fitted to the hypothesis that these “snapshots” are due to a combination of 1) elastic electrons (with and without accompanying tracks due to tracking inefficiencies), 2) luminosity-independent sources, and 3) possible luminosity-dependent backgrounds including luminescence. Using this technique, it should be possible to measure the detector current-weighted yield of soft backgrounds with a sensitivity approaching 0.1%. Hall C is now working with the JLab electronics group to manufacture 64 channels of 10 bit, 250 MHz Flash ADC for our purposes.

For pulsed-mode soft background measurements to be applicable to our high current, PV measurements, the beam halo must not change significantly. This can be easily checked with a combination of solid and “hole” targets, using the current signal from a downstream PMT as an approximately linear measure of the amount of intercepted beam.

The major limitation of the pulsed-mode soft background measurements is that, due to limited statistics, the PV asymmetry of the soft backgrounds cannot be measured. One does not expect that low energy photons, whose dominant source term is the  $Q^2 \simeq 0$  tail of multiple-scattered primary beam interacting with a scrape-off collimator, will have a significant asymmetry. However, this assumption should be verified experimentally – we will see in the next section that this can be done in current mode.

### Current mode measurements

Dedicated current mode measurements with the main detectors, while the collimator holes are plugged, may give the best estimate for beamline backgrounds of photons, electrons and positrons. However, extensive GEANT studies are still needed for the final beamline configuration to verify that the collimators themselves are not the dominant source term, and that blocking them will not create a significant new source term.

Some soft backgrounds such as neutrons may not be strongly position dependent inside the detector hut (*i.e.*, the source terms are the beamline section which passes through the detector hut, or the front walls where many hard photons and inelastic electrons are dumped). In this case, we can obtain valuable information about such backgrounds by locating complete detector assemblies inside the shield house which are *outside* the beam envelope. To avoid having to move them too frequently, we require two such complete background detectors. (Figure 56) Other background detectors, some lacking the quartz bar, and others lacking both the quartz and the PMT’s (leaving only the amplifier connected to an unenergized PMT base), will help us isolate the source of light or current generation.

It is of course not possible to place the background detectors at exactly the same position as the main detectors. However, by moving the background detectors to different locations outside the beam envelope during the experiment, and combining this information with GEANT simulations, we should be able to understand the position dependence of any significant backgrounds. Background sources can be further isolated by plugging the collimator holes, plugging the detector

---

<sup>16</sup>Our quartz is specially selected to have negligible luminescence, but the decay of short-lived radioisotopes in the air can produce  $\beta$  rays or gamma rays which strike the quartz, produce Cerenkov light, and mimic luminescence.

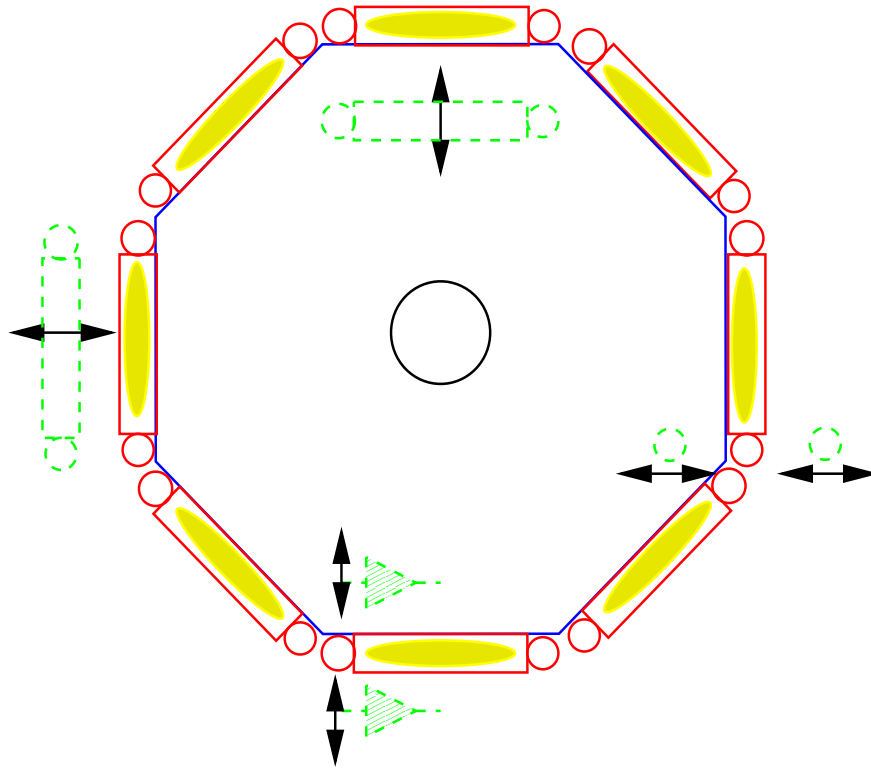


Figure 56: *Schematic of the detector hut. The main detectors are outlined in solid red, with a yellow ellipse denoting the elastic envelope. The various background detectors are outlined in green dashes. A circle represents the location of a PMT, while a triangle represents an amplifier. Hard photons are dumped on the front of the shield house wall at smaller radius than the main detectors, while inelastic electrons are dumped at a larger radius.*

windows, and changing the QTOR field.

The main advantage of these current mode measurements is that they would have the statistical power, and the proper electronics, for measuring the PV asymmetry of any soft backgrounds. While the background detectors might not show the same luminescence characteristics as the main detectors (depending on whether the source is the quartz itself or radioactive gas), beam trips will give us plenty of opportunities to study any apparent luminescence which may build up in the main detector bars.

## 9 Systematic Errors

### 9.1 Overview

Changes of beam properties with helicity can lead to false parity asymmetries. Parity violating scattering experiments generally have dealt with this by keeping helicity correlations as low as possible, by measuring residual correlations and by making corrections for them based on measured sensitivities. The measured parity asymmetry,  $A_{meas}$ , is written in terms of the physics asymmetry,  $A_{phys}$ , in the following way for sufficiently small helicity correlations:

$$A_{meas} = A_{phys} + \sum_{i=1}^n \left( \frac{\partial A}{\partial P_i} \right) \delta P_i, \quad (12)$$

where beam parameter  $P_i$  changes on helicity reversal to  $P_i^\pm = P_i \pm \delta P_i$ . The detector sensitivities  $\partial A / \partial P_i$  can be determined preferably by deliberate modulation of the relevant beam parameter or from natural variation of beam parameters. The helicity-correlated beam parameter differences,  $\delta P_i$ , are measured continuously during data-taking. From estimates of the sensitivity of our apparatus to beam parameter variations, we can set requirements on how accurately beam parameters have to be measured and how small helicity correlations in these parameters must be. The goal is to constrain systematic uncertainties from each source to be no more than the statistical uncertainty on the measurement of the parity asymmetry, i.e., no more than  $6 \times 10^{-9}$ , and that corrections are accurate to 10%.

### 9.2 Sensitivity to Helicity-Correlated Beam Motion

A perfectly symmetric detector system, magnet and collimator aligned precisely with the beam should be insensitive to small modulations of beam position on helicity flip. If the beam is moved away from this “position neutral axis”, however, symmetry is broken and false parity-violating effects are seen. These effects have been investigated with the help of the LaTech Monte Carlo simulation package for  $Q_{Weak}^p$ . The  $Q^2$ -weighted event rate,  $N(x, y)$ , seen by a Čerenkov bar is mapped out as a function of the position of the beam on target. By assuming smooth variation of event rate with position, it is then possible to estimate the false parity asymmetry due to changes of beam properties on helicity flip and to set tolerances.

Figure 57 shows the calculated event rate on a Čerenkov bar whose center lies in the  $x - z$  plane as a function of the position  $(x, y)$  on target at which an electron scatters. The plot covers a 2 cm by 2 cm area; the rastered beam lies in the central 4 mm by 4 mm. The scale at the side of the plot shows the rate in MHz per bin when a 180  $\mu$ A beam is rastered to the full area of the plot. The total rate is approximately 800 MHz. The slope in  $x$  and the symmetry about  $y = 0$  are seen. The variation of event rate per bin with position on target is well-represented over the area of the plot by,

$$n(x, y) = 1 + ax + by^2,$$

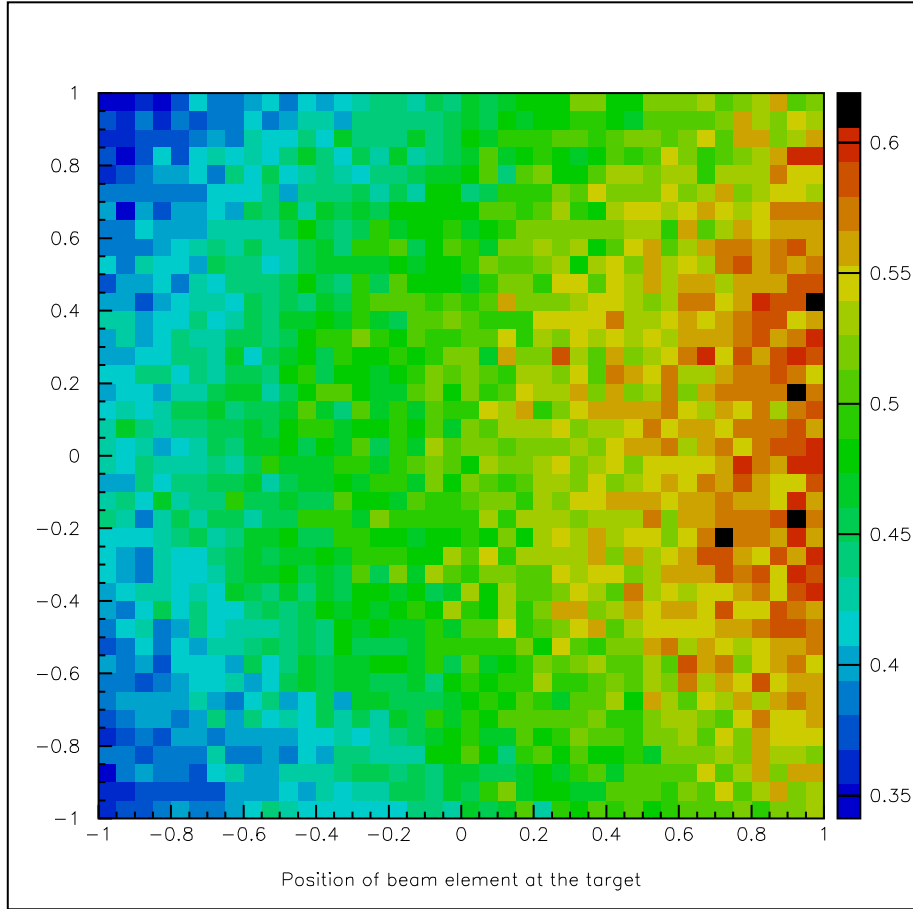


Figure 57: *Calculated variation of event rate on a Čerenkov bar as a function of the position at which a beam element strikes the target. The area shown is 2 cm vertical and horizontal. The rastered Qweak beam covers the central 4 mm by 4 mm.*

with  $a = 0.0181 \text{ mm}^{-1}$ ,  $b = -0.00118 \text{ mm}^{-2}$ . Summing event rate per bin over a 4 mm by 4 mm area yields the event rate  $N(x, y)$  for the rastered beam.

From the map of event rates, the false parity asymmetry measured by a single detector is:

$$\epsilon = \frac{N(x^+, y^+) - N(x^-, y^-)}{N(x^+, y^+) + N(x^-, y^-)},$$

where the beam position is  $x^\pm = x_0 \pm \delta x$ ,  $y^\pm = y_0 \pm \delta y$  for the two helicity states. The position neutral axis is nominally at  $x = y = 0$ . Matching acceptance and response of Čerenkov bars is not necessary when single detector asymmetries are calculated. For motion of the beam in the  $x$  direction alone, false asymmetries for the left-right detector pair are reduced through cancellations, as the coefficient  $a$ , above, has opposite sign for left and right detectors. There is no such cancellation for the top and bottom detectors and partial cancellation for the four diagonal detectors.

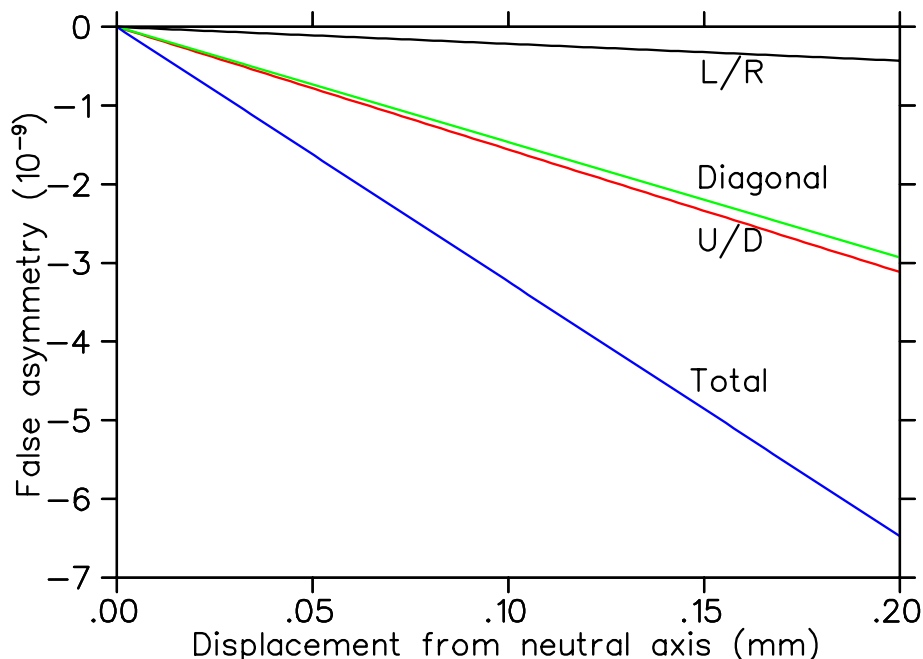


Figure 58: Contributions to the false asymmetry due to beam motion for a 4 mm raster size and a 40 nm shift of beam position on helicity flip. The asymmetry is proportional to this shift. Curves are labelled ‘L/R’ for the left-right detector pair, ‘U/D’ for up-down, ‘Diagonal’ for the diagonal pairs and ‘Total’ for the sum.

Figure 58 shows contributions to the false parity asymmetry for the left-right, up-down and the two diagonal pairs of detectors for  $\delta x = 20$  nm (i.e. for a 40 nm shift of beam position on helicity flip) as a function of displacement from the neutral axis for a 4 mm raster size. The dc position of the beam should be set to within  $180 \mu\text{m}$  of the neutral axis to limit the false asymmetry to  $6 \times 10^{-9}$ . The 1999 HAPPEX experiment was able to keep the run-averaged position difference below the 50 nm level. The false parity asymmetry is proportional to the product of displacement from the neutral axis and beam motion on helicity flip.

It is assumed that effects of varying target thickness, due for example to the windows of the hydrogen target being curved, are removed by normalizing the Čerenkov detectors to the luminosity monitors. Effects of target bubbling are removed in the same way.

### 9.3 Sensitivity to Beam Size Modulation

The diameter of the beam from the source may change on spin flip. This will induce a modulation of beam size on target that is, however, much diluted by the  $\simeq 100 \mu\text{m}$  size of the unrastered beam compared to the 4 mm raster pattern. Size modulation due to rastering should not be correlated with spin state from the source and will average to zero over time. The effect of size modulation of the unrastered beam is estimated by folding an unrastered beam distribution into

a square raster pattern and summing  $n(x, y)$  over the resulting profile to find the event rate on a Čerenkov bar as a function of unrastered beam size. For an unrastered beam of 100  $\mu\text{m}$  diameter, a false asymmetry of  $6 \times 10^{-9}$  results from a change in diameter of 1.2  $\mu\text{m}$  in the unrastered beam. The false asymmetry is proportional to the product of unrastered beam size and diameter change.

## 9.4 Sensitivity to Angle of Beam on Target

As the angle of incidence of the beam on target is changed, so the range of  $Q^2$  accepted by the collimators changes and with it the event rate. There is in addition a variation of effective thickness of the target, but the effect is small compared with the variation of cross-section and is, in any case, removed by normalization to the luminosity monitors. The results correspond to the beam being pivoted by  $\pm\delta\theta$  about a vertical axis through the center of the target. There is then some cancellation for the left-right detector pair and none for the up-down detectors.  $\theta_0$  is the spin-averaged angle of the beam relative to the symmetry axis of detectors and collimators. The systematic error requirement becomes  $|\theta_0\delta\theta| \leq 6.3 \times 10^{-6} \text{ mrad}^2$ .

## 9.5 Summary of Beam Requirements

The table summarizes the requirements for the beam based on the correction for the associated systematic error being no greater than the expected  $Q_{weak}$  statistical error, i.e. no greater than  $6 \times 10^{-9}$ . The maximum DC value for each quantity is given in column 2. Column 3 shows the requirements on helicity-correlated quantities averaged over a 2200 hour period. The false asymmetries due to beam position and direction modulations are proportional to the product of the numbers in columns 2 and 3, so one requirement can be relaxed if the other is tightened. Column 4 shows what has been achieved to date. Beam requirements have been met, that for position modulation by a wide margin. Helicity-correlated size modulation should be on a scale no larger than position modulation. Column 5 shows how well beam properties should be measured during a four spin state cycle so that the uncertainty of the systematic error correction is no more than 10% of the correction itself. For the beam energy entries, columns 3 and 5 of the table show the displacement of the beam that results at the hall C pivot when dispersion is set to 35 mm/%.

Summary of systematic error requirements

Parameter	Max. DC value	Max. run-averaged helicity-correlated value (2200 hours)	Achieved to date	Max. noise during quartet spin cycle (66 ms)
Beam energy	$10^{-4}$	$10^{-8}$ 35 nm @ 35 mm/%	$10^{-8}$ (G0)	$10^{-5}$ 35 $\mu\text{m}$ @ 35 mm/%
Average current	180 $\mu\text{A}$	< 0.1 ppm	$0.14 \pm 0.32$ ppm (G0)	< 70 ppm
Beam position	180 $\mu\text{m}$	40 nm	< 3 nm (HAPPEX-II)	20 $\mu\text{m}$
Beam angle	60 $\mu\text{rad}$	100 nrad	< 2 nrad (G0)	0.1 mrad
Beam diameter (unrastered)	< 150 $\mu\text{m}$	< 1.2 $\mu\text{m}$	(see text)	< 10 $\mu\text{m}$

## 9.6 Feedback for Control of Helicity-Correlated Beam Parameters

Significant effort has been invested in the past several years by the JLAB polarized source group, the HAPPEX, and the  $G^0$  collaborations to minimize helicity-correlations in the JLAB beam properties (intensity, energy, angle, and beam position). The result has been that the specifications for helicity-correlated beam properties for the HAPPEX-I/II and  $G^0$  experiments have been met, as shown in Table 16. With the exception of helicity-correlations in the beam intensity, the already achieved performance is acceptable for the  $Q_{Weak}^p$  experiment. (Note: even in the case of intensity the specification was very nearly satisfied:  $0.14 \pm 0.32$  ppm for  $G^0$  and 0.2 ppm for HAPPEX-II compared to the  $Q_{Weak}^p$  specification of 0.1 ppm.) These results came from a combination of careful laser table and injector setup and the implementation of various feedback systems. Clearly, all the existing systems will be available for the use of  $Q_{Weak}^p$ . In this section, we briefly discuss which of the systems we will most likely use, and where we anticipate making improvements for more robust and reliable performance.

The feedback system used by  $G^0$  and HAPPEX-II to reduce helicity-correlated intensity asymmetries is referred to as the “IA system”. Without this system, the smallest intensity asymmetries that can be achieved with careful setup are  $\sim 20$ -30 ppm. With the system on, the  $\sim 0.2$  ppm results quoted above are achieved. The system consists of a Pockels cell sandwiched between linear polarizers and a waveplate. Application of relatively small voltages (<10 V) can be used to control the intensity of the laser beam. The intensity asymmetry is measured continuously using beam charge monitors in the experimental halls. The resulting values are used to determine the needed control voltage to be applied to the IA to null the intensity asymmetry. For  $Q_{Weak}^p$ , we anticipate using this system with little change.

To control helicity-correlations in beam position, different strategies were employed by  $G^0$  and HAPPEX-II.  $G^0$  used the “PZT system”, which consists of a mirror in the laser beam path mounted on a piezo-electric transducer. The laser beam position could be adjusted in a helicity-correlated

way to compensate for any helicity-correlated beam position measured in the experimental halls. While this system did achieve the desired specifications, it was difficult to maintain for two reasons. The response of the system would change with the tune of the accelerator, so the system had to be recalibrated every 2-3 days. Secondly, there was a significant coupling between helicity-correlated position differences and intensity asymmetries due to scraping at apertures in the injector. HAPPEXII ran without any position feedback and they were able to achieve their objectives overall, but there were periods during their running when their position difference were outside their specifications.

For  $Q_{Weak}^p$ , we plan to develop the capability to control the position and angle of the beam using corrector coils either in the Hall C beamline or in the 5 MeV region of the injector, which is downstream of where most of the significant interception of the beam on apertures occurs. This will eliminate the problem of the coupling between helicity-correlated position differences and intensity asymmetries. If the corrector coils are implemented in the Hall C line, then the calibration of the system should be much more constant and independent of the accelerator tune. Finally, the current PZT system only really allows adjustment of helicity-correlated position differences at the experimental target. A system based on correction coils could be used to independently null both helicity-correlated position and angle differences at the  $Q_{Weak}^p$  target.

## 9.7 Luminosity monitor

The luminosity monitor will consist of an array of Čerenkov detectors located downstream of the  $Q_{Weak}^p$  experiment at a small scattering angle ( $< 1^\circ$  compared to the central  $Q_{Weak}^p$  scattering angle of  $\sim 8^\circ$ ). Because of its location, the luminosity monitor will have a small statistical error (due to the high count rates) and a small expected physics asymmetry (due to the low average  $Q^2$ ). These properties make it useful for two purposes. It can be used to do detailed studies of the possibility of target density fluctuations. Since it has a much smaller statistical error per measurement period than the main detector, it is much more sensitive to the onset of target density fluctuations. Secondly, the luminosity monitor can be used as a very valuable “null asymmetry monitor”. It is expected to have a much smaller asymmetry than the main detector; thus, if its asymmetry is non-zero it could indicate the presence of a false helicity-correlated effect in the experiment. Specifically, we will apply our standard corrections procedure (using Equation 12 for helicity-correlated beam properties) to the luminosity monitor, as well. If we are properly accounting for all helicity-correlated beam properties, we should be able to correct the luminosity monitor to zero asymmetry within errors. Finally, it is not currently planned that this detector will be used explicitly for luminosity normalization in the experiment, but it is being designed with that capability in mind should it be necessary.

The current reference design for the luminosity monitor calls for it to be located 17 meters downstream of the  $Q_{Weak}^p$  target as shown in Figure 59 at a mean scattering angle of about  $0.75^\circ$ . It will be an array of 8 Čerenkov detectors placed symmetrically about the beampipe as shown. Each detector will consist of a small 5 cm x 3 cm x 2 cm block of quartz as the Čerenkov radiator. Since the detectors will exist in a harsh environment, the Čerenkov light

will be transported about 50 cm further away from beam centerline using air light guides made out of a reflective aluminum material (Anolux Miro IV PVD [51]) that was successfully used for this purpose for the luminosity monitors in the HAPPEXII experiment. The quartz blocks will be cut at an appropriate angle at one end so that the light can be transmitted into the air light guides. The photodetector will consist of 2 inch diameter radiation hardened vacuum photodiodes. Further details about the photodetector and electronic readout scheme are given below. The active medium of the detectors will be located in "cups" mounted in the beampipe as shown in the figure. This arrangement was successfully used to mount luminosity monitors during the recent  $G^0$  forward angle running.

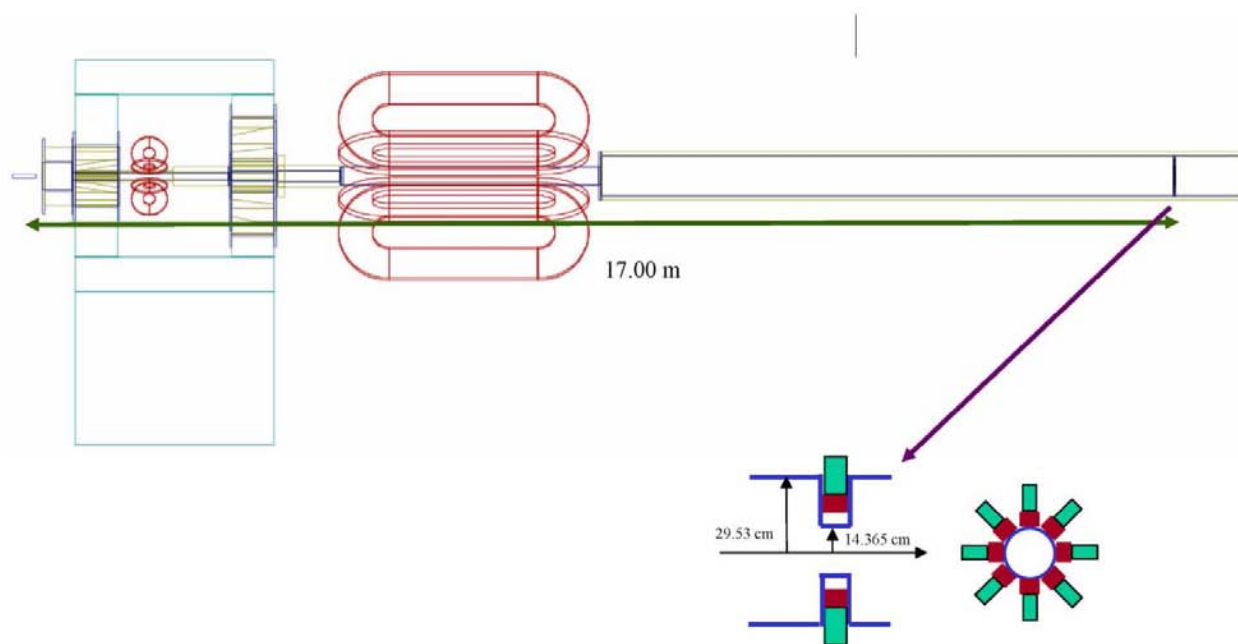


Figure 59: *Schematic of the location of the luminosity monitor array relative to the rest of the experiment. The inset shows how the luminosity monitor array will be mounted into the beamline using "cups" inserted into the beampipe. The location of the main  $Q_{W_{eak}}^p$  detector is indicated by the vertical line at the top of the figure.*

A complete GEANT simulation of the signals expected in the luminosity monitor in the physical arrangement shown in Figure 59 was performed. The simulation had all the geometry shown in the figure, including the aluminum beampipe and its lead shielding to properly simulate any backgrounds generated there. The physical processes considered included e-p elastic scattering in the target, Møller scattering in the target, generation of electromagnetic shower products in the target and from interaction of scattered particles in the beampipe and shielding, and elastic electron scattering on the aluminum nuclei in the target container windows. The latter process was considered explicitly because its asymmetry is about ten times greater at a given scattering angle than that of e-p elastic scattering. The resulting expected count rates along with some other important results are shown in Table 13.

Table 13: *Results of GEANT simulations of the contributions to the luminosity monitor signal for the detector arrangement shown in Figure 59. The rates are calculated for 180  $\mu$ A of beam on a 35 cm LH<sub>2</sub> target.*

e-p elastic (rate/detector)	11 GHz
e-e Møller (rate/detector)	12 GHz
EM showers (rate/detector)	6 GHz
Total rate/detector	29 GHz
Expected photocathode current/detector	1160 nA
Fraction of multi-step processes from target	1%
Radiation dose to quartz detector in 2200 hours	0.5 GRad

The luminosity monitor will live in a harsh environment. The simulations indicate that the radiation dose over the course of the experiment will be about 0.5 GRad. Thus radiation hard materials are essential. The quartz chosen for the Čerenkov radiator will be the same grade (Spectrosil 2000) as that used for the main  $Q_{Weak}^p$  detectors. Luminosity monitors with that type of quartz were used successfully in PEP-II at SLAC. They used 2.7 x 6 x 3 cm<sup>3</sup> blocks of quartz, and they reported no observable radiation damage after a 2 GRad dose [50]. The same grade of quartz is also being used in the ongoing HAPPEX-II experiment for their very forward angle ( $< 1^\circ$ ) luminosity monitors; these devices are expected to take 1-2 GRad over the course of the entire run, so by the conclusion of their run in Summer 2005 we will have valuable data on radiation damage under conditions very similar to those expected for the  $Q_{Weak}^p$  luminosity monitors.

From the relative weighting of the various physical processes determined in the GEANT simulation, the expected physics asymmetry, statistical error, and sensitivities to beam parameter variations were determined for the luminosity monitor. The results are tabulated in Table 14. They are compared to the same parameters for the main  $Q_{Weak}^p$  quartz detectors.

The parameters in Table 14 are adequate for the luminosity monitor to perform its two primary functions. For the target density fluctuation monitor, the most critical parameter is that fact that the luminosity monitor's statistical error per helicity pulse pair is about 1/6 that of the main detector. If the target density is varying on a time scale comparable to the helicity-flip time, it will add in quadrature to the statistical width. So the luminosity monitor will be a much more sensitive target density fluctuation measuring device than the main detector. It will be used during diagnostic measurements to determine the optimum target operating parameters (beam raster size, target pump speed, target temperature, etc.). During regular production running, the luminosity monitor will serve as an "early-warning" device of any potential changes in target operating conditions that make affect the target density fluctuations.

Table 14: *Luminosity monitor parameters at the nominal  $0.75^\circ$  scattering angle compared to the main  $Q_{weak}$  detector. The statistical errors on the asymmetry are for all eight lumi or main detectors combined. The quoted sensitivities to beam parameter variations are for a single detector, before use is made of symmetry by averaging over detectors.*

Parameter	Luminosity monitor	Main detector
$\langle A \rangle$	0.003 ppm	-0.29 ppm
Count rate	29 GHz/det.	0.8 GHz/det.
$\delta A_{stat}$ , complete experiment	0.0008 ppm	0.005 ppm
$\delta A_{stat}$ , per pair	$0.8 \times 10^{-5}$	$5 \times 10^{-5}$
Energy sensitivity	-0.0020 MeV $^{-1}$	-0.0020 MeV $^{-1}$
Angle sensitivity	-260 rad $^{-1}$	-27 rad $^{-1}$
Position sensitivity	-20 m $^{-1}$	-18 m $^{-1}$

For the other primary use of the luminosity monitor as a “null-asymmetry” monitor, it is also clear from Table 14 that the parameters should be acceptable. The expected luminosity monitor physics asymmetry is much smaller (about 1%) of the main detector asymmetry; it is comparable to the main detector’s statistical error. The luminosity monitor has comparable sensitivities to beam parameter variations as the main detector. Non-zero helicity-correlations in the beam parameters will lead to false asymmetries in both detectors that will be corrected for using the standard corrections procedure defined in Equation 12. If the asymmetry of the luminosity monitor after this corrections procedure is at the level of the small asymmetry in Table 14, then we will be confident that we have corrected for all possible helicity-correlated beam parameters that could lead to a false asymmetry.

As noted above, we plan to use 2 inch vacuum photodiodes for readout of the luminosity monitor Čerenkov detectors. Due to the large expected photocathode current under regular operating conditions (about 1160 nA  $\sim$  1  $\mu$ A) these very linear, unity-gain devices are an appropriate choice. (We note that the photocathode current of  $\sim$  1  $\mu$ A is comparable to the photoanode current of  $\sim$  6  $\mu$ A expected for the main detectors, so the two detector systems will have similar current outputs). For electronics, we intend to use the same low-noise, high gain I-to-V preamp design developed for the main  $Q_{Weak}^p$  detector. The voltage output will then feed into the same chain of digitizing electronics described in the main detector section.

During the recent  $G^0$  forward angle production run, two of the eight luminosity monitor detectors were instrumented in a way that we would like to do for  $Q_{Weak}^p$ . They consisted of 3.5 x 3.5 x 1.6 cm of Spectrosil 2000 quartz optically coupled to 3 inch diameter Hamamatsu R2046 vacuum photodiodes. They were read out with a low-noise, high gain I-to-V preamp box from our Triumph collaborators, and the resulting voltage signal (about 1.5 volts per 10 nA of photocathode current) was sent into 2 MHz voltage-to-frequency converts that fed scalers that were read out every 33

msec. The prototype luminosity monitors were located about 10 m downstream of the  $G^0$  target at a mean scattering angle of about  $1.2^\circ$ . Under conditions of  $40 \mu\text{A}$  of beam current incident on a 20 cm liquid hydrogen target, the observed photocathode currents were 23.5 and 31 nA compared to an estimated 24 nA from simulations. The implied count rate from these numbers was about 0.5 GHz per detector. The smallest statistical width observed during our running with these detectors was about 180 ppm for a single detector with a 2mm aluminum target where no target boiling is expected; this was consistent with our expectation for the statistical width. The measured contribution of random electronic noise to this width was only 13 ppm, so the electronics were performing acceptably for this application. No visible radiation damage to the quartz was observed after the run, corresponding to a dose of about 4 MRad. The borosilicate windows of the unshielding vacuum photodiodes suffered significant darkening as could be expected. Even though we will have our vacuum photodiodes shielded during the  $Q_{Weak}^p$  experiment, we will try to get vacuum photodiodes with quartz windows for extra protection against radiation damage problems.

Finally, as noted earlier, it is not currently planned that this detector will be used explicitly for luminosity normalization in the experiment, but it is being designed with that capability in mind should it be necessary. If target density fluctuations are significant, the collaboration has a plan to employ a higher helicity reversal rate as described elsewhere in the proposal to minimize the effect. Another possible strategy would be to use the luminosity monitor to normalize away the target density fluctuations, as was done in the PVA4 experiment at Mainz. The currently proposed luminosity monitor would be adequate for this purpose. For this purpose, it is important that the processes that generate signal in the luminosity monitor be linear in the target density. An example of a process that is non-linear in the target density would be a multi-step process such as emission of an energetic bremsstrahlung photon followed by Compton scattering or pair production resulting in the detection of the secondary electron or positron. As shown in Table 13, the GEANT simulation showed that the contribution of such “multi-step” processes to the total rate is about 1%.

## 9.8 Effects due to transverse polarization

If the electron beam has a non-zero transverse polarization component, then our experiment will be sensitive to the parity-conserving vector analyzing power arising from the interaction of the electron spin with the nuclear current in the electron’s rest frame. For spin-0 nuclei this is referred to as the Mott asymmetry [83]. This is a parity-conserving left-right analyzing power, so it vanishes for a perfectly symmetric detector. This vector analyzing power has received considerable attention recently because it is dominated by a 2 photon exchange graph, which is related to the Rosenbluth/polarization transfer discrepancy in the determination of  $G_E^p/G_M^p$ .

The Mott asymmetry formula [83] is known for spin-0 nuclei, and it has been extensively tested at low energies. However, for nucleons with non-zero spin at finite  $Q^2$ , there were no theoretical formulae or measurements for this asymmetry, until recently. The SAMPLE [84] collaboration measured a value of  $A = -15.4 \pm 5.4$  ppm at  $E = 200$  MeV and  $\theta \sim 145^\circ$ . At forward angles,

the Mott asymmetry formula predicts a much smaller value, but surprisingly, the MAMI A4 collaboration [85] found comparably large values at  $\theta \sim 35^\circ$ . They measured  $A = -8.59 \pm 1.2$  ppm at  $E = 569$  MeV and  $A = -8.52 \pm 2.5$  ppm at  $E = 855$  MeV.

There have been several calculations recently of this single spin asymmetry. The calculation of Pasquini and Vanderhaeghen [86] agrees with the MAMI A4 data to about  $\sim 50\%$ . So we take their calculation to set the scale of the expected single-spin transverse asymmetry at the  $Q_{Weak}^p$  kinematics at about  $A \sim -3$  ppm. If we assume that there is a residual 5% relative transverse polarization component in the JLAB beam, and we assume that the acceptance of the  $Q_{Weak}^p$  focal plane detectors is matched to 1%, then the overall contribution to the asymmetry from this effect is 0.0015 ppm, which is  $< 1\%$  of our expected physics asymmetry. We can check for any presence of this in our data by looking for an azimuthal  $\cos(\phi)$  dependence in our measured asymmetry for the different octants. We will also directly measure the size of transverse asymmetry at our kinematics. Running just a few hours with fully transversely polarized beam will be sufficient to determine the asymmetry adequately, if it is as large as  $\sim 3$  ppm.

## 9.9 Hadronic Structure Contributions

As shown in Equation 4, the parity-violating asymmetry expression contains contributions from nucleon structure form factors. They increase in relative importance as one moves away from  $Q^2 = 0$ . To consider the impact of these contributions on our measurement, we write the asymmetry as follows:

$$A = A_{Q_W^p} + A_{hadV} + A_{hadA} \quad (13)$$

The first term involves the quantity of interest,  $Q_W^p$ . The second term involves the vector electromagnetic and weak hadronic form factors. It reduces to the  $Q^4 B(Q^2)$  term in Equation 4 for small  $Q^2$ . The third term involves the e-N axial form factor  $G_A^e$ . We exhibit these terms separately because there are two different types of experiments that are used to constrain them, and they have different kinematic dependences.

Our experiment aims to determine  $A_{Q_W^p}$  (and therefore  $Q_W^p$ ) from the measured physics asymmetry  $A$ . We will determine the values of the hadronic terms ( $A_{hadV}$  and  $A_{hadA}$ ) from the results of parity-violating electron scattering experiments at higher  $Q^2$  that are more sensitive to these terms. For the acceptance averaged values of the asymmetry in our experiment, we expect the following contributions to the total asymmetry of -0.293 ppm:

$$A_{Q_W^p} = -.180 \text{ ppm (61\%)} \quad A_{hadV} = -.101 \text{ ppm (35\%)} \quad A_{hadA} = -0.012 \text{ ppm (4\%)} \quad (14)$$

assuming a value of  $Q_W^p = .0716$  (with all radiative corrections included). The procedure for determining the expected errors on the hadronic terms,  $\delta A_{hadV}$  and  $\delta A_{hadA}$ , is explained below. Their contribution to the error on  $Q_W^p$  is written as:

$$\frac{\delta Q_W^p}{Q_W^p} = \sqrt{\left(\frac{\delta A}{A_{Q_W^p}}\right)^2 + \left(\frac{\delta A_{hadV}}{A_{Q_W^p}}\right)^2 + \left(\frac{\delta A_{hadA}}{A_{Q_W^p}}\right)^2} \quad (15)$$

The term  $A_{hadV}$  can be constrained from the achieved and anticipated results of the worldwide program of parity-violating electron scattering experiments on the proton. Completed results are available from SAMPLE [80], HAPPEX I [71], and MAMI A4 [74,75]. Experiments in progress or in the analysis phase are HAPPEX II [72] and  $G^0$  forward angle [73]. For these two experiments in progress, we use the two collaborations' most recent projections for their final error bars in our estimates. All of these experiments will be performed at higher  $Q^2$  values than  $Q_{Weak}^p$ , so we must extrapolate from their results to determine the value of  $A_{hadV}$  at our  $Q^2$ . To extrapolate, we must assume a functional form for the  $Q^2$  dependence of  $A_{hadV}$ . For this extrapolation, we assume conventional dipole and Galster parameterizations for the electric and magnetic proton and neutron form factors. For the electric and magnetic strange form factors,  $G_E^s$  and  $G_M^s$ , we use two different reasonable functional forms that are supported by calculations in the theoretical literature. The two free parameters in each model are the strange magnetic moment ( $\mu_s \equiv G_M^s(Q^2 = 0)$ ) and the strangeness radius  $\rho_s$  ( $\rho_s \equiv [dG_E^s/d\tau]_{\tau=0}$ ), where  $\tau = Q^2/(4M_N^2)$  and  $M_N$  is the nucleon mass. For Model 1, we use the data available at all  $Q^2$  values with  $G_E^s(Q^2) = \rho_s \tau G_D(Q^2)$  and  $G_M^s(Q^2) = \mu_s G_D(Q^2)$  where  $G_D(Q^2) = 1/(1 + Q^2/(.711 \text{ GeV}^2))^2$  is the ordinary dipole form factor. This behavior is similar to that of the "kaon asymptotic" form in the recent chiral quark-soliton model calculations of Silva, *et al.* [76]. For Model 2, we restrict ourselves to data at  $Q^2 < 0.25 \text{ GeV}^2$  and take a form more appropriate in this restricted  $Q^2$  range:  $G_E^s(Q^2) = \rho_s \tau$  and  $G_M^s(Q^2) = \mu_s$ . This behavior is similar to that obtained in the chiral perturbation theory work of Hemmert, *et al.* [77]. For each model, a global fit is done to all of the data described above. The two free parameters,  $\mu_s$  and  $\rho_s$ , are varied to determine the  $1\sigma$  confidence level ellipse. From that range of  $\mu_s$  and  $\rho_s$  values, the range of allowed  $A_{hadV}$  values at  $Q^2 = 0.03 \text{ GeV}^2$  (at  $1\sigma$  confidence level) is determined. In Figure 60, we show the results of the fits to the two models. At  $Q^2 = 0.030 \text{ GeV}^2$ , both fits give a fractional error of 2.8% on the  $A_{hadV}$  term. This implies a 1.5% contribution to the fractional error on  $Q_W^p$  from the vector hadronic component.

The axial contribution,  $A_{hadA}$ , depends on the e-N axial-vector form factor  $G_A^e$ . At tree level, this is known from neutron beta decay and neutrino scattering. However, this term also contains significant contributions from higher order electroweak corrections. The full axial form factor observed in electron scattering can be written as:

$$G_A^e(Q^2) = -\tau_3(1 + R_A^{T=1})G_A + \sqrt{3}R_A^{T=0}G_A^8 + \Delta s. \quad (16)$$

The latter two terms are an isoscalar form factor and the strange axial form factor, respectively. The combined estimated absolute error on  $G_A^e$  associated with these two terms is  $\sim \pm 0.04$ . The most significant and uncertain electroweak radiative corrections occur in the first term and are denoted by  $R_A^{T=1}$ . They have been theoretically calculated [78,79] to be  $R_A^{T=1} = -0.23 \pm 0.24$ . Two measurements by the SAMPLE experiment [80,81] at  $Q^2 = 0.1 \text{ GeV}^2$  and  $Q^2 = 0.04 \text{ GeV}^2$  are in agreement with this calculation. The experimental errors on this quantity will be measured more precisely in parity-violating quasielastic electron scattering on deuterium in the  $G^0$  backward angle measurements [82]. Combining the three expected  $G^0$  backward angle measurements of  $G_A^e$  (at  $Q^2 = 0.3, 0.5, 0.8 \text{ GeV}^2$ ) assuming a dipole form for the  $Q^2$  variation of the axial form factor yields an extrapolated absolute error on  $G_A^e$  at  $Q^2 = 0.03 \text{ GeV}^2$  of  $\pm 0.16$ . This implies an 18% fractional error on the  $A_{hadA}$  term, which leads to a 1.2% contribution to the fractional error on  $Q_W^p$  from the axial hadronic component.

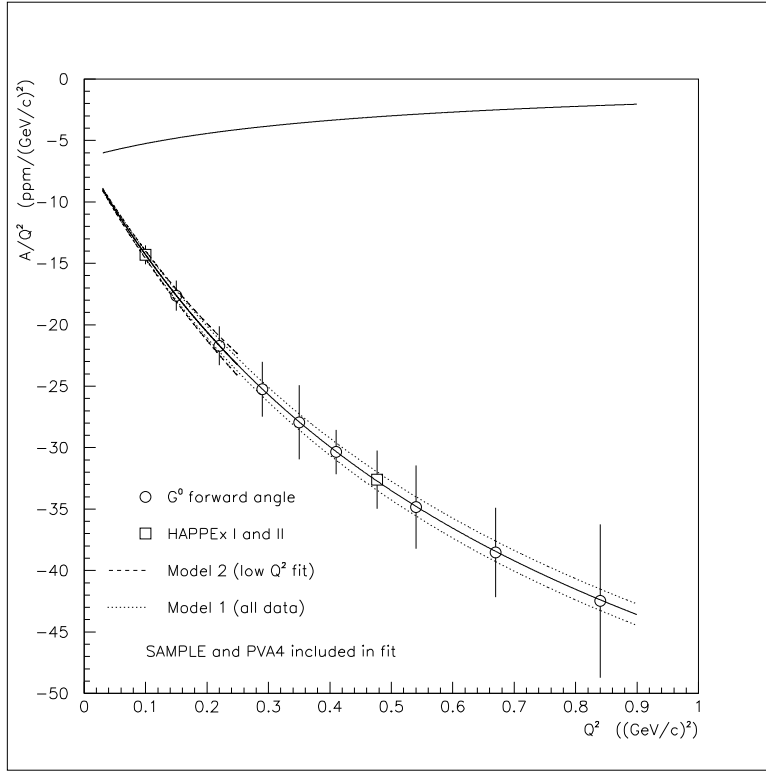


Figure 60: *The data points represent published or anticipated errors on  $A/Q^2$  from the experiments discussed in the text. The central values of all the data points have been adjusted to correspond to the strange form factors being zero. The central solid line assumes the strange form factors are zero. The dashed lines show the  $1\sigma$  range from fits under the two models for the strange form factor  $Q^2$  dependence discussed in the text. The free parameters in each case are the strange magnetic moment,  $\mu_s$ , and the strangeness radius,  $\rho_s$ . The SAMPLE and MAMI PVA4 results are included in the global fit, but they are not shown on the plot because they were taken at very different scattering angles than the other data. The line near the top of the plot shows the value of the  $Q_{W^{eak}}^p$  contribution,  $A_{Q_W^p}/Q^2$ , as a function of  $Q^2$ .*

For our total estimate of the error stemming from hadronic structure contributions, we combine our two estimates for the errors on the vector (1.5%) and axial (1.2%) hadronic components in quadrature. The final estimate for the fractional error on  $Q_W^p$  from hadronic structure is 1.9%.

## 10 Beam Diagnostics

In this section we discuss the measurement of beam properties other than beam polarization.

### 10.1 Current mode

The  $Q_{Weak}^p$  experiment requires highly linear, low noise beam property measurements in order to correct helicity-correlated false asymmetries, set the beam on the neutral axis, provide feedback, measure  $Q^2$ , and determine whether the beam is good enough for data taking. These measurements must be made at the sampling frequency throughout the entire experiment. A beam monitor should provide a relatively “pure” measurement of the respective beam property without the need for additional regression. The beam properties which  $Q_{Weak}^p$  needs to measure are:

- The beam charge difference,  $\Delta Q$ .
- The beam energy,  $E$ , and the energy difference,  $\Delta E$ .
- The beam position and angle at the target  $X, X', Y, Y'$  as well as  $\Delta X, \Delta X', \Delta Y, \Delta Y'$ .
- The beam spot size changes,  $\Delta\sigma_X$  and  $\Delta\sigma_Y$ . If too small to be directly measurement, the size changes must still be bounded at the  $<1$  micron level.
- The beam halo.

Most of our measurements will be made with RF beam monitors. JLab’s RF beam monitors can make continuous, non-invasive beam property measurements without serious concerns about radiation damage. The output RF signals can be downconverted to lower frequencies, filtered to improve S/N, and converted to DC signals for digitization. The AC-to-DC stage becomes nonlinear at the low end of the dynamic range<sup>17</sup> which raises two technical issues for parity violation measurements. The first is that turning off the beam gives the wrong pedestal, and the use of this incorrect pedestal in the analysis may subsequently increase the overall nonlinearity of the beam monitor in question. The second problem is that if one attempts to measure the isolation of the reversal signal from the beamline monitors during beam off periods, any non-zero result may be extremely difficult to convert to a false asymmetry. In our presentation below we will discuss different ways of coping with low-end nonlinearity for our various charge and position monitors.

Finally, integrating experiments like  $Q_{Weak}^p$  can be perturbed by the interaction of detector or beam monitor nonlinearities with helicity-correlated beam properties at frequencies *higher* than the sampling frequency. It is straightforward to model or measure the nonlinearity of a given detector or beam monitor. However, placing bounds on the helicity-correlated difference of the

---

<sup>17</sup>The diode networks which chop AC to DC either do not turn on or do so only sluggishly at low signal inputs.

variance for a given beam property,  $(\sigma_i^+)^2 - (\sigma_i^-)^2$ , where  $i = Q, E, X, X', Y, Y'$  at frequencies *higher* than the experiment sampling frequency, will require measurements with high-bandwidth spectrum analyzers as discussed below.

A summary of the primary and alternate beam monitors needed for  $Q_{Weak}^p$  are listed in Table 15. Standard diagnostics for the MCC to tune up the beamline and deliver high power CW beam are not covered here.

### 10.1.1 Cavity-Style Beam Charge Monitors

Current monitoring is done using cylindrical (“pillbox”) cavities resonant in the  $TM_{010}$  mode at the frequency of 1.497 GHz. (Figure 61) Beam electrons entering the cavity encounter an electric field which slows them down infinitesimally, extracting power from the beam and storing it temporarily in the cavity. While half the RF power goes into heating the cavity walls, the other half is extracted magnetically by a loop antenna and sent to the processing electronics by RF cable. Hall C normally operates its BCM’s at a loaded  $Q$  of  $\sim 500$  for ease of tuning and long term stability. At this  $Q$  the cavity time constant is only  $\tau = Q/\omega = 53$  nsec, so processing electronics will determine the bandwidth. The BCM’s in Hall C are normally calibrated absolutely with respect to the Unser monitor, which is itself cross-calibrated to an absolute current source which runs through the Unser monitor by a wire. Absolute charge normalization is only needed in  $Q_{Weak}^p$  to determine the luminosity. A *linear*, low noise charge monitor is essential for the asymmetry measurements.

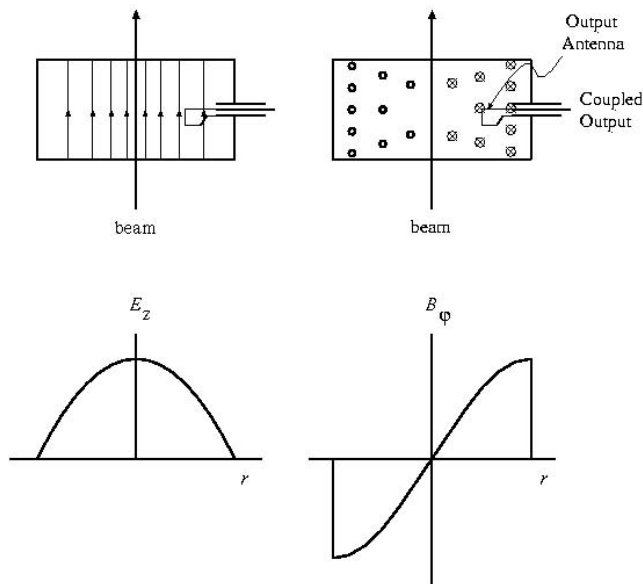


Figure 61: Schematic of the electric and magnetic fields in a cavity charge monitor.[64].

The position dependence of the cavity charge monitors is generally ignored in cross section measurements, since the electric field near the center of the cavity is quite flat, being described (for the ideal case with no apertures in the cavity) by the Bessel function

$$E_Z \propto J_0(\chi_{01} \frac{\rho}{R})$$

with cavity radius  $R = 7.6$  cm. With such a relatively large cavity radius, excursions of 2 mm from the axis only decrease the calculated beam current by 0.1%.<sup>[65]</sup> However, the error is increasing quadratically with the excursion, and at 2 mm displacement already produces a cross-correlation between the charge asymmetry  $\Delta Q$  and the position asymmetry  $\Delta X$  at the level of 1 ppm/ $\mu m$ . The input and output beam pipes presumably modify the naive Bessel function solution, and the single signal antenna too will (asymmetrically) perturb the eigenfunction. We will estimate these effects with finite element analyses, and modify the cavities if needed. Our past attempts to measure the position dependence were only able to set lower bounds of about 0.25% for several mm excursions. Fortunately, the comparison of widely separated BCM's (the Hall C BCM's and the Parity Girder BCM's) with plenty of steering elements in between, will allow us to unambiguously measure the position dependence of the downstream charge monitoring cavities.

To estimate the noise level of a BCM, we take the difference of two adjacent charge monitors with beam passing through them. The rms width of the result is  $\sqrt{2}$  times larger than the (non common-mode) noise of either cavity assuming they are identical and see the same beam. The noise in the charge measurement must be small with respect to the counting statistical error of 50 ppm (assuming 30 Hz reversal). During the G0 experiment, the noise was roughly consistent with the least count of the 1 MHz V-to-F's ( $\sim 50$  ppm) which were used to digitize the signal. To reduce this noise by at least another order of magnitude, we have decided to use 18-bit sampling ADC's for digitization.<sup>18</sup> A detailed noise analysis will also be made. In addition to switching to high resolution ADC's, we can improve the S/N by another magnitude by filtering the downconverted signal to a bandwidth as small as 10 kHz.

In order to obtain unambiguous pedestals for the charge monitors, we are investigating the possibility of using small amplitude, low-noise oscillators to bias the AC-to-DC conversion electronics into lower end of their linear regime. This will not affect the accuracy of the charge measurement, and should permit essentially instantaneous measurements of the charge monitor pedestals during every beam trip. Alternative approaches using the Unser monitor and beam, or RF of various magnitudes from a signal generator, are time-consuming and less precise.

Intermittent measurements of the isolation of the charge monitors to the reversal signal can be done during no-beam periods by increasing the strength of the oscillators mentioned above until they mimic 180  $\mu A$  beam. The highest sensitivity will require a permanent "isolation BCM" which would simply consist of an RF cable with the right ground hooked to an oscillator which mimics 180  $\mu A$  beam. The other end of the RF cable will be processed in exactly the same manner as the real beam charge monitors.

---

<sup>18</sup>Faster, 10 MHz V-to-F's are no longer commercially available. Furthermore, V-to-F's are a dead-end technology since they contribute more noise to the final result as the reversal and sampling rate are increased, whereas ADC's may contribute less.

To bound the helicity correlated beam intensity variance,  $(\sigma_I^+)^2 - (\sigma_I^-)^2$ , for frequencies above the sampling frequency, we will connect the output of a cavity charge monitor to a spectrum analyzer, acquire separate spectra for + and - helicity, normalize the two spectra at a frequency below the sampling frequency, and take the difference of the two spectra. Since the nonlinearity of the detector system (including target density changes) will be less than 1%, the bounds we have to place on  $(\sigma_I^+)^2 - (\sigma_I^-)^2$  are not very stringent. However, we have to make the measurement or in principle the experiment will not be interpretable. Since we will have to switch to direct reporting of the helicity signal in order to trigger the spectrum analyzers, these measurements can only be made intermittently.

### 10.1.2 Beam Position Monitors

#### 4-wire BPM's:

Stripline BPM's consist of 4 quarter-wave antennae ( $X^+, X^-, Y^+, Y^-$ ) oriented at 90 degrees to one another. The antennae are normally rotated 45 degrees with respect to a TRANSPORT coordinate system to minimize interference with the beam or synchrotron radiation. (Figure 62) The  $Q$  is of order 3, so the integration time constant is completely determined by the processing electronics.[66] Beam power coupled into the antennae at 1497 MHz is downconverted to a lower frequency, filtered, and converted to a DC voltage. Instrumented with Switched Electrode Electronics (SEE), these BPM's are stable, linear over large current ranges, have good S/N, and have useful bandwidths well into the 10's of kHz range. The output of SEE sample-and-hold modules is made available to experimenters for digitization.

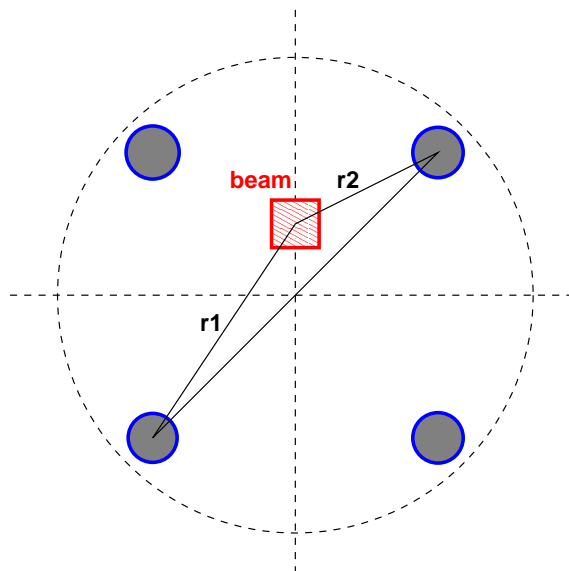


Figure 62: Schematic of a 4-wire BPM. A large, square-rastered beam is shown off the central axis of the BPM can.

Neglecting the finite length and radii of the antennae, as well as the finite size of the beam, to first order the coupling of the beam to each antenna is  $V \propto constant + r$ , where  $r$  is the distance of the beam from the BPM center.[66] Assuming the beam is at  $Y = 0$ , then  $r$  is simply  $X$ , and the beam position is therefore

$$X \propto \frac{V^+ - V^-}{V^+ + V^-}$$

which is the expression normally employed. The main advantage of the SEE concept[67] is that a single electronics chain is rapidly switched between the antenna. One can see from the above expression that gain drifts must cancel exactly leaving the beam position unaffected. Offset drifts and nonlinearities in the electronics will approximately cancel only if the beam is centered in the BPM so that the  $V^+$  and  $V^-$  signals are of comparable magnitude. The result is a beam position monitor with excellent long term stability whose calibration is set simply by geometry.

The noise of the 4-wire SEE BPM's for beam currents above  $10 \mu\text{A}$  has been measured on the bench[68] to be approximately

$$\sigma_{x,y} = \frac{3.2\mu\text{m}}{\sqrt{t}}$$

This corresponds to about  $25 \mu\text{m}$  per pulse pair at  $30 \text{ Hz}$  reversal, or  $1 \text{ nm}$  for our  $2200 \text{ hour}$  experiment. This is consistent with the experience of previous JLab parity experiments and is adequate for the  $Q_{Weak}^p$  experiment. Data in the same JLab technical note[68] also indicate that once the SEE BPM's are optimized for operation at  $180\mu\text{A}$ , the beam position should be *profoundly* insensitive to beam current (less than  $0.04 \text{ nm/ppm}$ ).

While noise and current insensitivity of the 4-wire BPM measurements at  $180 \mu\text{A}$  are very good, we are just beginning to look at more complex technical issues such as X-Y coupling and nonlinearities. For the case of off-axis beams, the above simple expression for the beam position is not exact. (Typical residuals for beam orbits are  $\pm 1 \text{ mm}$ , but can be up to  $\pm 3 \text{ mm}$  in the 3C arc in the not-infrequent case of an energy mismatch.) The resulting position errors are  $< 100 \mu\text{m}$  for excursions from the axis of less than  $5 \text{ mm}$ . However, these errors will produce X-Y correlations which could affect the accuracy of the our regressions as well as the stability of our sensitivities. We will investigate this quantitatively and will derive new expressions for beam  $X$  and  $Y$  which are free of such pathologies to the required order.

Another issue we will soon address is the question of nonlinearities. Since the coupling to the antennae is generally slightly nonlinear except near  $r = 0$ , the calculated beam position away from  $r = 0$  contains a small contribution from the rms size of the beam. This effect will be largest in front of the  $Q_{Weak}^p$  target where a  $4 \text{ mm} \times 4 \text{ mm}$  rastered beam may be up to a few mm off axis. One would like the calculated beam position to be independent of other beam parameters like beam spot size and changes in raster amplitude, both for the accuracy of the regressions and the stability of our sensitivities. It will be easy to reduce any offending nonlinearity simply by switching to M20 BPM cans which have a larger antenna spacing than standard BPM cans.

It is important to be able to measure the noise of each beam monitor in place. Position errors can be estimated if there are three identical BPM's in a drift region. If a line is drawn between any two of them, then the residual of the third to that line is a measure of the position noise. If

there are only two closely-spaced BPM's (such as our case with the two cavity position monitors on the parity girder), then we can estimate the noise from the position monitors by taking the difference of the positions. However, the latter result must be interpreted cautiously since the beam phase space in  $XX'$  is not generally identical at the two different locations.

Intermittent tests of the isolation of all the SEE BPM's from the reversal signal can be done by turning on their internal test oscillators. These oscillators provide a signal of known magnitude which biases the electronics into a linear regime, so if any non-zero cross-talk with the injector is observed it will be easy to convert into equivalent nanometers. For higher sensitivity, longer integration times can be obtained by leaving the oscillators permanently enabled in a few "isolation BPM's".

The pedestals obtained when the beam is off are probably useless. Fortunately, pedestal errors are not as serious for 4-wire BPM's as they are for the charge monitors since the resulting nonlinearities tend to cancel when the beam is roughly centered between the antennae. One technique that has been used recently to measure meaningful BPM pedestals is to vary the beam current (as measured with a linear BCM with high S/N) at a fixed beam position, then extrapolate the BPM signals linearly to zero current. It may be possible to quickly measure accurate pedestals for the SEE BPM's by turning on their internal test oscillators and vary the magnitude of this signal. The SEE dynamic gain-scaling feature must be disabled.

Finally, most of the SEE BPM's in Hall C have been converted to the more sensitive, but lower bandwidth, Transport-style electronics for 100 nA operation with polarized targets. This is not appropriate for extended operation at 180  $\mu$ A since we lose almost a factor of two in resolution, and a factor of almost 20 in bandwidth.[69] The ability to study beam position variations up to 50 kHz with relatively little distortion could be invaluable for bounding the the helicity-correlated beam position variances,  $(\sigma_i^+)^2 - (\sigma_i^-)^2$ . For  $Q_{Weak}^p$  we would like to convert back to Linac-style electronics. Low current operation down to  $\simeq 1 \mu$ A will still be possible for Møller polarimeter measurements, etc.

### **Cavity position monitors:**

Several cavity position monitors will be available. While we assume they will be much more sensitive than the 4-wire SEE BPM's, we have little experience with them since they were not working during all of G0.

Now that we have introduced the beam diagnostics, we will talk about specific applications.

### **Energy measurement**

Hall C experiments normally use the 3C arc as a spectrometer to monitor beam energy changes, basically using position shifts at a high dispersion point 3C12 in the middle of the arc. One must take care however that changes in position and angle at the input of the arc are not confused with energy changes. From the first-order matrix equation[70] (in units of  $cm - rad$ )

$$X_i(3C12) = M_{ij}X_j(3C07) \quad (i = X, X', Y, Y', dL, \Delta p/p)$$

Using matrix elements for the "standard 3C beamline" and selecting an expression which em-

phasizes position over angle measurements

$$\Delta p/p = \frac{X(3C12) + 1.477X(3C07) - 1140X'(3C07)}{-399.3}$$

we can then derive the helicity-correlated energy difference as

$$\Delta E = \frac{E}{-399.3}(\Delta X(3C12) + 1.477\Delta X(3C07) - 1140\Delta X'(3C07))$$

In this example, the beam energy measurement requires position measurements at the middle and beginning of the arc, and an angle measurement at the entrance to the arc (all in the dispersive direction). Existing 4-wire BPM's are already at these locations. They and their alternates are listed in Table 15.

### Target position and angle

Two BPM's are needed to calculate the beam position and angle at the target. We plan to use the cavity BPM's, but SEE BPM's are available.

Table 15: Beam monitors are listed for each beam parameter whose helicity-correlated properties we need to measure. The primary monitor is listed in bold. We assume that cavity position monitors will be more sensitive than 4-wire BPM's, but they still need to be commissioned. The location comments are with respect to the cryotarget. The spot size monitors and the halo monitors don't have names yet.

Beam Parameter	Beam Monitor Name	Comment
Charge: (all $TM_{0101}$ cavities)	IBC3C18, IBC3C18A	unrastered beam (aka Hall C BCM1,2)
	<b>IBC3C20</b>	small rastered beam, far upstream
	IBC3HG0	large rastered beam, just upstream
Energy: (all SEE 4-wire BPMs)	<b>IPM3C06X, IPM3C07X</b>	beam unrastered in this region
	alt: IPM3C05X	
	<b>IPM3C12X</b> alt: IPM3C11X	beam relatively large here
Target X,X',Y,Y': (cavities)	<b>IPM3HG0AH,V</b>	large rastered beam, just upstream (requires <b>IBC3HG0</b> to calculate position)
	<b>IPM3C20AH,V</b>	small rastered beam, far upstream (requires <b>IBC3C20</b> to calculate position)
(SEE 4-wire BPMs)	IPM3HG0,G0A,G0B alt: IPM3H00A,B,C	large rastered beam, just upstream ditto

### Beam spot size

We have only recently become aware of our need to bound helicity-correlated beam spot size changes at the micron level. The most promising approach to access beam size modulation appears to be to use the interaction of a large, rastered beam with the nonlinear position dependence

of a beam position monitor. The idea is most easily explained by imagining two closely-spaced, 4-wire BPM's, one (the "linear BPM") aligned with the beam axis which has an antenna spacing four times the rastered beam size, the other (the "nonlinear BPM") offset by a few mm and with an antenna spacing only twice the rastered beam size. (Figure 63) The linear BPM will measure the mean beam position with negligible higher order corrections. The nonlinear BPM will measure the mean beam position plus aberrations due to the rms size of the beam. By taking the ratio of the two BPM's, and calculating the helicity correlated piece, one will have a measure of the helicity correlated beam spot size changes (modulo a calculable geometric factor).

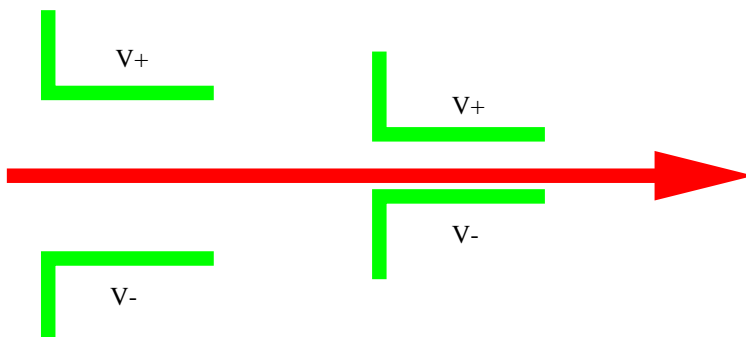


Figure 63: Schematic of two sequential 4-wire BPM's which might be used to measure (or bound) helicity-correlated beam size modulation.

Regressions would be minimized if the two BPM's were right on top of one another. This is actually possible if one uses two resonant modes in the same cavity, one with a much larger nonlinear interaction with the beam than the other. This (more difficult to explain) approach is the one we will investigate first. We are confident that such an approach will bear fruit. Indeed, once one begins to study the nonlinear effects caused by large, rastered beams, the more difficult problem appears to be how *not* to allow hypothetical beam spot size changes to affect the beam monitors.

### Halo Monitors:

Beam halo will be estimated using the main detectors (or luminosity monitors) while employing hole targets of varying diameters as well as a solid target for normalization.

## 10.2 Low Current Diagnostics

For event mode operation at 1-10 nA, tight control of helicity-correlated beam properties is not an issue. Our preliminary specifications for the low current beam are:

- stability of the beam current to  $\pm 10\%$  for stable tracking efficiencies
- reproducibility of the beam position to  $\pm 100\mu\text{m}$  of the current mode value for  $Q^2$  measurements

- reproducibility of the beam energy to  $\pm 10^{-4}$  of the current mode value for the  $Q^2$  determination
- reproducibility of the beam halo specification of  $< 10^{-6}$  for beam at such large radii that it hits the target vessel

Before tuning up Hall C for nA beam, we will first make an entry to get the detectors ready for pulsed mode data taking, leaving the HV off. Next a witness beam of several  $\mu\text{A}$  will be brought into Hall C. This beam will be visible to all the standard beam monitors. Then a luminescent beam viewer will be inserted near the Hall C target to display this several  $\mu\text{A}$  beam. After turning off the orbit locks, the beam current will be reduced 3 orders of magnitude by a combination of closing the Hall C slit and attenuating the laser light with neutral density filters. The combination of slit and filters must have a dynamic range of 5 orders of magnitude in order to operate from the nA level to 180  $\mu\text{A}$ .

Removing the viewer, measurements of the beam profile and centroid can be made using slow superharp scans using downstream phototube (rather than secondary emission) readout. Slow superharp scans can also be made in the 3C arc to check the beam energy. Beam halo measurements can be made by inserting a hole target and using the main detector (now in high gain mode) for readout. The luminescent viewer screen can be reinserted at any point to check the beam position, and if it has drifted the MCC can then resteer the beam. During this time the GEM's and other tracking detectors can be turned on and begin observations.

## 11 Polarized Source Issues for the $Q_{Weak}^p$ Experiment

The  $Q_{Weak}^p$  experiment poses reasonable challenges for the CEBAF polarized electron source. This section describes these challenges in light of developments since the submission of the original  $Q_{Weak}^p$  experiment proposal.

The  $Q_{Weak}^p$  experiment has helicity correlated beam requirements similar to those of other parity violation experiments conducted at Jefferson lab. Recent successful completion of portions of the HAPPEX and G0 experiments suggests that  $Q_{Weak}^p$  beam specifications can met with similar care and diligence. Most of the  $Q_{Weak}^p$  helicity correlated beam specifications have already been met with the exception of current asymmetry (Table 16). It is likely that continued efforts to understand the origins of helicity correlated beam asymmetries (e.g., Pockels cell, photocathode) and new feedback algorithms will help meet the  $Q_{Weak}^p$  intensity asymmetry specification.

Beam Parameter	$Q_{Weak}^p$ Specification	Achieved to date	Comments
Maximum run-averaged helicity correlated charge asymmetry	0.1 ppm	0.14 +/- 0.32 ppm	G0 Forward
		0.2 ppm	HAPPEX-II
Maximum run-averaged helicity correlated position difference	40 nm	$4 \pm 4$ nm	G0 Forward
		< 3 nm	HAPPEX-II
Maximum run-averaged helicity correlated angle difference	100 nrad	< 2 nrad	G0 Forward
		< 2 nrad	HAPPEX-II
Maximum run-averaged helicity correlated energy difference	10 ppb	10 ppb	G0 Forward
		13 ppb	HAPPEX-II
Beam Current	180 $\mu$ A	140 $\mu$ A unpolarized	Max current delivered to a single Hall Max high pol beam extracted from gun
		$\sim 220$ $\mu$ A	
Polarization	> 80%	73–78% $\sim 85\%$	Strained GaAs Superlattice GaAs

Table 16: Partial list of  $Q_{Weak}^p$  beam specifications compared with beam specifications already achieved during HAPPEX- II and G0 Forward Angle running.

The most challenging aspect of the  $Q_{Weak}^p$  experiment from a polarized source perspective is long-term delivery of high current beam with high polarization (one year of beam at 180  $\mu$ A and polarization greater than 80%). Success will require good photocathode material, a reliable Ti-Sapphire laser and long photogun operating lifetime. Gun lifetime is already adequate at CEBAF, however, it will be prudent to continue developing a load-lock gun to replace one of the baked guns at the CEBAF photoinjector. The load locked gun will allow rapid photocathode replacement. Beam from as many as 5 different photocathode samples can be quickly evaluated,

to find material that provides the highest possible beam polarization.  $Q_{Weak}^p$  also will benefit from the use of new commercial lasers and strained-superlattice GaAs photocathode material, described below.

For the  $Q_{Weak}^p$  experiment, we must extract 225  $\mu\text{A}$  from the photocathode to deliver 180  $\mu\text{A}$  to Hall C (80% injector transmission, with beam loss on emittance filter apertures A1, A2 and the chopper master slit). This corresponds to 19.4 Coulombs/day. During Fall 2000 when the  $G_E^p$  and  $G_E^n$  experiments were performed at Hall A and C respectively, a comparable amount of high polarization beam was extracted from the gun. Reliable, uninterrupted operation at 200  $\mu\text{A}$  proceeded for approximately 1 week, at which point quantum efficiency (QE) had degraded sufficiently such that continued high current beam delivery required operation from a fresh photocathode location. After running beam from 5 photocathode locations, subsequent high current operation required heating and reactivating the photocathode. This process took approximately 8 hours and completely restored the photocathode QE.

We expect similar gun operation during  $Q_{Weak}^p$  using "standard" strained-layer GaAs photocathode material. "Standard" photocathode material used at CEBAF is strained-layer GaAs from Bandwidth Semiconductor. This material provides polarization between 73% and 78% with a maximum QE of about 0.15%. It would take approximately 220 mW from the Ti-Sapphire laser to provide 180  $\mu\text{A}$  at Hall C (including losses at injector apertures). The QE and laser headroom from one photocathode location would be exhausted in 5 days.

A new type of photocathode material has recently become available - strained- superlattice GaAs from SVT Associates. This material provides polarization 85% with five times greater QE than standard strained layer GaAs. Superlattice material could provide 180  $\mu\text{A}$  beam to Hall C with only 50 mW laser power, allowing uninterrupted beam delivery from a single photocathode location for weeks.

Numerous superlattice samples have been studied at the Building 58 injector test stand. These samples have consistently provided beam polarization of around 85% with a QE as high as 1%. This material was used for the HAPPEX-II Helium experiment. Beam polarization was 86% as measured by the injector 5 MeV Mott and Hall A Compton and Møller polarimeters (Figure 64). Unfortunately, maximum QE was a factor of two lower than expected and lifetime was very poor (spot moves were required daily to provide 40  $\mu\text{A}$  to Hall A). We attribute poor lifetime to bad vacuum conditions in gun3, and not something associated with the photocathode material itself, however verification of long-lifetime operation at high current from new superlattice photocathode material remains to be seen. It is important that the source group begin using this material on a regular basis, to gain more experience and learn about potential drawbacks and limitations of this material.

There are other concerns associated with high current delivery to Hall C. The highest current delivered to a single user to date has been 140  $\mu\text{A}$ . Reliable 180  $\mu\text{A}$  beam delivery to Hall C will likely require modification of standard injector parameters, for example, laser spot size, prebuncher amplitude, RF phase adjustments of the capture, buncher and cryo unit sections. We also recommend that the combined current extracted for experiments at the other halls be kept to less than 50  $\mu\text{A}$ , to ease the burden on the photocathode and prolong operating lifetime.

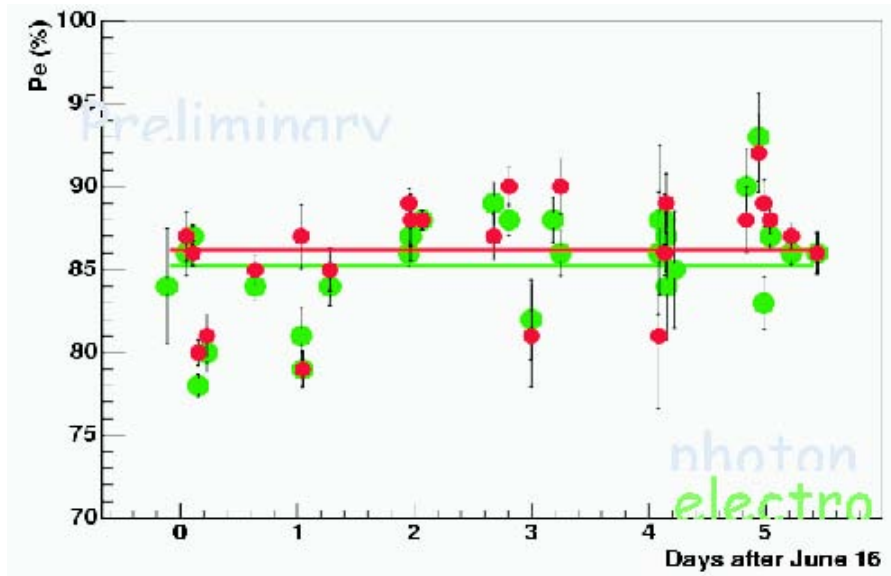


Figure 64: *Beam polarization from strained-superlattice GaAs as measured at Hall A Compton polarimeter.*

During the  $G_E^p$  and  $G_E^n$  experiments of Fall 2000 mentioned above, a homemade mode locked Ti-Sapphire laser was used. This laser suffered instability that created considerable beam noise.  $Q_{Weak}^p$  will benefit from the use of a new commercial Ti-Sapphire laser from vendor Time Bandwidth Incorporated (Figure 65). Although the two lasers (commercial and homemade) provide roughly the same output power, the commercial laser is more reliable, producing electron beam with low noise. Ti-Sapphire lasers from this vendor have been used to deliver beam to many experiments, including the parity violation experiments HAPPEX-II and g0 Forward Angle.

Finally, there are additional challenges that must be addressed including fast Pockels cell switching at  $\approx 300$  Hz. A Source Group staff member is presently constructing a fast Pockels cell switch and evaluating its performance using laser light and a photodiode. We recommended that  $Q_{Weak}^p$  staff members evaluate the performance of the new switch using a sensitive DAQ to measure rise/fall times and the stability of the Pockels cell voltage during each helicity state, similar to measurements made by the HAPPEX collaboration.

$Q_{Weak}^p$  also specifies low duty factor modes of operation. Diode laser solutions are appealing because they occupy a small footprint on the laser table; they can be quickly installed and removed. A "beat frequency" technique has been proposed, whereby a 10 MHz beam passes through the injector when a diode laser is gain switched at 489 MHz. It would be extremely helpful if  $Q_{Weak}^p$  could evaluate the quality of this beam. The "beat frequency" method would likely preclude normal beam delivery to other halls. Although more labor-intensive than diode laser solutions, the G0 laser could be installed at the photoinjector to provide a 31 MHz beam.



Figure 65: *Commercial Ti-Sapphire lasers from Time Bandwidth Inc. These lasers provide 499 MHz pulse repetition rate with low noise. The new clean room at the injector tunnel ensures that beam interruption due to laser maintenance will be minimized.*

## 12 Precision Beam Polarimetry

The  $Q_{Weak}^p$  experiment requires that the electron beam polarization be measured with an absolute uncertainty of 1%. This will be achieved using the existing Basel Møller polarimeter [87] upgraded to be able to run at higher currents in combination with a new Compton polarimeter. The Møller polarimeter is presently capable of better than 1% measurements at low currents ( $< 10 \mu\text{A}$ ). Plans are underway to enable the Møller to run and retain this precision at currents of  $100 \mu\text{A}$  or higher. While this Møller upgrade includes plans to allow the Møller to be used in a “quasi-continuous” mode, it is unlikely that this will be compatible with the feedback systems required by  $Q_{Weak}^p$  to control helicity-correlated beam properties. Hence, each Møller measurement will interrupt beam delivery to the main experiment, and must be done at discrete intervals. The Compton polarimeter will provide a continuous monitor of the beam polarization during  $Q_{Weak}^p$  data-taking. A conceptual design for the new Compton polarimeter has been completed, and the detailed design phase is beginning.

### 12.1 Basel Møller Polarimeter in Hall C

The Basel Møller polarimeter (see Fig. 66) makes use of the well-known  $\vec{e}\vec{e} \rightarrow ee$  process to measure the electron beam polarization. The design of the Hall C Møller helps reduce many systematic effects found in earlier generation polarimeters. Coincidence detection of the scattered and recoiling electrons allows suppression of the significant backgrounds from Mott scattering. The large acceptance of the Møller detectors reduces sensitivity to atomic Fermi motion effects. Finally, the most significant limiting systematic uncertainty, knowledge of the target electron polarization, has been improved by using a pure iron foil driven into saturation perpendicular to the foil plane with a 3 T superconducting solenoid. This results in electrons polarized parallel (or anti-parallel) to the electron beam direction with a polarization known to better than 0.5%.

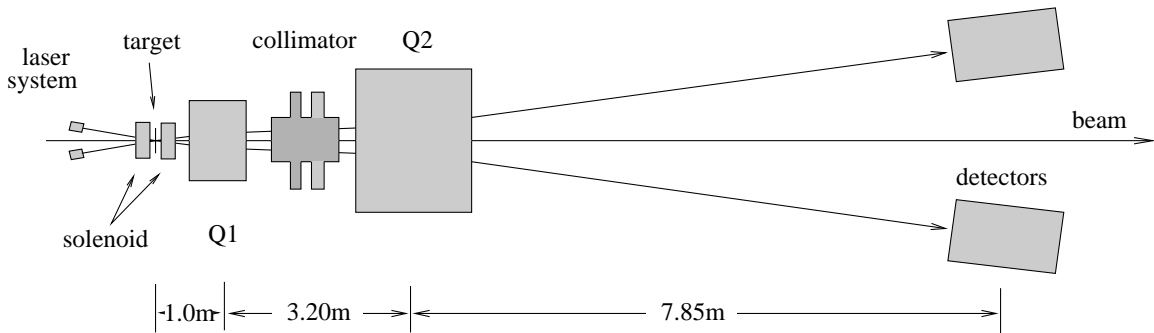


Figure 66: *Layout of the Hall C Møller polarimeter. Note especially the superconducting solenoid which is used to drive the pure iron target foil into saturation. The magnetic field and the foil are oriented perpendicular to the beam.*

Beam-heating effects result in depolarization of the iron foil, hence the Møller polarimeter is typically used at currents for which the heating effects are negligible. With no rastering of the electron beam, the Møller can be used up to  $2\ \mu\text{A}$  and with a circular raster of 2 mm diameter, can be used up to currents of  $10\ \mu\text{A}$  (see Fig. 67).

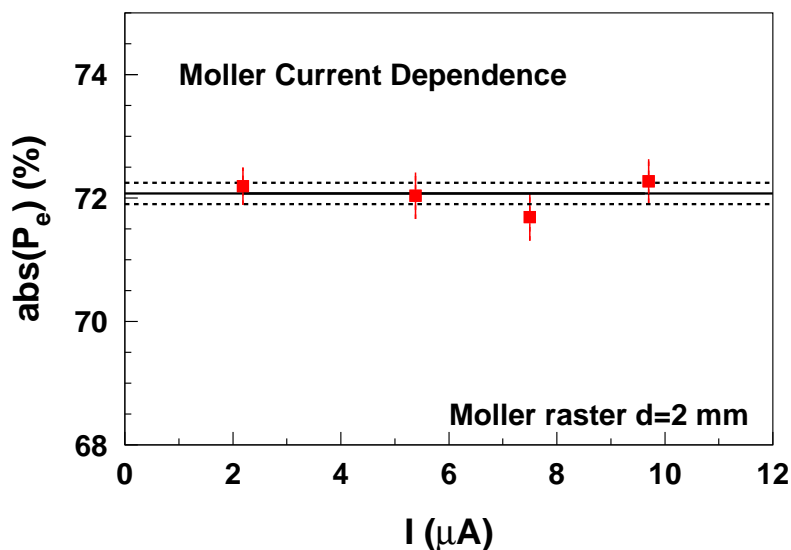


Figure 67: *Beam current dependence of polarization measurements using the Hall C Møller polarimeter. Data were taken using a  $1\ \mu\text{m}$  thick pure iron foil target at 2-10  $\mu\text{A}$ . Using a 2 mm diameter raster, there are no detectable foil depolarization effects.*

A planned upgrade of the Møller polarimeter will allow operation up to  $100\ \mu\text{A}$  or higher. The main component of this upgrade is a fast kicker system that scans the electron beam over a thin target. This kicker will move the beam on the order of 1-2 mm in 1-10  $\mu\text{s}$ . The heating effects are minimized by operating the kicker at very low duty cycle. Operating parameters for the kicker at various beam currents are shown in Table 17.

A first-generation kicker was tested in December 2003 during the second G0 engineering run. This kicker was used in combination with a set of iron “wire” targets,  $25\ \mu\text{m}$  in diameter. Results of this test are shown in Fig. 68. While the results indicate that use of such a kicker system is indeed possible, a few shortcomings were identified and will be addressed in the next generation system. In particular, the thick iron wire targets resulted in large instantaneous rates leading to significant random coincidence backgrounds. The improved design will make use of a thinner,  $1\ \mu\text{m}$  foil. This foil will either be in a “strip”, or half-target geometry that allows the kicker to scan the beam on, and then off the foil. Conservative heating calculations indicate that the existing, 20  $\mu\text{s}$  waveform kicker, operated at  $100\ \mu\text{A}$  will result in less than 1% polarization reduction of the iron foil if special care is taken to ensure that the intrinsic beam size is not too

small. With an improved, faster kicker, this current can be increased to  $\approx 200 \mu\text{A}$  and one is essentially insensitive to the intrinsic size of the electron beam.

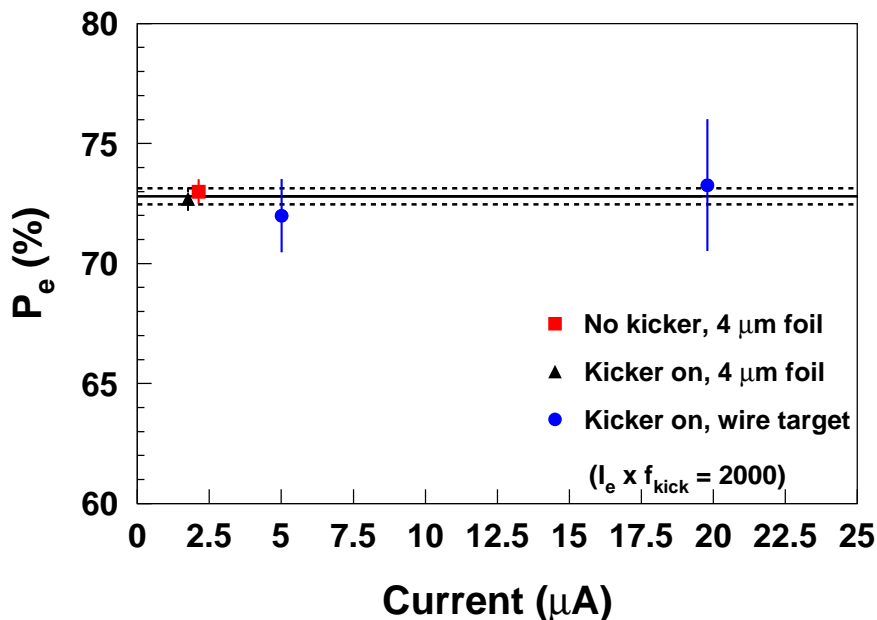


Figure 68: Results from first test run of the Hall C Møller kicker used with a  $25 \mu\text{m}$  diameter iron wire target. The kicker induced a 1 mm beam deflection at the Møller target, scanning the electron beam across the pure iron wire. Within the precision of the measurements, the kicker and iron-wire system yields results consistent with those obtained using the typical Møller running configuration.

Table 17: Operating parameters for a planned beam-kicker system that will allow operation of the Hall C Møller polarimeter at high currents.  $\Delta t_{kick}$  refers to the total interval of time for which the beam will be deflected from its nominal path onto a half-foil or strip target. In order to keep beam heating effects to a minimum, the kick interval must be shorter at higher currents.

$I_{beam}$ ( $\mu\text{A}$ )	$\Delta t_{kick}$ ( $\mu\text{s}$ )	$f_{kick}$ (Hz)
200	2	2500
100	4	2500
50	8	2500
20	20	2500

Tests of a slightly improved kicker with a new, half-foil target will be carried out either in late 2004 or early 2005. We are confident that a workable system for high-current measurements of the electron beam polarization using the Møller polarimeter will be in place within the next 1 to 1.5 years.

## 12.2 Hall C Compton Polarimeter

In large part motivated by the  $Q_{Weak}^p$  experiment, Hall C is in the process of designing and constructing a general purpose Compton polarimeter. This polarimeter will operate from 1 to 6 GeV with the capability to be rather easily upgraded to 11 GeV. Initially, this Compton polarimeter will provide an accurate relative monitor of the beam polarization, to complement the absolute precision of the Hall C Møller. It is hoped that with adequate commissioning and study, the Compton polarimeter will become capable of absolute measurements on par with the Møller.

The conceptual design of the Hall C Compton polarimeter is similar to its existing counterpart in Hall A [88]. The electron beam will interact with low-energy photons from a high-power laser system yielding Compton backscattered photons of tens of MeV. The backscattered photons as well as the scattered electrons will be detected and the resulting asymmetry from the Compton scattering process will be used to determine the electron beam polarization.

Since the backscattered photons are emitted in a narrow cone about the incident electron's direction, the photon detector must be placed on axis with the electron beam. A four-dipole chicane will be used to steer the beam to an interaction region where it will intersect the beam of the high-power laser system and then be bent back to its nominal path. This allows one to position the photon detector downstream of the interaction region with no interference from the electron beam.

The Hall C Compton polarimeter will require two dipole chicane configurations to be able to function over the full 6 GeV CEBAF energy range. A schematic of the layout as envisioned for  $Q_{Weak}^p$  is shown in Fig. 69. The beam deflection angle for each dipole is  $\theta = 10.0^\circ$  and the entrance and exit pole edge angles are  $\theta/2 = 5.0^\circ$ . The separation between dipoles D1 and D2 as well as between dipoles D3 and D4 is 2.3 m, while the separation between D2 and D3 is 2 m and the beam offset,  $D$ , is 0.57 m. The dispersion following D4 is 5.7 mm/%, so for a 1 GeV incident beam, the separation of the scattered electron corresponding to the maximum energy of the back-scattered photons is 20 mm for a green laser.

The beamline configuration can be easily accomplished using non-superconducting magnets up to an incident electron beam energy of about 2.5 GeV. At this energy, the dipoles run out of bending power and between 2.5 and 6 GeV, the middle two dipoles (D2 and D3) must be moved closer to the nominal beamline such that the beam offset is reduced to  $D=0.25$  m. At 2.5 GeV, this still allows separation of the scattered electrons and the nominal beam path (the separation increases with increasing beam energy). Finally, for the JLab 12 GeV upgrade, the beam offset can be reduced even more to 0.13 m.

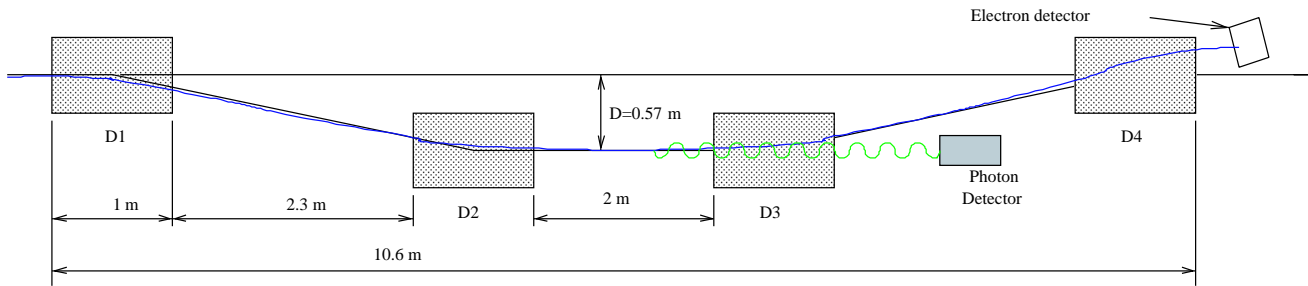


Figure 69: *Schematic diagram of the Compton polarimeter chicane.*

Since the Hall C arc was not originally designed to accommodate a Compton polarimeter, significant changes will be required to make space for the 10.6 m chicane. JLab’s CASA group has assisted this effort by providing an initial beam optics solution that will allow quasi-independent focusing at the Compton interaction point and the nominal Hall C target [89]. In this plan, the Compton dipole chicane will be inserted immediately downstream of the Hall C Møller, and two quadrupoles must be added to the Hall C beamline. Some space can be saved by using the space between the Møller legs (see Fig. 70), but it will still be necessary to move all existing beamline components downstream of the Møller closer to the Hall C pivot by about 7.5 m.

The design, construction, and installation of the Compton chicane will be a large job and will require significant involvement from the  $Q_{Weak}^p$  Collaboration, Hall C, and the Jefferson Lab Accelerator Division. Currently, the Jefferson Lab Mechanical Engineering Group is in the process of reviewing the scope of work for the project (including magnet and stand design, beamline modifications, etc.). It is hoped that detailed design work on the Compton dipoles (the longest lead item in the Compton polarimeter chicane) can begin as early as January 2005.

The Hall C Compton polarimeter will make use of a commercially available, high power pulsed green laser system. Initially, much consideration had been given to various external and internal resonating cavity designs. However, the simplicity and ease of use of an “off-the-shelf” system holds much appeal. The Coherent EVOLUTION-90 provides greater than 90 W average laser power at a repetition rate of 5-10 kHz and pulse-widths of order 200 ns [90]. At 100 W average power, a 1% (statistics) measurement can be achieved in about 1.5 hours at  $Q_{Weak}^p$  currents (180  $\mu$ A). Ideally, one would like to make measurements on a bit smaller time scale. An easy way to achieve this is to recirculate the laser after it has passed through the beam pipe, thus approximately doubling the effective luminosity.

Use of a pulsed laser means that one cannot form a counting asymmetry in the conventional sense since there will be more than one Compton backscattered photon per laser pulse. Rather, one must form an energy-weighted asymmetry. This method has been extensively employed by the HERMES Longitudinal Polarimeter at HERA [91] and has been demonstrated to work well. One significant advantage of a pulsed laser system is the corresponding reduction of backgrounds due to Bremsstrahlung from residual gas in the beam pipe. A 200 ns pulse at 5 kHz increases the signal-to-background ratio by a factor of 1000.

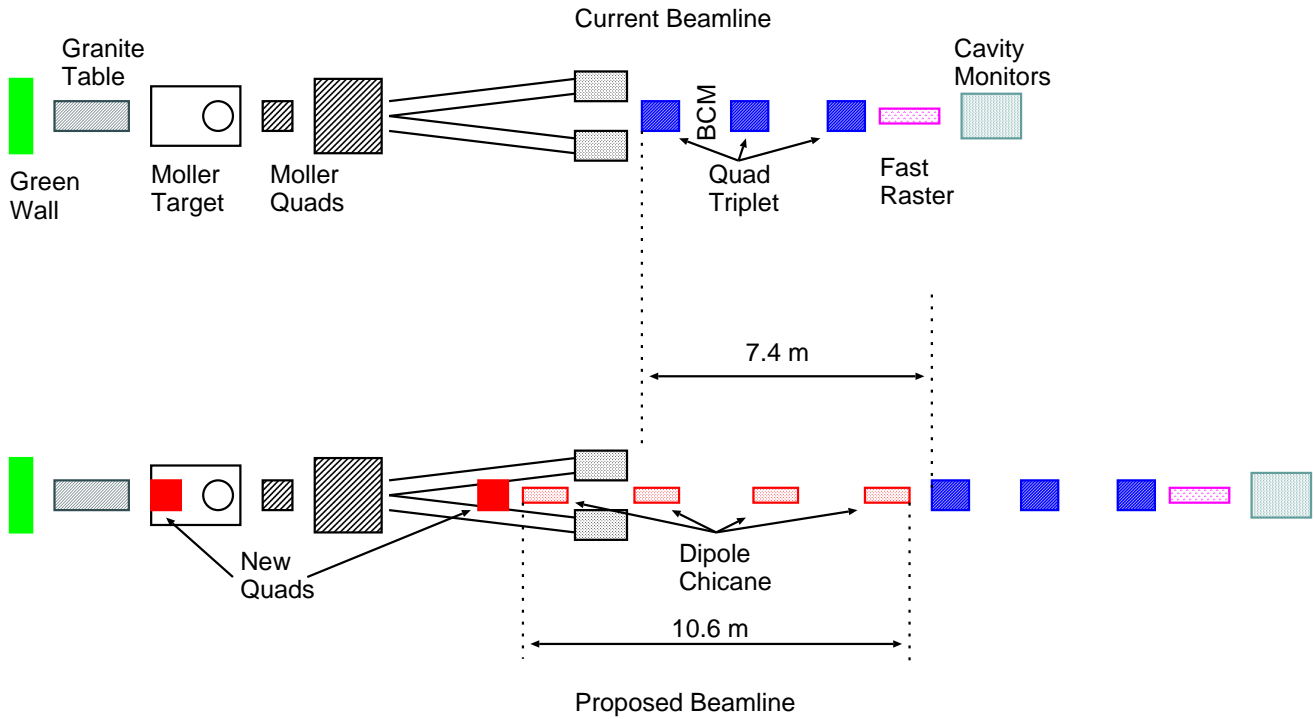


Figure 70: *Rough schematic of the Hall C beamline before (top) and after (bottom) the addition of the Compton polarimeter dipole chicane. The space between the Møller polarimeter detector legs will accommodate a new quadrupole and a narrow profile dipole. However, 7.5 m of additional space along the beamline is required for the remainder of the chicane.*

The Compton polarimeter will require a compact, fast photon detector that can survive in a high radiation environment. Since the asymmetry measurements will be energy-weighted, the absolute energy calibration is less critical than the linearity of the detector. Some non-linearity is of course acceptable, so long as the non-linearity is well characterized.  $\text{PbWO}_4$  satisfies most of the above criteria and studies using a 9 block prototype detector are underway. One potential drawback to  $\text{PbWO}_4$  is the  $2\%/^{\circ}\text{C}$  variation in light output [92], but this should be relatively easily overcome using a temperature stabilization system.

Since the scattered electron loses some energy during the Compton interaction, it will undergo a larger deflection in the Compton dipole chicane than the primary electron beam. The chicane then acts as a spectrometer, and by measuring the electrons that have been separated from the nominal beam path, one can form the Compton asymmetry using only the electrons. As noted above, there will be several Compton events per laser pulse, and since electron calorimetry is not practical given the space considerations, one will need a finely segmented detector that will be able to handle high multiplicity events. One of the options being considered is a ribbon of scintillating fibers oriented in a plane perpendicular to the beam direction, although lack of radiation hardness is a potential problem. Another potential solution is the use silicon microstrips as is used in Hall A.

The Hall C Compton Polarimeter Working Group consists of collaborators from Jefferson Lab, MIT, the University of Connecticut, and the Yerevan Physics Institute. The MIT group is actively involved in the Mainz A4 Compton polarimeter and has been extremely active in the Hall C Compton dipole chicane design. The Yerevan group is pursuing studies involving the potential  $\text{PbWO}_4$  photon detector, while collaborators from Jefferson Lab and Connecticut have been extensively involved in studies relevant to the choice of laser for the Compton polarimeter.

## 13 Data Acquisition

The  $Q_{Weak}^p$  experiment requires two distinct modes of data acquisition: the current mode measurement of the quartz bar signals, and the low current tracking mode measurements in which individual particles will trigger the DAQ. These two DAQ schemes will be implemented as two essentially independent systems with separate crates and DAQ/analysis software with some sharing of beamline instrumentation electronics.

### 13.1 Current mode DAQ

The experimental asymmetry measurements will be made with the Current mode data acquisition. The core of this system is the readout of the TRIUMF ADC modules, described in section 5. These ADC modules integrate the current from each quartz bar photomultiplier tube. The integrated signals can be made available for readout at the helicity reversal rate, or at a multiple of this rate. It is expected that the normal scheme will be to oversample the 250 Hz helicity reversal by reading out the ADCs at 1000 Hz. The DAQ will have the option to readout at the reversal rate, or with higher oversampling for rates above a kilohertz.

In addition to digitizing the current from the quartz bar PMTs and several shielded background detectors, the same type of ADC will be used to digitize beam line information which will be read at the same rate as the main detector data. This beam line information will include a charge cavity, BPMs and Luminosity monitors. The ADCs for these signals will be located in a separate crate so that any small helicity correlations in beam parameter signals will not be present in the same crate as the detector ADCs.

The rate and volume of data for current mode acquisition is modest compared to typical DAQ and analysis capabilities. Assuming a 32 bit data word per ADC channel, 64 total ADC channels (both detector and beamline), and a 50% overhead for headers, an event size of 384 bytes is estimated. With a readout rate of 1000 Hz, the  $Q_{weak}$  data rate is about 500 kBytes/second, so the DAQ can easily operate with 0% downtime. At this rate, a 2200 hour run would produce a data set of less than 4 TB. Scaling G0 analysis rates, an analysis on this data set using a single fast CPU would take less than a month.

### 13.2 Low current tracking DAQ

The  $Q_{Weak}^p$  apparatus will be partially instrumented with tracking detectors as described in section 6, in order to study optics and acceptance. Measurements with the tracking system will be done at low beam current, so that individual particles can be tracked through the magnet. For this mode of measurement, the quartz bar photomultiplier tubes will be instrumented with parallel electronics so that the timing and amplitude of individual particles can be recorded.

The tracking data acquisition will operate like a conventional DAQ, triggering on individual particles. The front end electronics will be all VME, using the JLAB F1TDC for wire chambers

and timing signals, and commercial VME ADC modules for the GEM detectors and PMT amplitudes. As the hardware needed for tracking measurements is different from the current mode hardware, the tracking DAQ can be operated as a distinct system, allowing development of the two DAQ modes to proceed in parallel. The tracking DAQ will have the option of reading beam line information from the same VME crate used for this purpose in the current mode DAQ.

### **13.3 Beam Feedback**

A real-time analysis, similar to that used for G0, is planned. In addition to providing prompt diagnostic information, this analysis will calculate helicity correlated beam properties such as current, position and energy. The results of these calculations can be used for feedback on the beam.

## 14 Beam Request

At this time we request approval for a first run of 35 days. The goal of the first run will be to check out the  $Q_{Weak}^p$  apparatus and calibration tracking system, carry out systematic studies, check out of the polarized source and associated feedback systems, make an 8% (combined statistical and systematic errors) measurement of the proton's weak charge, and obtain a total uncertainty on an extracted  $\sin^2 \theta_W$  comparable to the SLAC E-158 PV Møller scattering measurement.

It would be ideal if the first run were preceded by facility development periods where, for example, 2.4 kW cooling power could be delivered to the target, followed by a later full power test of the target with beam. Parasitic and dedicated-user studies of the beam and various monitors will also precede the first run.

We also request conditional approval of an additional 108 days (2,592 hours) under the provision that we demonstrate during the first run the technical feasibility to successfully perform a 4% (combined statistical and systematic errors) measurement of  $Q_{Weak}^p$  with the long production run. Our beam request is summarized in tables 18 and 19.

In the tables, 'Production' refers purely to running on a  $LH_2$  target. Allowable overhead includes time for background measurements,  $Q^2$  calibrations, beam polarization measurements, systematic checks, and the configuration changes needed to accomplish these. We assume that time needed to optimize  $P^2I$  in the injector will come out of the factor of 2 in scheduled days versus PAC days (*i.e.*, it is unallowed overhead).

The time for Run I has been increased from the previous PAC request. This takes into account lessons about systematics and backgrounds from G0 (the first parity experiment to run in Hall C), and allows for commissioning our extensive new tracking hardware, mini-torus, and the Hall C beamline at the extremely low beam currents needed to operate the tracking detectors at high efficiency. None of this hardware, for which the collaboration has received approximately 1M\$ in funding, was in the original proposal. The additional days requested for Run I is 12.

For Run II we have assumed 2200 hours of production, minimal time for re-commissioning (3 days), and that better optimized background measurements will go much more quickly the second time around. We are asking for conditional approval.

Table 18: *Itemized beam request for Run I.*

Category	Time	Comment
<b>Production:</b>	14 days	$e + p$ elastic on $LH_2$ only
<b>Overhead:</b>		
configuration changes	1 day	spread over 5 weeks
Al window background	2 days	
Inelastic background	1 day	
soft background	1 day	
polarimetry	1 day	spread over 5 weekly measurements
$Q^2$ measurement	1 day	
systematics	2 days	$I_{beam}$ dependence, etc.
overhead subtotal	9 days	
<b>Commissioning:</b>		
high power cryotarget, QTOR, main detectors, lumi, and neutral axis	5 days	
Region I, II, III tracking, 1-5 nA beam and diagnostics, and mini-torus setting	7 days	
commissioning subtotal	12 days	
<b>Total Run I:</b>	<b>35 days</b>	requesting reapproval of 23 days + 12 additional days

Table 19: *Itemized beam request for Run II.*

Category	Time	Comment
<b>Production:</b>	91.7 days (2200 hours)	$e + p$ elastic on $LH_2$ only
<b>Overhead:</b>		
configuration changes	3 days	spread over 15 weeks
Al window background	1 day	
Inelastic background	0.5 day	
soft background	0.5 day	
polarimetry	3 days	spread over 15 weekly measurements
$Q^2$ measurement	3 days	assuming 3 gradient changes
systematics	2 days	$I_{beam}$ dependence, etc.
overhead subtotal	13 days	
<b>Re-Commissioning:</b>		
high power cryotarget, QTOR, main detectors, lumi, and neutral axis		
Region I, II, III tracking, 1-5 nA beam and diagnostics, and mini-torus setting	3 days	
<b>Total Run II:</b>	<b>108 days</b>	requesting conditional approval for 108 days

## 15 Collaboration and Management Issues

The  $Q_{Weak}^p$  collaboration presently consists of 63 individuals from 18 institutions. The collaboration list is kept at the experiment's web page, at <http://www.jlab.org/qweak>. Quarterly progress reports are also posted at the  $Q_{Weak}^p$  web site. The  $Q_{Weak}^p$  collaboration meets as a group three or four times a year.

A Cost and Technical Design Review of the  $Q_{Weak}^p$  experiment was held at Jefferson Lab on January 27–28, 2003. The review committee was chaired by David Cassel (Cornell Univ.). The committee members were Jian-Ping Chen (JLab), Krishna Kumar (Univ. of Massachusetts), Bill Schneider (JLab), Charlie Sinclair (Cornell Univ.), Jean-Michel Poutissou (TRIUMF), and Chris Tschalaer (MIT - Bates). The committee produced a detailed, 15 page report which critically examined all facets of the experiment. The full report is available at the  $Q_{Weak}^p$  web site. Here, for brevity, we simply quote the primary conclusions from the Executive Summary of the committee's report:

*The primary conclusions of the committee are:*

- *The committee concurs that the results of the proposed  $Q_{Weak}^p$  experiment will be an outstanding contribution to physics, with the possibility of discovering evidence for physics beyond the Standard Model.*
- *The experiment is very challenging, but with proper attention to detail it should be possible to reach the proposed level of precision.*
- *However, achieving this level will require substantial coordinated R&D effort from the Collaboration and JLab.*
- *The committee recommends that the Collaboration and JLab aggressively pursue timely funding for the experiment.*

Also available on the  $Q_{Weak}^p$  web site is the “input document” prepared by the collaboration for the Cost & Technical Design Review committee. This document, titled the  $Q_{Weak}^p$  *Technical Design Report* (TDR), provides a more detailed description of the experiment than is provided in this proposal. However, the TDR was written two years ago, in January, 2003; we anticipate that an updated TDR will be prepared in 2005.

The  $Q_{Weak}^p$  experiment operates as a managed project. A Project Management Plan dated June 28, 2004 is in place and defines our interaction with the DOE. In addition, the management plan describes the management organization, the cost, schedule, and performance requirements and controls, contingency plans, and reporting. The individual Work Packages of the experiment are described there along with their detailed cost and schedule breakdowns.

All the necessary funding for the project has been secured.  $Q_{Weak}^p$  is supported by the US DOE through Jefferson Lab (\$1.91M), the US NSF through a MRI (\$590k) which has University matching funds (\$452k) associated with it, and the Canadian NSERC (~\$315k). Including a

small additional NSF grant (\$50k), the total budget for the experiment is \$3.316M. The project aims to begin installation in Hall C at Jefferson Lab in the fall of 2007.

Besides the Spokespersons, and the Work Package Leaders referred to below, the collaboration has a Principal Investigator, a Project Manager, and an Institutional Council. The Institutional Council consists of representatives from each of the major institutions of the collaboration.

The work of the  $Q_{Weak}^p$  project has been broken down according to a Work Breakdown Structure described in the  $Q_{Weak}^p$  Project Management Plan. Each major WBS line item has a Work Package Leader associated with it. The Work Package Leaders for the main WBS categories of the  $Q_{Weak}^p$  experiment are listed in Table 20.

Work Package ID	Work Package Title	Work Package Leader	Institute
WP1	Detector System	Dave Mack	JLab
WP1.1	Detector Design	Dave Bowman	LANL
WP1.2	Detector Bars	Dave Mack	JLab
WP1.3	Detector Electronics	Larry Lee & Des Ramsay	TRIUMF/UMan
WP1.4	Detector Support	Allena Opper	OhioU
WP2	Target System	Greg Smith	JLab
WP3	Experiment Simulation	Neven Simicevic	LaTech
WP4	Magnet	Stan Kowalski	MIT/Bates
WP5	Tracking System	Dave Armstrong	W&M
WP5.1	WC1–GEMs	Tony Forest	LaTech
WP5.2	WC2–HDCs	Mark Pitt	VPI
WP5.3	WC3–VDCs	J. Mike Finn	W&M
WP5.4	Trigger Counters	Allena Opper	OhioU
WP6	Infrastructure	Roger Carlini	JLab
WP7	Magnet Fabrication	Wim van Oers	TRIUMF/UMan
WP8	Luminosity Monitor	Mark Pitt	VPI

Table 20: *Work Breakdown Structure and Work Package Leaders of the  $Q_{Weak}^p$  experiment.*

## References

- [1] S.C. Bennett and C.E. Wieman, Phys. Rev. Lett. **82**, 2484, (1999); C.S. Wood *et al.*, Science **275**, 1759 (1997).
- [2] NuTeV Collaboration: G. P. Zeller *et al.* “Precise Determination of Electroweak Parameters in Neutrino-Nucleon Scattering”, Phys. Rev. Lett. **88**, 091802 (2002)
- [3] P.L. Anthony *et al.*, “Observation of Parity Nonconservation in Møller Scattering”, Phys. Rev. Lett **92**, 181602-6, (2004)
- [4] C.Y. Prescott *et al.*, Phys. Lett. **B77**, 347 (1978).
- [5] C.Y. Prescott *et al.*, Phys. Lett. **B84**, 524 (1979).
- [6] J. Erler, A. Kurylov, and M.J. Ramsey-Musolf, “Weak Charge of the Proton and New Physics”, Phys. Rev. **D 68**, 016006 (2003)
- [7] J. Erler and M. J. Ramsey-Musolf, “The weak mixing angle at low energies,” arXiv:hep-ph/0409169.
- [8] For a review, see I. Hinchcliffe, Eur. Phys. J. **C 15**, 85 (2000)
- [9] TOPAZ Collaboration: I. Levine *et al.* Phys. Rev. Lett. **78**, 424 (1997);  
VENUS Collaboration: S. Odaka *et al.* Phys. Rev. Lett. **81**, 2428 (1998);  
OPAL Collaboration: G. Abbiendi *et al.* Eur. Phys. J. C **13**, 553 (2000);  
L3 Collaboration: M. Acciarri *et al.* Phys. Lett. B **476**, 40 (2000).
- [10] D.B. Leinweber *et al.* “Precise Determination of the Strangeness Magnetic Moment of the Nucleon”, preprint: hep-lat/0406002
- [11] D.H. Beck and B.R. Holstein, “Nucleon Structure and Parity Violating Electron Scattering”, Int. J. Mod.Phys. **E10**, 1-41, (2001)
- [12] M. J. Musolf *et al.*, Phys. Rep. **239**, 1 (1994).
- [13] S. Eidelman *et al.* “The Review of Particle Physics”, Phys. Lett. **B592**, 1 (2004)
- [14] P.A. Souder *et al.*, PRL **65**, 694-697 (1990).
- [15] M. J. Ramsey-Musolf, Phys. Rev. C **60**, 015501 (1999)
- [16] M. Cvetič and P. Langacker, “Z’ physics and supersymmetry,” e-print hep-ph/9707451, published in “Perspectives in Supersymmetry”, World Scientific, 1998
- [17] J. E. Kim and H. P. Nilles, Phys. Lett. B **138**, 150 (1984).
- [18] J. Erler, Nucl. Phys. B **586**, 73 (2000).

- [19] CDF Collaboration: F. Abe *et al.* Phys. Rev. Lett. **79**, 2192 (1997).
- [20] CDF Collaboration: T. Affolder *et al.* Phys. Rev. Lett. **87**, 141802 (2001).
- [21] The LEP Collaborations ALEPH, DELPHI, L3, OPAL, the LEP Electroweak Working Group and the SLD Heavy Flavour and Electroweak Groups: D. Abbaneo *et al.*, preprint CERN-EP-2001-021, hep-ex/0212036
- [22] P. Langacker and M. Luo, Phys. Rev. D **45**, 278 (1992).
- [23] A. Kurylov and M. J. Ramsey-Musolf, “Charged current universality in the MSSM,” Phys. Rev. Lett. **88**, 071804 (2002)
- [24] M. J. Ramsey-Musolf, Phys. Rev. D **62**, 056009 (2000)
- [25] W. Buchmuller, R. Ruckl and D. Wyler, Phys. Lett. B **191**, 442 (1987) [Erratum-ibid. B **448**, 320 (1987)].
- [26] J.L. Hewett and T.G. Rizzo, Phys. Rev. **D56**, 5709 (1997).
- [27] V. Barger and K. Cheung, Phys. Lett. **B480**, 149 (2000).
- [28] K. Cheung, Phys. Lett. **B517**, 167 (2001).
- [29] ‘Operational Experience with the DIRC Detector,’ SLAC-PUB-9088, I. Adam, *et al.*, IEEE Trans. Nucl. Sci. 49:1071-1076, 2002.  
‘Optical Properties of the DIRC Fused Silica Čerenkov Radiator,’ J. Cohen-Tanugi, *et al.*, ICFA Instrum. Bull. 21:20-44, 2001.  
And references contained therein.
- [30] ‘Design of a Čerenkov Counter for the  $Q_{Weak}^p$  Experiment II,’ Simicevic, N., LATECH-CAPS-02-06a, 6/13/2002.
- [31] “Understanding Photomultipliers”, Electron Tubes Inc., <http://www.electrontubes.com>
- [32] Hamamatsu PMT Handbook, available from <http://usa.hamamatsu.com/>. (Hamamatsu Corporation, 360 Foothill Rd, Bridgewater, NJ 08807.)
- [33] Qweak Technical Report: “Non-linearity Specification for the Qweak Detector Chain”, 17pp, D.J. Mack, September 8, 2004.
- [34] K.A. Aniol *et al.*, Phys. Rev. Lett. **82**, 1096 (1999); Phys. Rev. Lett. B **509**, 211 (2001).
- [35] M.J. Musolf *et al.*, Physics Reports **239**, 1 (1994).
- [36] J.M. Finn *Monte Carlo Analysis of HAPPEX Systematic Errors*, HAPPEX Collaboration internal report, Version 2, Aug. 22, 1998 (unpublished).

- [37] COMPASS Experiment (COMmon Muon and Proton Apparatus for Structure and Spectroscopy: NA 58) CERN/SPSLC 96-14(1996); M. Lamanna, Nucl. Phys. A **711**, 50 (2002); [wwwcompass.cern.ch](http://wwwcompass.cern.ch).
- [38] C. Altunbas, M. Capans, K. Dehmelt, J. Ehlers, J. Friedrich, I. Konorov, A. Gandi, S. Kappler, B. Ketzer, R. De Oliveira, S. Paul A. Placcib, L. Ropelewski, F. Sauli, F. Simon and M. van Stenis Nucl. Instrum. Meth. A **490**, 177 (2002).
- [39] A.Oed, Nucl. Instrum. Methods A **263** (1988) 351.
- [40] <http://gdd.web.cern.ch/GDD>
- [41] Model TCL 2530, TRUMPF Inc.,111 Hyde Rd , Farmington, CT 06032 ,Phone- (860) 255-6000, Fax- (860) 678-1704
- [42] Helix 128 or beetle chip, ASIC laboratories, Heidelberg, <http://wwwasic.kip.uni-heidelberg.de/~trunk/projects/Helix>
- [43] J.T. Brack *et al.*, Nucl. Instrum. Methods A **469**, 47 2001.
- [44] K. Fissum, W. Bertozzi, J. P. Chen, D. Dale, H. C. Fenker, J. Gao, A. Gavalya, S. Gilad, C. R. Leathers, N. Liyanage, R. O. Michaels, E. A. J. M. Offermann, J. Segal, J. A. Templon, R. Wechsler, B. Wojtsekhowski J. Zhao, Nucl. Instrum. Methods A **474**, 108 (2001).
- [45] Garfield: [garfield.web.cern.ch/garfield/](http://garfield.web.cern.ch/garfield/)
- [46] MAD chip: IEEE Trans. Nucl. Sci.: 47 (2000) 791; <http://www.pd.infn.it/cms/DTFB/electronics/frontend/homepage.html>
- [47] E.S. Smith *et al.*, NIM A **432**, 265 (1999).
- [48] D.S. Armstrong, B. Moffit, and R. Suleiman, JLab technical note JLAB-TN-03-017 (2003)
- [49] E.Beise, G. Cardell & R. Carr, “The SAMPLE Liquid Hydrogen Target Users’ Guide”, Kellogg Radiation Lab, CalTech, Mar. 23, 1999
- [50] S.Ecklund, C. Field, G. Mazaheri, NIM **463**, (2001) 68.
- [51] <http://www.anomet.com/mirfuture.html>
- [52] N. Simicevic, LaTech Technical Report LATECH-CAPS-01-03a, 2001. (<http://www.jlab.org/qweak/>)
- [53] N. Simicevic, LaTech Technical Report LATECH-CAPS-02-06a, 2002. (<http://www.jlab.org/qweak/>)
- [54] D. Mack, 2002 (<http://www.jlab.org/qweak/>)
- [55] N. Simicevic, LaTech Technical Report LATECH-CAPS-04-07a, 2004. (<http://www.jlab.org/qweak/>)

- [56] M. Pitt, Qweak technical report.
- [http://www.phys.vt.edu/~pitt/qweak/aluminum\\_report/report.ps](http://www.phys.vt.edu/~pitt/qweak/aluminum_report/report.ps)
- [57] E. Hadjimichael, G.I. Poulis, T.W. Donnelly, Phys. Rev. C **45**, 2666 (1992)
- [58] H.-W. Hammer and D. Drechsel, Zeit. Physik A **353**, (1995) 321-331.
- [59] ‘Operational Experience with the DIRC Detector,’ SLAC-PUB-9088, I. Adam, *et al.*, IEEE Trans. Nucl. Sci. 49:1071-1076, 2002.
- ‘Optical Properties of the DIRC Fused Silica Čerenkov Radiator,’ J. Cohen-Tanugi, *et al.*, ICFA Instrum. Bull. 21:20-44, 2001.
- And references contained therein.
- [60] ‘Design of a Čerenkov Counter for the  $Q_{Weak}^p$  Experiment II,’ Simicevic, N., LATECH-CAPS-02-06a, 6/13/2002.
- [61] “Understanding Photomultipliers”, Electron Tubes Inc., <http://www.electrontubes.com>
- [62] Hamamatsu PMT Handbook, available from <http://usa.hamamatsu.com/>. (Hamamatsu Corporation, 360 Foothill Rd, Bridgewater, NJ 08807.)
- [63] Qweak Technical Report: “Non-linearity Specification for the Qweak Detector Chain”, 17pp, D.J. Mack, September 8, 2004.
- [64] C.S. Armstrong, “Beam Current Measurement in Hall C”, Hall C Technical Note, July 29, 1996, unpublished.
- [65] G. Niculescu, from Figure 4 in “Resonant Cavities Used as Beam Current Monitors”, Hall C Technical Note, unpublished.
- [66] W. Barry, “A General Analysis of Thin Wire Pickups for High Frequency Beam Position Monitors”, CEBAF Technical Note.
- [67] T. Powers *et al.*, “Design, Commissioning and Operational Results of a Wide Dynamic Range BPM with Switched Electrode Electronics”, CEBAF Technical Note, 1996, unpublished.
- [68] *ibid*, Figure 3b.
- [69] T. Powers, “Tradeoffs between Linac Style and Transport Line Style SEE BPM Electronics for the Hall A Line”, 8/13/98, personal communication.
- [70] Y.C. Chao, private communication.
- [71] K.A. Aniol, *et al.*, Phys. Lett. B **509**, (2001) 211.
- [72] TJNAF experiment E-99-115 (K.S. Kumar and D. Lhullier, spokespersons)

- [73] TJNAF experiment E-00-006 (D.H. Beck, spokesperson)
- [74] F.E. Maas, *et al.*, Phys. Rev. Lett. **93**, (2004) 022002.
- [75] F.E. Maas, *et al.*, see proceedings at <http://lpscwww.in2p3.fr/congres/pavi2004/>
- [76] A. Silva, *et al.*, see proceedings at <http://lpscwww.in2p3.fr/congres/pavi2004/>
- [77] T.R. Hemmert, *et al.*, Phys. Rev. C **60**, (1999) 045501.
- [78] M.J. Musolf and B.R. Holstein, Phys. Lett. B **242**, (1990) 461.
- [79] S-L. Zhu, *et al.*, Phys. Rev. D **62**, (2000) 033008.
- [80] D.T. Spayde, *et al.*, Phys. Lett. B **58**, (2004) 79.
- [81] T. Ito *et al.*, Phys. Rev. Lett. **92**, (2004) 102003.
- [82] TJNAF experiment E-01-116 (D.H. Beck, spokesperson)
- [83] N.F. Mott, Proc. R. Soc. London, Ser. A **135**, (1932) 429.
- [84] S.P. Wells, *et al.*, Phys. Rev. C **63**, (2001) 064001.
- [85] F.E. Maas, *et al.*, nucl-ex/0410013.
- [86] B. Pasquini and M. Vanderhaeghen, hep-ph/0405303.
- [87] M. Hauger *et al.*, Nucl. Instrum. Meth. A **462**, 382 (2001).
- [88] M. Baylac *et al.*, Phys. Lett. B **539**, 8 (2002).
- [89] A. Bogacz, presentation to the Hall C Compton Polarimeter Working Group, Feb. 2003.
- [90] Coherent Evolution data sheet. Available at <http://www.coherent.com/Lasers/>.
- [91] M. Beckmann *et al.*, Nucl. Instrum. Meth. A **479**, 334 (2002).
- [92] D. Neyret *et al.*, Nucl. Instrum. Meth. A **443**, 231 (2000).

# A Miscellaneous Administrative Limits

## A.1 Beam Dump Current Density Limit

JLab imposes a beam current limit of  $12 \mu\text{A}/\text{cm}^2$  at the face of the beam dump for all experiments (the ‘‘Sinclair limit’’). In order to check whether this limit would interfere with the  $180 \mu\text{A}$  beam current we propose to use, we consider the effects of multiple scattering in some of the beam-line elements. The rms multiple scattering angle encountered by a beam of momentum  $p$  after traversing a thickness  $x$  of material characterized by a radiation length  $X_0$  is  $\theta_0 = \frac{13.6 \text{ MeV}}{p\beta} \sqrt{x/X_0}(1 + .038 \ln(x/X_0))$ . Over a distance  $z$  to the dump, the rms deflection in the plane of the dump corresponding to this multiple scattering angle is  $y_{plane}^{rms} = \frac{1}{\sqrt{3}}z\theta_0$ .

In our case,  $p \simeq 1 \text{ GeV}/c$  and  $\beta = 1$ . The contributions from various multiple scattering sources is summarized in Table 21. From this table we see that the  $12\mu\text{A}/\text{cm}^2$  beam dump current limit is not a problem for this experiment, even without rastering. In fact, the existing diffuser at the mid-point of the beam dumpline provides enough diffusion by itself to permit currents up to  $200\mu\text{A}$ .

Item	dx to dump z(m)	$\bar{X}_0$ cm	x cm	$\theta_0$ mrad	y mm	Individual $I_{max}$ $\mu\text{A}$	Cumulative $I_{max}$ $\mu\text{A}$
Diffuser	12.3	35.6	1’’	3.3	23.2	203	203
Dump window	24.3	8.9	0.02	0.5	7.0	18	<b>343</b>
Target windows	32	8.9	0.01’’	0.6	10.4	41	621
Helium in upstream half of dumpline	18	$5.2 \times 10^5$	1190	0.5	5.2	10	790
$LH_2$	32	866	35	2.4	44	741	3064
$2 \times 2 \text{mm}^2$ raster					$\pm 4$	8	3341

Table 21: Calculation of our beam current limits, assuming the ‘‘Sinclair current density limit’’ of  $12 \mu\text{A}/\text{cm}^2$ , a beam energy of  $\simeq 1 \text{ (GeV}/c)$ , and the expected materials in our beamline. In the worst case scenario of no raster and no target, the maximum current would be  $343 \mu\text{A}$  which is almost a factor of 2 larger than our proposed production current of  $180 \mu\text{A}$ .

## A.2 Site Boundary Dose

The JLab limit for the site boundary dose is  $10 \text{ mRem}/\text{year}$ , or 10% of the DOE limit. To put this number in perspective, natural background is approximately  $300 \text{ mRem}/\text{year}$ , hence the JLab limit is only 3% of the natural background level. It is therefore not surprising that estimation of the site boundary dose is a routine part of submitting a JLab beam scheduling request.

The proposed target radiation length (4%) and the proposed current of  $180 \mu\text{A}$  are each about a factor of two larger than the running conditions of the Madey/Kowalski  $G_E^n$  experiment which ran in Hall C in 2000-2001. Thus if there were no mitigating circumstances, the site boundary dose rate for the  $Q_{Weak}^p$  experiment could be expected to be roughly 4 times larger than than in the Madey/Kowalski experiment for roughly the same beam energy. Using site boundary data provided by the Radiation Control group [?], and attributing half the dose to simultaneous high luminosity Hall A operations, a reasonable estimate for the Madey/Kowalski experiment site boundary dose rate is 0.8 mRem per 1000 hours of floor time. Our estimated dose rate for a 2000 hour  $Q_{Weak}^p$  run, assuming twice as many hours of floor time, is therefore  $0.8 \times 4 \times 2 = 6.4$  mRem, or 64% of the JLab limit (or 2% above the natural background level).<sup>19</sup> This unrealistically assumes our experiment would take 2000 hours of beam time in a single calendar year, but provides an upper estimate. In order to stay well below the JLab limit, and to permit other high luminosity experiments to run the same year, one would like to reduce this naive dose estimate by a factor of 2.

GEANT simulations by the Radiation Control group typically show that the site boundary dose due to Hall C operations is dominated by high energy neutrons which leave the target at small vertical angles, pass through the base of the dome and earth berm, enter the atmosphere, and are subsequently downscattered to the site boundary (*ie*, skyshine). The beam dump makes a relatively small contribution. Thus, luminosity in the Hall, rather than total current, is the source term. Knowing this immediately suggests that the  $Q_{Weak}^p$  experiment will have three important mitigating conditions:

- Except for particles scattered into the solid angle of interest, the remaining forward scattered particles will encounter heavy metal collimators.
- The  $Q_{Weak}^p$  target will be located significantly downstream of the standard Hall pivot. Thus a larger fraction of the beam scattered to small angles will be captured by the beam dump line, and the neutrons which do exit the dome will do so at larger average scattering angle.
- The production target will be Hydrogen rather than Deuterium as was used in the Madey/Kowalski experiment.

If, despite these mitigating conditions, RadCon GEANT simulations of the  $Q_{Weak}^p$  experiment suggest that the basic design of the experiment still produces too large a fraction of the site boundary dose (and we emphasize that we are still talking about a very small fraction of the natural background dose), then additional skyshine shielding can be emplaced before or after the top of the collimator. For example, the addition of 5 cm of lead (the thickness of a brick) can be expected to reduce the flux of high energy neutrons by a factor of 2.

---

<sup>19</sup>This is a working estimate by our collaboration and not by the Radiation Control group. When the experiment parameters are finalized we will consult with RadCon to get a firmer estimate and discuss mitigation if necessary.

### A.3 Beam Containment Policy Current Limit

During early operations at JLab, the easiest way to implement protection for the 1 MWatt beam dumps in Hall A and C was to hardware-limit the Hall currents each to  $180 \mu\text{A}$ . For example, assuming 5-pass beam at 5.56 GeV, then  $180 \mu\text{A}$  would correspond to 1.0 MWatts. However, since the  $Q_{Weak}^p$  experiment employs a beam energy of only 1.165 GeV, the beam power dissipated in the dump will be only 210 kWatts. There is clearly no threat from our experiment to the dump due to total power dissipation, nor due to the dump window current density limit which was examined above.

In order for the  $Q_{Weak}^p$  experiment to run reliably near  $180 \mu\text{A}$ , the Hall C current limit would have to be raised slightly. Of course, if we are only permitted to receive  $170 \mu\text{A}$ , for example, the target length could be increased a few cm to keep the luminosity constant.

### A.4 Physics Division Administrative Limit

There is also a Physics Division Administrative limit of about  $120 \mu\text{A}$  which would be waived by Larry Cardman for experiments which make a sufficiently compelling physics case. This limit is put in place to simplify the routine scheduling of multiple high current, high beam energy experiments.

## Weak charge of the proton and new physics

Jens Erler,<sup>1,2,\*</sup> Andriy Kurylov,<sup>3,†</sup> and Michael J. Ramsey-Musolf<sup>2,3,4,‡</sup>

<sup>1</sup>*Instituto de Física, Universidad Nacional Autónoma de México, 04510 México D.F., Mexico*

<sup>2</sup>*Institute for Nuclear Theory, University of Washington, Seattle, Washington 98195, USA*

<sup>3</sup>*Kellogg Radiation Laboratory, California Institute of Technology, Pasadena, California 91125, USA*

<sup>4</sup>*Department of Physics, University of Connecticut, Storrs, Connecticut 06269, USA*

(Received 27 February 2003; published 17 July 2003)

We address the physics implications of a precise determination of the weak charge of the proton,  $Q_W(p)$ , from a parity violating elastic electron proton scattering experiment to be performed at the Jefferson Laboratory. We present the standard model (SM) expression for  $Q_W(p)$  including one-loop radiative corrections, and discuss in detail the theoretical uncertainties and missing higher order QCD corrections. Owing to a fortuitous cancellation, the value of  $Q_W(p)$  is suppressed in the SM, making it a unique place to look for physics beyond the SM. Examples include extra neutral gauge bosons, supersymmetry, and leptoquarks. We argue that a  $Q_W(p)$  measurement will provide an important complement to both high energy collider experiments and other low energy electroweak measurements. The anticipated experimental precision requires the knowledge of the  $O(\alpha_s)$  corrections to the pure electroweak box contributions. We compute these contributions for  $Q_W(p)$ , as well as for the weak charges of heavy elements as determined from atomic parity violation.

DOI: 10.1103/PhysRevD.68.016006

PACS number(s): 11.30.Er, 25.30.Bf, 12.15.Lk

### I. INTRODUCTION

Precision tests continue to play an essential role in elucidating the structure of the electroweak (EW) interaction [1–4]. Such tests include the complete high energy program on top of the  $Z$  resonance at the  $e^+e^-$  accelerators, the CERN  $e^+e^-$  collider LEP 1 and SLAC Linear Collider (SLC); precision measurements at LEP 2 and the Fermilab  $p\bar{p}$  collider Tevatron; and deep inelastic scattering (DIS) at the DESY  $ep$  collider HERA [5]. Recent precision measurements at lower energies, such as a determination of the muon anomalous magnetic moment  $a_\mu$  [6] and of cross sections for neutrino-nucleus DIS [7], have shown deviations from the standard model (SM) expectations and generated some excitement about possible signatures of new physics, although theoretical uncertainties from the strong interaction presently cloud the interpretation of the results [8–13].

In this paper we focus on the prospective impact of a precision low energy measurement of the weak charge of the proton,  $Q_W(p)$ , using parity violating (PV) elastic  $ep$  scattering. Such an experiment has recently been proposed [14] and approved at the Thomas Jefferson National Accelerator Facility (JLab) using the Continuous Electron Beam Accelerator Facility (CEBAF). Historically, semileptonic neutral current experiments have contributed substantially to our understanding of the EW interaction. In particular, the deep inelastic  $eD$  asymmetry measurement at SLAC [15] in the late 1970s played a crucial role in singling out the SM over its alternatives at that time, and provided first measurements of the effective PV electron-quark couplings,  $2C_{1u} - C_{1d}$  and  $2C_{2u} - C_{2d}$  (defined in Sec. IV). Subsequently, the latter

combination was determined more precisely in DIS of muons from carbon at CERN [16]. Quasielastic and elastic electron scattering, respectively, from  $^9\text{Be}$  at Mainz [17] and  $^{12}\text{C}$  at MIT-Bates [18], constrained the remaining linear combinations. More recently, measurements of the elastic  $ep$  and  $eD$  asymmetries at MIT-Bates [19] and JLab [20] have been used to derive information on the neutral weak magnetic, electric, and axial vector form factors of the proton at  $q^2 \neq 0$ , and yielded a value for  $C_{2u} - C_{2d}$  [19]. Experiments probing atomic PV (APV) provided further precise information on various linear combinations of the  $C_{1i}$  [21–23]. On the other hand, the neutral weak charge of the proton, proportional to  $2C_{1u} + C_{1d}$ , has never been measured.

In its own right,  $Q_W(p)$  is a fundamental property of the proton, being the neutral current analog of the vector coupling  $G_V$ , which enters neutron and nuclear  $\beta$  decay. While measurements of  $G_V$  provide the most precise determination of the Cabibbo-Kobayashi-Maskawa (CKM) matrix element  $V_{ud}$ , a precise determination of  $Q_W(p)$  may provide insight into the SM and its possible extensions. Because the value of the weak mixing angle  $\sin^2\theta_W$  is numerically close to 1/4,

$$Q_W(p) = 1 - 4 \sin^2\theta_W \quad (1)$$

is suppressed in the SM (see Sec. III). This suppression is characteristic for protons (and electrons) but not neutrons, and therefore it is absent in any other nucleus. As a consequence,  $Q_W(p)$  is unusually sensitive to  $\sin^2\theta_W$  and offers a unique place to extract it at low momentum transfer. Doing so will provide a test for the renormalization group evolution (RGE) of  $\sin^2\theta_W$ .

To put this statement in context, we note that the strong coupling  $\alpha_s$  is routinely subjected to analogous RGE tests, whose results provide crucial evidence that QCD is the correct theory of strong interaction. As we discuss in Sec. III, a precise measurement of  $Q_W(p)$ —along with the analogous

\*Email address: erler@fisica.unam.mx

†Email address: kurilov@krl.caltech.edu

‡Email address: mjrm@krl.caltech.edu

measurement of the weak charge of the electron,  $Q_W(e)$ , currently measured by the E-158 Collaboration at SLAC [24]—will provide this important test for the EW sector of the theory. An observed deviation of the running of  $\sin^2\theta_W$  from the SM prediction could signal the presence of new physics, whereas agreement would place new constraints on possible SM extensions. This test has taken on added interest recently in light of the  $\nu$ -nucleus DIS results obtained by the NuTeV Collaboration [7] which show a  $3\sigma$  deviation from the SM prediction. In contrast, the most recent determination of the weak charge of cesium,  $Q_W(\text{Cs})$ , obtained in an APV experiment at Boulder [23], agrees with the SM value for this quantity and confirms the predicted SM running. However, the interpretation of both the cesium and NuTeV results has been a subject of debate. For example, the extraction of  $Q_W(\text{Cs})$  from the experimental PV amplitude relies on intricate atomic structure computations [25–32], and the level of agreement with the SM has varied significantly as additional atomic structure effects have been incorporated in the calculations (see Sec. II for a discussion). Similarly, the NuTeV discrepancy may result from previously unaccounted effects in parton distribution functions [12,13]. At present, there are no other determinations of  $\sin^2\theta_W$  off the  $Z$  peak which have comparable precision.

Our discussion of the physics of  $Q_W(p)$  is organized as follows. In Sec. II, we review some general considerations of the PV  $ep$  asymmetry and how  $Q_W(p)$  is extracted from it. We argue that this will be a theoretically cleaner procedure than the current extraction of  $Q_W(\text{Cs})$  from APV. Section III gives details of the SM prediction for  $Q_W(p)$ , which provides the baseline for comparison with experiment. Section IV is devoted to the prospective model independent constraints the new  $Q_W(p)$  experiment would generate. In Secs. V and VI we analyze the sensitivity of  $Q_W(p)$  to extra neutral gauge bosons, supersymmetry (SUSY), and leptoquarks (LQs). We summarize our conclusions in Sec. VII.

## II. PARITY VIOLATING $ep$ SCATTERING AND $Q_W(p)$

The PV  $ep$  asymmetry has the simple form [33],

$$A_{LR} = \frac{\sigma_L - \sigma_R}{\sigma_L + \sigma_R} = -\frac{G_F Q^2}{4\sqrt{2}\pi\alpha} [Q_W(p) + F^p(Q^2, \theta)], \quad (2)$$

where  $G_F$  is the Fermi constant,  $Q^2$  is the momentum transfer, and  $F^p$  is a form factor. At forward angles, one has  $F^p = Q^2 B(Q^2)$ , where  $B(Q^2)$  depends on the nucleon, electromagnetic (EM), and strangeness form factors. The present program of PV  $ep$  scattering experiments—which involve measurements [19,20,34,35] of  $A_{LR}$  over a wide kinematic range—is designed to determine  $F^p$  for forward angles at  $Q^2$  values as low as  $\sim 0.1$  GeV<sup>2</sup>. The determination of  $Q_W(p)$  involves an additional  $A_{LR}$  measurement at  $Q^2 \sim 0.03$  GeV<sup>2</sup>. Such a value of  $Q^2$  is optimal for separating  $Q_W(p)$  from  $F^p$  with sufficient precision, while retaining sufficient statistics (note that  $A_{LR}$  is itself proportional to  $Q^2$ ). The E-158 experiment is being carried out at almost the same value of  $Q^2$ .

An important feature of the asymmetry in Eq. (2) is its interpretability. Current conservation implies that  $Q_W(p)$  is protected from large strong interaction corrections involving the low energy structure of the proton. As we note in Sec. III, residual strong interaction corrections involving, e.g., two boson exchange box diagrams, are suppressed at  $Q^2=0$ . Effects that depend on  $Q^2$  are included in  $F^p$  and will be constrained by the aforementioned program of experiments, thereby eliminating the need for a first principles nucleon structure calculation. Based on present and future measurements, the extrapolation of  $F^p$  to  $Q^2=0$  is expected to induce a 2% uncertainty and will thus be considered a part of the experimental error budget.<sup>1</sup>

In this respect, the extraction of  $Q_W(p)$  from  $A_{LR}$  is complementary to the recent determination of  $Q_W(\text{Cs})$  in APV. The latter relies on an advanced atomic theory calculation of the small PV  $6s \rightarrow 7s$  transition amplitude. Experimentally, the transition amplitude has been measured [23] to a relative precision of 0.35%. Subsequently, by measuring the ratio of the off-diagonal hyperfine amplitude (which is known precisely [36]) to the tensor transition polarizability [37], it was possible to determine  $Q_W(\text{Cs})$  with a combined experimental and theoretical uncertainty of 0.6%. The result differed by  $2.3\sigma$  from the SM prediction [4] for  $Q_W(\text{Cs})$ . However, updating the corrections from the Breit interaction [25–27] and to a lesser degree from the neutron distribution [25,38] reduced the difference to only  $1.0\sigma$ , seemingly removing the discrepancy. Subsequent calculations included other large and previously underestimated contributions (e.g., from QED radiative corrections), some increasing [28–30], others decreasing [31,32] the deviation. The atomic theory community now appears to agree on a 0.5% atomic structure uncertainty for  $Q_W(\text{Cs})$ , and in what follows we adopt the value

$$Q_W(\text{Cs}) = -72.69 \pm 0.48. \quad (3)$$

There is also a noteworthy but less precise determination in TI [21,22],  $Q_W(\text{TI}) = -116.6 \pm 3.7$ .

A possible strategy for circumventing atomic theory uncertainties is to measure APV for different atoms along an isotope chain. Isotope ratios  $\mathcal{R}$  are relatively insensitive to details of the atomic structure and the attendant theoretical uncertainties, making them attractive alternatives to the weak charge of a single isotope as a new physics probe. As shown in Ref. [2], any shift in  $\mathcal{R}$  from its SM value due to new physics would be dominated by the change in  $Q_W(p)$ , as the effects on  $\mathcal{R}$  of new physics corrections to the weak charge of the neutron,  $Q_W(n)$ , are suppressed. Moreover,  $\mathcal{R}$  receives important contributions from changes in the neutron distribution along the isotope chain [38–41]. At present, the corresponding nuclear structure uncertainties seem larger than needed to make  $\mathcal{R}$  a useful probe of new physics effects

<sup>1</sup>In practice, this extrapolation can be implemented using chiral perturbation theory. Present and future measurements will determine all the relevant low energy constants.

on  $Q_W(p)$ . In contrast,  $ep$  scattering will yield  $Q_W(p)$  without nuclear structure complications.

Given the suppression of  $Q_W(p)$  in the SM tree level expression (1), a 4% measurement would provide a theoretically clean probe of new physics with a sensitivity comparable to that achieved by a 0.5% total error in  $Q_W(\text{Cs})$ , but with entirely different systematical and theoretical uncertainties. Note, however, that measurements of  $A_{LR}$  and single isotope APV are complementary as they probe different combinations of the  $C_{1i}$ . For example, in contrast to the weak charges of heavy elements,  $Q_W(p)$  depends significantly on the oblique parameter  $T$ , introduced in Ref. [42].

### III. $Q_W(p)$ IN THE STANDARD MODEL

At tree level in the SM,  $Q_W(p)$  is given by Eq. (1). Including radiative corrections one can write

$$Q_W(p) = [\rho_{NC} + \Delta_e][1 - 4\sin^2\hat{\theta}_W(0) + \Delta'_e] + \square_{WW} + \square_{ZZ} + \square_{\gamma Z}. \quad (4)$$

The parameter  $\rho_{NC} = 1 + \Delta\rho$  [43] renormalizes the ratio of neutral to charged current interaction strengths at low energies, and is evaluated including higher order QCD [44–47] and EW [48–50] corrections. We also include relatively small electron vertex and external leg corrections, which are corrections to the axial-vector  $Zee$  and  $\gamma ee$  couplings, respectively [51],

$$\Delta_e = -\frac{\alpha}{2\pi}, \quad \Delta'_e = -\frac{\alpha}{3\pi}(1 - 4\hat{s}^2) \left[ \ln\left(\frac{M_Z^2}{m_e^2}\right) + \frac{1}{6} \right]. \quad (5)$$

The latter, which corresponds to the anapole moment of the electron, depends on the choice of EW gauge and is not by itself a physical observable [52]. The purely weak box contributions are given by [51,53]

$$\square_{WW} = \frac{7\hat{\alpha}}{4\pi\hat{s}^2}, \quad \square_{ZZ} = \frac{\hat{\alpha}}{4\pi\hat{s}^2\hat{c}^2} \left( \frac{9}{4} - 5\hat{s}^2 \right) (1 - 4\hat{s}^2 + 8\hat{s}^4), \quad (6)$$

where  $\hat{\alpha} \equiv \hat{\alpha}(M_Z)$  and  $\hat{s}^2 \equiv 1 - \hat{c}^2 \equiv \sin^2\hat{\theta}_W(M_Z)$  are the modified minimal subtraction ( $\overline{\text{MS}}$ ) renormalized QED coupling and the weak mixing angle at the  $Z$  scale, respectively. Numerically, the  $WW$  box amplitude generates an important 26% correction to  $Q_W(p)$ , while the  $ZZ$  box effect about 3%.

These diagrams are dominated by intermediate states having  $p^2 \sim O(M_{W,Z}^2)$ . The corresponding QCD corrections are, thus, perturbative and can be evaluated by relying on the operator product expansion (OPE). At short distances, the product of weak currents entering the hadronic side of the box graphs is equivalent to a series of local operators whose Wilson coefficients can be evaluated by matching with a free field theory calculation. Because the weak (axial) vector current is (partially) conserved, the resulting operators have no

anomalous dimensions. Consequently, the perturbative QCD (PQCD) contributions introduce no large logarithms.

In order to evaluate the  $O(\alpha_s)$  corrections to these graphs, we follow Ref. [54] where analogous corrections for neutron  $\beta$  decay are computed. For the  $WW$  box graphs, we have the amplitude

$$i\mathcal{M}_{WW} = i \left( \frac{g}{2\sqrt{2}} \right)^4 \int \frac{d^4k}{(2\pi)^4} \bar{e}(K') \gamma^\nu (1 - \gamma_5) \times k \gamma^\mu (1 - \gamma_5) e(K) T_{\mu\nu}(k) \frac{1}{k^2} \frac{1}{(k^2 - M_W^2)^2}, \quad (7)$$

where

$$T_{\mu\nu}(k) = \int d^4x e^{-ik \cdot x} \langle p' | T(J_\mu^+(0) J_\nu^-(x)) | p \rangle, \quad (8)$$

with  $J_\mu^\pm(x)$  being the charge changing weak currents. Since the loop integral is infrared finite and is dominated by intermediate states having  $k \sim M_W$ , we have dropped all dependence on  $m_e$  and the electron momenta  $K$  and  $K'$ . The error introduced by this approximation is of order  $(E_e/M_W)^2 \sim 0.02\%$  for the kinematics of the planned experiment, and is negligible for our purposes. A little algebra allows us to rewrite Eq. (7) as

$$i\mathcal{M}_{WW} = 2i \left( \frac{g}{2\sqrt{2}} \right)^4 \int \frac{d^4k}{(2\pi)^4} \bar{e}(K') [k^\nu \gamma^\mu + k^\mu \gamma^\nu - g^{\mu\nu} k] + i\epsilon^{\mu\nu\alpha\lambda} \gamma_\lambda \gamma_5 k_\alpha (1 - \gamma_5) e(K) T_{\mu\nu}(k) \frac{1}{k^2} \times \frac{1}{(k^2 - M_W^2)^2}. \quad (9)$$

The terms proportional to  $k^\mu T_{\mu\nu}$  and  $k^\nu T_{\mu\nu}$  are protected from large PQCD corrections by symmetry considerations. This feature may be seen by observing that

$$k^\nu T_{\mu\nu} = \int d^4x (i\partial^\nu e^{-ik \cdot x}) \langle p' | T(J_\mu^+(0) J_\nu^-(x)) | p \rangle = i \int d^4x e^{-ik \cdot x} \delta(x_0) \langle p' | [J_\mu^+(0), J_0^-(x)] | p \rangle - i \int d^4x e^{-ik \cdot x} \langle p' | T(J_\mu^+(0) \partial^\nu J_\nu^-(x)) | p \rangle \quad (10)$$

after integration by parts. The divergence  $\partial^\nu J_\nu^-(x)$  vanishes in the chiral limit, and in keeping with the high-momentum dominance of the integral, may be safely neglected. On the other hand, the equal time commutator gives  $-4i \langle p' | J_\mu^3(0) | p \rangle$ , where  $J_\mu^3 = \bar{q}_L \gamma_\mu \tau_3 q_L$  and  $q = (u, d)$ . Note that the commutator term results from the  $SU(2)_L \times U(1)_Y$  symmetry of the theory, so it is not affected by QCD corrections.

In contrast, terms involving  $T_\mu^\mu$  and  $\epsilon^{\mu\nu\alpha\lambda}T_{\mu\nu}$  cannot be related to equal time commutators and, thus, involve bona fide short distance operator products. In the OPE, the leading local operator appearing in  $T_\mu^\mu$  is just  $J_\mu^3$ , whereas for the antisymmetric part, one has the isoscalar current,  $J_\mu^{I=0} = \bar{q}_L \gamma_\mu q_L$ . The leading PQCD contributions to the corresponding Wilson coefficients have been worked out in Refs. [54–56]. For both  $T_\mu^\mu$  and  $\epsilon^{\mu\nu\alpha\lambda}T_{\mu\nu}$ , the correction factor is  $1 - \alpha_s(k^2)/\pi$ . Since the loop integrals are dominated by  $k^2 \sim M_W^2$ , one may approximate the impact on  $i\mathcal{M}_{WW}$  by factoring  $1 - \alpha_s(M_W^2)/\pi$  out of the corresponding parts of the integral in Eq. (9). The error associated with this approximation is of order  $\alpha_s^2$  and is devoid of any large logarithms. The resulting expression for the  $WW$  box contribution to  $Q_W(p)$  is

$$\square_{WW} = \frac{\hat{\alpha}}{4\pi\hat{s}^2} \left[ 2 + 5 \left( 1 - \frac{\alpha_s(M_W^2)}{\pi} \right) \right], \quad (11)$$

where the first term inside the square brackets arises from the equal time commutator. Numerically, the  $O(\alpha_s)$  term yields an  $\approx -3\%$  correction to  $\square_{WW}$ , for an  $\approx -0.7\%$  correction to  $Q_W(p)$ . Higher order PQCD corrections should be an order of magnitude smaller, so the error in  $Q_W(p)$  associated with truncation at  $O(\alpha_s)$  is well below the expected experimental uncertainty.

The calculation of PQCD corrections to  $\square_{ZZ}$  follows along similar lines. In this case, however, all equal time commutators vanish, so that the entire integral carries a  $1 - \alpha_s(M_Z^2)/\pi$  correction factor. The resulting shift in  $Q_W(p)$  is  $-0.1\%$ , and higher order PQCD effects are negligible. For both  $\square_{WW}$  and  $\square_{ZZ}$  contributions from lower loop momenta ( $k^2 \ll M_W^2$ ) are associated with non-perturbative QCD effects. Such contributions, however, carry explicit  $(p/M_{W,Z})^2$  suppression factors, where  $p$  is an external momentum or mass. Taking  $p \sim E_e \sim 1$  GeV implies that these non-perturbative contributions are suppressed by at least a few  $\times 10^{-4}$ , so we may safely neglect them here. A similar conclusion applies to matrix elements of higher order operators in the OPE analysis of  $T_{\mu\nu}$  given above.

As a corollary, we have also computed the analogous correction to  $Q_W(n)$ . Again, the  $ZZ$  box contribution receives an overall factor,  $1 - \alpha_s(M_Z^2)/\pi$ , while for the  $WW$  box we obtain

$$\square_{WW}^{(n)} = \frac{\hat{\alpha}}{4\pi\hat{s}^2} \left[ -2 + 4 \left( 1 - \frac{\alpha_s(M_W^2)}{\pi} \right) \right]. \quad (12)$$

Notice that the sum of Eqs. (11) and (12) is also corrected by an overall factor,  $1 - \alpha_s(M_W^2)/\pi$ , as is expected from an isoscalar combination where no equal time commutator should be involved. The resulting shifts in the SM predictions for  $Q_W(\text{Cs})$  and  $Q_W(\text{Ti})$  are  $-0.07$  and  $-0.11$ , respectively, or  $+0.1\%$ .

In contrast, the  $\gamma Z$  box contribution,

$$\square_{\gamma Z} = \frac{5\hat{\alpha}}{2\pi} (1 - 4\hat{s}^2) \left[ \ln \left( \frac{M_Z^2}{\Lambda^2} \right) + C_{\gamma Z}(\Lambda) \right], \quad (13)$$

contains some sensitivity to the low momentum regime. The scale  $\Lambda \sim O(1 \text{ GeV})$  appearing here denotes a hadronic cut-off associated with the transition between short and long distance contributions to the loop integral. The former are calculable and are dominated by the large logarithm  $\ln M_Z^2/\Lambda^2$ . At present, however, one cannot compute long distance contributions from first principles in QCD. Consequently, we parametrize them by the constant  $C_{\gamma Z}(\Lambda)$ , whose  $\Lambda$  dependence must cancel that associated with the short distance logarithm. We note that a similar situation arises in radiative corrections to  $G_V$  in neutron and nuclear  $\beta$  decay, where the  $\gamma W$  box diagram contains a short distance logarithm and a presently uncalculable long distance term  $C_{\gamma W}(\Lambda)$ .

In the case of  $Q_W(p)$ , the uncertainty associated with  $C_{\gamma Z}(\Lambda)$  is suppressed by the  $(1 - 4\hat{s}^2)$  prefactor<sup>2</sup> in Eq. (13). This factor arises from the sum of box and crossed-box diagrams, leading to an antisymmetric product of the lepton EM and weak neutral currents [2,51]. Since the resulting leptonic part of the box amplitude must be axial vector in character, only the vector part of the weak neutral current of the electron enters which is proportional to  $1 - 4\hat{s}^2$ . This result is quite general and independent of the hadronic part of the diagram. To estimate this uncertainty numerically, we follow Ref. [57] setting  $\Lambda = m_\rho$  and  $C_{\gamma Z}(m_\rho) = 3/2 \pm 1$ , which translates into a  $\pm 0.65\%$  uncertainty in  $Q_W(p)$ . The central value for  $C_{\gamma Z}(m_\rho)$  is obtained from a free quark calculation. A more detailed analysis, taking into account contributions from intermediate excited states of the proton, is likely to shift  $C_{\gamma Z}$ , but we do not expect the change to be considerably larger than the estimated uncertainty. In any case, increasing the error bar on  $C_{\gamma Z}$  by a factor of 5 would still imply an uncertainty in  $Q_W(p)$  below the expected experimental error. For comparison, we note that a change in the value of  $C_{\gamma W}(\Lambda)$  of similar magnitude would substantially affect the extraction of  $|V_{ud}|^2$  from light quark  $\beta$  decays, causing the first row of the CKM matrix to deviate from unitarity by several standard deviations. Since the dynamics entering  $C_{\gamma Z}$  and  $C_{\gamma W}$  are similar, it appears unlikely that the uncertainty in  $C_{\gamma Z}$  could differ significantly from  $\pm 1$ .

The remaining hadronic contribution to  $Q_W(p)$  arises from the low energy weak mixing angle  $\sin^2 \hat{\theta}_W(0)$ , which is the EW analog of the EM coupling  $\hat{\alpha}$ . The latter is measured very precisely in the Thomson limit ( $q^2=0$ ), but hadronic contributions induce a sizable uncertainty for large  $q^2$ , and most importantly for  $q^2 = M_Z^2$  [58]. Conversely,  $\hat{s}^2$  is measured precisely at the  $Z$  pole, but hadronic loops induce an uncertainty for  $q^2=0$ , which is correlated but not identical to the one in  $\hat{\alpha}$ . Note that effects due to  $q^2 \neq 0$  are already taken into account experimentally via the  $Q^2$  expansion and extrapolation of  $F^p$  (see Sec. II). One can then define

<sup>2</sup>Additional contributions arise that are not suppressed by this factor, but are negligible because they go as  $(E_e/M_Z)^2$ .

$$\begin{aligned} \sin^2 \hat{\theta}_W(0) &= \hat{s}^2 + \Delta \kappa_{\text{had}}^{(5)} \\ &+ \frac{\alpha}{\pi} \left\{ \frac{(1-4\hat{s}^2)}{12} \left[ \sum_{\ell} \ln \left( \frac{M_Z^2}{m_{\ell}^2} \right) \left( 1 + \frac{3\alpha}{4\pi} \right) \right. \right. \\ &\left. \left. + \frac{135\alpha}{32\pi} \right] - \left[ \frac{7\hat{c}^2}{4} + \frac{1}{24} \right] \ln \left( \frac{M_Z^2}{M_W^2} \right) + \frac{\hat{s}^2}{6} - \frac{7}{18} \right\}, \end{aligned} \quad (14)$$

where the sum is over the charged leptons, and we find, for the hadronic contribution,

$$\Delta \kappa_{\text{had}}^{(5)} = (7.90 \pm 0.05 \pm 0.06) \times 10^{-3}, \quad (15)$$

inducing a 0.4% uncertainty in  $Q_W(p)$ . The first error in Eq. (15) is correlated with the uncertainty in  $\Delta \hat{\alpha}_{\text{had}}^{(5)}(M_Z^2)$  [59]. The second error is from the conversion of  $\Delta \kappa_{\text{had}}^{(5)}$  which induces an uncertainty from the flavor separation of the  $e^+e^-$  annihilation and  $\tau$  decay data. This updates the value in Ref. [57],  $\Delta \kappa_{\text{had}}^{(5)} = (7.96 \pm 0.58) \times 10^{-3}$ . Note that the uncertainty in  $\Delta \kappa_{\text{had}}^{(5)}$  is also related to the vacuum polarization uncertainty [10,11] in  $a_{\mu}$ . These correlations should be properly treated in global analyzes of precision data. With  $\hat{s}^2 = 0.23112 \pm 0.00015$  from a SM fit to all current data, Eqs. (4) and (14) yield

$$\sin^2 \hat{\theta}_W(0) = 0.23807 \pm 0.00017,$$

$$Q_W(p) = 0.0716 \pm 0.0006, \quad (16)$$

where the uncertainty in the prediction for  $Q_W(p)$  is from the input parameters and dominated by the error in  $\hat{s}^2$ . The latter will decrease significantly in the future [60]. Taken together, the hadronic effects arising from  $\Delta \kappa_{\text{had}}^{(5)}$  and the box graphs combine to give a theoretical uncertainty of 0.8%.

The QWEAK experiment [14] seeks to perform the most precise determination of the weak mixing angle off the Z pole. For example, a 4% determination  $\Delta Q_W(p) = \pm 0.0029$  [14] (assuming a 2.8% statistical plus 2.8% systematic plus 0.8% theoretical error) would yield an uncertainty

$$\Delta \sin^2 \hat{\theta}_W(0) = \pm 7.2 \times 10^{-4}. \quad (17)$$

While the precise definition of  $\sin^2 \hat{\theta}_W(0)$  is scheme dependent, this quantity is nonetheless useful for comparing different low energy experiments. Furthermore, as illustrated in Fig. 1, the  $q^2$  evolution from the Z pole as predicted by the SM,

$$\sin^2 \hat{\theta}_W(0) - \hat{s}^2 = 0.00694 \pm 0.00074, \quad (18)$$

could be established with more than 9 standard deviations. For comparison, the cleanest test of PQCD can be obtained by contrasting the  $\tau$  lepton lifetime with the hadronic Z decay width: when interpreted as the RGE evolution of  $\alpha_s$  from  $m_{\tau}$  to  $M_Z$ , the result of the latest analysis [61] corresponds to an  $11\sigma$  effect.

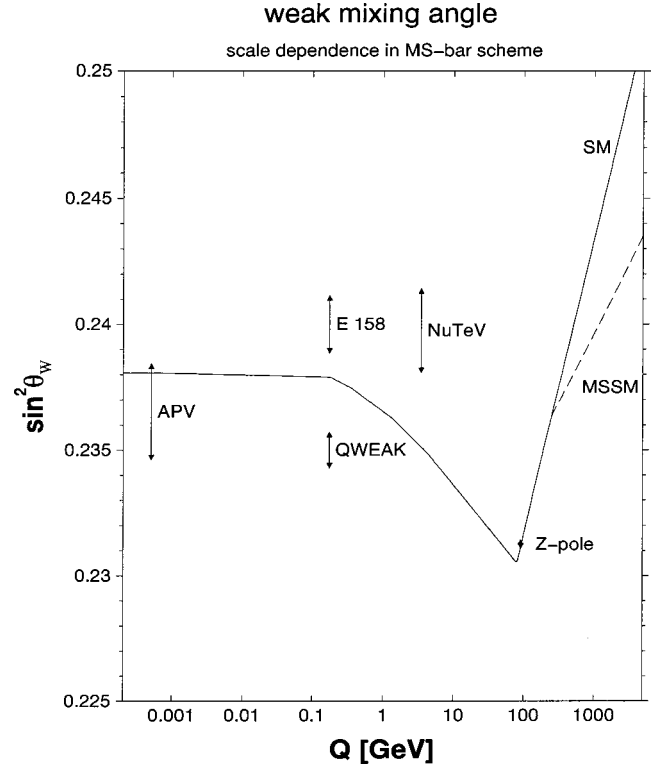


FIG. 1. Calculated running of the weak mixing angle in the SM, defined in the  $(\overline{\text{MS}})$  renormalization scheme (the dashed line indicates the reduced slope typical for the minimal supersymmetric standard model). Shown are the results from APV (Cs and Tl), NuTeV, and the Z pole. QWEAK and E 158 refer to the future  $Q_W(p)$  and  $Q_W(e)$  measurements and have arbitrarily chosen vertical locations.

Before proceeding, we comment on one additional possible source of hadronic effects in  $Q_W(p)$ : isospin admixtures in the proton wave function. The SM value quoted above implicitly assumes that the proton is an exact eigenstate of isospin. The EM and weak neutral vector currents for light quarks can then be decomposed according to their isospin content,

$$J_{\mu}^{EM} = \sum_{q=u,d} Q_q \bar{q} \gamma_{\mu} q = J_{\mu}^{I=1} + J_{\mu}^{I=0}, \quad (19)$$

$$\begin{aligned} J_{\mu}^{NC} &= -2 \sum_{q=u,d} C_{1q} \bar{q} \gamma_{\mu} q \\ &= -2(C_{1u} - C_{1d}) J_{\mu}^{I=1} - 6(C_{1u} + C_{1d}) J_{\mu}^{I=0}, \end{aligned} \quad (20)$$

where the  $C_{1q}$  are defined in Eq. (26). For the purpose of this discussion, we neglect contributions from strange quarks, which are effectively contained in  $F^p$  term in Eq. (2). To the extent to which the nucleon is a pure  $I=1/2$  isospin eigenstate, one has  $F_1^p(0)^{I=1} = F_1^p(0)^{I=0} = 1/2$ , where the  $F_1^p(0)^I$  are the Dirac form factors associated with the proton matrix elements of the  $J_{\mu}^I$ . In principle, these form factor relations receive small corrections due to isospin breaking light quark mass differences ( $m_u \neq m_d$ ) and EM effects. However, con-

servation of EM charge implies that such corrections vanish. To see this, assume that the proton state contains a small,  $O(\epsilon)$ , admixture of an  $I' \neq 1/2$  state

$$|p\rangle = \sqrt{1 - \epsilon^2} |1/2, 1/2\rangle + \epsilon |I', I'_3\rangle, \quad (21)$$

where, for the purpose of this illustration, we drop explicit  $O(\epsilon^2)$  terms involving the  $|I', I'_3\rangle$  state. At  $q^2=0$ , the charges  $J_0^I$  are equivalent to the operators  $\hat{I}_3$  and  $\frac{1}{2}\hat{1}$ . Since these operators cannot connect states of different total isospin, one has

$$F_1^p(0)^{I=1} = \frac{1}{2}(1 - \epsilon^2) + \epsilon^2 I'_3, \quad (22)$$

$$F_1^p(0)^{I=0} = \frac{1}{2}. \quad (23)$$

Since the proton charge is  $1 = F_1^p(0)^{I=1} + F_1^p(0)^{I=0}$ , one must have  $I'_3 = 1/2$ , so that there are no corrections to  $F_1^p(0)^I$  through  $O(\epsilon^2)$ . Thus, one has to this order for the neutral current Dirac form factor,

$$Q_W(p) \equiv F_1^p(0)^{NC} = -2(2C_{1u} + C_{1d}), \quad (24)$$

which is the same result obtained in the absence of any isospin impurities. Similar arguments prevent the appearance of any higher order terms in  $\epsilon$ .

#### IV. FOUR-FERMI OPERATORS AND MODEL INDEPENDENT ANALYSIS

Before considering the consequences for particular models of new physics, it is instructive to consider the model independent implications of a 4%  $Q_W(p)$  measurement. The low energy effective electron-quark Lagrangian of the form  $A(e) \times V(q)$  is given by

$$\mathcal{L} = \mathcal{L}_{SM}^{PV} + \mathcal{L}_{NEW}^{PV}, \quad (25)$$

where

$$\mathcal{L}_{SM}^{PV} = -\frac{G_{F^-}}{\sqrt{2}} \bar{e} \gamma_\mu \gamma_5 e \sum_q C_{1q} \bar{q} \gamma^\mu q, \quad (26)$$

$$\mathcal{L}_{NEW}^{PV} = \frac{g^2}{4\Lambda^2} \bar{e} \gamma_\mu \gamma_5 e \sum_f h_V^q \bar{q} \gamma^\mu q, \quad (27)$$

and where  $g$ ,  $\Lambda$ , and  $h_V^q$  are, respectively, the coupling constant, the mass scale, and effective coefficients associated with the new physics.<sup>3</sup> The latter are in general of order unity; the explicit factor of 4 arises from the projection operators on left and right (or vector and axial-vector) chiral fermions. In the same normalization, the SM coefficients take the values (see Ref. [4])  $C_{1u}/2 = -0.09429 \pm 0.00011$  and  $C_{1d}/2 = +0.17070 \pm 0.00007$  for up and down quarks,

<sup>3</sup>The couplings  $C_{2q}$  are defined as in Eq. (26) with  $\gamma_5$  appearing between the quark fields instead of the electron fields.

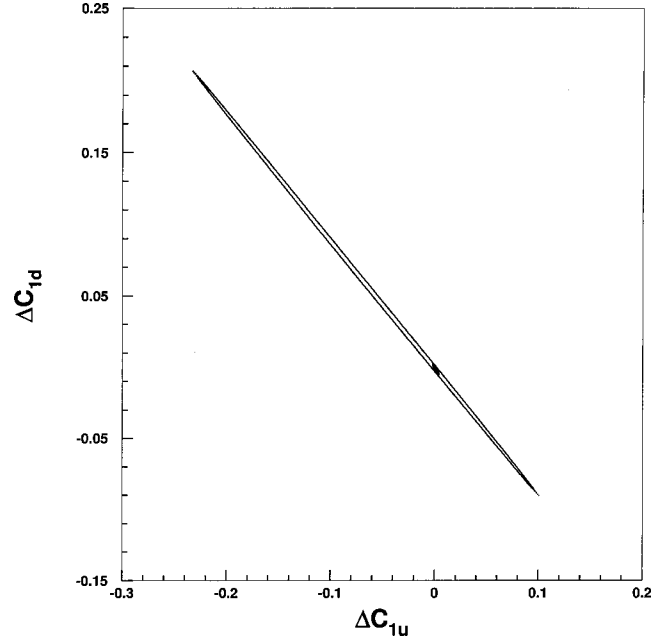


FIG. 2. Present and prospective 90% C.L. constraints on new physics contributions to the  $eq$  couplings  $C_{1u}$  and  $C_{1d}$ . The larger ellipse represents the present constraints, derived from APV in Cs [23], and polarized electron scattering at MIT-Bates [18] and SLAC [15]. The smaller ellipse indicates the constraints after the inclusion of the  $Q_W(p)$  measurement, assuming that the central experimental value coincides with the SM prediction.

respectively, where we included the QCD corrections obtained in Eqs. (11) and (12), and where the uncertainties are from the SM inputs. We find

$$Q_W^p(\text{SM}) = -2(2C_{1u} + C_{1d}) = 0.0716 \pm 0.0006. \quad (28)$$

A 4% measurement of  $Q_W(p)$  would thus test new physics scales up to

$$\frac{\Lambda}{g} \approx \frac{1}{(\sqrt{2}G_F |\Delta Q_W^p|)^{1/2}} \approx 4.6 \text{ TeV}. \quad (29)$$

The sensitivity to non-perturbative theories (such as technicolor, models of composite fermions, or other strong coupling dynamics) with  $g \sim 2\pi$  could even reach  $\Lambda \approx 29$  TeV. As another example, for extra  $Z'$  bosons from simple models based on grand unified theories (GUT), one expects  $g \sim 0.45$ , so that one can study such bosons (with unit charges) up to masses  $M_{Z'} \approx 2.1$  TeV.  $Z'$  bosons are predicted in many extensions of the SM ranging from the more classical GUT and technicolor models to SUSY and string theories. We discuss the sensitivity of  $Q_W(p)$  to  $Z'$  bosons, as well as other scenarios, in the subsequent sections.

In Fig. 2 we plot the present constraints on  $\Delta C_{1u}$  and  $\Delta C_{1d}$ , the shifts in the  $C_{1q}$  caused by new physics. They are derived from  $Q_W(\text{Cs})$  [23], as well as the MIT-Bates <sup>12</sup>C [18] and SLAC deuterium [15] parity violation measurements. As long as  $\Delta C_{1u}$  and  $\Delta C_{1d}$  are almost perfectly correlated, the result is an elongated ellipse. The impact of the proposed  $Q_W(p)$  measurement is indicated by the smaller

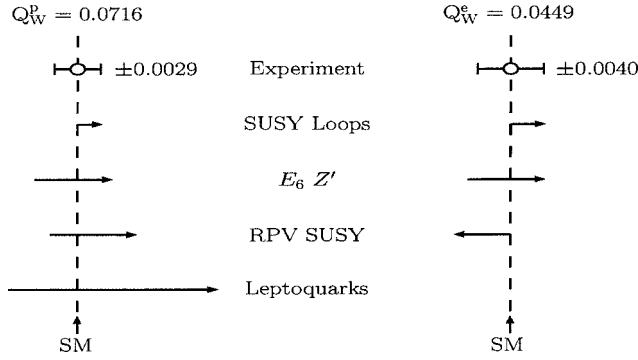


FIG. 3. Comparison of anticipated errors for  $Q_W(p)$  and  $Q_W(e)$  with deviations from the SM expected from various extensions and allowed (at 95% C.L.) by fits to existing data. Note that the two measurements are highly complementary. They would shift in a strongly correlated manner due to SUSY loops or a (1 TeV)  $Z'$  and thus together they could result in evidence for such new physics. In the case of RPV SUSY, the two measurements are somewhat anti-correlated. Finally, only  $Q_W(p)$  is sensitive to LQs, while  $Q_W(e)$  would serve as a control.

ellipse. The dramatic reduction in the allowed parameter space will be possible because  $Q_W(p)$  probes a very different linear combination than the existing data.

In the next two sections we turn to specific extensions of the SM, of which there are many, and focus on three particularly well motivated types: gauge bosons, SUSY, and LQs. In doing so, we emphasize on the complementarity of the PV Møller asymmetry measured by the SLAC-E-158 experiment [24] which has comparable anticipated precision and (as a purely leptonic observable) has a clean theoretical interpretation. Some new physics scenarios appear more strongly in the semileptonic channel than in the purely leptonic channel and vice versa. The complementarity of the two measurements is advantageous in attempting to distinguish among various new physics scenarios and is summarized in Fig. 3.

## V. EXTRA NEUTRAL GAUGE INTERACTIONS

The introduction of neutral gauge symmetries beyond those associated with the photon and the  $Z$  boson have long been considered as one of the best motivated extensions of the SM. Such  $U(1)'$  symmetries are predicted in most GUTs and appear copiously in superstring theories. In the context of SUSY, they do not spoil the approximate gauge coupling unification predicted by the simplest and most economic scenarios. Moreover, in many SUSY models [though not the simplest  $SO(10)$  ones], the enhanced  $U(1)'$  gauge symmetry forbids an elementary bilinear Higgs  $\mu$  term, while allowing an effective  $\mu$  to be generated at the scale of  $U(1)'$  breaking without introducing cosmological problems [62]. In various string motivated models of radiative breaking, this scale is comparable to the EW scale (i.e.,  $\lesssim 1$  TeV) [62,63], thereby providing a solution [64] to the  $\mu$  problem [65] and enhancing the prospects that a  $Z'$  could be in reach in collider experiments or seen indirectly in the precision EW data. An extra  $U(1)'$  symmetry could also explain proton stability, which is not automatic in supersymmetric models, or it

could solve both the proton lifetime puzzle and the  $\mu$  problem simultaneously [66].

From a phenomenological standpoint, direct searches at the Tevatron [67] have as yet yielded no evidence<sup>4</sup> for the existence of an extra neutral  $Z'$  boson associated with the  $U(1)'$ , providing instead only lower bounds of about 600 GeV (depending on the precise nature of the  $Z'$ ). This implies a hierarchy of an order of magnitude between the  $Z$  and  $Z'$  masses. Recently, using approximately flat directions in moduli space, it was shown that such a hierarchy can arise naturally in SUSY models [69].

On the other hand, several indirect effects could be attributed to a  $Z'$ . The  $Z$  line shape fit at LEP [70] yields a significantly larger value for the hadronic peak cross section  $\sigma_{\text{had}}^0$  than is predicted in the SM. This implies, for example, that the effective number of massless neutrinos,  $N_\nu$ , is  $2.986 \pm 0.007$ , which is  $2\sigma$  lower than the SM prediction,  $N_\nu = 3$ . As a consequence, the  $Z$  pole data currently favors  $Z'$  scenarios with a small amount of  $Z$ - $Z'$  mixing ( $\sin \theta \neq 0$ ) [71] which mimics a negative contribution to the invisible  $Z$  decay width. The result by the NuTeV Collaboration [7] can be brought into better agreement when one allows a  $Z'$ , especially when family non-universal couplings are assumed [71,72].

To analyze the impact of a  $Z'$  on  $Q_W(p)$ , we employ Eq. (27) with  $\Lambda = M_{Z'}$  and  $g = g_{Z'} = \sqrt{5/3} \sin \theta_W \sqrt{\lambda} g_Z$  [73], where  $\lambda = 1$  in the simplest models.  $g_Z^2 = \sqrt{3} 2 G_F M_Z^2$  is the SM coupling constant for the ordinary  $Z$ . Consider the Abelian subgroups of the  $E_6$  GUT group,

$$E_6 \rightarrow SO(10) \times U(1)_\psi \rightarrow SU(5) \times U(1)_\chi \times U(1)_\psi \\ \rightarrow SU(3)_C \times SU(2)_L \times U(1)_Y \times U(1)_\chi \times U(1)_\psi.$$

The most general  $Z'$  boson from  $E_6$  can be written as the linear combination [71]

$$Z' \sim -\cos \alpha \cos \beta Z_\chi + \sin \alpha \cos \beta Z_Y - \sin \beta Z_\psi. \quad (30)$$

Considerations of gauge anomaly cancellation as well as the proton lifetime and  $\mu$  problems in SUSY models mentioned earlier, also favor a  $Z'$  of that type [66]. The assignment of SM fermions to representations of  $SO(10)$  implies that  $Z_\psi$  has only axial-vector couplings and can generate no PV  $ef$  interactions of the type in Eq. (27), whereas the  $Z_\chi$  generates only PV  $ed$  and  $ee$  interactions of this type. Moreover, unlike in most other classes of models, the contributions to the weak charges of the proton and the electron would have equal magnitude. Thus, should  $Q_W(p)$  show a deviation from the SM prediction, a comparison with  $Q_W(e)$  would be a powerful tool to discriminate between  $Z'$  and other SM extensions. This statement is illustrated in Fig. 3 where the sensitivities of  $Q_W(p)$  and  $Q_W(e)$  are contrasted.

If  $Z'$  were detected at the Tevatron or the CERN Large Hadron Collider (LHC), it would be important to constrain

<sup>4</sup>See, however, Ref. [68] which reports a  $2\sigma$  deficit in the highest mass bin of the leptonic forward-backward asymmetry seen by the Collider Detector at Fermilab (CDF) Collaboration.

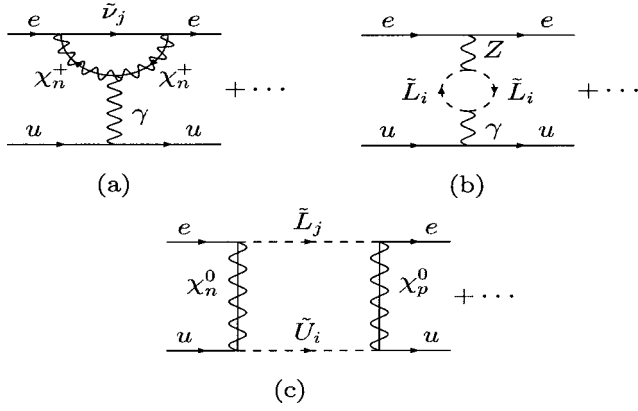


FIG. 4. Representative examples of SUSY loop corrections to  $Q_W(p)$ . Shown are corrections from (a) charginos and sneutrinos; (b) sleptons contributing to  $\gamma$ - $Z$  mixing [ $\Delta \sin^2 \hat{\theta}_W(0)_{\text{SUSY}}$ ]; and (c) a box graph containing neutralinos, sleptons, and squarks.

its properties. Its mass would be measured in course of the discovery, while  $\sin \theta$  is mainly constrained by LEP 1. The  $U(1)'$  charges and the couplings to quarks and leptons, however, are best determined by low energy precision measurements. Currently, the best fit values are  $\alpha = -0.8_{-1.2}^{+1.4}$ ,  $\beta = 1.0_{-0.8}^{+0.4}$ , and  $\sin \theta = 0.0010_{-0.0006}^{+0.0012}$ , obtained for  $\lambda = 1$  and  $M_{Z'} = 1$  TeV. In this case,  $Q_W(p) = 0.0747$  is predicted, i.e., a  $1.1\sigma$  effect. The impact of the QWEAK measurement would be to reduce the allowed region of the parameters  $\alpha$  and  $\beta$  by  $\sim 30\%$ .

## VI. SUPERSYMMETRY AND LEPTOQUARKS

As in the case of extended gauge symmetry, the theoretical motivation for supersymmetric extensions of the SM is strong. SUSY is a prediction of superstring theories; and if the SUSY breaking scale is at the EW scale, it stabilizes the latter and is consistent with coupling unification. Conversely, minimal SUSY introduces a new set of issues, including the scale of the  $\mu$  parameter mentioned above and the presence of 105 parameters [74,75] in the soft SUSY breaking Lagrangian. In order to be predictive, additional theoretical constraints must be invoked, such as those provided by gauge, gravity, or anomaly mediated SUSY breaking models. The phenomenological evidence for SUSY thus far is sparse, though hints exist. For example, the neutralino is a natural candidate for cold dark matter, and the possible deviation of  $a_\mu$  points suggestively toward SUSY. Since, in the end, the experiment will determine what form of SUSY (if any) is applicable to EW phenomena, it is of interest to discuss the prospective implications of a  $Q_W(p)$  measurement for this scenario.

While baryon number  $B$  and lepton number  $L$  are exact symmetries of the SM, they are not automatically conserved in the minimal supersymmetric standard model (MSSM). In order to avoid proton decay,  $B$  and  $L$  conservation—in the guise of  $R$  parity conservation—is often imposed by hand. In this case, every MSSM vertex contains an even number of superpartners, and the effects of SUSY appear in  $Q_W(p)$  only via loops, such as those shown in Fig. 4. Recently, such

loop corrections to a variety of low and medium energy precision observables were computed in Refs. [76–78]. These analyses were completed without invoking any assumptions about the mechanism for soft SUSY breaking. The implications of charged current data for the SUSY spectrum appear to conflict with those derived from typical models for SUSY breaking mediation [76]. This conflict may be alleviated by allowing for  $R$  parity violation (RPV) [3], though doing so would eliminate the lightest neutralino as a dark matter candidate. From this perspective, independent low energy probes of the MSSM spectrum take on added importance.

A measurement of  $Q_W(p)$ , when considered in tandem with  $Q_W(e)$  and  $Q_W(\text{Cs})$ , could provide such a probe. The MSSM loop corrections to the weak charges can be analyzed efficiently by modifying Eq. (4),

$$Q_W(p) = [\rho_{NC} + \Delta_e + \Delta \rho_{\text{SUSY}}] [1 - 4 \sin^2 \hat{\theta}_W(0) + \Delta'_e] \\ + \square_{WW} + \square_{ZZ} + \square_{\gamma Z} + \lambda_{\text{SUSY}}, \\ \sin^2 \hat{\theta}_W(0) = \sin^2 \hat{\theta}_W(0)_{\text{SM}} + \Delta \sin^2 \hat{\theta}_W(0)_{\text{SUSY}}, \quad (31)$$

where  $\sin^2 \hat{\theta}_W(0)_{\text{SM}}$  is the SM prediction given in Eq. (14) and  $\Delta \sin^2 \hat{\theta}_W(0)_{\text{SUSY}}$  is the correction induced by SUSY loops.<sup>5</sup> All SUSY box graph contributions, as well as non-universal vertex and external leg corrections, are contained in  $\lambda_{\text{SUSY}}$ . Flavor-independent corrections are given by  $\Delta \rho_{\text{SUSY}}$  and  $\Delta \sin^2 \hat{\theta}_W(0)_{\text{SUSY}}$ .

The effects of SUSY loops on  $Q_W(p)$  and  $Q_W(e)$  are dominated by  $\Delta \sin^2 \hat{\theta}_W(0)_{\text{SUSY}}$ , because present bounds on the  $T$  parameter from precision data [4] limit the magnitude of  $\Delta \rho_{\text{SUSY}}$ . Moreover, box graph contributions are numerically small, while cancellations reduce the impact of vertex and external leg corrections. Consequently, the shifts in the proton and electron weak charges are similar over nearly all allowed SUSY parameter space. This is in contrast to  $Q_W(\text{Cs})$  due to canceling the corrections to  $u$  and  $d$  quark weak charges. Thus, should the QWEAK and SLAC E-158 experiments observe a correlated deviation, and should  $Q_W(\text{Cs})$  remain in agreement with the SM, the MSSM would be a favored explanation compared to many other scenarios.

The situation changes considerably in the presence of RPV effects. The most general gauge invariant, renormalizable RPV extension of the MSSM is generated by the superpotential [79]

$$W_{\text{RPV}} = \frac{1}{2} \lambda_{ijk} L^i L^j \bar{e}^k + \lambda'_{ijk} L^i Q^j \bar{d}^k + \frac{1}{2} \lambda''_{ijk} \bar{u}^i \bar{d}^j \bar{d}^k + \mu'_i L^i H_u, \quad (32)$$

where  $L^i$  and  $Q^i$  denote the left-handed lepton and quark doublet superfields, respectively; the barred quantities denote the right-handed singlet superfields;  $H_u$  is the hypercharge  $Y = 1$  Higgs superfield; and the indices indicate generations. The bulk of studies of  $W_{\text{RPV}}$  have been phenomenological

<sup>5</sup>In the notation of Ref. [77],  $\Delta \sin^2 \hat{\theta}_W(0)_{\text{SUSY}} = 4 s^2 \delta \kappa_{PV}^{\text{SUSY}}$ .

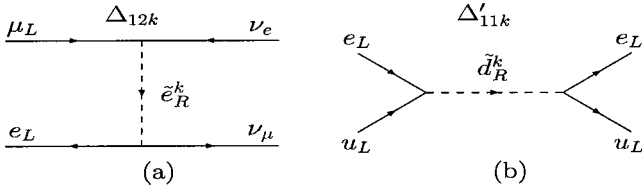


FIG. 5. Representative examples of tree level SUSY corrections in the case of RPV. Shown are (a) a contribution to  $\mu$  decay which affects  $Q_W(p)$  through a modification of  $G_F$  and  $\sin^2\theta_W$ , and (b) squark exchange.

[80]. The strongest constraint comes from the proton lifetime, which generally forbids the  $B$  violating  $\lambda''$  terms unless all other ( $L$  violating) terms in  $W_{RPV}$  vanish. Consequently, we restrict our attention to  $\lambda''_{ijk}=0$  and, for simplicity, we also set  $\mu'_i=0$ . When inserted into the amplitudes of Fig. 5, the remaining interactions in Eq. (32) generate corrections in terms of the quantities  $\Delta_{ijk}(\tilde{f})$  and  $\Delta'_{ijk}(\tilde{f})$ , where, for example,

$$\Delta_{12k}(\tilde{e}_R^k) = \frac{|\lambda_{12k}|^2}{4\sqrt{2}G_F M_{\tilde{e}_R^k}^2}, \quad (33)$$

with  $\tilde{e}_R^k$  being the exchanged slepton, and where the  $\Delta'_{ijk}(\tilde{f})$  are defined similarly by replacing  $\lambda_{ijk} \rightarrow \lambda'_{ijk}$ . One obtains tree level contributions to  $Q_W(p)$  such as those shown in Fig. 5. Similar corrections affect other EW observables, such as  $Q_W(e)$ ,  $Q_W(Cs)$ , and  $G_V$ . Specifically [3],

$$\begin{aligned} \Delta Q_W(p)/Q_W(p) \approx & \left( \frac{2}{1-4\sin^2\theta_W} \right) [-2\lambda_x \Delta_{12k}(\tilde{e}_R^k) \\ & + 2\Delta'_{11k}(\tilde{d}_R^k) - \Delta'_{1j1}(\tilde{q}_L^j)], \end{aligned} \quad (34)$$

$$\Delta Q_W(e)/Q_W(e) \approx - \left( \frac{4}{1-4\sin^2\theta_W} \right) \lambda_x \Delta_{12k}(\tilde{e}_R^k), \quad (35)$$

where  $\lambda_x = \hat{s}^2 \hat{c}^2 / (1-2\hat{s}^2) \approx 0.33$ . In contrast to MSSM loop effects,  $Q_W(p)$  and  $Q_W(e)$  display complementary sensitivities to RPV effects. To illustrate, we consider a multi-parameter fit to precision data, allowing  $\Delta_{12k}$ ,  $\Delta'_{11k}$ ,  $\Delta'_{1j1}$ , and  $\Delta'_{21k}$  to be non-zero. The results imply that the possible shifts in  $Q_W(p)$  and  $Q_W(e)$  have opposite relative signs over nearly all the presently allowed parameter space. We find that shifts of the order  $\Delta Q_W(p)/Q_W(p) \sim 10\%$  are allowed at the 95% C.L. Thus, a comparison of  $Q_W(p)$  and  $Q_W(e)$  could help distinguish between the versions of SUSY with and without RPV.

The effects of  $\lambda' \neq 0$  are similar to those generated by scalar LQs. While RPV SUSY provides a natural context in which to discuss the latter, vector LQs arise naturally in various GUT models [81,82]. Assuming  $SU(3)_C \times SU(2)_L \times U(1)_Y$  invariance one obtains the Lagrangian [83]

$$\begin{aligned} \mathcal{L} = & h_2^L \bar{u} \ell R_2^L + h_2^R \bar{q} i \tau_2 e R_2^R + \tilde{h}_2 \bar{d} \ell \tilde{R}_2^L + g_1^L \bar{q}^c i \tau_2 \ell S_1^L \\ & + g_1^R \bar{u}^c e S_1^R + \tilde{g}_1 \bar{d}^c e \tilde{S}_1^R + g_3 \bar{q}^c i \tau_2 \tilde{\tau} \ell S_3 + h_1^L \bar{q} \gamma^\mu \ell U_{1\mu}^L \\ & + h_1^R \bar{d} \gamma^\mu e U_{1\mu}^R + \tilde{h}_1 \bar{u} \gamma^\mu e \tilde{U}_{1\mu}^R + h_3 \bar{q} \gamma^\mu \tilde{\tau} \ell U_{3\mu} \\ & + g_2^L \bar{d}^c \gamma^\mu \ell V_{2\mu}^L + g_2^R \bar{q}^c \gamma^\mu e V_{2\mu}^R + \tilde{g}_2 \bar{u}^c \gamma^\mu \ell \tilde{V}_{2\mu}^L + \text{H.c.}, \end{aligned} \quad (36)$$

where  $q$  and  $l$  and the left-handed quark and lepton doublets and  $u$ ,  $d$ , and  $e$  are the right-handed singlets. Since we are interested in the implications for  $Q_W(p)$ , we only consider first generation LQs. The first two rows in Eq. (36) involve scalar LQs, while the others involve vector types. The LQs in the first and third rows have fermion number  $F=3B+L=0$ , while the others have  $F=-2$ . The indices  $\ell$  refer to their isospin representation.

A recent global analysis of scalar LQ constraints from EW data is given in Ref. [84]. Here, we extend this analysis to include vector LQ interactions. We also update it by including the new  $Q_W(Cs)$  in Eq. (3), hadronic production cross sections at LEP 2 up to 207 GeV [70], and the analysis of nuclear  $\beta$  decay given in Ref. [85]. We only consider one LQ

TABLE I. Possible impact of LQ interactions on  $Q_W(p)$ . The left-hand side shows scalar and the right-hand side vector LQ species. The columns denote *consistency* which gives the fractions of the distribution of operator coefficients having the same sign as implied by the LQ model. The final columns give the fractional shifts in  $Q_W(p)$  allowed by the data. In more statistical terms, consistency is the result of a hypothesis test, while the shifts in  $Q_W(p)$  reflect parameter estimations that are irrespective of the outcome of the hypothesis test.

LQ	Consistency	$\Delta Q_W(p)/Q_W(p)$	LQ	Consistency	$\Delta Q_W(p)/Q_W(p)$
$S_1^L$	0.57	9%	$U_{1\mu}^L$	0.26	-8%
$S_1^R$	0.01	-6%	$U_{1\mu}^R$	0.56	6%
$\tilde{S}_1^R$	0.44	-6%	$\tilde{U}_{1\mu}^R$	0.99	25%
$S_3$	0.76	10%	$U_{3\mu}$	0.31	-4%
$R_2^L$	0.44	-13%	$V_{2\mu}^L$	0.87	9%
$R_2^R$	0.89	15%	$V_{2\mu}^R$	0.11	-7%
$\tilde{R}_2^L$	0.13	-4%	$\tilde{V}_{2\mu}^L$	0.56	14%

species at a time. We fit the data and determine the consistency (shown in Table I) of the result with the sign predicted by a given LQ model. The latter is the probability, conditional on the data, that the coefficient has the same sign as implied by the model. For example, the data favor the presence of  $\tilde{U}_{1\mu}^R$ , while  $S_1^R$  is virtually excluded. Assuming a given LQ model, we then determine the 95% C.L. upper limit on  $Q_W(p)$ . Note that this involves a renormalization to the physical parameter space of the model. We observe that the LQ model most favored by the data is  $\tilde{U}_{1\mu}^R$  for which shifts in  $Q_W(p)$  as large as 25% are allowed. Since the impact of LQs on  $Q_W(e)$  is loop suppressed, one would not expect it to deviate significantly from the SM prediction. Thus, if one observes a large effect in  $Q_W(p)$ ,  $Q_W(e)$  would serve as a diagnostic tool to distinguish LQ effects from SUSY.

## VII. CONCLUSIONS

Precise measurements of relatively low energy EW observables continue to play an important part in the search for physics beyond the SM. When taken in the proper context, such studies can provide unique clues about the nature of the EW symmetry breaking, grand unification, etc. We have shown that the weak charge of the proton constitutes a theoretically clean probe of new physics. Presently uncalculable, non-perturbative QCD effects are either sufficiently small or

can be constrained by the current program of parity violation measurements so as to render  $Q_W(p)$  free from potentially worrisome nucleon structure uncertainties. Within the SM, a 4% determination of  $Q_W(p)$ —as planned at JLab—would yield a  $9\sigma$  determination of the running of the weak mixing angle. Looking beyond the SM, a measurement at this level would provide an effective diagnostic tool for new physics, particularly when considered in tandem with complementary precision low energy studies, such as the SLAC PV Møller scattering experiment, cesium APV,  $a_\mu$ ,  $\beta$  decay, and others. Should future experimental developments make an even more precise  $Q_W(p)$  measurement possible, the physics impact would be correspondingly more powerful. Given its theoretical interpretability, pursuing such experimental developments appear to be well worth the effort.

## ACKNOWLEDGMENTS

We thank K. Cheung, A. Derevianko, V. Flambaum, P. Herczeg, P. Langacker, W. Marciano, S. Su, and O. P. Sushkov for helpful discussions. This work was supported by the U.S. Department of Energy contracts DE-FG02-00ER41146, DE-FG03-02ER41215, DE-FG03-00ER4112, by NSF contract PHY00-71856, by CONACYT (México) contract 42026-F, and by DGAPA-UNAM contract PAPIIT IN112902.

- 
- [1] P. Langacker, *Precision Tests of the Standard Electroweak Model*, Advanced Series on Directions in High Energy Physics Vol. 14 (World Scientific, Singapore, 1995).
  - [2] M.J. Ramsey-Musolf, Phys. Rev. C **60**, 015501 (1999).
  - [3] M.J. Ramsey-Musolf, Phys. Rev. D **62**, 056009 (2000).
  - [4] J. Erler and P. Langacker, in [5], p. 98.
  - [5] Particle Data Group, K. Hagiwara *et al.*, Phys. Rev. D **66**, 010001 (2002).
  - [6] Muon  $g-2$  Collaboration, G.W. Bennett *et al.*, Phys. Rev. Lett. **89**, 101804 (2002).
  - [7] NuTeV Collaboration, G.P. Zeller *et al.*, Phys. Rev. Lett. **88**, 091802 (2002).
  - [8] M. Knecht and A. Nyffeler, Phys. Rev. D **65**, 073034 (2002).
  - [9] M. Ramsey-Musolf and M.B. Wise, Phys. Rev. Lett. **89**, 041601 (2002).
  - [10] M. Davier, S. Eidelman, A. Höcker, and Z. Zhang, Eur. Phys. J. C **27**, 497 (2003).
  - [11] K. Hagiwara, A.D. Martin, D. Nomura, and T. Teubner, Phys. Lett. B **557**, 69 (2003).
  - [12] A. Bodek *et al.*, Phys. Rev. Lett. **83**, 2892 (1999).
  - [13] S. Davidson *et al.*, J. High Energy Phys. **02**, 037 (2002).
  - [14] QWEAK Collaboration, R. Carlini *et al.*, “The Q(Weak) Experiment: A Search for Physics at the TeV Scale Via a Measurement of the Proton’s Weak Charge,” JLAB Report No. E-02-020.
  - [15] SLAC-E-122 Collaboration, C.Y. Prescott *et al.*, Phys. Lett. **84B**, 524 (1979).
  - [16] CERN-NA-004 Collaboration, A. Argento *et al.*, Phys. Lett. **120B**, 245 (1983).
  - [17] W. Heil *et al.*, Nucl. Phys. **B327**, 1 (1989).
  - [18] P.A. Souder *et al.*, Phys. Rev. Lett. **65**, 694 (1990).
  - [19] SAMPLE Collaboration, R. Hasty *et al.*, Science **290**, 2117 (2000).
  - [20] HAPPEX Collaboration, K.A. Aniol *et al.*, Phys. Lett. B **509**, 211 (2001).
  - [21] N.H. Edwards *et al.*, Phys. Rev. Lett. **74**, 2654 (1995).
  - [22] P.A. Vetter *et al.*, Phys. Rev. Lett. **74**, 2658 (1995).
  - [23] C.S. Wood *et al.*, Science **275**, 1759 (1997).
  - [24] SLAC-E-158 Collaboration, E.W. Hughes *et al.*, “A Precision Measurement of the Weak Mixing Angle in Møller Scattering,” SLAC Report No. E-158.
  - [25] A. Derevianko, Phys. Rev. Lett. **85**, 1618 (2000).
  - [26] V.A. Dzuba, C. Harabati, W.R. Johnson, and M.S. Safronova, Phys. Rev. A **63**, 044103 (2001).
  - [27] M.G. Kozlov, S.G. Porsev, and I.I. Tupitsyn, Phys. Rev. Lett. **86**, 3260 (2001).
  - [28] A.I. Milstein and O.P. Sushkov, Phys. Rev. A **66**, 022108 (2002).
  - [29] W.R. Johnson, I. Bednyakov, and G. Soff, Phys. Rev. Lett. **87**, 233001 (2001).
  - [30] V.A. Dzuba, V.V. Flambaum, and J.S. Ginges, Phys. Rev. D **66**, 076013 (2002).
  - [31] M.Y. Kuchiev and V.V. Flambaum, Phys. Rev. Lett. **89**, 283002 (2002).
  - [32] A.I. Milstein, O.P. Sushkov, and I.S. Terekhov, Phys. Rev. Lett. **89**, 283003 (2002).
  - [33] M.J. Musolf *et al.*, Phys. Rep. **239**, 1 (1994).

- [34] A4 Collaboration, D. von Harrach *et al.* (unpublished).
- [35]  $G\theta$  Collaboration, D.H. Beck *et al.*, “Parity Violation in ep and eD Scattering: The  $G\theta$  Experiment,” JLAB Report No. E-00-006.
- [36] M.A. Bouchiat and J. Guéna, *J. Phys. (France)* **49**, 2037 (1988).
- [37] S.C. Bennett and C.E. Wieman, *Phys. Rev. Lett.* **82**, 2484 (1999).
- [38] S.J. Pollock and M.C. Welliver, *Phys. Lett. B* **464**, 177 (1999).
- [39] B.Q. Chen and P. Vogel, *Phys. Rev. C* **48**, 1392 (1993).
- [40] D. Vretenar, G.A. Lalazissis, and P. Ring, *Phys. Rev. C* **62**, 045502 (2000).
- [41] P.K. Panda and B.P. Das, *Phys. Rev. C* **62**, 065501 (2000).
- [42] M.E. Peskin and T. Takeuchi, *Phys. Rev. Lett.* **65**, 964 (1990).
- [43] M. Veltman, *Nucl. Phys.* **B123**, 89 (1977).
- [44] A. Djouadi and C. Verzegnassi, *Phys. Lett. B* **195**, 265 (1987).
- [45] A. Djouadi, *Nuovo Cimento Soc. Ital. Fis., A* **100**, 357 (1988).
- [46] L. Avdeev, J. Fleischer, S. Mikhailov, and O. Tarasov, *Phys. Lett. B* **336**, 560 (1994).
- [47] K.G. Chetyrkin, J.H. Kühn, and M. Steinhauser, *Phys. Lett. B* **351**, 331 (1995).
- [48] R. Barbieri *et al.*, *Phys. Lett. B* **288**, 95 (1992); *Nucl. Phys.* **B409**, 105 (1993).
- [49] J. Fleischer, O.V. Tarasov, and F. Jegerlehner, *Phys. Lett. B* **319**, 249 (1993).
- [50] G. Degrassi, P. Gambino, and A. Vicini, *Phys. Lett. B* **383**, 219 (1996).
- [51] W.J. Marciano and A. Sirlin, *Phys. Rev. D* **27**, 552 (1983); **29**, 75 (1984).
- [52] M.J. Musolf and B.R. Holstein, *Phys. Rev. D* **43**, 2956 (1991).
- [53] M.J. Musolf and B.R. Holstein, *Phys. Lett. B* **242**, 461 (1990).
- [54] A. Sirlin, *Rev. Mod. Phys.* **50**, 573 (1978).
- [55] S.L. Adler and W.K. Tung, *Phys. Rev. Lett.* **22**, 978 (1969).
- [56] M.A.B. Bég, *Phys. Rev. D* **11**, 1165 (1975).
- [57] W.J. Marciano, *Precision Tests of the Standard Electroweak Model*, Advanced Series on Directions in High Energy Physics Vol. 14 [1], p. 170.
- [58] J. Erler, “Determinations of  $\alpha(M_Z)$ : Comparison and Prospects,” hep-ph/0111005.
- [59] J. Erler, *Phys. Rev. D* **59**, 054008 (1999).
- [60] Snowmass Working Group on Precision Electroweak Measurements, U. Baur *et al.*, “Present and Future Electroweak Precision Measurements and the Indirect Determination of the Mass of the Higgs Boson,” hep-ph/0202001.
- [61] J. Erler and M. Luo, *Phys. Lett. B* **558**, 125 (2003).
- [62] M. Cvetič and P. Langacker, “Z’ Physics and Supersymmetry,” hep-ph/9707451.
- [63] P. Langacker, “Z’ Physics from Strings,” hep-ph/9805486.
- [64] M. Cvetič and P. Langacker, *Phys. Rev. D* **54**, 3570 (1996).
- [65] J.E. Kim and H.P. Nilles, *Phys. Lett.* **138B**, 150 (1984).
- [66] J. Erler, *Nucl. Phys.* **B586**, 73 (2000).
- [67] CDF Collaboration, F. Abe *et al.*, *Phys. Rev. Lett.* **79**, 2192 (1997).
- [68] CDF Collaboration, T. Affolder *et al.*, *Phys. Rev. Lett.* **87**, 131802 (2001).
- [69] J. Erler, P. Langacker, and T. Li, *Phys. Rev. D* **66**, 015002 (2002).
- [70] ALEPH, DELPHI, L3, and OPAL Collaborations, LEP Electroweak Working Group, and SLD Heavy Flavour Working Group, D. Abbaneo *et al.*, “A Combination of Preliminary Electroweak Measurements and Constraints on the Standard Model,” hep-ex/0212036.
- [71] J. Erler and P. Langacker, *Phys. Rev. Lett.* **84**, 212 (2000).
- [72] P. Langacker and M. Plümacher, *Phys. Rev. D* **62**, 013006 (2000).
- [73] P. Langacker and M. Luo, *Phys. Rev. D* **45**, 278 (1992).
- [74] S. Dimopoulos and D.W. Sutter, *Nucl. Phys.* **B452**, 496 (1995).
- [75] H.E. Haber, *Nucl. Phys. B (Proc. Suppl.)* **62A**, 469 (1998).
- [76] A. Kurylov and M.J. Ramsey-Musolf, *Phys. Rev. Lett.* **88**, 071804 (2002).
- [77] A. Kurylov, M.J. Ramsey-Musolf, and S. Su, “Parity-violating Electron Scattering as a Probe of Supersymmetry,” hep-ph/0205183.
- [78] A. Kurylov, M.J. Ramsey-Musolf, and S. Su, “Supersymmetric Effects in Deep Inelastic Neutrino Nucleus Scattering,” hep-ph/0301208.
- [79] L.J. Hall and M. Suzuki, *Nucl. Phys.* **B231**, 419 (1984).
- [80] B.C. Allanach, A. Dedes, and H.K. Dreiner, *Phys. Rev. D* **60**, 075014 (1999).
- [81] J.C. Pati and A. Salam, *Phys. Rev. Lett.* **32**, 1083 (1974).
- [82] G. Senjanovic and A. Sokorac, *Z. Phys. C* **20**, 255 (1983).
- [83] W. Buchmüller, R. Rückl, and D. Wyler, *Phys. Lett. B* **191**, 442 (1987).
- [84] K.M. Cheung, *Phys. Lett. B* **517**, 167 (2001).
- [85] I.S. Towner and J.C. Hardy, *Phys. Rev. C* **66**, 035501 (2002).